General Neutrino Interactions, Dark Matter, and Electroweak Phase Transition

by

Hongkai Liu

Bachelor of Science, China University of Mining and Technology, 2012

Master of Science, University of Mississippi, 2015

Submitted to the Graduate Faculty of
the Dietrich School of Arts and Sciences in partial fulfillment of
the requirements for the degree of

Doctor of Philosophy

University of Pittsburgh

2021

UNIVERSITY OF PITTSBURGH

DIETRICH SCHOOL OF ARTS AND SCIENCES

This dissertation was presented

by

Hongkai Liu

It was defended on

April 29, 2021

and approved by

Tao Han, Distinguished Professor, University of Pittsburgh

Brian Batell, Assistant Professor, University of Pittsburgh

Joseph Boudreau, Professor, University of Pittsburgh

W. Vincent Liu, Professor, University of Pittsburgh

Ira Rothstein, Professor, Carnegie Mellon University

Dissertation Director: Tao Han, Distinguished Professor, University of Pittsburgh

General Neutrino Interactions, Dark Matter, and Electroweak Phase Transition

Hongkai Liu, PhD

University of Pittsburgh, 2021

This thesis consists of several projects in two major directions: (1) neutrino non-standard interactions and (2) weakly interacting massive particle (WIMP) as cold dark matter (DM). In the neutrino physics studies, we work on searching general neutrino interactions (GNI) at both high-energy experiments, such as (HL -) LHC, LHeC, and low-energy experiments, like COHERENT. We consider GNI arose from two different scenarios. One is from a UV-complete flavored Z' model. Another one is in the Standard Model Effective Field Theory framework extended with right-handed neutrinos N (SMNEFT) framework. Along the line of the SMNEFT, we present the gauge coupling terms of the one-loop anomalous dimension matrix for renormalization group evolution (RGE) of the Wilson coefficients between a new physics scale and the electroweak scale. We calculate the Yukawa coupling contributions to the one-loop anomalous dimension matrix for the 11 dimension-six four-fermion SMNEFT operators. We also present the new contributions to the anomalous dimension matrix for the 14 four-fermion SMEFT operators that mix with the SMNEFT operators through the Yukawa couplings of the right-handed neutrinos. In the DM aspect, we work on a WIMP scenario with vanishingly small tree-level spin-independent (SI) scattering cross-sections. To thoroughly probe interesting and well-motivated WIMP scenarios, we calculate the electroweak corrections to the SI scattering amplitude at the tree-level blind spot from the next-to-leading-order (NLO). It is observed that in a significant region of the singlet-doublet model-space, the one-loop corrections “unblind” the tree-level blind spots and lead to detectable SI scattering rates at future multi-ton scale liquid Xenon experiments. We consider another WIMP DM candidates in a non-Abelian dark $\mathrm{SU(2)_D}$ model where the dark sector couples to the Standard Model (SM) through a Higgs portal. We utilize the existing collider results of the Higgs signal rate, direct heavy Higgs searches, and electroweak precision observables to constrain the model parameters. The resulting two stable massive dark gauge bosons and pseudo-Goldstone bosons from symmetry breaking can be viable cold

DM candidates. We study in detail the pattern of strong first-order phase transition and gravitational wave (GW) production triggered by the dark sector symmetry breaking.

Table of Contents

List of Tables

List of Figures

Preface

Foremost, I would like to thank my adviser, Dr. Tao Han for his continued guidance, mentorship, and support over the past six years, and the members of my committee for their support, advice, patience, and guidance.

I also would like to thank my research collaborators and colleagues. The interactions with them are very inspiring and fruitful.

A special thank you is deserved for my wife, Chao Zhou, for her unfailing support and encouragement, and my son, Zhoushu Liu, as he is an endless source of strength and joy during this special time.

Finally, I thank my parents for all their support and encouragement. I could not ask for a more loving, helpful support family, and I realize how lucky I am.

1.0 Introduction

The milestone discovery of the Higgs boson predicted in the Standard Model (SM) at the CERN Large Hadron Collider (LHC) has deepened our understanding of nature at the shortest distances, and in the same time sharpened our questions about the Universe. The three of the most pressing mysteries in contemporary particle physics and cosmology are the origin of neutrino masses and baryon asymmetry, and the nature of the dark matter (DM). The new physics accounting for the neutrino masses may be at very high scale and beyond the reach of our high-energy experiments. In this sense, a model-independent framework is appropriate to describe the new physics in the neutrino sector. In this thesis, we mainly focus on the general neutrino interaction, including all kinds of Lorentz structure. Weakly interacting massive particles (WIMP) is the mostly studied DM candidate as it can naturely obtaine the correct DM relic density. We consider two WIMP models one carries SM charges and the other does not. The new physics may be responsible for both DM and the baryon asymmetry in the Universe. In this thesis, we study one of such possibilities.

1.1 Neutrino General Interactions

Neutrino oscillations have been confirmed by many neutrino experiments using solar, atmospheric, reactor, and accelerator neutrinos in the last two decades. Since the explanation of neutrino oscillations requires nonvanishing neutrino masses, the observation of neutrino oscillation provides clear evidence of new physics beyond the Standard Model (BSM) [8]. A model-independent way of studying new physics in neutrino oscillations was first formulated in Ref. [9], and is now generalized in the framework of an effective field theory (EFT) for nonstandard interactions (NSI); for reviews see Ref. [10, 11, 12].

Generically, departures from the SM at energies below a new physics scale can be described by a model-independent EFT after integrating out the heavy degrees of freedom in the new physics sector. Such an effective Lagrangian was first constructed by Fermi for the 4-

fermion contact interaction involving a neutrino in nuclear β-decay. In the SM language, the contact interaction is a result of integrating out a heavy particle, the electroweak W-boson. Neutrino interactions at low energies can be obtained in this framework by integrating out the heavy particles $t, W^{\pm}, Z$ and the Higgs boson h. The 4-fermion neutrino interactions via the SM neutral and charged currents at the leading order (LO), after integrating out the Z and $W^{\pm}$ propagators, are

$$\mathscr{L}_{\text{SM}}^{NC} = -\frac{G_F}{\sqrt{2}}\delta^{\alpha\beta}\delta^{\gamma\delta}[\overline{\nu}_\alpha\gamma_\mu(1-\gamma_5)\nu_\beta][g_{L,f}\overline{f}_\gamma\gamma^\mu(1-\gamma_5)f_\delta + g_{R,f}\overline{f}_\gamma\gamma^\mu(1+\gamma_5)f_\delta]\,, \tag{1.1}$$

$$\mathscr{L}_{\text{SM}}^{CC} = -\frac{G_F}{\sqrt{2}}V^*_{\delta\gamma}\delta^{\alpha\beta}[\overline{\nu}_\alpha\gamma_\mu(1-\gamma_5)\ell_\beta][\overline{d}_\gamma\gamma^\mu(1-\gamma_5)u_\delta] + \text{h.c.}\,, \tag{1.2}$$

where the Fermi constant $G_F/\sqrt{2} = (2v^2)^{-1} = g_2^2/8M_W^2$. f denotes quarks and charged leptons, V is the CKM quark-mixing matrix, g_2 is the SM $\text{SU}(2)_\text{L}$ gauge coupling, M_W is the mass of the W boson given by the Higgs vacuum expectation value $gv_2/2$, and $\alpha,\ \beta,\ \gamma,$ and δ are flavor indices. The chiral couplings $g_{L,f}$ and $g_{R,f}$ are defined as

$$g_{L,f} = T_f^3 - Q_f\sin^2\theta_W\,, \quad g_{R,f} = -Q_f\sin^2\theta_W\,, \tag{1.3}$$

where Q_f is the fermion's charge in units of $+e$. We choose a flavor basis such that the down-type quark and the lepton Yukawa matrices are diagonal for convenience of calculation. The transformation for the up-type quarks between the flavor (primed) and mass basis (unprimed) reads

$$u'_{L,\alpha} = V^\dagger_{\alpha\beta}\, u_{L,\beta}\,. \tag{1.4}$$

In the spirit of EFT, the theory is valid only at low energies, $E \ll M_W$. To explore new physics near or above the electroweak scale, it is appropriate to adopt an EFT, respecting the full SM gauge symmetry $SU(3)_C \times SU(2)_L \times U(1)_Y$ with the SM field content, the so-called Standard Model Effective Field Theory (SMEFT) [13, 14, 15, 16].

Within the SMEFT framework, we can introduce neutrino non-standard interactions (NSI) at dimension-six level. To account for NSI, Wolfenstein proposed 4-fermion interactions with general couplings [9], that have helped understand matter effects in solar neutrino oscillation experiments. Much theoretical and experimental effort has been made to search for potential new physics along the lines of neutrino NSI; for reviews see Refs. [10, 11, 12].

Similar to the standard matter effect [9, 17], neutral current NSI affect neutrino propagation in matter via coherent forward scattering, in which the momentum transfer is negligibly small compared with other relevant scales involved. Therefore, the adoption of effective four-fermion interactions in Eq. (2.1) is well justified regardless of the mass of the mediator that induces NSI. Also, for neutrinos propagating in unpolarized matter at rest, only the vector combination contributes to the matter potential. To study NSI at both high-energy and low-energy experiments, we use a flavored Z' model as our benchmark model as discussed in Chapter 2. NSI only contains vector interactions as the absence of right-handed neutrinos in the SM.

However, the right-handed neutrino is one of most well studied extension of the SM motivated by, among other things, the observation of neutrino masses and mixing. There are well-motivated ultraviolet (UV) complete models that introduce SM singlet right-handed neutrinos. $U(1)_{B-L}$ extensions of the SM generate vector interactions between right-handed neutrinos and SM particles. In models with left-right symmetry [18, 19, 20], such interactions are generated after left-right symmetry breaking. Leptoquark models [21, 22] generate various neutrino-quark interactions. Each of these leads to model-dependent phenomenology if the new states are kinematically accessible, which we will not explore further. Instead of considering all possible models, an efficient alternative is to use a model independent approach based on the principles of effective theory. The idea is to construct all possible operators representing the interaction of the sterile neutrinos with the SM fields consistent with the symmetries of the SM. The validity of such a framework is between μ_{EW}- the scale of electroweak symmetry breaking- and Λ which is the cut-off scale for new physics. If light sterile neutrinos are now introduced in the theory, then one can construct the Standard Model Neutrino Effective Field Theory (SMNEFT) which augments SMEFT with sterile right-handed neutrinos n [23, 24, 25, 26, 22].

In Chapter 3 and 4, we adopt this framework including right-handed neutrino states n that are lighter than a keV. Naturally, they are "sterile neutrinos" with no SM gauge charges. However, we do not specify their possible Majorana mass terms. We restrict our study to the case in which the left-handed neutrino states are Dirac in nature. Then, new flavor-conserving neutral current vector and tensor interactions are possible. The SMNEFT has been presented in Ref. [26, 22]. We follow this well motivated formalism. A framework for model-independent General Neutrino Interactions (GNI) below the electroweak scale has been also constructed in Ref. [27]. All operators of scalar, pseudoscalar, vector, axial vector and tensor interactions of neutrinos with SM fermions are included, leading to potentially rich phenomenology. We note that scalar and tensor GNI operators cannot be embedded in SMEFT at the dimension-six level, but are present in SMNEFT.

1.2 WIMP Dark Matter

Another astonishing fact that cannot be explained by the SM is the existence of DM and matter (baryon asymmetry). There is mounting evidence for the existence of DM through its gravitational effects. WIMP, a possible candidate for the DM in the Universe, are being intensely searched for both in laboratory experiments and through a broad range of astrophysical probes [28, 29]. Among the laboratory probes, the decades-long programme looking for signals of nuclear recoil is the primary one, with increasing levels of sensitivity to the DM-nucleon scattering rate, owing to both larger fiducial detector volumes, as well as the construction of ultra-low noise detectors [30, 31, 32]. However, the null results of the last fifty years of searches challenge the most theoretically attractive candidates, namely, the standard weakly interacting massive particles (WIMPs), that are charged under the SM weak interactions (see Ref. [28] for review). We consider two different scenarios to go beyond the standard WIMP model. The first case is a WIMP DM but sit in a fine-tunning parameter space, called blind spot, in which the leading order predictions for DM-nucleon scattering cross-sections are negligibly small or even exactly zero either due to symmetry reasons or due to cancellations among different contributions to the relevant DM effective couplings. The details of this scenario are described in Chapter 5.

On the other hand, it is quite conceivable that the DM particles live in a dark sector that are not charged under the SM gauge group. Furthermore, the dark sector may have a rich particle spectrum, leading to other observable consequences [33]. A massless dark gauge field, dubbed as the dark radiation (DR), is one of the quite interesting extensions that could help to alleviate the tension between Planck and HST measurements of the Hubble constant [34]. DM-DR interactions and DM self-interactions can provide solutions to the small-scale structure problems which challenge the cold dark matter (CDM) paradigm [35, 36, 37].

In Chapter 6, we would like to explore the potentially observable effects beyond the gravitational interactions from a hypothetical dark sector. We assume that the dark sector interacts with the SM particles only through the Higgs portal [38]. An immediate consequence of this would be the modification of the Higgs boson properties that will be probed in the on-going and future high energy experiments [39, 40]. The DM searches from the direct and indirect detection experiments will provide additional tests for the theory [28]. Perhaps, an even more significant impact would be on the nature of the electroweak phase transition (EWPT) at the early Universe (see, e.g., [41, 42, 43] for recent reviews), which could shed light on another profound mystery: the origin of baryon asymmetry in the Universe. Indeed, one of the best-motivated solutions to this mystery is the electroweak baryogenesis (EWBG) [44, 45, 46, 47] (see also [48, 49] for pedagogical introductions). For a successful generation of the baryon asymmetry during the EWPT, all of the three Sakharov conditions [50] have to be satisfied. One of the three Sakharov conditions is to assure a strong first-order phase transition (FOPT), that is absent within the minimal SM, but could be achieved by the Higgs portal to a sector beyond the SM. It is important to note that many well-motivated extensions of the SM predict gravitational wave (GW) signals through a strong FOPT, that are potentially detectable at future LISA-like space-based GW detectors.

2.0 Non-Standard Neutrino Interactions with Flavored Gauge Boson Z'

In this chapter, we consider the NSI induced by a flavored gauge boson Z' [51]. In general, neutral and charged current NSI can be described by dimension-six four-fermion operators of the form [9, 52],

$$\begin{aligned}\mathscr{L}_{\rm NSI}^{\rm NC} &= -2\sqrt{2}G_F \sum_C \epsilon_{\alpha\beta}^{fP_C}(\bar{\nu}_\alpha\gamma^\mu P_L \nu_\beta)(\bar{f}\gamma_\mu P_C f)\\ &= -\sqrt{2}G_F\epsilon_{\alpha\beta}^{fV}(\bar{\nu}_\alpha\gamma^\mu P_L\nu_\beta)(\bar{f}\gamma_\mu f) - \sqrt{2}G_F\epsilon_{\alpha\beta}^{fA}(\bar{\nu}_\alpha\gamma^\mu P_L\nu_\beta)(\bar{f}\gamma_\mu\gamma^5 f)\,,\end{aligned} \tag{2.1}$$

$$\begin{aligned}\mathscr{L}_{\rm NSI}^{\rm CC} &= -2\sqrt{2}G_F \sum_C \epsilon_{\alpha\beta}^{ff',P_C}(\bar{\nu}_\alpha\gamma^\mu P_L \ell_\beta)(\bar{f}\gamma_\mu P_C f')\\ &= -\sqrt{2}G_F\epsilon_{\alpha\beta}^{ff',V}(\bar{\nu}_\alpha\gamma^\mu P_L\ell_\beta)(\bar{f}\gamma_\mu f') - \sqrt{2}G_F\epsilon_{\alpha\beta}^{ff',A}(\bar{\nu}_\alpha\gamma^\mu P_L\ell_\beta)(\bar{f}\gamma_\mu\gamma^5 f')\,,\end{aligned} \tag{2.2}$$

where α, β label the lepton flavors (e, μ, τ), f and f' denote the fermion fields (u, d, e), and C indicates the chirality (L, R). Here,

$$\epsilon_{\alpha\beta}^{fV} \equiv \epsilon_{\alpha\beta}^{fL} + \epsilon_{\alpha\beta}^{fR}\,, \quad \epsilon_{\alpha\beta}^{fA} \equiv \epsilon_{\alpha\beta}^{fR} - \epsilon_{\alpha\beta}^{fL}\,, \tag{2.3}$$

with $\epsilon_{\alpha\beta}^{fL}$, $\epsilon_{\alpha\beta}^{fR}$ being dimensionless parameters that quantify the strength of the new interactions in units of the Fermi constant, $G_F \equiv (\sqrt{2}v_h^2)^{-1}$, with $v_h = 246$ GeV, the electroweak scale. These contact interactions arise as a result of integrating out a vector mediator significantly heavier than the typical momentum transfer of the processes. As such, the dimensionless coupling parameters are naturally of the order of $\epsilon \sim g'^2 v_h^2/M^2$, where M and g' are the mediator's mass and coupling. Note that NSI are of the same form as Eqs. (1.1) and (1.2), but the scale and couplings are free parameters to reflect the unknown nature of new physics.

In this chapter, we focus on a simple model in which the NSI is induced by a gauge boson Z' associated with a new $U(1)'$ symmetry. Assuming the presence of three right-handed neutrinos, the most general anomaly-free $U(1)'$ model can be generated by

$$X = Q'_1 B_1 + Q'_2 B_2 + Q'_3 B_3 + Q'_e L_e + Q'_\mu L_\mu + Q'_\tau L_\tau\,, \tag{2.4}$$

with the quark charges $Q'_{1,2,3}$ and lepton charges $Q'_{e,\mu,\tau}$ satisfying the constraint [53]

$$3(Q'_1 + Q'_2 + Q'_3) + Q'_e + Q'_\mu + Q'_\tau = 0\,. \tag{2.5}$$

We further require $Q'_1 = Q'_2 = Q'_3 = Q'_q$ to avoid large flavor changing neutral currents in the quark sector. The Lagrangian can be written as

$$\mathscr{L} = \mathscr{L}_{\rm SM} - \frac{1}{4}Z'^{\mu\nu}Z'_{\mu\nu} + \frac{1}{2}M^2_{Z'}Z'^{\mu}Z'_{\mu} + Z'_{\mu}J^{\mu}_{X}, \tag{2.6}$$

where the current[1]

$$J^{\mu}_{X} = g'\left[\sum_q Q'_q\bar{q}\gamma^{\mu}q + \sum_{L_\ell=\nu_{\ell L},\ell} Q'_\ell\overline{L_\ell}\gamma^{\mu}L_\ell\right]\,, \tag{2.7}$$

with g' being the $U(1)'$ coupling constant. Since neutrino oscillations are not affected by flavor universal NSI, here we only consider nonuniversal flavor-conserving NSI. Also, because scenarios involving L_e are heavily constrained in the low-mass region by electron beam-dump experiments [54, 55, 56, 57, 58, 59], we set $Q'_e = 0$ and only consider the less constrained eletrophobic NSI. For the sake of illustration, we take the following three cases for our benchmark studies [60]:

(A) $Q'_q = 1/3, Q'_\mu = -3, Q'_e = Q'_\tau = 0.$
(B) $Q'_q = 1/3, Q'_\mu = Q'_\tau = -3/2, Q'_e = 0.$
(C) $Q'_q = 1/3, Q'_\tau = -3, Q'_e = Q'_\mu = 0.$

Note that in all three cases the new gauge boson couples to quarks universally. The partial decay width to a pair of fermions is given by

$$\Gamma(Z' \to f\bar{f}) = \frac{N_f Q'^2_f g'^2}{12\pi M_{Z'}}(M^2_{Z'} + 2m^2_f)\sqrt{1 - \frac{4m^2_f}{M^2_{Z'}}}\,, \tag{2.8}$$

where $N_q = 3$, $N_l = 1$, and $N_\nu = 1/2$. The branching fractions can then be calculated assuming that the total decay width of the Z' is the sum over the SM fermion final states given in Fig. 1. It is important to note that a SM gauge-invariant formulation of NSI often leads to simultaneous couplings to charged leptons due to the symmetry nature of the gauge doublet[2] (ν, ℓ). This opens up new avenues to search for the new physics associated with

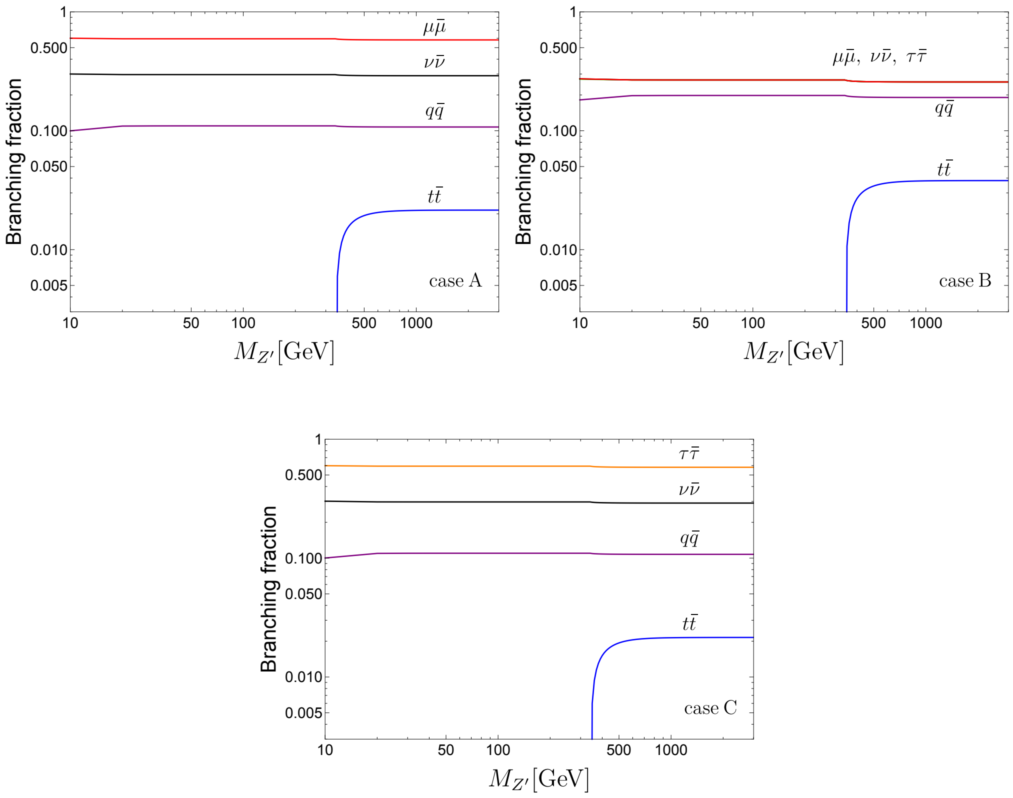

Figure 1: The branching fractions of Z' for Case A (upper right), B (upper left), and C (bottom), with $q = \{u, d, c, s, b\}$.

NSI, and it also results in stringent constraints on NSI owing to the correlation with the charged leptons. As such, the new gauge boson, if heavy, can be most conveniently searched for at high-energy colliders, especially at the LHC in the di-lepton final state,

$$p\,p \to \ell^+\ell^- + X\,, \tag{2.9}$$

where X denoted everything in an inclusive search. For our benchmark choices, we have $\ell = \mu$ for Cases A and B, and $\ell = \tau$ for Case C. We note that in Cases A and B, where muon number L_μ is involved, one also can make use of $e^+e^-/pp \to 4\mu$ decays at the B-factories

---

[1] We have decoupled ν_R assuming they are heavy and inaccessible.

[2] It is possible, though, to arrange for the charged lepton coupling to vanish [61, 62].

and LHC to search for a relatively low mass gauge boson. We do not consider Z' bosons lighter than 5 MeV to avoid affecting big bang nucleosynthesis. Once a signal for new physics is observed, it is ultimately important to seek other complementary signals to establish a consistent picture of the underlying physics. In this thesis, we set out to consider correlated signatures between CEνNS and collider searches.

2.1 Neutrino Oscillation Experiments

The Hamiltonian for neutrino propagation in the presence of neutral current NSI is

$$H = \frac{1}{2E} U \begin{pmatrix} 0 & 0 & 0 \\ 0 & \Delta m^2_{21} & 0 \\ 0 & 0 & \Delta m^2_{31} \end{pmatrix} U^\dagger + V \,, \tag{2.10}$$

where E is the neutrino energy and U is the Pontecorvo-Maki-Nakagawa-Sakata (PMNS) mixing matrix [8]

$$U = \begin{pmatrix} c_{13}c_{12} & c_{13}s_{12} & s_{13}e^{-i\delta} \\ -s_{12}c_{23} - c_{12}s_{23}s_{13}e^{i\delta} & c_{12}c_{23} - s_{12}s_{23}s_{13}e^{i\delta} & c_{13}s_{23} \\ s_{12}s_{23} - c_{12}c_{23}s_{13}e^{i\delta} & -c_{12}s_{23} - s_{12}c_{23}s_{13}e^{i\delta} & c_{13}c_{23} \end{pmatrix} , \tag{2.11}$$

and V is the potential from interactions of neutrinos in matter, which can be expressed using the NSI operators in Eq. (2.1) as

$$V = V_{CC} \begin{pmatrix} 1 + \epsilon_{ee} & \epsilon_{e\mu} & \epsilon_{e\tau} \\ \epsilon^*_{e\mu} & \epsilon_{\mu\mu} & \epsilon_{\mu\tau} \\ \epsilon^*_{e\tau} & \epsilon^*_{\mu\tau} & \epsilon_{\tau\tau} \end{pmatrix} . \tag{2.12}$$

Here, $V_{CC} \equiv \sqrt{2} G_F N_e$, is the standard matter potential, and the effective NSI parameters are

$$\epsilon_{\alpha\beta} \equiv \sum_q \epsilon^{qV}_{\alpha\beta} \frac{N_q}{N_e} \tag{2.13}$$

with $N_{q,e}$ the number density of fermions $q = u, d$ and e. The diagonal elements are real and can lead to lepton flavor non-universality. The off-diagonal terms are complex and can generate flavor-changing processes. There are a total of 3 ($f = \{u, d, e\}$) × 2 ($C = \{R, L\}$) × 9 = 54 free parameters in the NSI parameterization. Neutrino oscillation experiments are not sensitive to the absolute matter potential. Thus, without loss of generality, the $\epsilon_{\mu\mu}$ can be subtracted out and the diagonal parts are $\mathrm{diag}(1+\epsilon_{ee}-\epsilon_{\mu\mu}, 0, \epsilon_{\tau\tau}-\epsilon_{\mu\mu})$. This degeneracy can be probed by scattering experiment, like COHERENT. As a consequence of the CPT symmetry, neutrino propagation is invariant under $H \to -H^*$, which lead to

$$\begin{aligned}
\Delta m^2_{31} &\to -\Delta m^2_{31} + \Delta m^2_{21} = -\Delta m^2_{32}, && (2.14)\\
\theta_{12} &\to \pi/2 - \theta_{12}, && (2.15)\\
\delta_{CP} &\to \pi - \delta_{CP}, && (2.16)\\
\epsilon_{ee} - \epsilon_{\mu\mu} &\to -(\epsilon_{ee} - \epsilon_{\mu\mu}) - 2, && (2.17)\\
\epsilon_{\tau\tau} - \epsilon_{\mu\mu} &\to -(\epsilon_{\tau\tau} - \epsilon_{\mu\mu}), && (2.18)\\
\epsilon_{\alpha\beta} &\to -\epsilon^*_{\beta\alpha} \quad (\alpha \neq \beta). && (2.19)
\end{aligned}$$

The transformation in Eq. (2.14) will flip the mass spectrum. So, there is degeneracy in NSI parameters with different mass ordering. This is also probable via scattering experiments.

The charged-current NSI can modify the production and detection in the neutrino oscillation experiments. In this work, we will noly consider neutral-current NSI induced from a Z' model. Since neutrino propagation in matter is affected by coherent forward scattering, in which the momentum transfer is zero, the effective Lagrangian from Eq. (2.6) that is relevant for NSI can be written as

$$\mathscr{L}_{\text{eff}} = -\frac{(g')^2}{M^2_{Z'}} \left[\sum_q Q'_q \bar{q}\gamma^\mu q\right] \left[\sum_\alpha Q'_\alpha \bar{\nu}_\alpha \gamma^\mu P_L \nu_\alpha\right], \tag{2.20}$$

regardless of the Z' mass. Comparing Eqs. (2.1) and (2.20), we have

$$\epsilon^{qV}_{\alpha\alpha} = \frac{(g')^2 Q'_\alpha Q'_q}{\sqrt{2} G_F M^2_{Z'}}. \tag{2.21}$$

We can then use the bounds on the NSI parameters from neutrino oscillation experiments to constrain the parameter spaces in the Z' models. For Case A (C), the model predicts

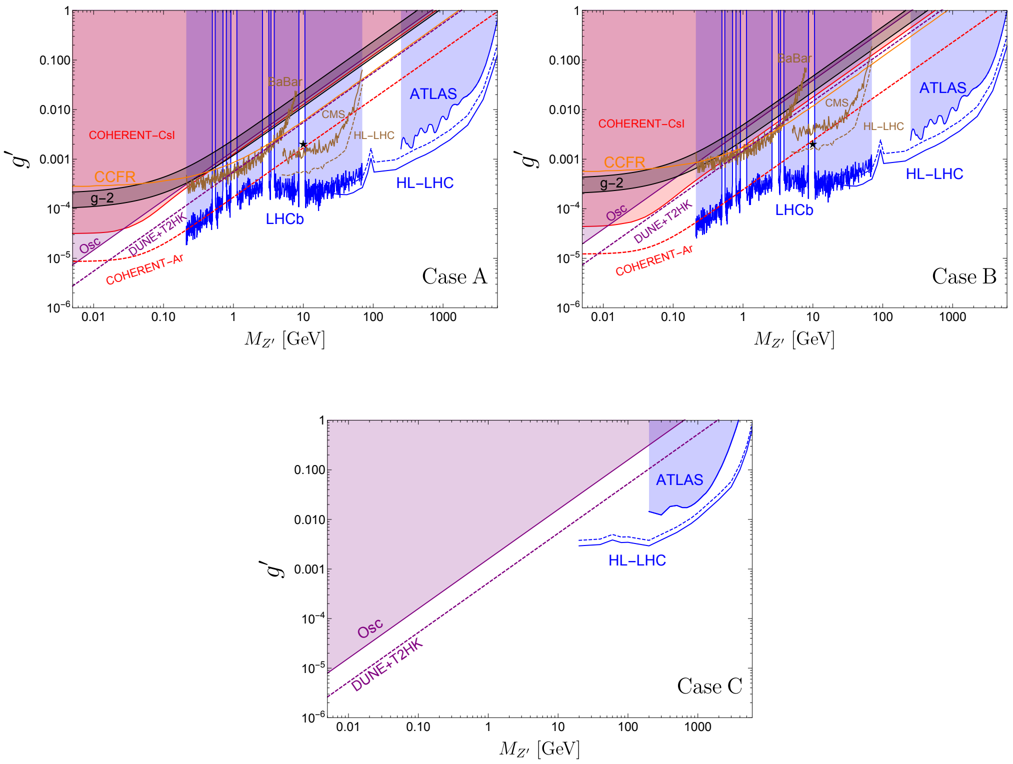

Figure 2: Bounds on g' for Cases A (upper left panel), B (upper right panel) and C (lower panel). The details of descriptions are in the main text.

that only $\epsilon_{\mu\mu}$ ($\epsilon_{\tau\tau}$) is nonzero. For Case B, since $\epsilon_{\mu\mu}$ is equal to $\epsilon_{\tau\tau}$, and neutrino oscillation probabilities are not affected by a subtraction of a diagonal contribution from the full Hamiltonian, we can obtain constraints on Case B from bounds on NSI with only ϵ_{ee} being nonzero.

We adopt the 2σ bounds on $\epsilon^u_{\alpha\alpha}$ from the global analysis of current oscillation data [1] as compiled in Table 1. Note that neutrino oscillation data constrain differences between two diagonal ϵ's, not individual diagonal ϵ's. To obtain bounds on a single ϵ, we set one of the two ϵ's to be zero. We bound $\epsilon^u_{\mu\mu}$ by choosing the smaller of the values obtained by setting $\epsilon^u_{ee} = 0$ in $\epsilon^u_{ee} - \epsilon^u_{\mu\mu}$ and $\epsilon^u_{\tau\tau} = 0$ in $\epsilon^u_{\tau\tau} - \epsilon^u_{\mu\mu}$. We apply them to constrain the theory parameter space in the $(M_{Z'}, g')$ plane and the exclusion regions are shown as the

	Current data	DUNE+T2HK
ϵ^u_{ee}	$[-1.192, -0.802] \oplus [-0.020, +0.456]$	$[-0.407, -0.270] \oplus [-0.072, +0.064]$
$\epsilon^u_{\mu\mu}$	$[-0.130, 0.152]$	$[-0.019, +0.018]$
$\epsilon^u_{\tau\tau}$	$[-0.152, 0.130]$	$[-0.017, +0.017]$

Table 1: 2σ allowed ranges for the diagonal NSI parameters from the global analysis of current neutrino oscillation data [1], and from a simulation of DUNE and T2HK.

purple areas in Fig. 2. Note that the bounds from the global analysis are obtained under the assumption that all NSI parameters are nonzero and then projected to one NSI parameter. Since degeneracies among NSI parameters can significantly weaken the constraints on an individual NSI parameter [63], the current bounds from the global analysis of oscillation data should be considered to be conservative.

We also consider the sensitivity of the next generation long-baseline neutrino oscillation experiments, DUNE [64] and T2HK [65]. We follow the procedure of Ref. [66], and simulate the DUNE and T2HK data assuming the normal neutrino mass hierarchy, the neutrino CP phase $\delta = 0$, and $\epsilon_{\alpha\alpha} = 0$. We scan over both the mass hierarchies, the neutrino oscillation parameters and take only one diagonal $\epsilon_{\alpha\alpha}$ to be nonzero at a time. The 2σ allowed ranges for the diagonal NSI parameters are provided in the last column of Table 1. The expected sensitivities in the $(M_{Z'}, g')$ parameter space are shown as the purple dashed lines in Fig. 2. As expected, it simply scales linearly with $g'/M_{Z'}$. The reaches for the three cases are roughly similar. For instance, at $M_{Z'} \sim 10$ GeV, the sensitivity for the couplings can reach $g' \sim 0.008\,(0.02)\,[0.008]$ for Case A (B) [C]. We see that future bounds on NSI will be improved by a factor of a few compared to current bounds, and the current constraints on the parameter space in Case C for $M_{Z'} \lesssim 200$ GeV only come from neutrino oscillation data.

2.2 CEνNS

CEνNS has recently been measured by the COHERENT experiment, which detects neutrinos from the Spallation Neutron Source (SNS) at Oak Ridge National Laboratory. Neutrinos at the SNS [67] consist of a prompt component of monoenergetic ν_μ from the stopped pion decays, $\pi^+ \to \mu^+ + \nu_\mu$, and two delayed components of $\bar{\nu}_\mu$ and ν_e from the subsequent muon decays, $\mu^+ \to e^+ + \bar{\nu}_\mu + \nu_e$. As a result of two-body decay, the ν_μ is monochromatic with energy to be $E_{\nu_\mu} = (m_\pi^2 - m_\mu^2)/(2m_\pi) \approx 29.7$ MeV, where m_π and m_μ are the pion and muon masses, respectively. The delayed neutrinos ν_e and $\bar{\nu}_\mu$ follow a continuous distribution with a kinematic upper bound, $m_\mu/2 \approx 50$ MeV. The normalized fluxes of three neutrino flavors (ν_μ, $\bar{\nu}_\mu$ and ν_e) are well known and given by

$$\begin{aligned}
\phi_{\nu_\mu}(E_{\nu_\mu}) &= \mathcal{N} \frac{2m_\pi}{m_\pi^2 - m_\mu^2}\, \delta \left(1 - \frac{2E_{\nu_\mu} m_\pi}{m_\pi^2 - m_\mu^2}\right) \,, \\
\phi_{\nu_e}(E_{\nu_e}) &= \mathcal{N} \frac{192}{m_\mu} \left(\frac{E_{\nu_e}}{m_\mu}\right)^2 \left(\frac{1}{2} - \frac{E_{\nu_e}}{m_\mu}\right) \,, \\
\phi_{\bar{\nu}_\mu}(E_{\bar{\nu}_\mu}) &= \mathcal{N} \frac{64}{m_\mu} \left(\frac{E_{\bar{\nu}_\mu}}{m_\mu}\right)^2 \left(\frac{3}{4} - \frac{E_{\bar{\nu}_\mu}}{m_\mu}\right) \,,
\end{aligned} \tag{2.22}$$

where $\mathcal{N}$ is a normalization factor determined by the experimental setup. The expected number of events with recoil energy in the energy range $[E_r,\, E_r + \Delta E_r]$ and arrival time in the time interval $[t,\, t + \Delta t]$ is given by

$$N_{th}(t, E_r, \epsilon) = \sum_\alpha \frac{m_{\rm det} N_A}{M} \int_{\Delta E_r} dE_r \int_{\Delta t} dt \rho_\alpha(t) \int_{E_\nu^{\rm min}}^{E_\nu^{\rm max}} dE_\nu\, \phi_\alpha(E_\nu) \, \frac{d\sigma_\alpha(\epsilon)}{dE_r} \,, \tag{2.23}$$

where $m_{\rm det}$ is the detector mass, M is the molar mass of the target nucleus, $N_A = 6.022 \times 10^{23}\,{\rm mol}^{-1}$, $\rho_\alpha(t)$ is the arrival time Probability Density Function (PDF) provided in the COHERENT data release [68], and $\alpha = \nu_\mu, \bar{\nu}_\mu, \nu_e$. We assume that the presence of new neutral current interactions do not modify the arrival time PDF.

Neglecting radiative corrections, the differential cross section for a given neutrino flavor ν_α scattering off a nucleus is given by

$$\frac{d\sigma_\alpha(\epsilon)}{dE_r} = \frac{G_F^2}{2\pi} Q_\alpha^2 F^2(Q^2) M (2 - \frac{M E_r}{E_\nu^2}) \,, \tag{2.24}$$

where $F(Q^2)$ refers to the nuclear form factor taken from Ref. [69]. In the presence of NSI, the effective charge can be written as

$$Q_\alpha^2 = [Z(g_p^V + 2\epsilon_{\alpha\alpha}^{uV} + \epsilon_{\alpha\alpha}^{dV}) + N(g_n^V + \epsilon_{\alpha\alpha}^{uV} + 2\epsilon_{\alpha\alpha}^{dV})]^2 \,, \tag{2.25}$$

where Z (N) is the number of protons (neutrons) in the nucleus, $g_p^V = \frac{1}{2} - 2\sin^2\theta_W$ and $g_n^V = -\frac{1}{2}$ are the SM weak couplings, and θ_W is the weak mixing angle. The NSI parameters for coupling to up and down quarks can be written as

$$\begin{aligned} \epsilon_{ee}^{uV} = \epsilon_{ee}^{dV} &= \frac{g'^2 Q'_q Q'_e}{\sqrt{2} G_F (2ME_r + M_{Z'}^2)} \,, \\ \epsilon_{\mu\mu}^{uV} = \epsilon_{\mu\mu}^{dV} &= \frac{g'^2 Q'_q Q'_\mu}{\sqrt{2} G_F (2ME_r + M_{Z'}^2)} \,. \end{aligned} \tag{2.26}$$

For the CsI detector, the total cross section is a sum of the contributions of ^{133}Cs and ^{127}I, i.e.,

$$\frac{d\sigma_{\alpha,\mathrm{CsI}}}{dE_r} = \frac{d\sigma_{\alpha,\mathrm{Cs}}}{dE_r} + \frac{d\sigma_{\alpha,\mathrm{I}}}{dE_r} \,. \tag{2.27}$$

To compare with COHERENT data, we convert the nuclear recoil energy to the number of photoelectrons (n_{PE}) using the relation [70],

$$n_{\mathrm{PE}} = 1.17 (E_r/\mathrm{keV}) \,. \tag{2.28}$$

Note that we do not use the new quenching factor reported in Ref. [71] as it is still under investigation by the COHERENT collaboration [72]. We employ the acceptance function [68],

$$\mathcal{A}(n_{\mathrm{PE}}) = \frac{k_1}{1 + e^{-k_2 (n_{\mathrm{PE}} - x_0)}} \theta(n_{\mathrm{PE}} - 5) \,, \tag{2.29}$$

where $k_1 = 0.6655$, $k_2 = 0.4942$, $x_0 = 10.8507$ and $\theta(x)$ is the Heaviside step function.

Because the number of events is small and experimental uncertainties large, we use the energy spectrum (but not the timing information) measured by the CsI detector to evaluate the statistical significance of a nonstandard scenario. We define

$$\chi^2 = \sum_{i=4}^{15} \left[\frac{N_{\mathrm{meas}}^i - N_{\mathrm{th}}^i (1+\gamma) - B_{\mathrm{on}}(1+\beta)}{\sigma_{\mathrm{stat}}^i} \right]^2 + \left(\frac{\gamma}{\sigma_\gamma} \right)^2 + \left(\frac{\beta}{\sigma_\beta} \right)^2 \,, \tag{2.30}$$

where $N^i_{\rm meas}$ and $N^i_{\rm th}$is the number of measured and predicted events per energy bin, respectively. The statistical uncertainty per energy bin is $\sigma^i_{\rm stat} = \sqrt{N^i_{\rm exp} + 2B^i_{\rm SS} + B^i_{\rm on}}$, where $B_{\rm SS}$ and $B_{\rm on}$ are the estimated steady-state and beam-on backgrounds, respectively. $B_{\rm SS}$ is determined by the anti-coincident (AC) data, and $B_{\rm on}$ mainly consists of prompt neutrons. Both the spectral and temporal distributions of the backgrounds are provided by the COHERENT collaboration [68]. For the signal normalization uncertainty, we follow the original COHERENT analysis and choose $\sigma_\gamma = 0.28$, which includes the neutrino flux uncertainty (10%), form factor uncertainty (5%), signal acceptance uncertainty (5%), and quenching factor uncertainty (25%). For the beam-on background uncertainty, we fix $\sigma_\beta = 0.25$ [70]. We scan over values of the coupling g' and the mediator mass $M_{Z'}$. The 2σ exclusion regions in the $(M_{Z'}, g')$ plane are shown as the red regions in Fig. 2 for Cases A and B. For $M_{Z'} \gtrsim 50$ MeV, the current constraint from COHERENT CsI is comparable to the expected sensitivity of DUNE+T2HK for Case B, and is weaker by about a factor of two for Case A. For very small $M_{Z'}$ DUNE+T2HK has greater sensitivty than the current COHERENT bounds for both Cases A and B. Note that COHERENT data does not place bounds on Case C because the SNS beam does not have ν_τ and $\bar{\nu}_\tau$.

The COHERENT collaboration has an extensive upgrade plan [73], part of which is a 750 kg LAr detector located at $L = 29$ m from the source. We assume a 4-year exposure with the same neutrino production rate as the current setup, which corresponds to 8.4×10^{23} protons-on-target (POT) in total. Since both the spectral and temporal distributions of the recoil energy events depend on the flavor structure, we perform a two dimensional analysis that utilizes both the spectral and temporal information. To estimate the projected sensitivities at the LAr detector, we adopt the likelihood function from Ref. [74], i.e.,

$$\mathcal{L}(\vec{\theta}) \propto \prod_{(t,E_r)} \int\int \exp\{-\lambda(t,E_r)\} \frac{\{\lambda(t,E_r)\}^{N_{obs}(t,E_r)}}{N_{obs}(t,E_r)!} \times \frac{\exp(-\gamma^2/2\sigma_\gamma^2)}{\sqrt{\sigma_\gamma^2}} \\ \times \exp\{-\beta N_{obs,bg}(t,E_r)\} \frac{\{\beta N_{obs,bg}(t,E_r)\}^{N_{obs,bg}(t,E_r)}}{N_{obs,bg}(t,E_r)!} \, \mathrm{d}\gamma \, \mathrm{d}\beta \,. \tag{2.31}$$

where $\lambda(t,E_r) = (1+\gamma)N_{th}(t,E_r,\epsilon) + \beta N_{obs,bg}(t,E_r)$. We calculate the number of events expected in the SM for each bin within the range $0 < t < 6\,\mu s$ and 20 keV $< E_{\rm r} <$ 100 keV, with bin sizes of 0.5 μs and 2 keV, respectively. We assume that the steady-state background is uniform in energy and is 1/4 of the SM expectation. We also assume the systematic uncertainty σ_γ to be 17.5%, which corresponds to a reduced quenching factor uncertainty of 12.5% for LAr. A more precise treatment would include energy-dependent form factor uncertainties [75]. The projected sensitivities are shown by the purple dashed line in Fig. 2. A factor of three improvement is expected in the sensitivity to the coupling, compared to the current CsI results. We see that future CEνNS experiments will set stronger bounds than next generation neutrino oscillation experiments for most Z' masses in Cases A and B, and will provide the strongest constraints for 20 (10) MeV $\lesssim M_{Z'} \lesssim$ 1 GeV in Case A (B).

2.3 Collider Searches

As emphasized in the introduction, a SM gauge-invariant formulation of NSI often results in simultaneous couplings to charged leptons. This opens up new avenues to search for the new physics associated with NSI, in particular at colliders. We explore the sensitivity reach at the LHC for NSI via a di-lepton final state from the Drell-Yan (DY) production of a Z',

$$pp \to Z' \to \ell^+\ell^- + X \,, \tag{2.32}$$

with $\ell = \mu, \tau$ and X denotes other inclusive states (like a jet) when kinematically favorable for the signal identification. This is a particularly sensitive signal $M_{Z'} > M_Z$. We also include a four-lepton final state,

$$pp \to Z^*/\gamma^* \to \ell^+\ell^- + Z' \to \ell^+\ell^- + \ell^+\ell^- + X. \tag{2.33}$$

This channel is more suitable for a low mass Z' as we will see below.

We use the Monte Carlo event generator MadGraph5_aMC@NLO [76] to generate signal and background samples with the NN23LO1 PDF set [77]. The NSI Lagrangian is implemented in the FeynRules 2.0 [78] framework. Pythia 8.1 [79, 80] is used for parton showering and hadronization. Matching is performed with the MLM prescription [81]. The generated events are passed into Delphes 3.4.1 [82] for fast detector simulation.

2.3.1 Cases A and B: μ final states

In Case A, the new gauge boson couples to quarks universally, and only to second generation leptons. While in Case B, the new gauge boson couples equally to second and third generations leptons. We first apply the existing LHC bound on searches for the di-muon final state to both cases, given that muons are much easier to identify than taus at the LHC. ATLAS [83] has performed a search for di-lepton resonances in the 250 GeV $\lesssim M_{Z'} \lesssim 6$ TeV mass range setting a 2σ upper limit on the fiducial cross section times branching ratio with 139 fb^{-1} at $\sqrt{s} = 13$ TeV. The fiducial region is defined by the acceptance cuts,

$$p_T^\mu > 30 \text{ GeV}, \quad |\eta_\mu| < 2.5, \quad m_{\ell\ell} > M_{Z'} - 2\Gamma_{Z'} \,. \tag{2.34}$$

To extract limits on g', we calculate $\sigma(pp \to Z' + X) \cdot B(Z' \to \mu^+\mu^-)$ in the fiducial region at leading order (LO). The expected signal yields are rescaled to next-to-leading order (NLO) accuracy using a K-factor of 1.3 [84]. From the auxiliary figure 2c of Ref. [83], the upper limits at 2σ on the fiducial cross section from ATLAS are translated into the bounds on our model parameters, shown as the blue shaded regions in the upper panels of Fig. 2. This search excludes $g' \gtrsim 1.6$ (2.4) $\times 10^{-3}$ for $M_{Z'} \approx 250$ GeV in Case A (B).

Searches for dark photons decaying to di-leptons can shed light on new vector bosons, especially relatively light ones. In Cases A and B, we recast prompt-like dark photon searches at LHCb [85] to obtain constraints in the mass range 200 MeV to 70 GeV based on the framework developed in Ref. [86]. This is the most sensitive probe currently in this mass window except near the resonances like J/ψ, Υ and approaching the Z-pole. The corresponding upper limits on the coupling at 90% CL are shown by the blue shaded regions in Fig. 2.

Having discussed the bounds from the di-muon final state, we turn to the four-muon final state. Both the BaBar and CMS have performed searches for the decay, $\gamma^*/Z^* \to \mu^+\mu^- Z' \to 4\mu$. The BaBar searches [87] set a 90% CL upper limit on the new gauge coupling based on a $L_\mu - L_\tau$ model corresponding to $Q'_q = Q'_e = 0$, $Q'_\mu = -Q'_\tau = 1$ in our parameterization. The CMS searches [88] set a 2σ upper limit on g' by assuming the branching ratio $B(Z' \to \mu^+\mu^-) = 1/3$ and $Q'_\mu = 1$. By rescaling the observed bounds according to the branching fractions and production cross section, we extract bounds for our scenarios. The brown curves show the BaBar and CMS bounds in the upper panels of Fig. 2. We see that the current bound from the LHCb dark photon search is dominant in the medium mass range and disfavors $g' \gtrsim 10^{-4}$ for $M_{Z'} \approx 200$ MeV.

We further estimate the sensitivity reach via the di-muon channel $Z' \to \mu^+\mu^-$ for $10 \lesssim M_{Z'} \lesssim 6000$ GeV at the high-luminosity LHC (HL-LHC) with the full 3000 fb^{-1} integrated luminosity. The signal is from the DY process as in Eq. (2.32). We select events that contain at least two opposite-sign muons. The leading (subleading) muon is required to have $p_T > 22$ (10) GeV. All muons are required to have $|\eta| < 2.4$. Finally, in calculating the sensitivity, we apply a mass window cut $0.97\ M_{Z'} < M(\ell^+\ell^-) < 1.03\ M_{Z'}$ below 3 TeV, and use a $3-6$ TeV mass window to ensure enough background events in the high mass region, to optimize the signal observability. The dominant background is from the SM DY process. We also include smaller background contributions from $t\bar{t}$, tW, WW and ZZ. We generate the signal and DY background with up to two additional jets in the phase space $M_{\mu\mu} < 60$ GeV. This is so that for a lighter Z', the additional jets help to kick the leptons to a high momentum for more efficient triggering. For $M_{\mu\mu} > 60$ GeV, we generate the signal and DY background at LO and apply the combined QCD and electroweak corrections to the invariant mass distributions according to Ref. [89]. $t\bar{t}$ and tW backgrounds are generated at LO and normalized to NNLO + NNLL by a K-factor of 1.84 [90] and 1.35 [91] respectively. The WW, WZ, and ZZ backgrounds are normalized to NNLO QCD by a K-factor of 1.98 [92], 2.07 [93], and 1.74 [94] respectively. The local significance is defined as

$$S_l = \frac{N_S}{\sqrt{N_B}}, \tag{2.35}$$

where N_S (N_B) is the expected number of signal (SM background) events. The blue solid (dashed) curves in the upper panels of Fig. 2 show the 2σ (5σ) sensitivities. The sensitivity is significantly improved in a broad mass range.

2.3.2 Case C: τ final states

For Case C, the signal channel at the LHC is $pp \to Z' + X$ with Z' decaying to a tau pair. For a high-mass mediator decaying to di-tau, ATLAS [95] and CMS [96] have set a 2σ upper limit on inclusive $\sigma(pp \to Z' + X) \cdot B(Z' \to \tau^+\tau^-)$ in the 200 GeV $\lesssim M_{Z'} \lesssim$ 4 TeV (ATLAS) and 500 GeV $\lesssim M_{Z'} \lesssim$ 3 TeV (CMS) mass ranges with $\sqrt{s} = 13$ TeV and 36.1 fb^{-1} and 2.2 fb^{-1}, respectively. We only display the ATLAS constraint on g' in the lower panel of Fig. 2.

We also estimate the sensitivity reach for 20 GeV $\lesssim M_{Z'} \lesssim$ 6000 GeV at the HL-LHC with 3000 fb^{-1} of integrated luminosity. There are mainly four decay modes for di-tau, namely, $\tau_e\tau_\mu(6\%)$, $\tau_e\tau_h(23\%)$, $\tau_\mu\tau_h(23\%)$, and $\tau_h\tau_h(42\%)$, where h denotes a hadron. In this analysis, we use the TauDecay package [97] to model the relatively clean leptonic and semi-leptonic decay modes of the taus. The main backgrounds for $\tau_e\tau_\mu$ are $t\bar{t}$, WW, and DY. For the semi-leptonic modes, the main backgrounds are DY and W+jets. To include the QCD multijet background in the semi-leptonic modes, we add 6% and 28% of the sum of the DY and W+jets backgrounds for the $\tau_\mu\tau_h$ and $\tau_e\tau_h$ modes, respectively [96]. The signal and DY background events are generated at LO and scaled by a K-factor of 1.3 [84] for $M_{\tau\tau} > M_Z$, while for $M_{\tau\tau} < M_Z$, we generate the signal and DY background with up to two additional jets in the final states. We generate $t\bar{t}$, WW, and W+jets background events at LO. To take higher-order corrections into account, the LO cross section of $t\bar{t}$ is normalized to the NNLO + NNLL cross section by a factor of 1.84 [90]. The LO cross sections of WW and W+jets are normalized to NNLO QCD by a factor of 1.98 [92] and 1.46 [98], respectively. To reduce the background, we implement two different selection rules SR1 and SR2 for $M_{Z'}$ below and above the Z-pole. In the $\tau_e\tau_\mu$ mode, both SR1 and SR2 require:

- Only one muon and one oppositely charged electron with $p_T > 20$ GeV and $|\eta| < 2.4$,
- veto b-tagged jets,
- $0.2M_{Z'} < M_{\tau_1\tau_2} < 0.8M_{Z'}$,
- $M_T^\mu < 40\,\text{GeV}$,

where τ_1 and τ_2 are respectively e and μ, and M_T^μ is the transverse mass of the charged lepton μ and the missing transverse momentum $\vec{\not{E}}_T$ is defined as

$$M_T^\mu = \sqrt{2P_T^\mu \cdot \not{E}_T(1 - \cos\Delta\phi(\mu, \vec{\not{E}}_T))}\,.$$

In addition, SR1 requires

- $\Delta R(\tau_1, \tau_2) < \Delta R_{\text{cut}}\,,$ (2.36)

where ΔR is the angular distance between τ_1 and τ_2. ΔR_{cut} is varied with $M_{Z'}$ to maximize the local significance S_l. For example, we choose $\Delta R_{\text{cut}} = 1.0$ (1.6) for $M_{Z'} = 20$ (40) GeV. SR2 further requires

- $\cos\Delta\phi(\tau_1, \tau_2) < -0.95\,,$
- $\cos\Delta\phi(\tau_1, \vec{\not{E}}_T) + \cos\Delta\phi(\tau_2, \vec{\not{E}}_T) > -0.1\,,$ (2.37)
- $\not{E}_T > \not{E}_T^{\text{cut}}\,,$

where the missing energy cut $\not{E}_T^{\text{cut}}$ is varied with $M_{Z'}$ to maximize the local significance S_l. We take $\not{E}_T^{\text{cut}}$ to be 40 (450) GeV for $M_{Z'} = 500$ (2000) GeV. In the $\tau_\ell\tau_h$ modes, both SR1 and SR2 require:

- Only one charged lepton and at least one opposite-sign tau-tagged jet with $p_T > 20$ GeV and $|\eta| < 2.4$,
- veto b-tagged jets, (2.38)
- $0.3M_{Z'} < M_{\tau_1\tau_2} < 0.9M_{Z'}$,
- $M_T^\ell < 40\,\text{GeV}$.

The further requirements of SR1 and SR2 are the same as for the leptonic $\tau_e\tau_\mu$ mode, with τ_1 and τ_2 the charged lepton and tau-tagged jet, respectively. The blue solid (dashed) curve in the lower panel of Fig. 2 shows the 2σ (5σ) sensitivity for Case C using a combination of the three decay modes ($\tau_e\tau_\mu$, $\tau_e\tau_h$, and $\tau_\mu\tau_h$), respectively, with 3000 fb^{-1} at the HL-LHC.

2.4 Correlated Signatures at CEνNS and Collider Experiments

It is of fundamental importance that we observe correlated signals of NSI in different experiments. In this section, we study correlated signatures at future CEνNS and collider experiments. We first simulate spectra in the presence of NSI and then examine the consistency between the two experiments in the hope of identifying a correlated signal. We select the benchmark point,

$$M_{Z'} = 10 \text{ GeV and } \; g' = 0.002\,,$$

for Cases A and B and explore how a signal observed in one experiment will manifest in another. The point is marked with a star in Fig. 2. The point is chosen so that observable signals can be produced at COHERENT and at the LHC. Since this set of parameters does not produce a signal at DUNE and T2HK, we focus on correlated signatures at COHERENT with an upgraded LAr detector and the high luminosity LHC with $L = 3000\ \text{fb}^{-1}$. Note that the benchmark point is chosen in a currently allowed narrow region near $m(\Upsilon(1S))$, and that LHCb data impose strong constraints for $M_{Z'}$ below and above it.

We first study signatures at COHERENT with an upgraded LAr detector. The recoil energy and temporal distributions of the events are shown in the left and right panel of Fig. 3, respectively. As can be seen from the left panel, the event excess is mainly at low energies. From the right panel, we see that the event excess peaks at around $t = 1\ \mu s$. This is due to the fact that the prompt component of the COHERENT flux is primarily composed of ν_μ, and the NSI coupling to ν_μ leads to a modification of the number of events in Cases A and B. To analyze the spectra and to facilitate a joint analysis with simulated LHC data, we define

$$\chi^2(\vec{\theta}) = -2\,\ln(L(\vec{\theta}))\,, \tag{2.39}$$

where $L(\vec{\theta})$ is defined in Eq. (2.31) with $\vec{\theta} = \{g', M_{Z'}\}$. We then calculate $\Delta\chi^2 = \chi^2 - \chi^2_{\text{min}}$. The 2σ allowed region for Case A and 1σ allowed region for Case B, with data simulated with our benchmark point, are the regions between the red curves in Fig. 4. The 2σ regions for Case B are too large to display.

We now study signatures at the HL-LHC. Since we are interested in the low-mass region, we focus on the clean channel, $Z \to \mu^+\mu^- Z' \to 4\mu$. We generate the leading process $q\bar{q} \to 4\mu$

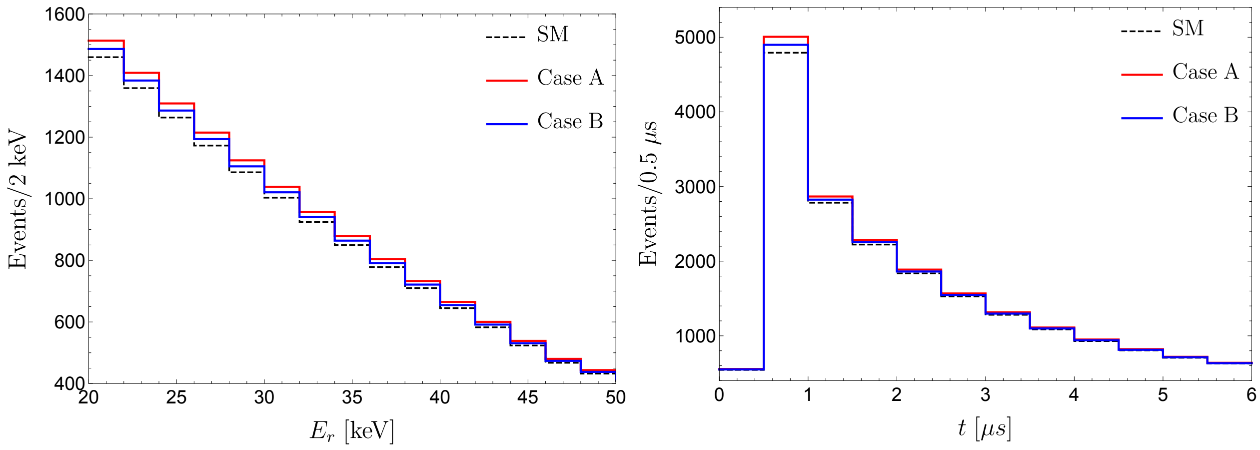

Figure 3: Recoil energy (left) and temporal (right) distributions in an upgraded COHERENT LAr detector with $m_{\rm det} = 750$ kg and 4 years of data. The black dashed histograms correspond to the SM case, the red (blue) lines correspond to Case A (B) with $M_{Z'} = 10$ GeV and $g' = 0.002$.

at the leading order (LO). Following the CMS analysis [88], we require at least four well-identified and isolated muons to have $p_T > 5$ GeV and to be in the central region of the detector $|\eta| < 2.4$, with at least two muons to have $p_T > 10$ GeV and at least one to have $p_T > 20$ GeV. Dimuon candidates formed from an opposite sign muon pair are required to have $4 < M_{\mu^+\mu^-} < 120$ GeV. The four selected muons are required to have zero net charge and $80 < M_{4\mu} < 100$ GeV. The NNLO/LO K-factor is chosen to be 1.29 [88]. By following the CMS procedure in Ref. [88], we are able to reconstruct $M_{Z'}$, whose distributions are shown in the left panel of Fig. 5. Unfortunately for Z's of GeV mass, COHERENT sees an overall suppression in the CEνNS event rate, but no spectral distortion, thereby precluding it from determining $M_{Z'}$. So a di-muon invariant mass cut cannot be applied and the look-elsewhere effect must be taken into account. Instead, we employ the $M_{4\mu}$ distributions (shown in the right panel of Fig. 5) to evaluate the precision with which the Z' parameters can be determined. We divide the range of $M_{4\mu}$ (80 GeV, 100 GeV) equally into 10 bins and perform a χ^2 analysis with

$$\chi^2 = \sum_i \frac{N_{S,i}^2}{N_{B,i} + (\sigma_B N_{B,i})^2}\,, \tag{2.40}$$

where $N_{S,i}$ ($N_{B,i}$) is the expected number of signal (background) events in the i^{th} bin. The background systematic uncertainty σ_B is chosen to be 5%. The parameters favored at 2σ for Case A and at 1σ for Case B lie between the blue curves in Fig. 4; Case B has no lower blue curve because the SM is allowed at 1σ. (The brown dashed curves in Fig. 2 for the 2σ sensitivity to the 4μ channel are produced by requiring the di-muon invariant mass $M_{\mu^+\mu^-}$ to be within 2% of $M_{Z'}$, and defining the local significance as $N_S/\sqrt{N_B + \sigma_B^2 N_B^2}$.)

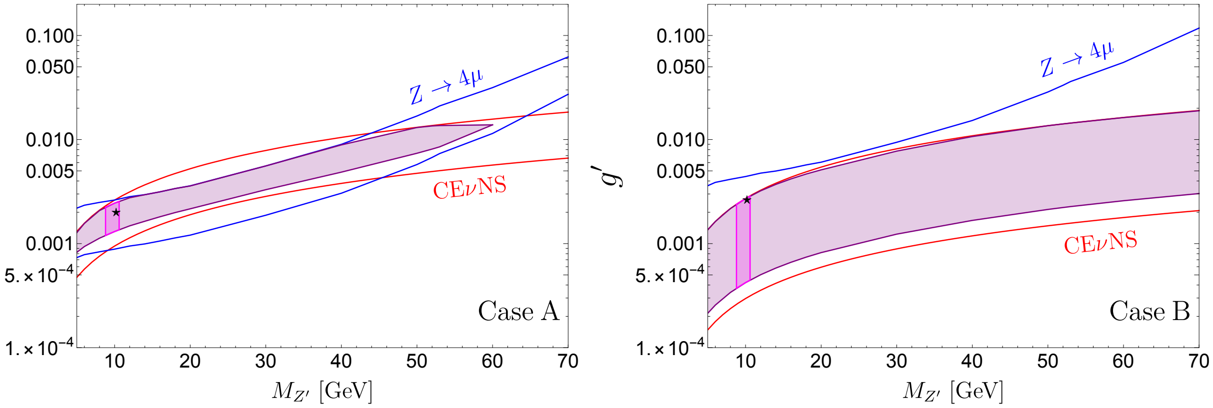

Figure 4: 2σ allowed regions for Case A (left) and 1σ allowed regions for Case B (right) from COHERENT with a large LAr detector (within the red curves) and HL-LHC $Z \to 4\mu$ decays (within the blue curves). The purple shaded regions (2σ for case A and 1σ for Case B) are from our joint analysis. The magenta shaded regions are the allowed regions after including the LHCb bound as a prior. The stars mark the best fit points from our joint analysis.

We perform a joint analysis of future COHERENT and HL-LHC data by combining the two χ^2 in Eqs. (2.39) and (2.40). The resulting 2σ allowed regions for Case A and 1σ allowed regions for Case B are shaded in purple in Fig. 4. Consider Case A. The fact that the allowed regions from COHERENT and LHC have different slopes enables a combination of their datasets to limit $M_{Z'}$ to be below about 60 GeV. However, a precise determination of $M_{Z'}$ is not achieved even by combining the datasets. For Case B, both COHERENT and HL-LHC only provide upper bounds on g' at 2σ. COHERENT dominates the sensitivity and the HL-LHC does not lead to a clear signal observation in the parameter region considered.

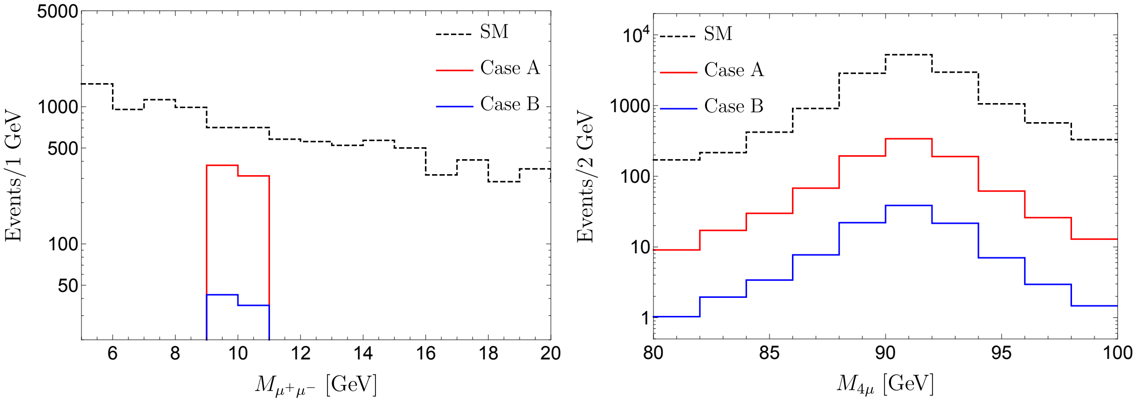

Figure 5: Distributions of the reconstructed $M_{Z'}$ (left) and $M_{4\mu}$ (right) at the HL-LHC with $\sqrt{s} = 14$ TeV and $L = 3000$ fb^{-1} for $M_{Z'} = 10$ GeV and $g' = 0.002$, for Case A (red curves) and Case B (blue curves).

We now impose the stringent bounds from LHCb. To include the LHCb constraint, for each value of $M_{Z'}$ we add $\chi^2_{\mathrm{LHCb}} = 2.71(g'/g'_{\mathrm{bound}})^2$ to our joint χ^2, where g'_{bound} is the 90% CL exclusion limit from LHCb at that value of $M_{Z'}$; note that the LHCb dark photon search [85] is performed independently at each mass, so that only one parameter, g', is varied in the analysis. On including the LHCb constraint, the allowed regions shrink significantly; see the magenta shaded regions in Fig. 4.

3.0 Renormalization Group Evolution of the SMNEFT Dimension Six Operators

The SM of particle physics is an effective theory valid to some mass scale Λ. New physics at the scale Λ may address important issues like the origin of the electroweak scale, μ_{EW}. In the SM, electroweak symmetry breaking arises from a complex fundamental Higgs scalar. Between μ_{EW} and Λ, an EFT framework can be used to describe new physics in a model independent way. In this approach, the leading terms are given by the SM, and corrections from an underlying theory beyond the SM are described by higher dimension operators,

$$\mathcal{L} = \sum_i \mathcal{C}_i \mathcal{O}_i \,. \tag{3.1}$$

The operators $\mathcal{O}_i$ are $SU(3)_C \times SU(2)_L \times U(1)_Y$ invariant and are constructed only from SM fields. The renormalization scale dependent Wilson coefficient (WC) $\mathcal{C}_i$, determines the size of the contribution of operator $\mathcal{O}_i$, and is calculated by matching the effective theory with the underlying theory.

Analyses of higher dimension operators [13] have begun anew in the study of the SM as an EFT. Due to the phenomenological success of the SM gauge theory and the Higgs mechanism, the most studied EFT is the SMEFT [14, 15, 16], which respects the SM gauge symmetry with only SM field content. The one-loop renormalization group evolution (RGE) of all dimension-six operators in SMEFT have been calculated in Refs. [99, 100, 101].

In the SMEFT framework, new physics is considered to be heavy with $\Lambda \gg \mu_{EW}$. However, many experiments point to new physics with a mass scale well below the electroweak scale, and many experiments to search for new light states are planned. Since these states do not appear in SMEFT, its Lagrangian must be supplemented by interactions between these new states and the SM fields. Possible new states are right-handed neutrinos that are sterile under SM gauge interactions. The masses of the sterile neutrinos can vary over a large range and can be heavy or light compared to the electroweak scale. Light sterile neutrinos have been invoked to explain many phenomena; see Ref. [102] for a review.

We consider the sterile neutrinos to be light so that they appear as explicit degree of freedoms in the EFT framework. We use the SMNEFT which augments SMEFT with right-handed neutrinos n [23, 24, 25, 26, 22]. The RGE of some SMNEFT operators have been calculated. The mixing between the bosonic operators has been calculated in Refs. [103, 104], and the one-loop RGE of a subset of four-fermion operators are given in Ref. [105]. In this chapter, we present the gauge terms of the one-loop RGE of all dimension-six operators in SMNEFT [106]. We also calculate the Yukawa coupling contributions to the one- loop anomalous dimension matrix for the 11 dimension-six four-fermion SMNEFT operators and the new contributions to the anomalous dimension matrix for the 14 four-fermion SMEFT operators that mix with the SMNEFT operators through the Yukawa couplings of the right-handed neutrinos [107].

3.1 Framework

In this section, we present the framework of SMNEFT. The dimension-six B and L conserving SMNEFT Lagrangian is

$$\mathscr{L}^{(6)}_{\rm SMNEFT} \supset \mathscr{L}_{\rm SM} + i\bar{n}\partial\!\!\!/ n + \mathscr{L}_{\rm Yukawa} + + \sum_i \mathcal{C}_i \mathcal{O}_i \,, \tag{3.2}$$

where $\mathcal{C}_i$ are the WCs with the scale of new physics absorbed in them, and the SM Lagrangian is given by

$$\begin{aligned}\mathscr{L}_{\rm SM} = \;&=\; -\frac{1}{4}G^A_{\mu\nu}G^{A\mu\nu} - \frac{1}{4}W^I_{\mu\nu}W^{I\mu\nu} - \frac{1}{4}B_{\mu\nu}B^{\mu\nu} \\ &+\; (D_\mu\phi)^\dagger(D^\mu\phi) + m^2\phi^\dagger\phi - \frac{\lambda}{2}(\phi^\dagger\phi)^2 \\ &+\; i(\bar{\ell}D\!\!\!\!/\,\ell + \bar{e}D\!\!\!\!/\,e + \bar{q}D\!\!\!\!/\,q + \bar{u}D\!\!\!\!/\,u + \bar{d}D\!\!\!\!/\,d) \\ &-\; (\bar{\ell}Y_e e\phi + \bar{q}Y_u u\tilde{\phi} + \bar{q}Y_d d\phi + \text{h.c.})\,.\end{aligned} \tag{3.3}$$

Here, $\tilde{\phi}^j = \epsilon^{jk}(\phi_k)^*$, and the Higgs vacuum expectation value is $\langle\phi\rangle = v_h/\sqrt{2}$ with $v_h = 246$ GeV. The covariant derivative and field strength tensors are defined by

$$\begin{aligned} D_\mu &= \partial_\mu + ig_1 y B_\mu + ig_2\frac{\tau^I}{2}W^I_\mu + ig_3\frac{T^a}{2}G^a_\mu\,, && (3.4)\\ B_{\mu\nu} &= \partial_\mu B_\nu - \partial_\nu B_\mu\,, && (3.5)\\ W^I_{\mu\nu} &= \partial_\mu W^I_\nu - \partial_\nu W^I_\mu - g_2\epsilon^{IJK}W^J_\mu W^K_\nu\,, && (3.6)\\ G^a_{\mu\nu} &= \partial_\mu G^a_\nu - \partial_\nu G^a_\mu - g_3 f^{abc}G^b_\mu G^c_\nu\,, && (3.7) \end{aligned}$$

where g_1, g_2, and g_3 are the gauge couplings of $U(1)_Y$, $SU(2)_L$, and $SU(3)_C$, respectively, and y is the hypercharge. ϵ^{IJK} and f^{abc} are the $SU(2)_L$ and $SU(3)_C$ structure constants, respectively. The Yukawa terms are

$$\mathscr{L}_{\text{Yukawa}} = -[\phi^{\dagger j}\bar{d}Y_d q_j + \tilde{\phi}^{\dagger j}\bar{u}Y_u q_j + \phi^{\dagger j}\bar{e}Y_e\ell_j + \tilde{\phi}^{\dagger j}\bar{n}Y_n\ell_j + \text{h.c.}], \tag{3.8}$$

The 16 baryon and lepton number conserving ($\Delta B = \Delta L = 0$) operators involving the field n in SMNEFT are shown in Table 2 [26] in the Warsaw basis convention [14]. The four types of Yukawa interaction vertices for the quark sector are shown in Fig. 6.

3.2 Anomalous Dimensions in SMNEFT

The Lagrangian can be written in terms of bare fields $\vec{\mathcal{O}}^{(0)}$

$$\mathscr{L}_{\text{SMNEFT}} \supset \vec{\mathcal{C}}^{\,T}\cdot\vec{\mathcal{O}} = \vec{\mathcal{C}}^{\,T}\cdot\mathbf{Z}\cdot\vec{\mathcal{O}}^{(0)}, \tag{3.9}$$

where $\mathbf{Z} = \mathbf{Z}_{\text{ct}}/\mathbf{Z}_{\text{wr}}$ is the renormalization constant matrix which depends on corrections from the counterterms, $\mathbf{Z}_{\text{ct}}$, and the wavefunction renormalizations, $\mathbf{Z}_{\text{wr}}$. Given that the bare operators and Lagrangian are independent of the renormalization scale μ, the RG equations for the Wilson coefficients are

$$\dot{\vec{\mathcal{C}}} \equiv 16\pi^2\mu\frac{d}{d\mu}\vec{\mathcal{C}} = -16\pi^2(\mathbf{Z}^T)^{-1}\mu\frac{d}{d\mu}\mathbf{Z}^T\vec{\mathcal{C}}. \tag{3.10}$$

The main task is to calculate the expressions for $\mathbf{Z}_{\text{wr}}$ and $\mathbf{Z}_{\text{ct}}$.

$(\bar{R}R)(\bar{R}R)$		$(\bar{L}L)(\bar{R}R)$		$(\bar{L}R)(\bar{R}L)$ and $(\bar{L}R)(\bar{L}R)$	
$\mathcal{O}_{nd}$	$(\bar{n}_p\gamma_\mu n_r)(\bar{d}_s\gamma^\mu d_t)$	$\mathcal{O}_{qn}$	$(\bar{q}_p\gamma_\mu q_r)(\bar{n}_s\gamma^\mu n_t)$	$\mathcal{O}_{\ell n\ell e}$	$(\bar{\ell}^j_p n_r)\epsilon_{jk}(\bar{\ell}^k_s e_t)$
$\mathcal{O}_{nu}$	$(\bar{n}_p\gamma_\mu n_r)(\bar{u}_s\gamma^\mu u_t)$	$\mathcal{O}_{\ell n}$	$(\bar{\ell}_p\gamma_\mu \ell_r)(\bar{n}_s\gamma^\mu n_t)$	$\mathcal{O}^{(1)}_{\ell nqd}$	$(\bar{\ell}^j_p n_r)\epsilon_{jk}(\bar{q}^k_s d_t)$
$\mathcal{O}_{ne}$	$(\bar{n}_p\gamma_\mu n_r)(\bar{e}_s\gamma^\mu e_t)$			$\mathcal{O}^{(3)}_{\ell nqd}$	$(\bar{\ell}^j_p \sigma_{\mu\nu} n_r)\epsilon_{jk}(\bar{q}^k_s \sigma^{\mu\nu} d_t)$
$\mathcal{O}_{nn}$	$(\bar{n}_p\gamma_\mu n_r)(\bar{n}_s\gamma^\mu n_t)$			$\mathcal{O}_{\ell nuq}$	$(\bar{\ell}^j_p n_r)(\bar{u}_s q^j_t)$
$\mathcal{O}_{nedu}$	$(\bar{n}_p\gamma_\mu e_r)(\bar{d}_s\gamma^\mu u_t)$				
$\psi^2\phi^3$		$\psi^2\phi^2 D$		$\psi^2 X\phi$	
$\mathcal{O}_{n\phi}$	$(\phi^\dagger\phi)(\bar{l}_p n_r\tilde{\phi})$	$\mathcal{O}_{\phi n}$	$i(\phi^\dagger \overleftrightarrow{D}_\mu\phi)(\bar{n}_p\gamma^\mu n_r)$	$\mathcal{O}_{nW}$	$(\bar{\ell}_p\sigma^{\mu\nu} n_r)\tau^I\tilde{\phi}W^I_{\mu\nu}$
		$\mathcal{O}_{\phi ne}$	$i(\tilde{\phi}^\dagger D_\mu\phi)(\bar{n}_p\gamma^\mu e_r)$	$\mathcal{O}_{nB}$	$(\bar{\ell}_p\sigma^{\mu\nu} n_r)\tilde{\phi}B_{\mu\nu}$

Table 2: The 16 SMNEFT operators involving the right-handed neutrinos n in the Warsaw convention which conserve baryon and lepton number ($\Delta B = \Delta L = 0$). The flavor indices '*prst*' are suppressed for simplicity. The fundamental $SU(2)_L$ indices are denoted by j, k, and I is the adjoint index.

3.3 Anomalous Dimensions in SMNEFT: Yukawa Dependence

Wavefunction renormalization is to renormalize the bare field$\psi^{(0)}$ into the renormalized fieldψ^{R} as

$$\psi^R = \frac{1}{\sqrt{Z}}\psi^{(0)}. \tag{3.11}$$

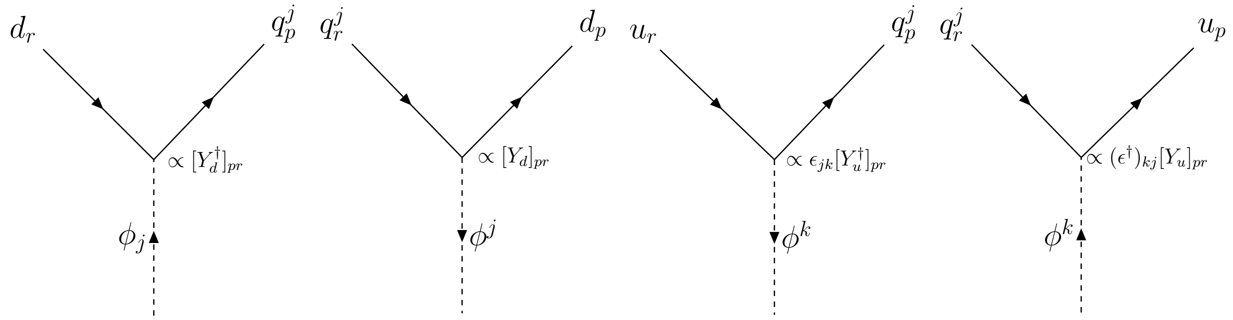

Figure 6: The four types of Yukawa interaction vertices. The flavor indices 'pr' and $SU(2)_L$ indices 'jk' are written explicitly.

Considering the four-fermion operator $\mathcal{O}_{4\psi} = \bar{\psi}_1\psi_2\bar{\psi}_3\psi_4$, the wavefunction renormalization constant is given as

$$\mathbf{Z}_{\text{wr}} \equiv \sqrt{\prod_{i=1}^{4} \mathbf{Z}_{\psi_i}}. \tag{3.12}$$

From Fig. 7 , the Yukawa dependent wavefunction renormlaization of right-handed neutrino n is

$$Z^{(Y)}_{\substack{n\\pr}} = 1 - \frac{\gamma^{(Y)}_{\substack{n\\pr}}}{16\pi^2\epsilon}, \tag{3.13}$$

where $\gamma^{(Y)}_{\substack{n\\pr}} = [Y_n Y_n^\dagger]_{pr}$ following the notation in Ref. [100] where we have assumed, in dimensional regulation, dimension $D = 4 - 2\epsilon$. And similarly, we have,

$$\begin{aligned} \gamma^{(Y)}_{\substack{\ell\\pr}} &= \frac{1}{2}[Y_e^\dagger Y_e + Y_n^\dagger Y_n]_{pr}, \quad \gamma^{(Y)}_{\substack{e\\pr}} = [Y_e Y_e^\dagger]_{pr}, \\ \gamma^{(Y)}_{q} &= \frac{1}{2}[Y_d^\dagger Y_d + Y_u^\dagger Y_u]_{pr}, \quad \gamma^{(Y)}_{\substack{d\\pr}} = [Y_d Y_d^\dagger]_{pr}, \quad \gamma^{(Y)}_{\substack{u\\pr}} = [Y_u Y_u^\dagger]_{pr}. \end{aligned} \tag{3.14}$$

The corrections from counterterms cancel the UV divergence from the one-loop diagrams. In the one-loop diagrams, there are 14 different structures as in Fig. 8; there are seven counterparts to those shown. We display the UV divergent part of each structure in Fig. 8.

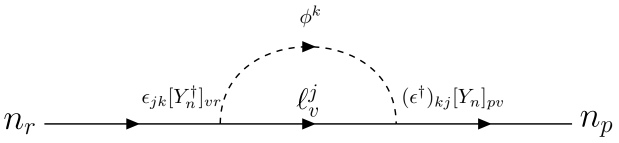

Figure 7: Self-energy of n.

The UV divergent parts in Figs. 8a to 8c are of the form

$$\begin{aligned} \mathcal{D}_a &= -\frac{1}{64\pi^2\epsilon}(\bar{\psi}_1\gamma^\mu\Gamma_1\gamma_\mu\psi_2)(\psi_3\Gamma_2\psi_4)\,, && (3.15)\\ \mathcal{D}_b &= -\frac{1}{64\pi^2\epsilon}(\bar{\psi}_1\gamma^\mu\Gamma_1\psi_2)(\bar{\psi}_3\gamma_\mu\Gamma_2\psi_4)\,, && (3.16)\\ \mathcal{D}_c &= -\frac{1}{64\pi^2\epsilon}(\bar{\psi}_1\Gamma_1\gamma^\mu\psi_2)(\bar{\psi}_3\gamma_\mu\Gamma_2\psi_4)\,, && (3.17) \end{aligned}$$

where Γ_1 and Γ_2 are the Lorentz structures for the upper and lower vertex, respectively. In Fig. 8d, Γ_1 has to be P_2, which is the projection operator of the chiral fermion field ψ_2, because for the other possibilities, the UV divergent parts vanish. Thus we obtain

$$\mathcal{D}_d = \frac{1}{16\pi^2\epsilon}(\bar{\psi}_1 P_2\psi_2)(\bar{\psi}_3 P_4\psi_4)\,. \tag{3.18}$$

The UV divergent part of Fig. 8e is

$$\mathcal{D}_e = -\frac{1}{32\pi^2\epsilon}(\bar{\psi}_1\gamma^\mu P_2\psi_2)(\bar{\psi}_3\gamma_\mu P_4\psi_4)\,. \tag{3.19}$$

For the dipole operators in Figs. 8f and 8g, the UV divergent parts are

$$\begin{aligned} \mathcal{D}_f &= \frac{i}{64\pi^2\epsilon}(\bar{\psi}_1\sigma^{\mu\nu}P_2\psi_2)(\bar{\psi}_3\gamma^\beta\gamma^\alpha P_4\psi_4)(g^{\mu\beta}g^{\nu\alpha}-g^{\mu\alpha}g^{\nu\beta}) \\ &= \frac{1}{32\pi^2\epsilon}(\bar{\psi}_1\sigma^{\mu\nu}P_2\psi_2)(\bar{\psi}_3\sigma_{\mu\nu}P_4\psi_4)\,, && (3.20)\\ \mathcal{D}_g &= \frac{i}{64\pi^2\epsilon}(\bar{\psi}_1\sigma^{\mu\nu}P_2\psi_2)(\bar{\psi}_3\gamma^\alpha\gamma^\beta P_4\psi_4)(g^{\mu\beta}g^{\nu\alpha}-g^{\mu\alpha}g^{\nu\beta}) \\ &= -\frac{1}{32\pi^2\epsilon}(\bar{\psi}_1\sigma^{\mu\nu}P_2\psi_2)(\bar{\psi}_3\sigma_{\mu\nu}P_4\psi_4)\,. && (3.21) \end{aligned}$$

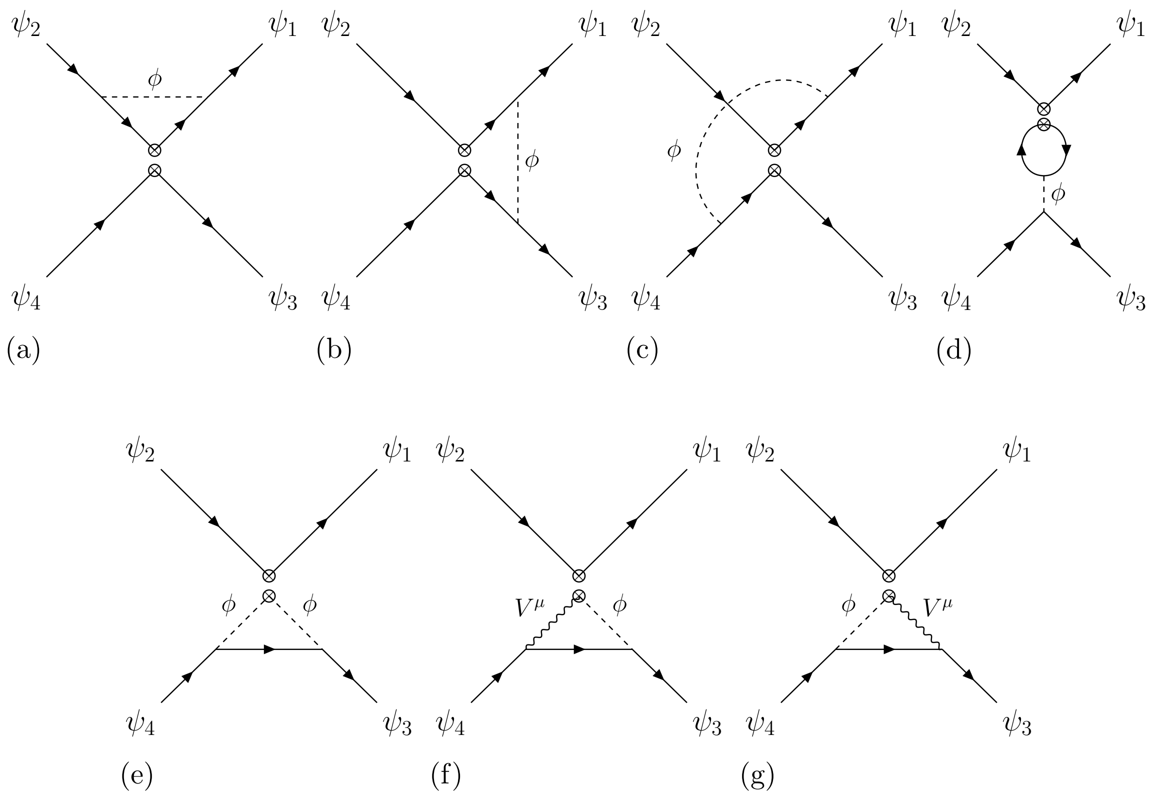

Figure 8: The seven structures that contribute to the four-fermion operator anomalous dimension matrix at the one-loop level.

To simplify our results further, we follow Ref. [100] and define the amplitudes in Fig. 9 in connection with Fig. 8d:

$$\begin{aligned}
\xi_{\underset{pr}{n}} &= 2\mathcal{C}_{\underset{pwvr}{\ell n}}[Y_n^\dagger]_{wv} - N_c\mathcal{C}^{(1)}_{\underset{prvw}{\ell nqd}}[Y_d]_{wv} - N_c\mathcal{C}_{\underset{prvw}{\ell nuq}}[Y_u^\dagger]_{wv} - \mathcal{C}_{\underset{prvw}{\ell n\ell e}}[Y_e]_{wv}\,, \\
\xi_{\underset{pr}{e}} &= 2\mathcal{C}_{\underset{pwvr}{\ell e}}[Y_e^\dagger]_{wv} - N_c\mathcal{C}_{\underset{prvw}{\ell edq}}[Y_d^\dagger]_{wv} + N_c\mathcal{C}^{(1)}_{\underset{prvw}{\ell equ}}[Y_u]_{wv} - \mathcal{C}_{\underset{vwpr}{\ell n\ell e}}[Y_n]_{wv}\,, \\
\xi_{\underset{pr}{u}} &= 2(\mathcal{C}^{(1)}_{\underset{pwvr}{qu}} + C_{F,3}\mathcal{C}^{(8)}_{\underset{pwvr}{qu}})[Y_u^\dagger]_{wv} - (N_c\mathcal{C}^{(1)}_{\underset{prvw}{quqd}} + \frac{1}{2}\mathcal{C}^{(1)}_{\underset{vrpw}{quqd}} + \frac{1}{2}C_{F,3}\mathcal{C}^{(8)}_{\underset{vrpw}{quqd}})[Y_d^\dagger]_{wv} \\
&\quad + \mathcal{C}^{(1)}_{\underset{vwpr}{\ell equ}}[Y_e]_{wv} - \mathcal{C}^{*}_{\underset{vwrp}{\ell nuq}}[Y_n^\dagger]_{vw}\,, \\
\xi_{\underset{pr}{d}} &= 2(\mathcal{C}^{(1)}_{\underset{pwvr}{qd}} + C_{F,3}\mathcal{C}^{(8)}_{\underset{pwvr}{qd}})[Y_d^\dagger]_{wv} - (N_c\mathcal{C}^{(1)}_{\underset{vrpw}{quqd}} + \frac{1}{2}\mathcal{C}^{(1)}_{\underset{prvw}{quqd}} + \frac{1}{2}C_{F,3}\mathcal{C}^{(8)}_{\underset{prvw}{quqd}})[Y_u^\dagger]_{wv} \\
&\quad - \mathcal{C}^{*}_{\underset{vwrp}{\ell edq}}[Y_e^\dagger]_{vw} - \mathcal{C}^{(1)}_{\underset{vwpr}{\ell nqd}}[Y_n]_{wv}\,,
\end{aligned} \tag{3.22}$$

where the quadratic Casimir $C_{F,3} = \frac{4}{3}$ and the number of colors $N_c = 3$. The ξ parameter

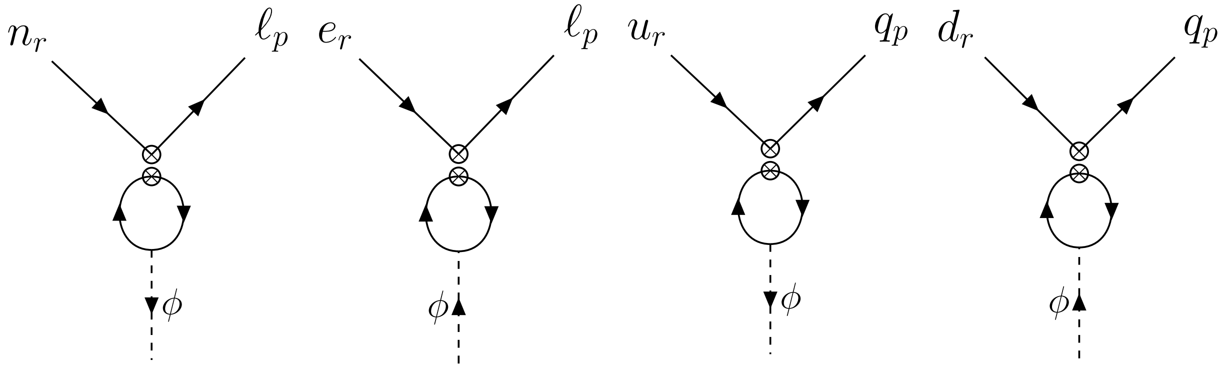

Figure 9: The Feynman diagrams associated with the ξ parameters.

for right-handed neutrinos n (ξ_n), corresponds to the new terms in SMNEFT, while the last terms in ξ_e, ξ_u and ξ_d are contributions from the right-handed neutrino Yukawa couplings not present in SMEFT.

In this section, we present the Yukawa coupling contributions to the one-loop RGE for all four-fermion SMNEFT operators, and the new RGE terms for the four-fermion SMEFT operators due to the mixing between SMEFT and SMNEFT operators via the right-handed neutrino Yukawa couplings Y_n. The contributions from the fermionic operators come from the Feynman diagrams in Figs. 8a to 8d, with contributions from Fig. 8d given by the ξ parameters.

The bosonic operators in Table 2 contribute to the SMNEFT ADM but not the SMEFT ADM. The contribution from the bosonic operator $\psi^2\phi^2 D$ is shown in Fig. 8e. The RGE of the dipole operators $\mathcal{O}_{\ell n\ell e}$ and $\mathcal{O}^{(3)}_{\ell nqd}$ is modified by the $\psi^2 X\phi$ operators in Table 2 and the relevant diagrams are shown in Figs. 8f and 8g. These terms contain both gauge and Yukawa coupling contributions.

3.3.1 SMNEFT: $(\bar{R}R)(\bar{R}R)$

$$\begin{aligned}
\dot{\mathcal{C}}_{\underset{prst}{nd}} = {} & -2[Y_nY_n^\dagger]_{pr}\mathcal{C}_{\underset{st}{\phi d}} + 2[Y_dY_d^\dagger]_{st}\mathcal{C}_{\underset{pr}{\phi n}} - 2[Y_n]_{pv}[Y_n^\dagger]_{wr}\mathcal{C}_{\underset{vwst}{\ell d}} - 2[Y_d]_{sv}[Y_d^\dagger]_{wt}\mathcal{C}_{\underset{vwpr}{qn}} \\
& -([Y_n]_{pv}[Y_d]_{sw}\mathcal{C}^{(1)}_{\underset{vrwt}{\ell nqd}} + [Y_n^\dagger]_{vr}[Y_d^\dagger]_{wt}\mathcal{C}^{(1)*}_{\underset{vpws}{\ell nqd}}) + 12([Y_n]_{pv}[Y_d]_{sw}\mathcal{C}^{(3)}_{\underset{vrwt}{\ell nqd}} + [Y_n^\dagger]_{vr}[Y_d^\dagger]_{wt}\mathcal{C}^{(3)*}_{\underset{vpws}{\ell nqd}}) \\
& +\gamma^{(Y)}_{\underset{pv}{n}}\mathcal{C}_{\underset{vrst}{nd}} + \gamma^{(Y)}_{\underset{sv}{d}}\mathcal{C}_{\underset{prvt}{nd}} + \mathcal{C}_{\underset{pvst}{nd}}\gamma^{(Y)}_{\underset{vr}{n}} + \mathcal{C}_{\underset{prsv}{nd}}\gamma^{(Y)}_{\underset{vt}{d}}\,,
\end{aligned} \tag{3.23}$$

$$\begin{aligned}
\dot{\mathcal{C}}_{\underset{prst}{nu}} = {} & -2[Y_nY_n^\dagger]_{pr}\mathcal{C}_{\underset{st}{\phi u}} - 2[Y_uY_u^\dagger]_{st}\mathcal{C}_{\underset{pr}{\phi n}} - 2[Y_n]_{pv}[Y_n^\dagger]_{wr}\mathcal{C}_{\underset{vwst}{\ell u}} - 2[Y_u]_{sv}[Y_u^\dagger]_{wt}\mathcal{C}_{\underset{vwpr}{qn}} \\
& +([Y_n]_{pv}[Y_u^\dagger]_{wt}\mathcal{C}_{\underset{vrsw}{\ell nuq}} + [Y_n^\dagger]_{vr}[Y_u]_{sw}\mathcal{C}^{*}_{\underset{vptw}{\ell nuq}}) \\
& +\gamma^{(Y)}_{\underset{pv}{n}}\mathcal{C}_{\underset{vrst}{nu}} + \gamma^{(Y)}_{\underset{sv}{u}}\mathcal{C}_{\underset{prvt}{nu}} + \mathcal{C}_{\underset{pvst}{nu}}\gamma^{(Y)}_{\underset{vr}{n}} + \mathcal{C}_{\underset{prsv}{nu}}\gamma^{(Y)}_{\underset{vt}{u}}\,,
\end{aligned} \tag{3.24}$$

$$\begin{aligned}
\dot{\mathcal{C}}_{\underset{prst}{ne}} = {} & -2[Y_nY_n^\dagger]_{pr}\mathcal{C}_{\underset{st}{\phi e}} + 2[Y_eY_e^\dagger]_{st}\mathcal{C}_{\underset{pr}{\phi n}} + 2[Y_eY_n^\dagger]_{sr}\mathcal{C}_{\underset{pt}{\phi ne}} + 2[Y_nY_e^\dagger]_{pt}\mathcal{C}^{*}_{\underset{rs}{\phi ne}} - 2[Y_n]_{pv}[Y_n^\dagger]_{wr}\mathcal{C}_{\underset{vwst}{\ell e}} \\
& -([Y_n]_{pv}[Y_e]_{sw}\mathcal{C}_{\underset{vrwt}{\ell n\ell e}} + [Y_n^\dagger]_{vr}[Y_e^\dagger]_{wt}\mathcal{C}^{*}_{\underset{vpws}{\ell n\ell e}}) + ([Y_n]_{pw}[Y_e]_{sv}\mathcal{C}_{\underset{vrwt}{\ell n\ell e}} + [Y_n^\dagger]_{wr}[Y_e^\dagger]_{vt}\mathcal{C}^{*}_{\underset{vpws}{\ell n\ell e}}) \\
& -2[Y_e]_{sv}[Y_e^\dagger]_{wt}\mathcal{C}_{\underset{vwpr}{\ell n}} + \gamma^{(Y)}_{\underset{pv}{n}}\mathcal{C}_{\underset{vrst}{ne}} + \gamma^{(Y)}_{\underset{sv}{e}}\mathcal{C}_{\underset{prvt}{ne}} + \mathcal{C}_{\underset{pvst}{ne}}\gamma^{(Y)}_{\underset{vr}{n}} + \mathcal{C}_{\underset{prsv}{ne}}\gamma^{(Y)}_{\underset{vt}{e}}\,,
\end{aligned} \tag{3.25}$$

$$\begin{aligned}
\dot{\mathcal{C}}_{\underset{prst}{nn}} = {} & -[Y_nY_n^\dagger]_{pr}\mathcal{C}_{\underset{st}{\phi n}} - [Y_nY_n^\dagger]_{st}\mathcal{C}_{\underset{pr}{\phi n}} - [Y_n]_{pv}[Y_n^\dagger]_{wr}\mathcal{C}_{\underset{vwst}{\ell n}} - [Y_n]_{sv}[Y_n^\dagger]_{wt}\mathcal{C}_{\underset{vwpr}{\ell n}} \\
& +\gamma^{(Y)}_{\underset{pv}{n}}\mathcal{C}_{\underset{vrst}{nn}} + \gamma^{(Y)}_{\underset{sv}{n}}\mathcal{C}_{\underset{prvt}{nn}} + \mathcal{C}_{\underset{pvst}{nn}}\gamma^{(Y)}_{\underset{vr}{n}} + \mathcal{C}_{\underset{prsv}{nn}}\gamma^{(Y)}_{\underset{vt}{n}}\,,
\end{aligned} \tag{3.26}$$

$$\begin{aligned}\dot{\mathcal{C}}_{\underset{prst}{nedu}} = {}& 2[Y_d Y_u^\dagger]_{st}\mathcal{C}_{\underset{pr}{\phi ne}} + 2[Y_n Y_e^\dagger]_{pr}\mathcal{C}^*_{\underset{ts}{\phi ud}} - [Y_n]_{pv}[Y_d]_{sw}(\mathcal{C}^{(1)}_{\underset{vrwt}{\ell equ}} - 12\mathcal{C}^{(3)}_{\underset{vrwt}{\ell equ}}) + [Y_n]_{pv}[Y_u^\dagger]_{wt}\mathcal{C}_{\underset{vrsw}{\ell edq}} \\ & +[Y_e^\dagger]_{vr}[Y_u^\dagger]_{wt}(\mathcal{C}^{(1)*}_{\underset{vpws}{\ell nqd}} - 12\mathcal{C}^{(3)*}_{\underset{vpws}{\ell nqd}}) + [Y_e^\dagger]_{vr}[Y_d]_{sw}\mathcal{C}^*_{\underset{vptw}{\ell nuq}} \\ & +\gamma^{(Y)}_{\underset{pv}{n}}\mathcal{C}_{\underset{vrst}{nedu}} + \gamma^{(Y)}_{\underset{sv}{d}}\mathcal{C}_{\underset{prvt}{nedu}} + \mathcal{C}_{\underset{pvst}{nedu}}\gamma^{(Y)}_{\underset{vr}{e}} + \mathcal{C}_{\underset{prsv}{nedu}}\gamma^{(Y)}_{\underset{vt}{u}}\,. \end{aligned} \tag{3.27}$$

3.3.2 SMNEFT: $(\bar{L}L)(\bar{R}R)$

$$\begin{aligned}\dot{\mathcal{C}}_{\underset{prst}{qn}} = {}& [Y_u^\dagger Y_u - Y_d^\dagger Y_d]_{pr}\mathcal{C}_{\underset{st}{\phi n}} - 2[Y_n Y_n^\dagger]_{st}\mathcal{C}^{(1)}_{\underset{pr}{\phi q}} - 2[Y_n]_{sv}[Y_n^\dagger]_{wt}\mathcal{C}^{(1)}_{\underset{vwpr}{\ell q}} - [Y_u]_{wr}[Y_u^\dagger]_{pv}\mathcal{C}_{\underset{stvw}{nu}} \\ & +\frac{1}{2}([Y_n]_{sw}[Y_d]_{vr}C^{(1)}_{\underset{wtpv}{\ell nqd}} + [Y_n^\dagger]_{wt}[Y_d^\dagger]_{pv}C^{(1)*}_{\underset{wsrv}{\ell nqd}}) + 6([Y_n]_{sw}[Y_d]_{vr}C^{(3)}_{\underset{wtpv}{\ell nqd}} + [Y_n^\dagger]_{wt}[Y_d^\dagger]_{pv}C^{(3)*}_{\underset{wsrv}{\ell nqd}}) \\ & -\frac{1}{2}([Y_n]_{sw}[Y_u^\dagger]_{pv}C_{\underset{wtvr}{\ell nuq}} + [Y_n^\dagger]_{wt}[Y_u]_{vr}C^*_{\underset{wsvp}{\ell nuq}}) - [Y_d]_{wr}[Y_d^\dagger]_{pv}\mathcal{C}_{\underset{stvw}{nd}} \\ & +\gamma^{(Y)}_{\underset{pv}{q}}\mathcal{C}_{\underset{vrst}{qn}} + \gamma^{(Y)}_{\underset{sv}{n}}\mathcal{C}_{\underset{prvt}{qn}} + \mathcal{C}_{\underset{pvst}{qn}}\gamma^{(Y)}_{\underset{vr}{q}} + \mathcal{C}_{\underset{prsv}{qn}}\gamma^{(Y)}_{\underset{vt}{n}}\,, \end{aligned} \tag{3.28}$$

$$\begin{aligned}\dot{\mathcal{C}}_{\underset{prst}{\ell n}} = {}& [Y_n^\dagger Y_n - Y_e^\dagger Y_e]_{pr}\mathcal{C}_{\underset{st}{\phi n}} - 2[Y_n Y_n^\dagger]_{st}\mathcal{C}^{(1)}_{\underset{pr}{\phi\ell}} + [Y_n^\dagger]_{pw}[Y_n]_{sv}\mathcal{C}_{\underset{vrwt}{\ell n}} + [Y_n^\dagger]_{vt}[Y_n]_{wr}\mathcal{C}_{\underset{pvsw}{\ell n}} \\ & -2[Y_n^\dagger]_{pv}[Y_n]_{wr}\mathcal{C}_{\underset{vtsw}{nn}} - 2[Y_n^\dagger]_{pv}[Y_n]_{wr}\mathcal{C}_{\underset{vwst}{nn}} - 2[Y_n^\dagger]_{vt}[Y_n]_{sw}\mathcal{C}_{\underset{pvwr}{\ell\ell}} - 4[Y_n^\dagger]_{wt}[Y_n]_{sv}\mathcal{C}_{\underset{prvw}{\ell\ell}} \\ & +\frac{1}{2}([Y_e]_{wr}[Y_n]_{sv}\mathcal{C}_{\underset{vtpw}{\ell n\ell e}} + [Y_e^\dagger]_{pv}[Y_n^\dagger]_{wt}\mathcal{C}^*_{\underset{wsrv}{\ell n\ell e}}) + ([Y_e]_{wr}[Y_n]_{sv}\mathcal{C}_{\underset{ptvw}{\ell n\ell e}} + [Y_e^\dagger]_{pv}[Y_n^\dagger]_{wt}\mathcal{C}^*_{\underset{rswv}{\ell n\ell e}}) \\ & +[Y_n]_{sr}\xi_{\underset{pt}{n}} + [Y_n^\dagger]_{pt}\xi^*_{\underset{rs}{n}} + \gamma^{(Y)}_{\underset{pv}{\ell}}\mathcal{C}_{\underset{vrst}{\ell n}} + \gamma^{(Y)}_{\underset{sv}{n}}\mathcal{C}_{\underset{prvt}{\ell n}} + \mathcal{C}_{\underset{pvst}{\ell n}}\gamma^{(Y)}_{\underset{vr}{\ell}} + \mathcal{C}_{\underset{prsv}{\ell n}}\gamma^{(Y)}_{\underset{vt}{n}} - [Y_e^\dagger]_{pv}[Y_e]_{wr}\mathcal{C}_{\underset{stvw}{ne}}\,. \end{aligned} \tag{3.29}$$

3.3.3 SMNEFT: $(\bar{L}R)(\bar{R}L)$ and $(\bar{L}R)(\bar{L}R)$

$$\begin{aligned}\dot{\mathcal{C}}_{\underset{prst}{\ell n\ell e}} = {}& -4([Y_n^\dagger]_{vr}[Y_e^\dagger]_{wt}\mathcal{C}_{\underset{pvsw}{\ell\ell}} - [Y_n^\dagger]_{vr}[Y_e^\dagger]_{wt}\mathcal{C}_{\underset{svpw}{\ell\ell}}) + 4([Y_n^\dagger]_{wr}[Y_e^\dagger]_{vt}\mathcal{C}_{\underset{pvsw}{\ell\ell}} - [Y_n^\dagger]_{wt}[Y_e^\dagger]_{vt}\mathcal{C}_{\underset{svpw}{\ell\ell}}) \\ & -4([Y_n^\dagger]_{pv}[Y_e^\dagger]_{sw}\mathcal{C}_{\underset{vrwt}{ne}} - [Y_n^\dagger]_{sv}[Y_e^\dagger]_{pw}\mathcal{C}_{\underset{vrwt}{ne}}) + 4[Y_n^\dagger]_{sw}[Y_e^\dagger]_{vt}\mathcal{C}_{\underset{pvwr}{\ell n}} + 4[Y_n^\dagger]_{vr}[Y_e^\dagger]_{pw}\mathcal{C}_{\underset{svwt}{\ell e}} \\ & +4g_1(y_e + y_\ell)\mathcal{C}_{\underset{pr}{nB}}[Y_e^\dagger]_{st} - 8g_1(y_e + y_\ell)\mathcal{C}_{\underset{sr}{nB}}[Y_e^\dagger]_{pt} - 6g_2\mathcal{C}_{\underset{pr}{nW}}[Y_e^\dagger]_{st} + 12g_2\mathcal{C}_{\underset{sr}{nW}}[Y_e^\dagger]_{pt} \\ & +4g_1(y_n + y_\ell)\mathcal{C}_{\underset{st}{eB}}[Y_n^\dagger]_{pr} - 8g_1(y_n + y_\ell)\mathcal{C}_{\underset{pt}{eB}}[Y_n^\dagger]_{sr} - 6g_2\mathcal{C}_{\underset{st}{eW}}[Y_n^\dagger]_{pr} + 12g_2\mathcal{C}_{\underset{pt}{eW}}[Y_n^\dagger]_{sr} \\ & -2\xi_{\underset{pr}{n}}[Y_e^\dagger]_{st} - 2\xi_{\underset{st}{e}}[Y_n^\dagger]_{pr} + \gamma^{(Y)}_{\underset{pv}{\ell}}\mathcal{C}_{\underset{vrst}{\ell n\ell e}} + \gamma^{(Y)}_{\underset{sv}{\ell}}\mathcal{C}_{\underset{prvt}{\ell n\ell e}} + \mathcal{C}_{\underset{pvst}{\ell n\ell e}}\gamma^{(Y)}_{\underset{vr}{n}} + \mathcal{C}_{\underset{prsv}{\ell n\ell e}}\gamma^{(Y)}_{\underset{vt}{e}}\,, \end{aligned} \tag{3.30}$$

$$\begin{aligned}\underset{prst}{\dot{\mathcal{C}}^{(1)}_{\ell nqd}} \;=\;& -2[Y_n^\dagger]_{vr}[Y_e^\dagger]_{pw}\underset{vwts}{\mathcal{C}^*_{\ell edq}} + 2[Y_n^\dagger]_{pw}[Y_d^\dagger]_{vt}\underset{svwr}{\mathcal{C}_{qn}} + 2[Y_e^\dagger]_{pw}[Y_u^\dagger]_{sv}\underset{rwtv}{\mathcal{C}^*_{nedu}} + 2[Y_n^\dagger]_{vr}[Y_d^\dagger]_{sw}\underset{pvwt}{\mathcal{C}_{\ell d}} \\ & -2[Y_d^\dagger]_{wt}[Y_u^\dagger]_{sv}\underset{prvw}{\mathcal{C}_{\ell nuq}} - 2[Y_n^\dagger]_{pw}[Y_d^\dagger]_{sv}\underset{wrvt}{\mathcal{C}_{nd}} - 2[Y_n^\dagger]_{vr}[Y_d^\dagger]_{wt}\underset{pvsw}{\mathcal{C}^{(1)}_{\ell q}} + 6[Y_n^\dagger]_{vr}[Y_d^\dagger]_{wt}\underset{pvsw}{\mathcal{C}^{(3)}_{\ell q}} \\ & -2\underset{pr}{\xi_n}[Y_d^\dagger]_{st} - 2\underset{st}{\xi_d}[Y_n^\dagger]_{pr} + \underset{pv}{\gamma^{(Y)}_\ell}\underset{vrst}{\mathcal{C}^{(1)}_{\ell nqd}} + \underset{sv}{\gamma^{(Y)}_q}\underset{prvt}{\mathcal{C}^{(1)}_{\ell nqd}} + \underset{pvst}{\mathcal{C}^{(1)}_{\ell nqd}}\underset{vr}{\gamma^{(Y)}_n} + \underset{prsv}{\mathcal{C}^{(1)}_{\ell nqd}}\underset{vt}{\gamma^{(Y)}_d}\,,\end{aligned} \tag{3.31}$$

$$\begin{aligned}\underset{prst}{\dot{\mathcal{C}}^{(3)}_{\ell nqd}} \;=\;& -\frac{1}{2}[Y_e^\dagger]_{pw}[Y_u^\dagger]_{sv}\underset{rwtv}{\mathcal{C}^*_{nedu}} + \frac{1}{2}[Y_n^\dagger]_{vr}[Y_d^\dagger]_{wt}\underset{pvsw}{\mathcal{C}^{(1)}_{\ell q}} - \frac{3}{2}[Y_n^\dagger]_{vr}[Y_d^\dagger]_{wt}\underset{pvsw}{\mathcal{C}^{(3)}_{\ell q}} \\ & \frac{1}{2}[Y_n^\dagger]_{vr}[Y_d^\dagger]_{sw}\underset{pvwt}{\mathcal{C}_{\ell d}} + \frac{1}{2}[Y_n^\dagger]_{pw}[Y_d^\dagger]_{vt}\underset{svwr}{\mathcal{C}_{qn}} + \frac{1}{2}[Y_n^\dagger]_{pw}[Y_d^\dagger]_{sv}\underset{wrvt}{\mathcal{C}_{nd}} \\ & -g_1(y_d+y_q)\underset{pr}{\mathcal{C}_{nB}}[Y_d^\dagger]_{st} - g_1(y_n+y_\ell)\underset{st}{\mathcal{C}_{dB}}[Y_n^\dagger]_{pr} + \frac{3}{2}g_2\underset{pr}{\mathcal{C}_{nW}}[Y_d^\dagger]_{st} + \frac{3}{2}g_2\underset{st}{\mathcal{C}_{dW}}[Y_n^\dagger]_{pr} \\ & +\underset{pv}{\gamma^{(Y)}_\ell}\underset{vrst}{\mathcal{C}^{(3)}_{\ell nqd}} + \underset{sv}{\gamma^{(Y)}_q}\underset{prvt}{\mathcal{C}^{(3)}_{\ell nqd}} + \underset{pvst}{\mathcal{C}^{(3)}_{\ell nqd}}\underset{vr}{\gamma^{(Y)}_n} + \underset{prsv}{\mathcal{C}^{(3)}_{\ell nqd}}\underset{vt}{\gamma^{(Y)}_d}\,,\end{aligned} \tag{3.32}$$

$$\begin{aligned}\underset{prst}{\dot{\mathcal{C}}_{\ell nuq}} \;=\;& 2[Y_n^\dagger]_{wr}[Y_e^\dagger]_{pv}\underset{wvts}{\mathcal{C}^{(1)*}_{\ell equ}} - 2[Y_n^\dagger]_{pw}[Y_u]_{sv}\underset{vtwr}{\mathcal{C}_{qn}} + 2[Y_n^\dagger]_{pw}[Y_u]_{vt}\underset{wrsv}{\mathcal{C}_{nu}} + 2[Y_e^\dagger]_{pw}[Y_d]_{vt}\underset{rwvs}{\mathcal{C}^*_{nedu}} \\ & +2[Y_n^\dagger]_{vr}[Y_u]_{wt}\underset{pvwt}{\mathcal{C}^{(1)}_{\ell q}} + 6[Y_n^\dagger]_{vr}[Y_u]_{wt}\underset{pvwt}{\mathcal{C}^{(3)}_{\ell q}} - 2[Y_n^\dagger]_{vr}[Y_u]_{wt}\underset{pvsw}{\mathcal{C}_{\ell u}} - 2[Y_u^\dagger]_{sv}[Y_d]_{wt}\underset{prvw}{\mathcal{C}^{(1)}_{\ell nqd}} \\ & -2\underset{pr}{\xi_n}[Y_u]_{st} - 2\underset{st}{\xi^*_u}[Y_n^\dagger]_{pr} + \underset{pv}{\gamma^{(Y)}_\ell}\underset{vrst}{\mathcal{C}_{\ell nuq}} + \underset{sv}{\gamma^{(Y)}_u}\underset{prvt}{\mathcal{C}_{\ell nuq}} + \underset{pvst}{\mathcal{C}_{\ell nuq}}\underset{vr}{\gamma^{(Y)}_n} + \underset{prsv}{\mathcal{C}_{\ell nuq}}\underset{vt}{\gamma^{(Y)}_q}\,,\end{aligned} \tag{3.33}$$

where $y_n = 0$, $y_e = -1$, $y_\ell = -1/2$, $y_u = 2/3$, $y_d = -1/3$, and $y_q = 1/6$ are the hypercharges. The Yukawa interactions of the right-handed neutrinos modify the RGE of the four-fermion SMEFT operators listed in Table 3. We only provide the additional terms induced by the right-handed neutrino Yukawa couplings Y_n. For the operators in the lower panel of Table 3, the anomalous dimensions are modified via the ξ parameters in Eq. (3.22).

3.3.4 SMEFT: $(\bar{L}L)(\bar{L}L)$

$$\begin{aligned}\underset{prst}{\dot{\mathcal{C}}_{\ell\ell}} \;\supset\;& \frac{1}{2}[Y_n^\dagger Y_n]_{pr}(\underset{st}{\mathcal{C}^{(1)}_{\phi\ell}} + \underset{st}{\mathcal{C}^{(3)}_{\phi\ell}}) + \frac{1}{2}[Y_n^\dagger Y_n]_{st}(\underset{pr}{\mathcal{C}^{(1)}_{\phi\ell}} + \underset{pr}{\mathcal{C}^{(3)}_{\phi\ell}}) \\ & -\frac{1}{2}[Y_n]_{sv}[Y_n]_{wt}\underset{prvw}{\mathcal{C}_{\ell n}} - \frac{1}{2}[Y_n]_{pv}[Y_n]_{wr}\underset{stvw}{\mathcal{C}_{\ell n}} \\ & -\frac{1}{2}([Y_n]_{vr}[Y_e]_{wt}\underset{pvsw}{\mathcal{C}_{\ell n\ell e}} + [Y_n]_{wt}[Y_e]_{vr}\underset{swpv}{\mathcal{C}_{\ell n\ell e}}) - \frac{1}{2}([Y_n^\dagger]_{pv}[Y_e^\dagger]_{sw}\underset{rvtw}{\mathcal{C}^*_{\ell n\ell e}} + [Y_n^\dagger]_{sw}[Y_e^\dagger]_{pv}\underset{twrv}{\mathcal{C}^*_{\ell n\ell e}}),\end{aligned} \tag{3.34}$$

$(\bar{L}L)(\bar{L}L)$		$(\bar{L}L)(\bar{R}R)$		$(\bar{L}R)(\bar{R}L)$ and $(\bar{L}R)(\bar{L}R)$	
$\mathcal{O}_{\ell\ell}$	$(\bar{\ell}_p\gamma_\mu\ell_r)(\bar{\ell}_s\gamma^\mu\ell_t)$	$\mathcal{O}_{\ell d}$	$(\bar{\ell}_p\gamma_\mu\ell_r)(\bar{d}_s\gamma^\mu d_t)$	$\mathcal{O}^{(1)}_{\ell equ}$	$(\bar{\ell}^j_p e_r)\epsilon_{jk}(\bar{q}^k_s u_t)$
$\mathcal{O}^{(1)}_{\ell q}$	$(\bar{\ell}_p\gamma_\mu\ell_r)(\bar{q}_s\gamma^\mu q_t)$	$\mathcal{O}_{\ell u}$	$(\bar{\ell}_p\gamma_\mu\ell_r)(\bar{u}_s\gamma^\mu u_t)$	$\mathcal{O}^{(3)}_{\ell equ}$	$(\bar{\ell}^j_p\sigma_{\mu\nu}e_r)\epsilon_{jk}(\bar{q}^k_s\sigma^{\mu\nu}u_t)$
$\mathcal{O}^{(3)}_{\ell q}$	$(\bar{\ell}_p\gamma_\mu\tau^I\ell_r)(\bar{q}_s\gamma^\mu\tau^I q_t)$	$\mathcal{O}_{\ell e}$	$(\bar{\ell}_p\gamma_\mu\ell_r)(\bar{e}_s\gamma^\mu e_t)$	$\mathcal{O}_{\ell edq}$	$(\bar{\ell}^j_p e_r)(\bar{d}_s q^j_t)$
		$\mathcal{O}^{(1)}_{qu}$	$(\bar{q}_p\gamma_\mu q_r)(\bar{u}_s\gamma^\mu u_t)$	$\mathcal{O}^{(1)}_{quqd}$	$(\bar{\ell}^j_p n_r)(\bar{u}_s q^j_t)$
		$\mathcal{O}^{(8)}_{qu}$	$(\bar{q}_p\gamma_\mu T^A q_r)(\bar{u}_s\gamma^\mu T^A u_t)$		
		$\mathcal{O}^{(1)}_{qd}$	$(\bar{q}_p\gamma_\mu q_r)(\bar{d}_s\gamma^\mu d_t)$		
		$\mathcal{O}^{(8)}_{qd}$	$(\bar{q}_p\gamma_\mu T^A q_r)(\bar{d}_s\gamma^\mu T^A d_t)$		

Table 3: The 14 four-fermion SMEFT operators whose anomalous dimensions are modified by right-handed neutrino Yukawa couplings. Here, $I(A)$ is the adjoint index of $SU(2)_L$ ($SU(3)_C$).

$$\begin{aligned}\dot{\mathcal{C}}^{(1)}_{\underset{prst}{\ell q}} \supset\ & [Y_n^\dagger Y_n]_{pr}\mathcal{C}^{(1)}_{\underset{st}{\phi q}} - [Y_n^\dagger]_{pv}[Y_n]_{wr}\mathcal{C}_{\underset{stvw}{qn}} + \frac{1}{4}([Y_n]_{vr}[Y_u]_{sw}\mathcal{C}_{\underset{pvwt}{\ell nuq}} + [Y_n^\dagger]_{pv}[Y_u^\dagger]_{wt}\mathcal{C}^*_{\underset{rvws}{\ell nuq}}) \\ & -\frac{1}{4}([Y_n]_{vr}[Y_d]_{wt}\mathcal{C}^{(1)}_{\underset{pvsw}{\ell nqd}} + [Y_n^\dagger]_{pv}[Y_d^\dagger]_{sw}\mathcal{C}^{(1)*}_{\underset{rvtw}{\ell nqd}}) + 3([Y_n]_{vr}[Y_d]_{wt}\mathcal{C}^{(3)}_{\underset{pvsw}{\ell nqd}} + [Y_n^\dagger]_{pv}[Y_d^\dagger]_{sw}\mathcal{C}^{(3)*}_{\underset{rvtw}{\ell nqd}})\,,\end{aligned} \tag{3.35}$$

$$\begin{aligned}\dot{\mathcal{C}}^{(3)}_{\underset{prst}{\ell q}} \supset\ & -[Y_n^\dagger Y_n]_{pr}\mathcal{C}^{(3)}_{\underset{st}{\phi q}} + \frac{1}{4}([Y_n]_{vr}[Y_u]_{sw}\mathcal{C}_{\underset{pvwt}{\ell nuq}} + [Y_n^\dagger]_{pv}[Y_u^\dagger]_{wt}\mathcal{C}^*_{\underset{rvws}{\ell nuq}}) \\ & +\frac{1}{4}([Y_n]_{vr}[Y_d]_{wt}\mathcal{C}^{(1)}_{\underset{pvsw}{\ell nqd}} + [Y_n^\dagger]_{pv}[Y_d^\dagger]_{sw}\mathcal{C}^{(1)*}_{\underset{rvtw}{\ell nqd}}) - 3([Y_n]_{vr}[Y_d]_{wt}\mathcal{C}^{(3)}_{\underset{pvsw}{\ell nqd}} + [Y_n^\dagger]_{pv}[Y_d^\dagger]_{sw}\mathcal{C}^{(3)*}_{\underset{rvtw}{\ell nqd}})\,.\end{aligned} \tag{3.36}$$

3.3.5 SMEFT: $(\bar{L}L)(\bar{R}R)$

$$\dot{\mathcal{C}}_{\substack{\ell d\\ prst}} \supset [Y_n^\dagger Y_n]_{pr}\mathcal{C}_{\substack{\phi d\\ st}} - [Y_n]_{pv}[Y_n^\dagger]_{wr}\mathcal{C}_{\substack{nd\\ vwst}} + \frac{1}{2}\big([Y_d]_{sw}[Y_n]_{vr}\mathcal{C}^{(1)}_{\substack{\ell nqd\\ pvwt}} + [Y_d^\dagger]_{wt}[Y_n^\dagger]_{pv}\mathcal{C}^{(1)*}_{\substack{\ell nqd\\ rvws}}\big)$$
$$+6\big([Y_d]_{sw}[Y_n]_{vr}\mathcal{C}^{(3)}_{\substack{\ell nqd\\ pvwt}} + [Y_d^\dagger]_{wt}[Y_n^\dagger]_{pv}\mathcal{C}^{(3)*}_{\substack{\ell nqd\\ rvws}}\big)\,, \tag{3.37}$$

$$\dot{\mathcal{C}}_{\substack{\ell u\\ prst}} \supset [Y_n^\dagger Y_n]_{pr}\mathcal{C}_{\substack{\phi u\\ st}} - [Y_n]_{pv}[Y_n^\dagger]_{wr}\mathcal{C}_{\substack{nu\\ vwst}} - \frac{1}{2}\big([Y_u^\dagger]_{wt}[Y_n]_{vr}\mathcal{C}_{\substack{\ell nuq\\ pvsw}} + [Y_u]_{sw}[Y_n^\dagger]_{pv}\mathcal{C}^{*}_{\substack{\ell nuq\\ rvtw}}\big), \tag{3.38}$$

$$\dot{\mathcal{C}}_{\substack{\ell e\\ prst}} \supset [Y_e]_{sr}\xi_{\substack{e\\ pt}} + [Y_e^\dagger]_{pt}\xi^*_{\substack{e\\ rs}} + [Y_n^\dagger Y_n]_{pr}\mathcal{C}_{\substack{\phi e\\ st}} - [Y_n]_{pv}[Y_n^\dagger]_{wr}\mathcal{C}_{\substack{ne\\ vwst}}$$
$$+\frac{1}{2}\big([Y_e]_{sw}[Y_n]_{vr}\mathcal{C}_{\substack{\ell n\ell e\\ pvwt}} + [Y_e^\dagger]_{wt}[Y_n^\dagger]_{pv}\mathcal{C}^*_{\substack{\ell n\ell e\\ rvws}}\big)\,, \tag{3.39}$$

$$\dot{\mathcal{C}}^{(1)}_{\substack{qu\\ prst}} \supset \frac{1}{N_c}[Y_u]_{sr}\xi_{\substack{u\\ pt}} + \frac{1}{N_c}[Y_u^\dagger]_{pt}\xi^*_{\substack{u\\ rs}}\,, \tag{3.40}$$

$$\dot{\mathcal{C}}^{(8)}_{\substack{qu\\ prst}} \supset 2[Y_u]_{sr}\xi_{\substack{u\\ pt}} + 2[Y_u^\dagger]_{pt}\xi^*_{\substack{u\\ rs}}\,, \tag{3.41}$$

$$\dot{\mathcal{C}}^{(1)}_{\substack{qd\\ prst}} \supset \frac{1}{N_c}[Y_d]_{sr}\xi_{\substack{d\\ pt}} + \frac{1}{N_c}[Y_d^\dagger]_{pt}\xi^*_{\substack{d\\ rs}}\,, \tag{3.42}$$

$$\dot{\mathcal{C}}^{(8)}_{\substack{qd\\ prst}} \supset 2[Y_d]_{sr}\xi_{\substack{d\\ pt}} + 2[Y_d^\dagger]_{pt}\xi^*_{\substack{d\\ rs}}\,. \tag{3.43}$$

3.3.6 SMEFT: $(\bar{L}R)(\bar{R}L)$ and $(\bar{L}R)(\bar{L}R)$

$$\dot{\mathcal{C}}_{\substack{\ell edq\\ prst}} \supset -2[Y_d]_{st}\xi_{\substack{e\\ pr}} - 2[Y_e^\dagger]_{pr}\xi^*_{\substack{d\\ ts}} + 2[Y_n^\dagger]_{pv}[Y_e^\dagger]_{wr}\mathcal{C}^{(1)*}_{\substack{\ell nqd\\ wvst}} + 2[Y_n^\dagger]_{pv}[Y_u]_{wt}\mathcal{C}_{\substack{nedu\\ vrsw}}\,, \tag{3.44}$$

$$\dot{\mathcal{C}}^{(1)}_{\substack{\ell equ\\ prst}} \supset 2[Y_u^\dagger]_{st}\xi_{\substack{e\\ pr}} + 2[Y_e^\dagger]_{pr}\xi_{\substack{u\\ st}} + 2[Y_n^\dagger]_{pv}[Y_e^\dagger]_{wr}\mathcal{C}^*_{\substack{\ell nuq\\ wvts}} - 2[Y_n^\dagger]_{pv}[Y_d^\dagger]_{sw}\mathcal{C}_{\substack{nedu\\ vrwt}}\,, \tag{3.45}$$

$$\dot{\mathcal{C}}^{(3)}_{\substack{\ell equ\\ prst}} \supset \frac{1}{2}[Y_n^\dagger]_{pv}[Y_d^\dagger]_{sw}\mathcal{C}_{\substack{nedu\\ vrwt}}\,, \tag{3.46}$$

$$\dot{\mathcal{C}}^{(1)}_{\substack{quqd\\prst}} \supset -2[Y_u^\dagger]_{pr}\xi_{\substack{d\\st}} - 2[Y_d^\dagger]_{st}\xi_{\substack{u\\pr}} \,. \tag{3.47}$$

3.4 Anomalous Dimensions in SMNEFT: Gauge Coupling Dependence

In this section, we compute one-loop contributions to the ADM due to SM gauge couplings. The four-fermion operators (ψ^4) in Table 2 can be divided into four categories: $(\bar{R}R)(\bar{R}R)$, $(\bar{L}L)(\bar{R}R)$, $(\bar{L}R)(\bar{R}L)$, and $(\bar{L}R)(\bar{L}R)$ on the basis of the chiralities of the fields. The remaining operators are of the form $\psi^2\phi^3$, $\psi^2\phi^2 D$ and $\psi^2 X\phi$. We focus on the ψ^4-ψ^4 and ψ^4 - $\psi^2\phi^2 D$ operator mixing since the mixing between $\psi^2\phi^3$, $\psi^2\phi^2 D$ and $\psi^2 X\phi$ has been computed in the Ref. [104] using the background field method. We have checked that the resulting 5×5 matrix is consistent with the result for the corresponding SMEFT operators [101] which have a similar ADM structure.

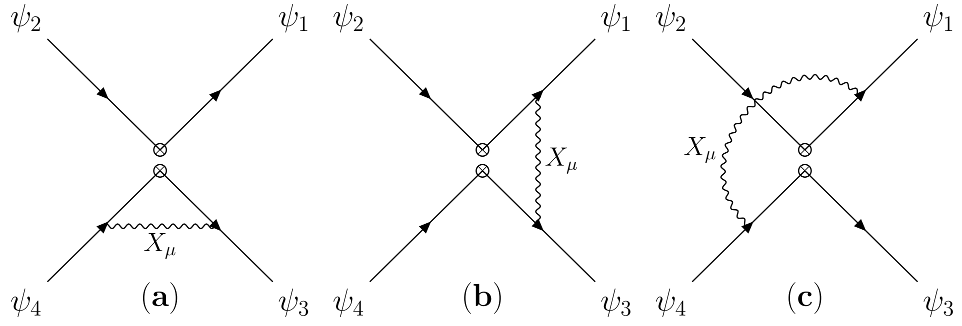

Figure 10: Current-current topologies with four-fermion insertions. Here X_μ represents the gauge bosons B_μ, W_μ and G_μ. The fermion fields q, u, d, ℓ, e and n are represented by ψ_I.

For the mixing between ψ^4-ψ^4 and ψ^4-$\psi^2\phi^2 D$, the current-current (Fig. 10) and penguin (Fig. 11) topologies mediated by the gauge bosons $X_\mu = B_\mu, W_\mu, G_\mu$, or the scalar, have to be calculated.

We now present terms for the one-loop ADM that depend on the gauge couplings α_1, α_2 and α_3 for all 16 SMNEFT operators. The ADM for bosonic SMNEFT operators is given in Ref. [104]. The ADM of most SMNEFT operators can be obtained from the ADM of the SMEFT operators [101] with a similar structure. For example, the ADM for the SMNEFT operators $\mathcal{O}_{\ell nuq}$, $\mathcal{O}^{(1)}_{\ell nqd}$ and $\mathcal{O}^{(3)}_{\ell nqd}$, can be obtained by replacing e with n, and switching u and

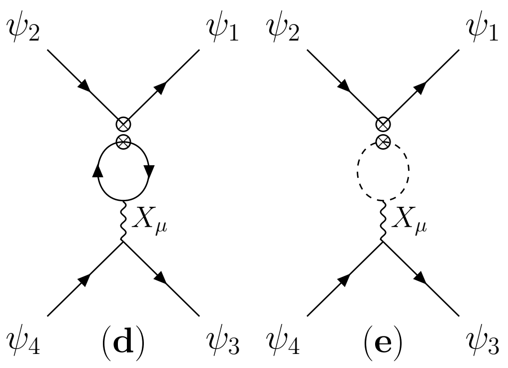

Figure 11: Penguin topologies with four-fermion (d) and boson (e) insertions.

d in the SMEFT operators $\mathcal{O}_{\ell edq}$, $\mathcal{O}^{(1)}_{\ell equ}$ and $\mathcal{O}^{(3)}_{\ell equ}$. We use this procedure as a cross-check when available. No such comparison is possible for $\mathcal{O}_{nedu}$, which has a structure not present in SMEFT.

3.4.1 ψ^4

The ADM for four-fermion operators are provided below.

$$\begin{aligned}
\dot{\mathcal{C}}_{\underset{prst}{nd}} &= \Big(\frac{4}{3}N_c y_d^2 \mathcal{C}_{\underset{prww}{nd}} + \frac{4}{3}N_c y_d y_u \mathcal{C}_{\underset{prww}{nu}} + \frac{4}{3} y_d y_e \mathcal{C}_{\underset{prww}{ne}} + \frac{8}{3}N_c y_d y_q \mathcal{C}_{\underset{wwpr}{qn}} + \frac{8}{3} y_d y_\ell \mathcal{C}_{\underset{wwpr}{\ell n}} \\
&\quad + \frac{4}{3} y_d y_h \mathcal{C}_{\underset{pr}{\phi n}}\Big) g_1^2 \delta_{st}\,, && (3.48) \\
\dot{\mathcal{C}}_{\underset{prst}{nu}} &= \Big(\frac{4}{3}N_c y_u y_d \mathcal{C}_{\underset{prww}{nd}} + \frac{4}{3}N_c y_u^2 \mathcal{C}_{\underset{prww}{nu}} + \frac{4}{3} y_u y_e \mathcal{C}_{\underset{prww}{ne}} + \frac{8}{3}N_c y_u y_q \mathcal{C}_{\underset{wwpr}{qn}} + \frac{8}{3} y_u y_\ell \mathcal{C}_{\underset{wwpr}{\ell n}} \\
&\quad + \frac{4}{3} y_u y_h \mathcal{C}_{\underset{pr}{\phi n}}\Big) g_1^2 \delta_{st}\,, && (3.49) \\
\dot{\mathcal{C}}_{\underset{prst}{ne}} &= \Big(\frac{4}{3}N_c y_e y_d \mathcal{C}_{\underset{prww}{nd}} + \frac{4}{3}N_c y_e y_u \mathcal{C}_{\underset{prww}{nu}} + \frac{4}{3} y_e^2 \mathcal{C}_{\underset{prww}{ne}} + \frac{8}{3}N_c y_e y_q \mathcal{C}_{\underset{wwpr}{qn}} + \frac{8}{3} y_e y_\ell \mathcal{C}_{\underset{wwpr}{\ell n}} \\
&\quad + \frac{4}{3} y_e y_h \mathcal{C}_{\underset{pr}{\phi n}}\Big) g_1^2 \delta_{st}\,, && (3.50) \\
\dot{\mathcal{C}}_{\underset{prst}{nedu}} &= \big((y_d - y_u)^2 + y_e(y_e + 8y_u - 2y_d)\big) g_1^2 \mathcal{C}_{\underset{prst}{nedu}}\,, && (3.51) \\
\dot{\mathcal{C}}_{\underset{prst}{nn}} &= 0\,, && (3.52)
\end{aligned}$$

$$
\begin{aligned}
\dot{\mathcal{C}}_{\substack{qn\\prst}} &= (\frac{4}{3}N_c y_q y_d \mathcal{C}_{\substack{nd\\stww}} + \frac{4}{3}N_c y_q y_u \mathcal{C}_{\substack{nu\\stww}} + \frac{4}{3}y_q y_e \mathcal{C}_{\substack{ne\\stww}} + \frac{8}{3}N_c y_q^2 \mathcal{C}_{\substack{qn\\wwst}} + \frac{8}{3}y_q y_\ell \mathcal{C}_{\substack{\ell n\\wwst}} \\
&\quad + \frac{4}{3}y_q y_h \mathcal{C}_{\substack{\phi n\\st}})g_1^2 \delta_{pr}\,, \qquad (3.53)\\
\dot{\mathcal{C}}_{\substack{\ell n\\prst}} &= (\frac{4}{3}N_c y_\ell y_d \mathcal{C}_{\substack{nd\\stww}} + \frac{4}{3}N_c y_\ell y_u \mathcal{C}_{\substack{nu\\stww}} + \frac{4}{3}y_\ell y_e \mathcal{C}_{\substack{ne\\stww}} + \frac{8}{3}N_c y_\ell y_q \mathcal{C}_{\substack{qn\\wwst}} + \frac{8}{3}y_\ell^2 \mathcal{C}_{\substack{\ell n\\wwst}} \\
&\quad + \frac{4}{3}y_\ell y_h \mathcal{C}_{\substack{\phi n\\st}})g_1^2 \delta_{pr}\,. \qquad (3.54)
\end{aligned}
$$

$$
\dot{\mathcal{C}}_{\substack{\ell n\ell e\\prst}} = ((y_e^2 - 8y_e y_\ell + 6y_\ell^2)g_1^2 - \frac{3}{2}g_2^2)\mathcal{C}_{\substack{\ell n\ell e\\prst}} - (4y_\ell(y_e + y_\ell)g_1^2 - 3g_2^2)\mathcal{C}_{\substack{\ell n\ell e\\srpt}}\,, \qquad (3.55)
$$

$$
\begin{aligned}
\dot{\mathcal{C}}^{(1)}_{\substack{\ell nqd\\prst}} &= ((y_d^2 - 2y_d(y_\ell + 4y_q) + (y_\ell + y_q)^2)g_1^2 - 8g_3^2)C^{(1)}_{\substack{\ell nqd\\prst}}\,,\\
&\quad + (-24y_\ell(y_d + y_q)g_1^2 + 18g_2^2)C^{(3)}_{\substack{\ell nqd\\prst}}\,, \qquad (3.56)\\
\dot{\mathcal{C}}^{(3)}_{\substack{\ell nqd\\prst}} &= (-\frac{1}{2}y_\ell(y_d + y_q)g_1^2 + \frac{3}{8}g_2^2)C^{(1)}_{\substack{\ell nqd\\prst}}\\
&\quad + ((y_d^2 - 6y_d y_\ell + y_\ell^2 + 6y_\ell y_q + y_q^2)g_1^2 - 3g_2^2 + \frac{8}{3}g_3{}^2)C^{(3)}_{\substack{\ell nqd\\prst}}\,, \qquad (3.57)\\
\dot{\mathcal{C}}_{\substack{\ell nuq\\prst}} &= (((y_\ell + y_u)^2 + y_q(y_q - 2y_\ell - 8y_u))g_1^2 - 8g_3^2)\mathcal{C}_{\substack{\ell nuq\\prst}}\,. \qquad (3.58)
\end{aligned}
$$

3.4.2 $\psi^2\phi^3$

$$
\begin{aligned}
\dot{\mathcal{C}}_{\underset{pr}{n\phi}} =& -(9y_\ell^2 g_1^2 + \frac{27}{4}g_2^2)\mathcal{C}_{\underset{pr}{n\phi}} - 6(4y_h^2 y_\ell g_1^3 - y_h g_1 g_2^2)\mathcal{C}_{\underset{pr}{nB}} \\
&+ 3(4y_h y_\ell g_1^2 g_2 - 3g_2^3)\mathcal{C}_{\underset{pr}{nW}}\,.
\end{aligned}
\tag{3.59}
$$

3.4.3 $\psi^2\phi^2 D$

$$
\begin{aligned}
\dot{\mathcal{C}}_{\underset{pr}{\phi n}} &= (\frac{4}{3}y_h^2\mathcal{C}_{\underset{pr}{\phi n}} + \frac{4}{3}N_c y_d y_h \mathcal{C}_{\underset{prww}{nd}} + \frac{4}{3}N_c y_u y_h \mathcal{C}_{\underset{prww}{nu}} + \frac{4}{3}y_e y_h \mathcal{C}_{\underset{prww}{ne}} + \frac{8}{3}N_c y_q y_h \mathcal{C}_{\underset{wwpr}{qn}} \\
&\quad + \frac{8}{3}y_\ell y_h \mathcal{C}_{\underset{wwpr}{\ell n}})g_1^2\,, \qquad (3.60)\\
\dot{\mathcal{C}}_{\underset{pr}{\phi ne}} &= (-3y_e^2\mathcal{C}_{\underset{pr}{\phi ne}})g_1^2\,. \qquad (3.61)
\end{aligned}
$$

3.4.4 $\psi^2 X\phi$

$$
\begin{aligned}
\dot{\mathcal{C}}_{\underset{pr}{nW}} &= ((3\mathcal{C}_{F,2} - b_{0,2})g_2^2 - 3y_\ell^2 g_1^2)\mathcal{C}_{\underset{pr}{nW}} + 3y_\ell g_1 g_2 \mathcal{C}_{\underset{pr}{nB}}\,, \qquad (3.62)\\
\dot{\mathcal{C}}_{\underset{pr}{nB}} &= (-3\mathcal{C}_{F,2}g_2^2 + (3y_\ell^2 - b_{0,1})g_1^2)\mathcal{C}_{\underset{pr}{nB}} + 12\mathcal{C}_{F,2}y_\ell g_1 g_2 C_{\underset{pr}{nW}}\,, \qquad (3.63)
\end{aligned}
$$

where the quadratic Casimir $C_{F,2} = \frac{3}{4}$. $b_{0,1} = -\frac{41}{6}$ and $b_{0,2} = \frac{19}{6}$ are the first coefficients in the g_1 and g_2 $\beta-$functions, respectively.

3.4.5 Operator mixing

We study operator mixing by solving the RG equations presented above in the leading-log approximation. The solution to these equations for running between scales Λ and μ is

$$
\mathcal{C}_i(\mu) = \left(\delta_{ij} + \frac{(\gamma_{\mathcal{C}})_{ij}}{16\pi^2}\ln\frac{\mu}{\Lambda}\right)\mathcal{C}_j(\Lambda)\,. \tag{3.64}
$$

Depending upon the mixing structure the operators an be divided into five subsets forming 6×6, 3×3, 3×3, 2×2, and 2×2 ADMs. Defining $\delta\mathcal{C}_i(\mu)=\mathcal{C}_i(\mu)-\mathcal{C}_i(\Lambda)$, the leading-log solution for the first group reads

$$\begin{pmatrix} \delta\mathcal{C}_{\underset{prst}{nd}} \\ \delta\mathcal{C}_{\underset{prst}{nu}} \\ \delta\mathcal{C}_{\underset{prst}{ne}} \\ \delta\mathcal{C}_{\underset{stpr}{qn}} \\ \delta\mathcal{C}_{\underset{stpr}{\ell n}} \\ \delta\mathcal{C}_{\underset{pr}{\phi n}} \end{pmatrix}_{(\mu)} = \frac{\alpha_1}{4\pi}\ln\frac{\mu}{\Lambda} \begin{pmatrix} \frac{4}{9}\delta_{st} & -\frac{8}{9}\delta_{st} & \frac{4}{9}\delta_{st} & -\frac{4}{9}\delta_{st} & \frac{4}{9}\delta_{st} & -\frac{2}{9}\delta_{st} \\ -\frac{8}{9}\delta_{st} & \frac{16}{9}\delta_{st} & -\frac{8}{9}\delta_{st} & \frac{8}{9}\delta_{st} & -\frac{8}{9}\delta_{st} & \frac{4}{9}\delta_{st} \\ \frac{4}{3}\delta_{st} & -\frac{8}{3}\delta_{st} & \frac{4}{3}\delta_{st} & -\frac{4}{3}\delta_{st} & \frac{4}{3}\delta_{st} & -\frac{2}{3}\delta_{st} \\ -\frac{2}{9}\delta_{st} & \frac{4}{9}\delta_{st} & -\frac{2}{9}\delta_{st} & \frac{2}{9}\delta_{st} & -\frac{2}{9}\delta_{st} & \frac{1}{9}\delta_{st} \\ \frac{2}{3}\delta_{st} & -\frac{4}{3}\delta_{st} & \frac{2}{3}\delta_{st} & -\frac{2}{3}\delta_{st} & \frac{2}{3}\delta_{st} & -\frac{1}{3}\delta_{st} \\ -\frac{2}{3} & \frac{4}{3} & -2 & \frac{2}{3} & -\frac{2}{3} & \frac{1}{3} \end{pmatrix} \begin{pmatrix} \mathcal{C}_{\underset{prww}{nd}} \\ \mathcal{C}_{\underset{prww}{nu}} \\ \mathcal{C}_{\underset{prww}{ne}} \\ \mathcal{C}_{\underset{wwpr}{qn}} \\ \mathcal{C}_{\underset{wwpr}{\ell n}} \\ \mathcal{C}_{\underset{pr}{\phi n}} \end{pmatrix}_{(\Lambda)} . \tag{3.65}$$

Summation over the repeated w index is implicit. Next, we have the 3×3 structure,

$$\begin{pmatrix} \delta\mathcal{C}_{\underset{pr}{n\phi}} \\ \delta\mathcal{C}_{\underset{pr}{nW}} \\ \delta\mathcal{C}_{\underset{pr}{nB}} \end{pmatrix}_{(\mu)} = \frac{1}{16\pi^2}\ln\frac{\mu}{\Lambda} \begin{pmatrix} -\frac{9}{4}(g_1^2+3g_2^2) & -3g_2(g_1^2+3g_2^2) & 6g_1^3 \\ 0 & -\frac{1}{12}(9g_1^2+11g_2^2) & -\frac{3g_1g_2}{2} \\ 0 & -\frac{9g_1g_2}{2} & \frac{9}{4}(\frac{91}{27}g_1^2-g_2^2) \end{pmatrix} \begin{pmatrix} \mathcal{C}_{\underset{pr}{n\phi}} \\ \mathcal{C}_{\underset{pr}{nW}} \\ \mathcal{C}_{\underset{pr}{nB}} \end{pmatrix}_{(\Lambda)} . \tag{3.66}$$

The operators $\mathcal{C}^{(1)}_{\ell nqd}$ and $\mathcal{C}^{(3)}_{\ell nqd}$ mix according to

$$\begin{pmatrix} \delta\mathcal{C}^{(1)}_{\underset{prst}{\ell nqd}} \\ \delta\mathcal{C}^{(3)}_{\underset{prst}{\ell nqd}} \end{pmatrix}_{(\mu)} = \ln\frac{\mu}{\Lambda}[\frac{\alpha_1}{4\pi} \begin{pmatrix} \frac{1}{3} & -2 \\ -\frac{1}{24} & -\frac{10}{9} \end{pmatrix} + \frac{\alpha_2}{4\pi} \begin{pmatrix} 0 & 18 \\ \frac{3}{8} & -3 \end{pmatrix} + \frac{\alpha_3}{4\pi} \begin{pmatrix} -8 & 0 \\ 0 & \frac{8}{3} \end{pmatrix}] \begin{pmatrix} \mathcal{C}^{(1)}_{\underset{prst}{\ell nqd}} \\ \mathcal{C}^{(3)}_{\underset{prst}{\ell nqd}} \end{pmatrix}_{(\Lambda)} . \tag{3.67}$$

The operator $\mathcal{C}_{\ell n\ell e}$ mix with different flavors:

$$\begin{pmatrix} \delta\mathcal{C}_{\underset{prst}{\ell n\ell e}} \\ \delta\mathcal{C}_{\underset{srpt}{\ell n\ell e}} \end{pmatrix}_{(\mu)} = \frac{\alpha_1+\alpha_2}{4\pi}\ln\frac{\mu}{\Lambda} \begin{pmatrix} -\frac{3}{2} & -3 \\ -3 & -\frac{3}{2} \end{pmatrix} \begin{pmatrix} \mathcal{C}_{\underset{prst}{\ell n\ell e}} \\ \mathcal{C}_{\underset{srpt}{\ell n\ell e}} \end{pmatrix}_{(\Lambda)} . \tag{3.68}$$

The remaining operators do not mix:

$$\begin{pmatrix} \delta\mathcal{C}_{\underset{prst}{nedu}} \\ \delta\mathcal{C}_{\underset{prst}{\ell nuq}} \\ \delta\mathcal{C}_{\underset{pr}{\phi ne}} \end{pmatrix}_{(\mu)} = \ln\frac{\mu}{\Lambda}[\frac{\alpha_1}{4\pi} \begin{pmatrix} -4 & & \\ & -\frac{2}{3} & \\ & & -3 \end{pmatrix} + \frac{\alpha_3}{4\pi} \begin{pmatrix} 0 & & \\ & -8 & \\ & & 0 \end{pmatrix}] \begin{pmatrix} \mathcal{C}_{\underset{prst}{nedu}} \\ \mathcal{C}_{\underset{prst}{\ell nuq}} \\ \mathcal{C}_{\underset{pr}{\phi ne}} \end{pmatrix}_{(\Lambda)} . \tag{3.69}$$

To study the running numerically, we set $\{prst\} = \{1111\}$ for illustration. We list the 16×16 ADM in the basis

$$\vec{\mathcal{C}} \;=\; \{\mathcal{C}_{nd},\, \mathcal{C}_{nu},\, \mathcal{C}_{ne},\, \mathcal{C}_{qn},\, \mathcal{C}_{\ell n},\, \mathcal{C}_{\phi n},\, \mathcal{C}_{n\phi},\, \mathcal{C}_{nW},\, \mathcal{C}_{nB},\, C^{(1)}_{\ell nqd},\, C^{(3)}_{\ell nqd},\, \mathcal{C}_{nedu},\, \mathcal{C}_{\ell n\ell e},\, \mathcal{C}_{\ell nuq},\, \mathcal{C}_{\phi ne},\, \mathcal{C}_{nn}\}\,. \tag{3.70}$$

The gauge couplings at 1 TeV are set to $g_1 = 0.36$, $g_2 = 0.64$, $g_3 = 1.1$. The 16 WCs at M_Z and at $\Lambda = 1$ TeV are related by

$$\frac{\delta\mathcal{C}(M_Z)}{10^{-3}} = \begin{pmatrix}
-0.92 & 1.8 & -0.92 & 0.92 & -0.92 & 0.46 \\
01.8 & -3.7 & 1.8 & -1.8 & 1.8 & -0.92 \\
-2.8 & 5.5 & -2.8 & 2.8 & -2.8 & 1.4 \\
0.46 & -0.92 & 0.46 & -0.46 & 0.46 & -0.23 \\
-1.4 & 2.8 & -1.4 & 1.4 & -1.4 & 0.69 \\
1.4 & -2.8 & 4.1 & -1.4 & 1.4 & -0.69 \\
 & & & & & & 49 & 41 & -4.5 \\
 & & & & & & 0 & 7.5 & 5.5 \\
 & & & & & & 0 & 17 & -1.1 \\
 & & & & & & & & & 160 & -110 \\
 & & & & & & & & & -2.4 & -30 \\
 & & & & & & & & & & & 8.3 \\
 & & & & & & & & & & & & -0.45 \\
 & & & & & & & & & & & & & 160 \\
 & & & & & & & & & & & & & & 6.2 \\
 & & & & & & & & & & & & & & & 0
\end{pmatrix} \mathcal{C}(\Lambda)\,. \tag{3.71}$$

The running effects in the 6×6 and 3×3 blocks are small because only electroweak gauge couplings contribute. The mixing in the 2×2 block is large as it is governed by QCD.

3.4.6 Phenomenology

We briefly comment on some phenomenological consequences of our results. Semileptonic decays of the b quark are topical given that both charged current and neutral current decay measurements are hinting at new physics. SMNEFT operators lead to the charged current decay $b \to c\ell\bar{n}$, which contributes at the hadronic level to $B \to D^{(*)}\tau\bar{\nu}_\tau$. They also generate the neutral current decay $b \to s\bar{n}n$ which contributes at the hadronic level to $B \to K^{(*)} +$ invisible decays, which is interpreted as $B \to K^{(*)}\bar{\nu}\nu$ in the SM. In the lepton sector, of interest are the FCNC decays $\tau \to \mu +$ invisible and $\mu \to e +$ invisible. To make contact with low-energy phenomenology, we first run the RG equations down to the weak scale and then match to the low-energy effective field theory extended with right-handed neutrinos n (LNEFT). Depending on the process, further RG running must be performed from the electroweak scale to the appropriate low energy scale such as the m_b scale for B meson decay and the m_τ scale for τ decay. Note that the sterile neutrino can mix with the active neutrinos, which in itself produces interesting phenomenology, but to keep our discussion simple we neglect this mixing. We select the following four types of process and list the SMNEFT operators relevant to them:

- $B \to D^{(*)}\tau\bar{\nu}_\tau$: $\mathcal{O}_{nedu}$, $\mathcal{O}_{\ell nuq}$, $\mathcal{O}^{(1)}_{\ell nqd}$, and $\mathcal{O}^{(3)}_{\ell nqd}$
- $B \to K^{(*)}\nu\bar{\nu}$ & $K \to \pi\nu\bar{\nu}$: $\mathcal{O}_{nd}$, $\mathcal{O}_{qn}$, $\mathcal{O}^{(1)}_{\ell nqd}$, and $\mathcal{O}^{(3)}_{\ell nqd}$
- $t \to c\nu\bar{\nu}$ & $c \to u\nu\bar{\nu}$: $\mathcal{O}_{nu}$, $\mathcal{O}_{qn}$, and $\mathcal{O}_{\ell nuq}$
- $\tau \to \mu\nu\bar{\nu}$ & $\mu \to e\nu\bar{\nu}$: $\mathcal{O}_{ne}$, $\mathcal{O}_{\ell n}$, and $\mathcal{O}_{\ell n\ell e}$

The FCNC operators, $\mathcal{O}_{nd}$, $\mathcal{O}_{nu}$, $\mathcal{O}_{ne}$, $\mathcal{O}_{qn}$ and $\mathcal{O}_{\ell n}$ do not run when only gauge interactions are considered. So we do not study these operators and focus on the five operators, $\mathcal{O}_{nedu}$, $\mathcal{O}_{\ell nuq}$, $\mathcal{O}^{(1)}_{\ell nqd}$, $\mathcal{O}^{(3)}_{\ell nqd}$ and $\mathcal{O}_{\ell n\ell e}$. Interestingly, $\mathcal{O}_{\ell nuq}$, $\mathcal{O}^{(1)}_{\ell nqd}$ and $\mathcal{O}^{(3)}_{\ell nqd}$ can contribute to both the charged current and neutral current decays, and to coherent elastic neutrino-nucleus scattering [105]. For certain flavor combinations, $\mathcal{O}_{\ell n\ell e}$ can produce both $\tau \to \mu$ and $\mu \to e$ decays.

Before studying the low-energy phenomenology, we first run the operators down from the new physics scale Λ to the weak scale μ_{EW}. By using the leading-log approximation in Eq. (3.64), we relate the values of the WCs at M_Z to their values at 1 TeV:

$$\begin{pmatrix} \underset{prst}{\mathcal{C}_{nedu}} \\ \underset{prst}{\mathcal{C}_{\ell nuq}} \\ \underset{prst}{\mathcal{C}^{(1)}_{\ell nqd}} \\ \underset{prst}{\mathcal{C}^{(3)}_{\ell nqd}} \end{pmatrix}_{(M_Z)} = \begin{pmatrix} 1.0 & 0 & 0 & 0 \\ 0 & 1.2 & 0 & 0 \\ 0 & 0 & 1.2 & -0.11 \\ 0 & 0 & -0.0024 & 0.97 \end{pmatrix} \begin{pmatrix} \underset{prst}{\mathcal{C}_{nedu}} \\ \underset{prst}{\mathcal{C}_{\ell nuq}} \\ \underset{prst}{\mathcal{C}^{(1)}_{\ell nqd}} \\ \underset{prst}{\mathcal{C}^{(3)}_{\ell nqd}} \end{pmatrix}_{(1\text{ TeV})}, \tag{3.72}$$

$$\begin{pmatrix} \underset{prst}{\mathcal{C}_{\ell n\ell e}} \\ \underset{srpt}{\mathcal{C}_{\ell n\ell e}} \end{pmatrix}_{(M_Z)} = \begin{pmatrix} 1.01 & -0.013 \\ -0.013 & 1.01 \end{pmatrix} \begin{pmatrix} \underset{prst}{\mathcal{C}_{\ell n\ell e}} \\ \underset{srpt}{\mathcal{C}_{\ell n\ell e}} \end{pmatrix}_{(1\text{ TeV})}. \tag{3.73}$$

To study the phenomenology at energies below the electroweak scale one can no longer use SMNEFT because of electroweak symmetry breaking. Instead, LNEFT, which respects the $SU(3)_C \times U(1)_Q$ symmetry must be employed to study the processes listed above. We introduce the relevant LNEFT operators and match them with the SMNEFT operators at the weak scale. The SMNEFT operators can generate both neutral and charged current processes after electroweak symmetry breaking. The induced LNEFT operators in the convention of Ref. [22] are displayed in Table 4 and their matching relations at tree level are

$$\begin{aligned} &C^{V,RR}_{\underset{prst}{nedu}} = \mathcal{C}_{\underset{prst}{nedu}}\,, \quad C^{S,RL}_{\underset{prst}{enud}} = \mathcal{C}_{\underset{prst}{\ell nuq}}\,, \quad C^{S,RR}_{\underset{prst}{enud}} = -C^{(1)}_{\underset{pr\delta t}{\ell nqd}}\frac{V_{s\delta}}{V_{st}}\,, \\ &C^{T,RR}_{\underset{prst}{enud}} = -C^{(3)}_{\underset{pr\delta t}{\ell nqd}}\frac{V_{s\delta}}{V_{st}}\,, \quad C^{S,RR}_{\underset{prst}{en\nu e}} = -\mathcal{C}_{\underset{prst}{\ell n\ell e}}\,, \end{aligned} \tag{3.74}$$

$$C^{S,RL}_{\underset{prst}{\nu nuu}} = \mathcal{C}_{\underset{prs\delta}{\ell nuq}} V^*_{t\delta}\,, \quad C^{S,RR}_{\underset{prst}{\nu ndd}} = C^{(1)}_{\underset{prst}{\ell nqd}}\,, \quad C^{T,RR}_{\underset{prst}{\nu ndd}} = C^{(3)}_{\underset{prst}{\ell nqd}}\,, \quad C^{S,RR}_{\underset{prst}{\nu nee}} = \mathcal{C}_{\underset{prst}{\ell n\ell e}}\,. \tag{3.75}$$

where we chose a flavor basis in which the left-handed down-type quarks and charged leptons are aligned. The flavor basis for up-type quarks in terms of the mass basis is given by $V^\dagger u_L$, where V is the SM CKM matrix. The neutrino fields are in the flavor basis for convenience. In the next subsections, we study the low-energy phenomenology of the listed processes.

3.4.6.1 $B \to D^{(*)}\tau\nu^-$ The CC LNEFT operators induced by the SMNEFT operators $\mathcal{O}_{\underset{\alpha 332}{nedu}}, \mathcal{O}_{\underset{3\alpha 23}{\ell nuq}}, \mathcal{O}^{(1)}_{\underset{3\alpha 23}{\ell nqd}}$ and $\mathcal{O}^{(3)}_{\underset{3\alpha 23}{\ell nqd}}$ can affect this process; see Table 4. Here, α is the flavor index of the right-handed neutrino n. Accounting for QED and QCD running below the weak scale, the one-loop RGE for the four LNEFT operators is given by

$$\begin{pmatrix} \dot{C}^{V,RR}_{\underset{\alpha 332}{nedu}} \\ \dot{C}^{S,RL}_{\underset{3\alpha 23}{enud}} \\ \dot{C}^{S,RR}_{\underset{3\alpha 23}{enud}} \\ \dot{C}^{T,RR}_{\underset{3\alpha 23}{enud}} \end{pmatrix}_{(\mu)} = [e^2 \begin{pmatrix} -4 & 0 & 0 & 0 \\ 0 & \frac{4}{3} & 0 & 0 \\ 0 & 0 & \frac{4}{3} & 8 \\ 0 & 0 & \frac{1}{6} & -\frac{40}{9} \end{pmatrix} + g_3^2 \begin{pmatrix} 0 & 0 & 0 & 0 \\ 0 & -8 & 0 & 0 \\ 0 & 0 & -8 & 0 \\ 0 & 0 & 0 & \frac{8}{3} \end{pmatrix}] \begin{pmatrix} C^{V,RR}_{\underset{\alpha 332}{nedu}} \\ C^{S,RL}_{\underset{3\alpha 23}{enud}} \\ C^{S,RR}_{\underset{3\alpha 23}{enud}} \\ C^{T,RR}_{\underset{3\alpha 23}{enud}} \end{pmatrix}_{(\mu)} \,, \tag{3.76}$$

SMNEFT	NC LNEFT	CC LNEFT
$\mathcal{O}_{\substack{nedu\\prst}}$	-	$O^{V,RR}_{\substack{nedu\\prst}} = (\bar{n}_{Rp}\gamma^{\mu}e_{Rr})(\bar{d}_{Rs}\gamma^{\mu}u_{Rt})$
$\mathcal{O}_{\substack{\ell nuq\\prst}}$	$O^{S,RL}_{\substack{\nu nuu\\prst}} = (\bar{\nu}_{Lp}n_{Rr})(\bar{u}_{Rs}u_{Lt})$	$O^{S,RL}_{\substack{enud\\prst}} = (\bar{e}_{Lp}n_{Rr})(\bar{u}_{Rs}d_{Lt})$
$\mathcal{O}^{(1)}_{\substack{\ell nqd\\prst}}$	$O^{S,RR}_{\substack{\nu ndd\\prst}} = (\bar{\nu}_{Lp}n_{Rr})(\bar{d}_{Ls}d_{Rt})$	$O^{S,RR}_{\substack{enud\\prst}} = (\bar{e}_{Lp}n_{Rr})(\bar{u}_{Ls}d_{Rt})$
$\mathcal{O}^{(3)}_{\substack{\ell nqd\\prst}}$	$O^{T,RR}_{\substack{\nu ndd\\prst}} = (\bar{\nu}_{Lp}\sigma^{\mu\nu}n_{Rr})(\bar{d}_{Ls}\sigma_{\mu\nu}d_{Rt})$	$O^{T,RR}_{\substack{enud\\prst}} = (\bar{e}_{Lp}\sigma^{\mu\nu}n_{Rr})(\bar{u}_{Ls}\sigma_{\mu\nu}d_{Rt})$
$\mathcal{O}_{\substack{\ell n\ell e\\prst}}$	$O^{S,RR}_{\substack{\nu nee\\prst}} = (\bar{\nu}_{Lp}n_{Rr})(\bar{e}_{Ls}e_{Rt})$	$O^{S,RR}_{\substack{en\nu e\\prst}} = (\bar{e}_{Lp}n_{Rr})(\bar{\nu}_{Ls}e_{Rt})$

Table 4: Operator structure matching between SMNEFT and LNEFT.

where e is the QED coupling. Using Eq. (3.64), we relate the four LNEFT operators at the m_b and M_Z scales:

$$\begin{pmatrix} C^{V,RR}_{\substack{nedu\\ \alpha 332}} \\ C^{S,RL}_{\substack{enud\\ 3\alpha 23}} \\ C^{S,RR}_{\substack{enud\\ 3\alpha 23}} \\ C^{T,RR}_{\substack{enud\\ 3\alpha 23}} \end{pmatrix}_{(m_b)} = \begin{pmatrix} 1.0 & 0 & 0 & 0 \\ 0 & 1.2 & 0 & 0 \\ 0 & 0 & 1.2 & -1.5\times 10^{-2} \\ 0 & 0 & -3.1\times 10^{-4} & 0.93 \end{pmatrix} \begin{pmatrix} C^{V,RR}_{\substack{nedu\\ \alpha 332}} \\ C^{S,RL}_{\substack{enud\\ 3\alpha 23}} \\ C^{S,RR}_{\substack{enud\\ 3\alpha 23}} \\ C^{T,RR}_{\substack{enud\\ 3\alpha 23}} \end{pmatrix}_{(M_Z)} . \tag{3.77}$$

The mixing between $O^{S,RR}_{enud}$ and $O^{T,RR}_{enud}$ is small as it is induced by QED. However, the corresponding mixing of the SMNEFT operators is relatively strong as it comes from electroweak effects.

3.4.6.2 $B \to K^{(*)}\nu\bar{\nu}$ & $K \to \pi\nu\bar{\nu}$ $B \to K^{(*)}$+invisible decay, which would be interpreted as $B \to K^{(*)}\nu\bar{\nu}$ in the SM, is produced by $O^{S,RR}_{\nu ndd}$ and $O^{T,RR}_{\nu ndd}$. The flavor structures are $\{prst\} = \{\alpha\beta 23\}$. The process $K \to \pi\nu\bar{\nu}$ can also be generated with the flavor structures, $\{prst\} = \{\alpha\beta 12\}$. The ADM for $O^{S,RR}_{\nu ndd}$ and $O^{T,RR}_{\nu ndd}$ is

$$\begin{pmatrix} \dot{C}^{S,RR}_{\substack{\nu ndd\\ \alpha\beta 23}} \\ \dot{C}^{T,RR}_{\substack{\nu ndd\\ \alpha\beta 23}} \end{pmatrix}_{(\mu)} = [e^2 \begin{pmatrix} -\frac{2}{3} & 0 \\ 0 & \frac{2}{9} \end{pmatrix} + g_3^2 \begin{pmatrix} -8 & 0 \\ 0 & \frac{8}{3} \end{pmatrix}] \begin{pmatrix} C^{S,RR}_{\substack{\nu ndd\\ \alpha\beta 23}} \\ C^{T,RR}_{\substack{\nu ndd\\ \alpha\beta 23}} \end{pmatrix}_{(\mu)} . \tag{3.78}$$

The WCs at m_b and M_Z are related by

$$\begin{pmatrix} C^{S,RR}_{\substack{\nu ndd\\ \alpha\beta 23}} \\ C^{T,RR}_{\substack{\nu ndd\\ \alpha\beta 23}} \end{pmatrix}_{(m_b)} = \begin{pmatrix} 1.2 & 0 \\ 0 & 0.92 \end{pmatrix} \begin{pmatrix} C^{S,RR}_{\substack{\nu ndd\\ \alpha\beta 23}} \\ C^{T,RR}_{\substack{\nu ndd\\ \alpha\beta 23}} \end{pmatrix}_{(M_Z)} . \tag{3.79}$$

While there is no mixing between the NC LNEFT operators, their corresponding SMNEFT operators can mix above the weak scale. For $K \to \pi\nu\bar{\nu}$ one has to run down to a scale appropriate for kaon decays.

3.4.6.3 $t \to c\nu\nu^{-}$ & $c \to u\nu\nu^{-}$ The NC LNEFT operator $O_{\nu}{}^{S,R}{}_{nuu}{}^{L}$ induced by $\mathcal{O}_{\ell nuq}$ can generate the rare decay $t \to c\nu\nu^{-}$ with $\{prst\} = \{\alpha\beta 23\}$. The RG equation for $O\,{}^{S,RL}_{\nu nuu}$ below the weak scale is

$$\dot{C}^{S,RL}_{\nu nuu}(\mu) = [e^2(-\frac{8}{3}) + g_3^2(-8)]C^{S,RL}_{\nu nuu}(\mu)\,, \tag{3.80}$$

and

$$C^{S,RL}_{\nu nuu}(\mu = m_b) = 1.2C^{S,RL}_{\nu nuu}(\mu = M_Z)\,. \tag{3.81}$$

3.4.6.4 $\tau \to \mu\nu\nu^{-}$ & $\mu \to e\nu\nu^{-}$ The decays $\tau \to \mu$ + invisible and $\mu \to e$ + invisible are generated by $O_{\nu}{}^{S,R}{}_{nee}{}^{R}$ and $O^{S}{}_{en\nu}{}^{,R}{}_{e}{}^{R}$. Note that the flavor is mixed for $\mathcal{O}_{\ell n\ell e}$. The flavor combination $\{prst\} = \{1132\}$ can generate both $\tau \to \mu$ and $\mu \to e$ decays. The relevant operators are $O^{S,RR}_{\underset{1132}{\nu nee}}$, $O^{S,RR}_{\underset{1132}{en\nu e}}$, $O^{S,RR}_{\underset{3112}{\nu nee}}$ and $O^{S,RR}_{\underset{3112}{en\nu e}}$. The running at one-loop order is given by

$$\begin{pmatrix} \dot{C}^{S,RR}_{\underset{1132}{\nu nee}} \\ \dot{C}^{S,RR}_{\underset{3112}{en\nu e}} \\ \dot{C}^{S,RR}_{\underset{1132}{en\nu e}} \\ \dot{C}^{S,RR}_{\underset{3112}{\nu nee}} \end{pmatrix}_{(\mu)} = e^2 \begin{pmatrix} -6 & 4 & & \\ 0 & 2 & & \\ & & -6 & 4 \\ & & 0 & 2 \end{pmatrix} \begin{pmatrix} C^{S,RR}_{\underset{1132}{\nu e}} \\ C^{S,RR}_{\underset{3112}{e\nu\nu e}} \\ C^{S,RR}_{\underset{1132}{e\nu\nu e}} \\ C^{S,RR}_{\underset{3112}{\nu e}} \end{pmatrix}_{(\mu)} . \tag{3.82}$$

The WCs at m_τ and M_Z are related by

$$\begin{pmatrix} C^{S,RR}_{\underset{1132}{\nu nee}} \\ C^{S,RR}_{\underset{3112}{en\nu e}} \\ C^{S,RR}_{\underset{1132}{en\nu e}} \\ C^{S,RR}_{\underset{3112}{\nu nee}} \end{pmatrix}_{(m_\tau)} = \begin{pmatrix} 1.01 & -9.6\times 10^{-3} & & \\ 0 & 0.995 & & \\ & & 1.01 & -9.6\times 10^{-3} \\ & & 0 & 0.995 \end{pmatrix} \begin{pmatrix} C^{S,RR}_{\underset{1132}{\nu nee}} \\ C^{S,RR}_{\underset{3112}{en\nu e}} \\ C^{S,RR}_{\underset{1132}{en\nu e}} \\ C^{S,RR}_{\underset{3112}{\nu nee}} \end{pmatrix}_{(M_Z)} . \tag{3.83}$$

The small mixing between these operators is a consequence of QED. For muon decay, one needs to run down to the muon mass.

3.4.6.5 Electroweak precision observables The operators $\mathcal{O}_{\phi n}$ and $\mathcal{O}_{\phi ne}$ give rise to RH Z-couplings to n and RH W couplings to n and leptons. The RH Z couplings to n can be parameterized in terms of the Wilson coefficient $\mathcal{C}_{\phi n}$ as

$$\delta\mathcal{L}_Z = -\frac{g_Z}{2} v^2 [\mathcal{C}_{\phi n}]_{pr} \; (\bar{n}_p \gamma_\mu n_r) \; Z_\mu \, , \tag{3.84}$$

where $g_Z^2 = g_1^2 + g_2^2$. Therefore, $\mathcal{C}_{\phi n}$ contributes to the Z-width via $\Gamma(Z \to n\bar{n})$. Similary, the RH W couplings can be parameterized in terms of $\mathcal{C}_{\phi ne}$ as

$$\delta\mathcal{L}_W = -\frac{g_2}{2\sqrt{2}} v^2 [\mathcal{C}_{\phi ne}]_{pr} \; (\bar{n}_p \gamma^\mu e_r) \; W_\mu^+ + h.c. \, . \tag{3.85}$$

Note that such leptonic RH W couplings are absent in SMEFT because the RH neutrino field is absent. The modified Z and W couplings affect electroweak precision observables. Interestingly, while $\mathcal{O}_{\phi ne}$ does not mix with the other operators as can be seen from Eq. (3.61), $\mathcal{O}_{\phi n}$ has mixing with other operators; see Eq. (3.60). Hence, electroweak precision observables can place indirect constraints on the $\mathcal{O}_{nd}$, $\mathcal{O}_{nu}$, $\mathcal{O}_{ne}$, $\mathcal{O}_{qn}$ and $\mathcal{O}_{\ell n}$ operators that mix with $\mathcal{O}_{\phi n}$, by a global fit.

4.0 General Neutrino Interactions in The SMNEFT

Going beyond the SM, the full list of dimension-six four-fermion SMNEFT operators, which include the left-handed and right-handed neutrino states, are given in Ref. [22]. Integrating out $W^\pm, Z, h$ and t leads to the low-energy effective field theory (LEFT), respecting $SU(3)_C \times U(1)_Q$. GNI via neutral and charged currents, containing scalar, pseudoscalar, vector, axial vector and tensor terms at dimension-six level can be parameterized as

$$\mathscr{L}_{\text{LEFT}}^{\text{NC}} \supset -\frac{G_F}{\sqrt{2}} \sum_{j=1}^{10} (\overset{(\sim)}{\epsilon}_{j,f})^{\alpha\beta\gamma\delta} (\overline{\nu}_\alpha O_j \nu_\beta)(\overline{f}_\gamma O'_j f_\delta)\,, \tag{4.1}$$

$$\mathscr{L}_{\text{LEFT}}^{\text{CC}} \supset -\frac{G_F V^*_{\delta\gamma}}{\sqrt{2}} \sum_{j=1}^{10} (\overset{(\sim)}{\epsilon}_{j,du})^{\alpha\beta\gamma\delta} (\overline{\nu}_\alpha O_j \ell_\beta)(\overline{d}_\gamma O'_j u_\delta) + \text{h.c.}\,, \tag{4.2}$$

where the operators O_j, O'_j and parameters $\overset{(\sim)}{\epsilon}$ are listed in Table 5. The Dirac spinor $\nu_\alpha = (\nu_{L\alpha}, N_\alpha)^T$, and u and d indicate the mass eigenstates of up- and down-type quarks, respectively.[1] Hermiticity of the Lagrangian requires the scalar and tensor effective couplings to satisfy

$$\begin{aligned} &\epsilon_{S,f}^{\alpha\beta\gamma\delta} = (\tilde{\epsilon}_{S,f}^{\beta\alpha\delta\gamma})^*, \quad \epsilon_{P,f}^{\alpha\beta\gamma\delta} = -(\tilde{\epsilon}_{P,f}^{\beta\alpha\delta\gamma})^*, \quad \epsilon_{T,f}^{\alpha\beta\gamma\delta} = (\tilde{\epsilon}_{T,f}^{\beta\alpha\delta\gamma})^*\,, \\ &\epsilon_{S,du}^{\alpha\beta\gamma\delta} = (\tilde{\epsilon}_{S,ud}^{\beta\alpha\delta\gamma})^*, \quad \epsilon_{P,du}^{\alpha\beta\gamma\delta} = -(\tilde{\epsilon}_{P,ud}^{\beta\alpha\delta\gamma})^*, \quad \epsilon_{T,du}^{\alpha\beta\gamma\delta} = (\tilde{\epsilon}_{T,ud}^{\beta\alpha\delta\gamma})^*\,. \end{aligned} \tag{4.3}$$

If the BSM new physics scale is Λ with a typical tree-level coupling κ, then parametrically $\overset{(\sim)}{\epsilon} \sim \kappa^2 v^2/\Lambda^2$. Note that the operators with $j = 1, 3$ are the familiar NSI terms, and are a subset of SMEFT.

In this chapter, we present the bounds on the WCs of three SMNEFT operators, from low-energy and high-energy experiments [105]. Those three chirality-flipping operators that couple to quarks are

1. $O_{NLQu}^{\alpha\beta\gamma\delta} = (\overline{N}_\alpha L^j_\beta)(\overline{Q}^j_\gamma u_\delta)\,,$
2. $O_{NLdQ}^{\alpha\beta\gamma\delta} = (\overline{N}_\alpha L^j_\beta)\epsilon_{jk}(\overline{d}_\gamma Q^k_\delta)\,,$
3. $O_{NLdQ}^{\prime\alpha\beta\gamma\delta} = (\overline{N}_\alpha \sigma_{\mu\nu} L^j_\beta)\epsilon_{jk}(\overline{d}_\gamma \sigma^{\mu\nu} Q^k_\delta)\,,$

---

[1] Our analysis can also be applied to Majorana neutrinos with the neutrino bilinears in Eqs. (1.1) and (4.1) replaced by $\overline{N}_{M\alpha} O \nu_{M\beta}$, where the Majorana spinors are $\nu_M = (\nu_L, \nu_L^c)^T$, $N_M = (N^c, N)^T$.

j	$\overset{(\sim)}{\epsilon}_j$	O_j	O'_j
1	ϵ_L	$\gamma_\mu(\mathbb{1}-\gamma^5)$	$\gamma_\mu(\mathbb{1}-\gamma^5)$
2	$\tilde{\epsilon}_L$	$\gamma_\mu(\mathbb{1}+\gamma^5)$	$\gamma_\mu(\mathbb{1}-\gamma^5)$
3	ϵ_R	$\gamma_\mu(\mathbb{1}-\gamma^5)$	$\gamma_\mu(\mathbb{1}+\gamma^5)$
4	$\tilde{\epsilon}_R$	$\gamma_\mu(\mathbb{1}+\gamma^5)$	$\gamma_\mu(\mathbb{1}+\gamma^5)$
5	ϵ_S	$\mathbb{1}-\gamma^5$	$\mathbb{1}$
6	$\tilde{\epsilon}_S$	$\mathbb{1}+\gamma^5$	$\mathbb{1}$
7	$-\epsilon_P$	$\mathbb{1}-\gamma^5$	γ^5
8	$-\tilde{\epsilon}_P$	$\mathbb{1}+\gamma^5$	γ^5
9	ϵ_T	$\sigma_{\mu\nu}(\mathbb{1}-\gamma^5)$	$\sigma_{\mu\nu}(\mathbb{1}-\gamma^5)$
10	$\tilde{\epsilon}_T$	$\sigma_{\mu\nu}(\mathbb{1}+\gamma^5)$	$\sigma_{\mu\nu}(\mathbb{1}+\gamma^5)$

Table 5: Effective coupling constants and operators.

where the fields are written in two-component spinors. L and Q are the left-handed lepton and quark doublet, respectively, and N is the right-handed neutrino state. Here, $\sigma^{\mu\nu} = \frac{i}{2}[\sigma^\mu\overline{\sigma}^\nu - \sigma^\nu\overline{\sigma}^\mu]$, with $\sigma^\mu = (\mathbb{1}, \vec{\sigma})$ and $\overline{\sigma}^\mu = (\mathbb{1}, -\vec{\sigma})$. We do not consider other dim-6 4-fermion SMNEFT operators since they lead to nonstandard charged lepton interactions and are therefore strongly constrained [22]. We can write the effective Lagrangian as

$$\mathscr{L}_{\text{eff}} = \mathscr{L}_{\text{SM}} + 2\sqrt{2}G_F[C_{NLdQ}O_{NLdQ} + C_{NLQu}O_{NLQu} + C'_{NLdQ}O'_{NLdQ}]\,, \tag{4.4}$$

where the flavor indices are omitted for simplicity. In the same spirit of power counting as in the last subsection, the Wilson coefficients (WCs) have the general dependence $C \sim \kappa^2 v^2/\Lambda^2$. For instance, $C \sim \mathcal{O}(10^{-4})$ if $\Lambda \sim 10$ TeV and $\kappa \sim 1$.

To jointly interpret the results of experiments at very different energy scales, a consistent theoretical framework is needed. LEFT and SMNEFT are the language we use to describe the physics below and above the electroweak scale v, respectively. The renormalization group (RG) running below and above the electroweak scale makes it possible to directly compare low-energy and high-energy probes. Leading-order (LO) matching between these two EFTs is performed at the electroweak scale.

4.1 Running and Matching

Since we will use both low-energy neutrino scattering experiments and high-energy colliders to constrain these Wilson coefficients (WCs), renormalization group (RG) running and matching have to be implemented. We perform leading-order (LO) matching of these two EFTs at the eletroweak scale:

$$\begin{aligned}
\epsilon_{S,d}^{\alpha\beta\gamma\delta} &= -C_{NLdQ}^{\alpha\beta\gamma\delta}\,, \quad \epsilon_{S,u}^{\alpha\beta\gamma\delta} = -C_{NLQu}^{\alpha\beta\rho\delta}V_{\rho\gamma}\,,\\
\epsilon_{P,d}^{\alpha\beta\gamma\delta} &= -C_{NLdQ}^{\alpha\beta\gamma\delta}\,, \quad \epsilon_{P,u}^{\alpha\beta\gamma\delta} = C_{NLQu}^{\alpha\beta\rho\delta}V_{\rho\gamma}\,,\\
\epsilon_{T,d}^{\alpha\beta\gamma\delta} &= -C_{NLdQ}^{\prime\alpha\beta\gamma\delta}\,,\\
\epsilon_{S,du}^{\alpha\beta\gamma\delta} &= \frac{C_{NLdQ}^{\alpha\beta\gamma\rho}V^{\dagger}_{\rho\delta} - C_{NLQu}^{\alpha\beta\gamma\delta}}{V^{*}_{\delta\gamma}}\,, \quad \epsilon_{P,du}^{\alpha\beta\gamma\delta} = \frac{C_{NLdQ}^{\alpha\beta\gamma\rho}V^{\dagger}_{\rho\delta} + C_{NLQu}^{\alpha\beta\gamma\delta}}{V^{*}_{\delta\gamma}}\,,\\
\epsilon_{T,du}^{\alpha\beta\gamma\delta} &= C_{NLdQ}^{\prime\alpha\beta\gamma\rho}\frac{V^{\dagger}_{\rho\delta}}{V^{*}_{\delta\gamma}}\,.
\end{aligned} \tag{4.5}$$

As we run down, both neutral and charged current WCs are induced by each of the three SMNEFT operators. Therefore they are not independent of each other. Their relations at the electroweak scale are

$$\begin{aligned}
\epsilon_{S,d}^{\alpha\beta\gamma\delta} &= -\frac{V^{\dagger}_{\gamma\rho}}{2V_{\delta\rho}}(\epsilon_{S,du}^{\alpha\beta\gamma\rho} + \epsilon_{P,du}^{\alpha\beta\gamma\rho})\,, \quad \epsilon_{P,d}^{\alpha\beta\gamma\delta} = -\epsilon_{S,d}^{\alpha\beta\gamma\delta}\,,\\
\epsilon_{S,u}^{\alpha\beta\gamma\delta} &= \frac{1}{2}V_{\gamma\rho}V^{*}_{\delta\rho}(\epsilon_{S,du}^{\alpha\beta\gamma\rho} - \epsilon_{P,du}^{\alpha\beta\gamma\rho})\,, \quad \epsilon_{P,u}^{\alpha\beta\gamma\delta} = -\epsilon_{S,u}^{\alpha\beta\gamma\delta}\,,\\
\epsilon_{T,d}^{\alpha\beta\gamma\delta} &= -\epsilon_{T,du}^{\alpha\beta\gamma\rho}\frac{V_{\rho\gamma}}{V^{*}_{\rho\delta}}\,.
\end{aligned} \tag{4.6}$$

We have performed the RG running above and below the weak scale, the details of which are described in section 3.4. The RG equations are run from 2 GeV to 1 TeV, which is the typical LHC scale. Eventually we place bounds on the SMNEFT WCs at 1 TeV. The anomalous dimension matrix we calculated at the one-loop level is

$$\begin{aligned}\mu\frac{d}{d\mu}\begin{pmatrix}C_{NLQu}\\ C_{NLdQ}\\ C'_{NLdQ}\end{pmatrix}_{(\mu)} &= [\frac{\alpha_1(\mu)}{2\pi}\begin{pmatrix}-1/3 & 0 & 0\\ 0 & 1/6 & -1\\ 0 & -1/48 & -5/9\end{pmatrix}+\frac{\alpha_2(\mu)}{2\pi}\begin{pmatrix}0 & 0 & 0\\ 0 & 0 & 9\\ 0 & 3/16 & -3/2\end{pmatrix}\\ &+\frac{\alpha_3(\mu)}{2\pi}\begin{pmatrix}-4 & 0 & 0\\ 0 & -4 & 0\\ 0 & 0 & 4/3\end{pmatrix}]\begin{pmatrix}C_{NLQu}\\ C_{NLdQ}\\ C'_{NLdQ}\end{pmatrix}_{(\mu)}\quad ,\end{aligned} \tag{4.7}$$

$$\mu\frac{d}{d\mu}\begin{pmatrix}\epsilon_{S,du}\\ \epsilon_{P,du}\\ \epsilon_{T,du}\end{pmatrix}_{(\mu)} = [\frac{\alpha_e(\mu)}{2\pi}\begin{pmatrix}2/3 & 0 & 4\\ 0 & 2/3 & 4\\ 1/24 & 1/24 & -20/9\end{pmatrix}+\frac{\alpha_3(\mu)}{2\pi}\begin{pmatrix}-4 & 0 & 0\\ 0 & -4 & 0\\ 0 & 0 & 4/3\end{pmatrix}]\begin{pmatrix}\epsilon_{S,du}\\ \epsilon_{P,du}\\ \epsilon_{T,du}\end{pmatrix}_{(\mu)}\quad , \tag{4.8}$$

$$\mu\frac{d}{d\mu}\begin{pmatrix}\epsilon_{S,d}\\ \epsilon_{P,d}\\ \epsilon_{T,d}\end{pmatrix}_{(\mu)} = [\frac{\alpha_e(\mu)}{2\pi}\begin{pmatrix}-1/9 & 0 & 0\\ 0 & -1/9 & 0\\ 0 & 0 & 5/36\end{pmatrix}+\frac{\alpha_3(\mu)}{2\pi}\begin{pmatrix}-4 & 0 & 0\\ 0 & -4 & 0\\ 0 & 0 & 4/3\end{pmatrix}]\begin{pmatrix}\epsilon_{S,d}\\ \epsilon_{P,d}\\ \epsilon_{T,d}\end{pmatrix}_{(\mu)}\quad , \tag{4.9}$$

$$\mu\frac{d}{d\mu}\begin{pmatrix}\epsilon_{S,u}\\ \epsilon_{P,u}\\ \epsilon_{T,u}\end{pmatrix}_{(\mu)} = [\frac{\alpha_e(\mu)}{2\pi}\begin{pmatrix}-4/9 & 0 & 0\\ 0 & -4/9 & 0\\ 0 & 0 & 5/9\end{pmatrix}+\frac{\alpha_3(\mu)}{2\pi}\begin{pmatrix}-4 & 0 & 0\\ 0 & -4 & 0\\ 0 & 0 & 4/3\end{pmatrix}]\begin{pmatrix}\epsilon_{S,u}\\ \epsilon_{P,u}\\ \epsilon_{T,u}\end{pmatrix}_{(\mu)}\quad , \tag{4.10}$$

where the flavor indices are implicit. The QED and weak couplings are important as they introduce mixing between different operators. Solving the differential equations with the three-loop β-functions and taking into account the top and bottom quark mass thresholds, we obtain the numerical relations between effective couplings at different energy scales:

$$\begin{pmatrix} C_{NLQu} \\ C_{NLdQ} \\ C'_{NLdQ} \end{pmatrix}_{(\mu=M_Z)} = \begin{pmatrix} 1.18 & 0 & 0 \\ 0 & 1.18 & -0.117 \\ 0 & -2.44\times 10^{-3} & 0.966 \end{pmatrix} \begin{pmatrix} C_{NLQu} \\ C_{NLdQ} \\ C'_{NLdQ} \end{pmatrix}_{(\mu=1\text{ TeV})} , \tag{4.11}$$

$$\begin{pmatrix} \epsilon_{S,du} \\ \epsilon_{P,du} \\ \epsilon_{T,du} \end{pmatrix}_{(\mu=2\text{ GeV})} = \begin{pmatrix} 1.52 & 2.34\times 10^{-6} & -0.0218 \\ 2.34\times 10^{-6} & 1.52 & -0.0218 \\ -2.26\times 10^{-4} & -2.26\times 10^{-4} & 0.878 \end{pmatrix} \begin{pmatrix} \epsilon_{S,du} \\ \epsilon_{P,du} \\ \epsilon_{T,du} \end{pmatrix}_{(\mu=M_Z)} , \tag{4.12}$$

$$\begin{pmatrix} \epsilon_{S,d} \\ \epsilon_{P,d} \\ \epsilon_{T,d} \end{pmatrix}_{(\mu=2\text{ GeV})} = \begin{pmatrix} 1.52 & 0 & 0 \\ 0 & 1.52 & 0 \\ 0 & 0 & 0.869 \end{pmatrix} \begin{pmatrix} \epsilon_{S,d} \\ \epsilon_{P,d} \\ \epsilon_{T,d} \end{pmatrix}_{(\mu=M_Z)} , \tag{4.13}$$

$$\begin{pmatrix} \epsilon_{S,u} \\ \epsilon_{P,u} \\ \epsilon_{T,u} \end{pmatrix}_{(\mu=2\text{ GeV})} = \begin{pmatrix} 1.53 & 0 & 0 \\ 0 & 1.53 & 0 \\ 0 & 0 & 0.867 \end{pmatrix} \begin{pmatrix} \epsilon_{S,u} \\ \epsilon_{P,u} \\ \epsilon_{T,u} \end{pmatrix}_{(\mu=M_Z)} . \tag{4.14}$$

The numerical relations between LEFT WCs at 2 GeV and SMNEFT WCs at 1 TeV, with $V_{ud} = 0.97420$ [8], are

$$\begin{aligned}
\epsilon_{S,du} &= -1.84 C_{NLQu} + 1.79 C_{NLdQ} - 0.199 C'_{NLdQ} , \\
\epsilon_{P,du} &= 1.84 C_{NLQu} + 1.79 C_{NLdQ} - 0.157 C'_{NLdQ} , \\
\epsilon_{T,du} &= 5.49\times 10^{-4} C_{NLQu} - 2.14\times 10^{-3} C_{NLdQ} + 0.849 C'_{NLdQ} , \\
\epsilon_{S,u} &= -1.76 C_{NLQu} , \\
\epsilon_{P,u} &= 1.76 C_{NLQu} , \\
\epsilon_{T,u} &= 0 , \\
\epsilon_{S,d} &= -1.80 C_{NLdQ} + 0.179 C'_{NLdQ} , \\
\epsilon_{P,d} &= -1.80 C_{NLdQ} + 0.179 C'_{NLdQ} , \\
\epsilon_{T,d} &= 2.12\times 10^{-3} C_{NLdQ} - 0.839 C'_{NLdQ} .
\end{aligned} \tag{4.15}$$

Low energy constraints on the SMNEFT WCs from nuclear beta decay, pseudoscalar meson decay, and coherent scattering have been discussed in Ref. [22] without accounting for the effects of RG running. The RG running is crucial, as it introduces operator mixing which produces degeneracies in the WCs. Here we first calculate the LEFT and SMNEFT WCs below and above the electroweak scale, respectively. After the RG running, we convert the low energy constraints on the LEFT WCs to the high energy constraints on the SMNEFT WCs, and compare them with those from high energy collider experiments at the same energy scale.

4.2 Neutrino Mass Bounds

Scalar and tensor interactions that flip the neutrino chirality contribute to the neutrino mass radiatively. Both one- and two-loop corrections to the neutrino mass can be generated by chirality-changing operators. Here we ignore the one-loop corrections since, except for the top quark, they are (counterintuitively) suppressed by a factor of $(m_q/M_Z)^2$ as compared to the two-loop corrections [108, 109]. The two-loop contribution is estimated as

$$\Delta m_\nu \simeq 3g^2 G_F \epsilon \frac{m_q M_W^2}{(4\pi)^4} (\ln \frac{\mu^2}{M_W^2})^2 \,, \tag{4.16}$$

where m_q is a quark mass, μ is the renormalization scale, and ϵ can be either a NC or CC GNI parameter. We conservatively take μ to not be too far above the electroweak scale so that the top quark loop correction is suppressed.

Bounds from neutrino masses and oscillations are very model specific because of the importance of the properties of the particles in the loops and the possibility of cancellations between loop and other contributions. However, barring fine-tuned cancellations, they provide an order of magnitude estimate of how much the new interactions may contribute to neutrino masses. For our estimates, we assume neutrinos acquire mass only from loop effects due to the new interactions, i.e., neutrino masses vanish as $\epsilon \to 0$. Then, constraints on the contact interactions can be obtained by requiring $\Delta m_\nu < \sum m_\nu$. A recent upper bound on the sum of neutrino mass from cosmological observations and particle physics experiments is $\sum m_\nu \lesssim 0.26$ eV [110], which is model dependent. The most recent model-independent bound is that obtained by the KATRIN Collaboration [111]. They reported a 1.1 eV upper bound on the effective neutrino mass based on the β-decay electron spectrum. The bounds on the scalar and tensor contact interactions from neutrino masses without (with) cosmological inputs are

$$|\epsilon^{\alpha\beta 11}_{S,P,T}| \lesssim 10^{-3}\,(10^{-4})\,, \quad |\epsilon^{\alpha\beta 22}_{S,P,T}| \lesssim 10^{-5}\,(10^{-6})\,, \quad |\epsilon^{\alpha\beta 33}_{S,P,T}| \lesssim 10^{-6}\,(10^{-7})\,. \tag{4.17}$$

The bounds using cosmological data are only suggestive because we have not evaluated how the relic neutrino abundance is affected by the new interactions. From Eq. (4.17), we see that if GNI are also coupled to heavy quark flavors, the bounds on the SMNEFT WCs $C_{NLQu},\ C_{NLdQ},\ \text{and}\, C'_{NLdQ}$ are too strong to be probed by other experiments, current or future. Despite the highly model-dependent nature of this conclusion, we focus on couplings to first generation quarks in the rest of this chapter.

Related bounds arise from neutrino magnetic moments via an external photon attached to the fermion loop responsible for neutrino mass generation. The magnetic moment induced by scalar and tensor GNI is bounded by [112]

$$\mu_\nu \approx \frac{eG_F m_d}{8\pi^2}\epsilon \lesssim 3\times 10^{-11}\mu_B\,, \tag{4.18}$$

where the Bohr magneton $\mu_B = \frac{e\hbar}{2m_e c} \simeq 2.9\times 10^{-7}$ eV^{-1}. This yields

$$|\,\epsilon^{\alpha\beta 11}_{S,P,T}\,| \lesssim 30\,, \tag{4.19}$$

which are much weaker than the bounds above.

4.3 Pseudoscalar Meson Decay

The pseudoscalar quark bilinear can contribute to the leptonic decay of a pseudoscalar meson (P). In the SM, the decay is helicity suppressed so that the width $\Gamma_{\rm SM}(P \to \ell\nu) \propto m_\ell^2$. The suppression is lifted by pseudoscalar GNI

$$\Gamma_{\rm GNI,p}(P \to \ell_\beta \nu_\alpha) \propto (\epsilon_{P,du}^{\alpha\beta 11})^2 \frac{m_\pi^4}{(m_u + m_d)^2} \,. \tag{4.20}$$

The branching ratio

$$R_\pi \equiv \frac{\Gamma(\pi \to e\nu[\gamma])}{\Gamma(\pi \to \mu\nu[\gamma])} = R_\pi^{(0)}[1 + \Delta_\pi], \quad \text{with} \;\; R_\pi^{(0)} = \frac{m_e^2}{m_\mu^2} (\frac{m_\pi^2 - m_e^2}{m_\pi^2 - m_\mu^2})^2 \,, \tag{4.21}$$

serves as a good observable, as the experiment systematic uncertainties shared by the two processes cancel in the ratio. Δ_π contains higher order corrections [113]. $\Gamma_{(\pi \to \ell\overline{\nu}[\gamma])}$ contains physical and virtual photons (radiative corrections). Including pseudoscalar GNI interactions [114],

$$\frac{R_\pi}{R_\pi^{SM}} = \frac{1+ \mid \frac{B_0}{m_e} \epsilon_{P,du}^{\alpha e 11} \mid^2}{1+ \mid \frac{B_0}{m_\mu} \epsilon_{P,du}^{\alpha \mu 11} \mid^2} \,, \tag{4.22}$$

where $B_0(\mu) = m_\pi^2/(m_u(\mu) + m_d(\mu))$. Taking $m_\pi = 139.57$ MeV, $m_u^{\overline{\rm MS}}(\mu = 2 \text{ GeV}) = 2.16$ MeV and $m_d^{\overline{\rm MS}}(\mu = 2 \text{ GeV}) = 4.67$ MeV [8], gives $B_0^{\overline{\rm MS}}(\mu = 2 \text{ GeV}) = 2.8 \times 10^3$ MeV. The current combined uncertainty in $R_\pi^{\rm exp}$ [115, 116, 117, 8] and $R_\pi^{\rm SM}$ [113, 118] are

$$R_\pi = 1.2327(23) \times 10^{-4} \,, \quad R_\pi^{SM} = 1.2352(1) \times 10^{-4} \,. \tag{4.23}$$

If both $\epsilon_{P,du}^{\alpha e 11}$ and $\epsilon_{P,du}^{\alpha\mu 11}$ are allowed to vary simultaneously, no bound on either parameter is obtained because they are degenerate, as is evident from Eq. (4.22). With the assumption that only one of $\epsilon_{P,du}$ is nonzero, the 90% C.L. bounds are

$$\mid \epsilon_{P,du}^{\alpha e 11} \mid < 6.2 \times 10^{-6}, \quad \text{and} \quad \mid \epsilon_{P,du}^{\alpha\mu 11} \mid < 2.7 \times 10^{-3} \,. \tag{4.24}$$

Because the measured branching to the electron channel is tiny, $\epsilon_{P,du}^{\alpha e 11}$ is highly constrained. These bounds are much stronger than the ones obtained in Ref. [114], which assumed that both $\epsilon_{P,du}$ and $\tilde{\epsilon}_{P,du}$ are simultaneously nonzero, which however, cannot be realized with the three SMNEFT operators considered here. The bounds on the coefficients of the low-energy effective Lagrangian can be translated to bounds on the three SMNEFT WCs by adopting the relations in Eq. (4.15), which display degeneracies between the SMNEFT WCs. We therefore bound the individual WCs by setting the other two to zero. The 90% C.L. bounds on the SMNEFT WCs are

$$| C^{\alpha e11}_{NLQu} |< 3.3 \times 10^{-6}\,, \quad | C^{\alpha e11}_{NLdQ} |< 3.4 \times 10^{-6}\,, \quad | C'^{\alpha e11}_{NLdQ} |< 3.9 \times 10^{-5}\,, \tag{4.25}$$

$$| C^{\alpha \mu 11}_{NLQu} |< 1.5 \times 10^{-3}\,, \quad | C^{\alpha \mu 11}_{NLdQ} |< 1.5 \times 10^{-3}\,, \quad | C'^{\alpha \mu 11}_{NLQu} |< 1.7 \times 10^{-2}\,. \tag{4.26}$$

The correlations between the C_{NLdQ} and C_{NLQu} (C'_{NLdQ}), with C'_{NLdQ} (C_{NLQu}) set to zero, are shown by the green lines in the upper (lower) panel of Fig. 12.

To circumvent the degeneracy in $\epsilon^{\alpha e11}_{P,du}$ and $\epsilon^{\alpha\mu 11}_{P,du}$ in Eq. (4.22), we now apply the individual decay width measurements of $\pi \to \ell\nu[\gamma]$ to set the bounds. In the SM, the decay width at tree level is

$$\Gamma_{(\pi\to\ell\overline{\nu}[\gamma])} = \frac{G_F^2}{8\pi} f_\pi^2 V_{ud}^2 m_\ell^2 m_\pi (1-\frac{m_\ell^2}{m_\pi^2})^2 (1+\Delta_\pi)\,. \tag{4.27}$$

The theoretical uncertainties are mainly from calculations of the decay constant and radiative corrections. According to Refs. [8, 119, 120, 118, 121],

$$\Delta_\pi = 0.0176 \pm 0.0021\,, \quad f_\pi = 130.2 \pm 1.2 \text{ MeV}\,. \tag{4.28}$$

The universal theoretical uncertainties yield

$$\frac{\delta\Gamma_{(\pi^+\to e^+\nu_e[\gamma])}}{\Gamma_{(\pi^+\to e^+\nu_e[\gamma])}} = \frac{\delta\Gamma_{(\pi^+\to \mu^+\nu_\mu[\gamma])}}{\Gamma_{(\pi^+\to \mu^+\nu_\mu[\gamma])}} = 1.9 \times 10^{-2}\,. \tag{4.29}$$

Measurements give $BR(\pi^+ \to e^+\nu_e[\gamma]) = (1.230 \pm 0.004) \times 10^{-4}\%$, $BR(\pi^+ \to \mu^+\nu_\mu[\gamma]) = (99.98770 \pm 0.00004)\%$, and $\tau_{\pi^\pm} = 26.033(5)$ ns [8]. The experimental uncertainties in the electron (muon) channel is 3.3×10^{-3} (1.9×10^{-4}) and can be neglected. Assuming that the new physics contributions do not exceed the theoretical uncertainties, the bounds on $\epsilon^{\alpha e11}_{P,du}$ and $\epsilon^{\alpha\mu 11}_{P,du}$ are given by

$$| \frac{B_0}{m_e}\epsilon^{\alpha e11}_{P,du} |^2 < \frac{\delta\Gamma_{(\pi^+\to e^+\nu_e[\gamma])}}{\Gamma_{(\pi^+\to e^+\nu_e[\gamma])}}, \qquad | \frac{B_0}{m_\mu}\epsilon^{\alpha \mu 11}_{P,du} |^2 < \frac{\delta\Gamma_{(\pi^+\to \mu^+\nu_\mu[\gamma])}}{\Gamma_{(\pi^+\to \mu^+\nu_\mu[\gamma])}}\,, \tag{4.30}$$

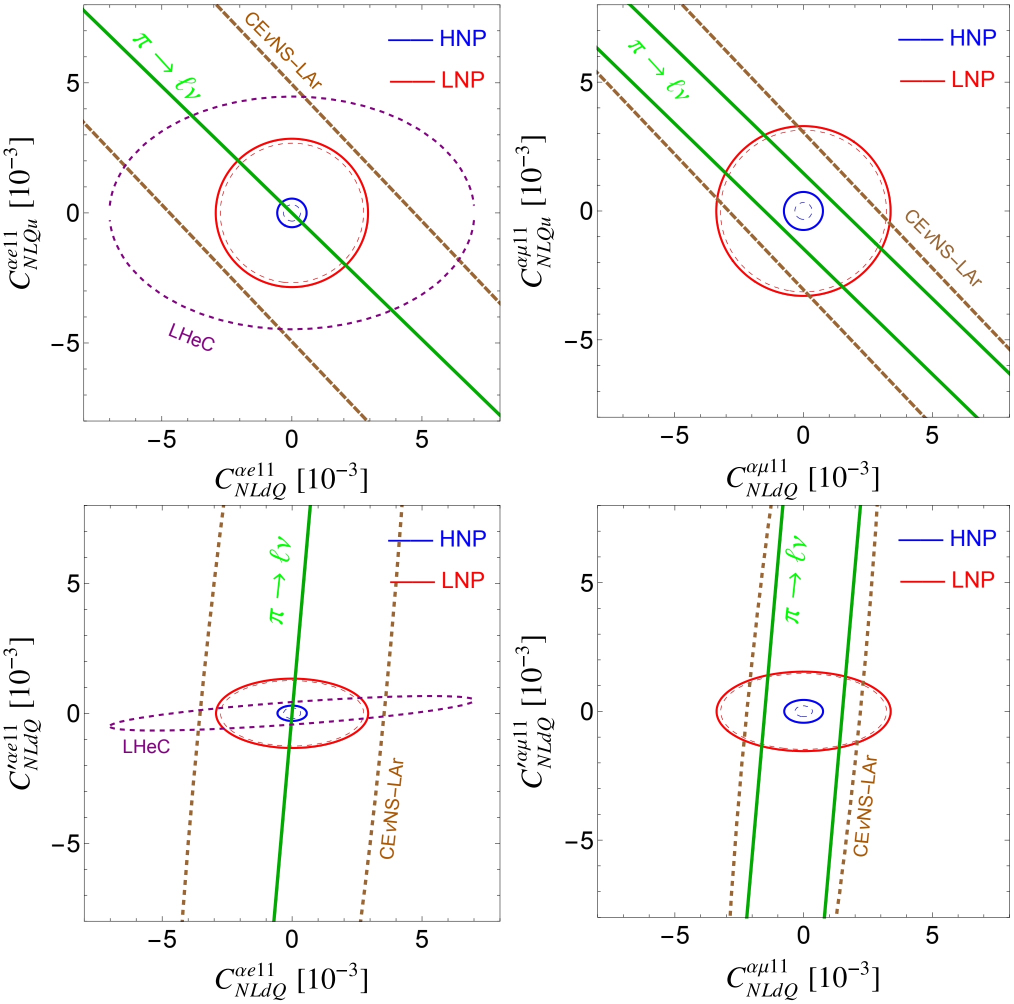

Figure 12: The 90% C.L. allowed regions in the C_{NLdQ}-C_{NLQu} planes (upper panels) and C_{NLdQ}-C'_{NLdQ} planes (lower panels) at 1 TeV with electron flavor (left panels) and muon flavor (right panels). The details of descriptions are in the main text.

which yield

$$|\,\epsilon^{\alpha e11}_{P,du}\,| < 3.4 \times 10^{-5}\,, \quad |\,\epsilon^{\alpha\mu 11}_{P,du}\,| < 6.6 \times 10^{-3}\,, \tag{4.31}$$

at the 90% C.L. By allowing only one WC to be nonzero at a time, the 90% C.L. bounds on the SMNEFT WCs derived from individual decay channels are

$$|\,C^{\alpha e11}_{NLQu}\,| < 1.9 \times 10^{-5}\,, \quad |\,C^{\alpha e11}_{NLdQ}\,| < 1.9 \times 10^{-5}\,, \quad |\,C'^{\alpha e11}_{NLdQ}\,| < 2.2 \times 10^{-4}\,, \tag{4.32}$$

$$|\, C^{\alpha\mu 11}_{NLQu} \,| < 3.6 \times 10^{-3}\,, \quad |\, C^{\alpha\mu 11}_{NLdQ} \,| < 3.7 \times 10^{-3}\,, \quad |\, C'^{\alpha\mu 11}_{NLQu} \,| < 4.2 \times 10^{-2}\,. \tag{4.33}$$

4.4 Nuclear Beta Decay

Nuclear β-decay is another low-energy probe that is sensitive to the new CC GNI interactions. The nucleon-level effective Lagrangian contributing to neutron beta decay, $n \to p + e^- + \overline{\nu}_e$, is using Eq. (4.3),

$$\begin{aligned} \mathscr{L}_N = & - \frac{G_F}{\sqrt{2}} V_{ud} [\overline{p}\gamma^\mu (g_V - g_A\gamma^5) n \cdot \overline{e}\gamma_\mu (1-\gamma^5)\nu_e + g_S (\epsilon^{\alpha e 11}_{S,du})^* \,\overline{p} n \cdot \overline{e}(1+\gamma^5)\nu_e \\ & - g_P (\epsilon^{\alpha e 11}_{P,du})^* \,\overline{p}\gamma^5 n \cdot \overline{e}(1+\gamma^5)\nu_e + 2 g_T (\epsilon^{\alpha e 11}_{T,du})^* \,\overline{p}\sigma^{\mu\nu} n \cdot \overline{e}\sigma_{\mu\nu}(1+\gamma^5)\nu_e] + \text{h.c} \end{aligned} \tag{4.34}$$

where $g_{V(A)}$ is the (axial-)vector charge and $g_{S,P,T}$ are the nonstandard charges. Neglecting nucleon recoil and the pseudoscalar contribution in the $q^2 \to 0$ limit, the neutron β decay width is

$$\Gamma = \frac{G_F^2 V_{ud}^2}{2\pi^3} [g_V^2 (3\lambda^2 + 1) + g_S^2 \mid \epsilon^{\alpha e 11}_{S,du} \mid^2 + 48 g_T^2 \mid \epsilon^{\alpha e 11}_{T,du} \mid^2]\, I\,, \tag{4.35}$$

where $\lambda \equiv g_V / g_A$ and

$$I = \int p_e E_e (M_n - M_p - E_e)^2 dE_e \approx 0.06\,\text{MeV}^5\,. \tag{4.36}$$

The decay width can also be written in terms of the NC effective couplings by using the relations in Eq. (4.6):

$$\Gamma = \frac{G_F^2 V_{ud}^2}{2\pi^3} [g_V^2 (3\lambda^2 + 1) + g_S^2 (\frac{\epsilon^{\alpha e 11}_{S,u}}{V_{ud}^2} - \epsilon^{\alpha e 11}_{S,d})^2 + 48 g_T^2 (\epsilon^{\alpha e 11}_{T,d})^2]\, I\,. \tag{4.37}$$

From Ref. [122], the 90% C.L. bounds, based on the differential observables from polarized nuclear beta decay, are

$$|\, \epsilon^{\alpha e 11}_{S,du} \,| < 0.063\,, \quad |\, \epsilon^{\alpha e 11}_{T,du} \,| < 0.024\,. \tag{4.38}$$

Bounds on the NC parameters can be computed by using the relations in Eq. (4.6) with $\epsilon^{\alpha e 11}_{P,du}$ taken to be 0:

$$|\, \epsilon^{\alpha e 11}_{S,d} \,|, |\, \epsilon^{\alpha e 11}_{P,d} \,| < 0.063\,, \quad |\, \epsilon^{\alpha e 11}_{S,u} \,|, |\, \epsilon^{\alpha e 11}_{P,u} \,| < 0.060\,, \quad |\, \epsilon^{\alpha e 11}_{T,d} \,| < 0.024\,. \tag{4.39}$$

Degeneracies do not permit simultaneous bounds on all the SMNEFT WCs. With the assumption that only one of them is nonzero, the 90% C.L. bounds are

$$| C_{NLQu}^{\alpha e11} |< 3.4 \times 10^{-2}\,, \quad | C_{NLdQ}^{\alpha e11} |< 3.5 \times 10^{-2}\,, \quad | C_{NLdQ}^{\prime\alpha e11} |< 2.8 \times 10^{-2}\,. \tag{4.40}$$

These constraints are much weaker than the ones from charged pion decay.

4.5 Neutrino Deep Inelastic Scattering

Neutrino deep inelastic scattering on nucleons can be modified by scalar, pseudoscalar, and tensor GNI. Please note that the charged current cannot be affected by the three GNI considered in this chapter, as the right-handed neutrino is absent in the neutrino beams. The total charged current and neutral current neutrino-nucleon scattering cross sections in the SM are

$$\sigma_{\nu N,SM}^{CC} = \frac{2G_F^2}{\pi} E_\nu M_N [\langle x d_N + x\frac{1}{3}\overline{u}_N\rangle], \tag{4.41}$$

$$\sigma_{\overline{\nu} N,SM}^{CC} = \frac{2G_F^2}{\pi} E_\nu M_N [\langle x\frac{1}{3} u_N + x\overline{d}_N\rangle], \tag{4.42}$$

$$\begin{aligned}\sigma_{\nu N,SM}^{NC} = \frac{2G_F^2}{\pi} E_\nu M_N [&(g_{L,u}^2 + \frac{1}{3}g_{R,u}^2)\langle xu_N\rangle + (g_{L,d}^2 + \frac{1}{3}g_{R,d}^2)\langle xd_N\rangle \\ &+(g_{R,u}^2 + \frac{1}{3}g_{L,u}^2)\langle x\overline{u}_N\rangle + (g_{R,d}^2 + \frac{1}{3}g_{L,d}^2)\langle x\overline{d}_N\rangle],\end{aligned} \tag{4.43}$$

$$\begin{aligned}\sigma_{\overline{\nu} N,SM}^{NC} = \frac{2G_F^2}{\pi} E_\nu M_N [&(g_{R,u}^2 + \frac{1}{3}g_{L,u}^2)\langle xu_N\rangle + (g_{R,d}^2 + \frac{1}{3}g_{L,d}^2)\langle xd_N\rangle \\ &+(g_{L,u}^2 + \frac{1}{3}g_{R,u}^2)\langle x\overline{u}_N\rangle + (g_{L,d}^2 + \frac{1}{3}g_{R,d}^2)\langle x\overline{d}_N\rangle],\end{aligned} \tag{4.44}$$

where we have neglected contributions from heavy quarks, and

$$\langle xq_N\rangle \equiv \int_0^1 xq_N(x)dx, \quad \langle x\overline{q}_N\rangle \equiv \int_0^1 x\overline{q}_N(x)dx\,, \tag{4.45}$$

determine the fraction of nucleon momentum carried by quarks and anti-quarks. $g_{L,f}$ and $g_{R,f}$ are the SM effective couplings given in Eq. (1.3). We take [123]

$$g_{L,u} = 0.3457\,, \quad g_{R,u} = -0.1553\,, \quad g_{L,d} = -0.4288\,, \quad g_{R,d} = 0.0777\,, \tag{4.46}$$

which include the one-loop and leading two-loop corrections. The neutral current is modified by scalar, pseudoscalar, and tensor GNI:

$$\sigma^{NC}_{\nu N,S(P)} = \sigma^{NC}_{\overline{\nu} N,S(P)} = \frac{G_F^2}{12\pi} E_\nu M_N [\epsilon^2_{S(P),u} \langle x(u_N + \overline{u}_N)\rangle + \epsilon^2_{S(P),d} \langle x(d_N + \overline{d}_N)\rangle]\,, \tag{4.47}$$

$$\sigma^{NC}_{\nu N,T} = \sigma^{NC}_{\overline{\nu} N,T} = \frac{56 G_F^2}{3\pi} E_\nu M_N [\epsilon^2_{T,u} \langle x(u_N + \overline{u}_N)\rangle + \epsilon^2_{T,d} \langle x(d_N + \overline{d}_N)\rangle]\,, \tag{4.48}$$

where the flavor indices are suppressed for simplicity. In the following analysis, we assume the target is isoscalar and composed of free nucleons, so that we may use the proton PDF. Under these assumptions, the nuclear PDFs become

$$\langle x d_N \rangle = \langle x u_N \rangle = \frac{N}{2} \langle x(u_p + d_p)\rangle\,, \quad \langle x \overline{d}_N \rangle = \langle x \overline{u}_N \rangle = \frac{N}{2} \langle x(\overline{d}_p + \overline{u}_p)\rangle\,. \tag{4.49}$$

4.5.1 CHARM: $\nu_e q \to \nu q$

The CHARM collaboration measured the ratio of total cross sections for semileptonic ν_e and $\overline{\nu}_e$ scattering to be [124]

$$R^e \equiv \frac{\sigma(\nu_e N \to \nu X) + \sigma(\overline{\nu}_e N \to \nu X)}{\sigma(\nu_e N \to e^- X) + \sigma(\overline{\nu}_e N \to e^+ X)} = 0.406 \pm 0.140\,. \tag{4.50}$$

The SM prediction from Eqs. (4.41) to (4.44) is

$$R^e = g_L^2 + g_R^2 = 0.3335\,, \tag{4.51}$$

where

$$g_L^2 = g_{L,u}^2 + g_{L,d}^2, \quad g_R^2 = g_{R,u}^2 + g_{R,d}^2\,. \tag{4.52}$$

Including the new GNI contributions from Eqs. (4.47) and (4.48), R^e becomes

$$R^e = g_L^2 + g_R^2 + \frac{1}{12} \sum_{q=u,d} ((\epsilon^{\alpha e 11}_{s,q})^2 + (\epsilon^{\alpha e 11}_{p,q})^2 + 224(\epsilon^{\alpha e 11}_{T,q})^2)\,. \tag{4.53}$$

The 90% C.L. bounds on the LEFT parameters are

$$\mid \epsilon^{\alpha e11}_{S,q} \mid , \mid \epsilon^{\alpha e11}_{P,q} \mid < 1.9\,, \quad \mid \epsilon^{\alpha e11}_{T,q} \mid < 0.13\,. \tag{4.54}$$

With only a single constraint on R^e, the degeneracy between the three SMNEFT WCs remains unbroken. The bounds on the SMNEFT WCs, with the assumption that only one of the WCs is nonzero at a time, are

$$\mid C^{\alpha e11}_{NLQu} \mid < 0.77\,, \quad \mid C^{\alpha e11}_{NLdQ} \mid < 0.75\,, \quad \mid C'^{\alpha e11}_{NLdQ} \mid < 0.15\,, \tag{4.55}$$

which are much weaker than the bounds from charged pion decay and nuclear beta decay.

4.5.2 NuTeV: $\nu_\mu q \to \nu q$

The NuTeV collaboration has measured the ratios of neutral current to charged current neutrino-nucleon cross sections [125]:

$$R^\nu \equiv \frac{\sigma(\nu_\mu N \to \nu X)}{\sigma(\nu N \to \mu^- X)} = 0.3916 \pm 0.0013, \quad R^{\overline{\nu}} \equiv \frac{\sigma(\overline{\nu}_\mu N \to \overline{\nu} X)}{\sigma(\overline{\nu} N \to \mu^+ X)} = 0.4050 \pm 0.0027\,. \tag{4.56}$$

In the SM, the cross section ratios on an isoscalar target composed of free nucleons are

$$R^\nu_{SM} = \frac{(g_L^2 + \frac{1}{3} g_R^2) f_q + (g_R^2 + \frac{1}{3} g_L^2) f_{\overline{q}}}{f_q + \frac{1}{3} f_{\overline{q}}}, \quad R^{\overline{\nu}}_{SM} = \frac{(g_R^2 + \frac{1}{3} g_L^2) f_q + (g_L^2 + \frac{1}{3} g_R^2) f_{\overline{q}}}{\frac{1}{3} f_q + f_{\overline{q}}}\,, \tag{4.57}$$

where f_q and $f_{\overline{q}}$ determine the fraction of proton momentum carried by the first generation of quarks and anti-quarks:

$$f_q = \langle xu + xd \rangle = 0.42,\; f_{\overline{q}} = \langle x\overline{u} + x\overline{d} \rangle = 0.068\,. \tag{4.58}$$

Here we used the CT10 PDFs [126] and the Mathematica package ManeParse [127] to obtain the numerical values of f_q and $f_{\overline{q}}$ at $Q^2 = 20\,\text{GeV}^2$. After including the contributions from scalar, pseudoscalar, and tensor GNI, R^ν and $R^{\overline{\nu}}$ are

$$R^\nu = \frac{(g_L^2 + \frac{1}{3} g_R^2) f_q + (\frac{1}{3} g_L^2 + g_R^2) f_{\overline{q}} + \frac{1}{24} \sum\limits_{q=u,d} ((\epsilon^{\alpha\mu 11}_{s,q})^2 + (\epsilon^{\alpha\mu 11}_{p,q})^2 + 224 (\epsilon^{\alpha\mu 11}_{T,q})^2)(f_q + f_{\overline{q}})}{f_q + \frac{1}{3} f_{\overline{q}}}, \tag{4.59}$$

$$R^{\overline{\nu}} = \frac{(\frac{1}{3} g_L^2 + g_R^2) f_q + (g_L^2 + \frac{1}{3} g_R^2) f_{\overline{q}} + \frac{1}{24} \sum\limits_{q=u,d} ((\epsilon^{\alpha\mu 11}_{s,q})^2 + (\epsilon^{\alpha\mu 11}_{p,q})^2 + 224 (\epsilon^{\alpha\mu 11}_{T,q})^2)(f_q + f_{\overline{q}})}{\frac{1}{3} f_q + f_{\overline{q}}}\,. \tag{4.60}$$

Using the numerical values in Eq. (4.46) and (4.58), we obtain our naive SM values $R^{\nu}_{SM} = 0.32$ and $R^{\overline{\nu}}_{SM} = 0.37$, which deviate significantly from the NuTeV measured values in Eq. (4.56). Including nuclear effects, partonic charge symmetry violation and strange quarks resolves the NuTeV anomaly [128], bringing the experimental measurements in good agreement with the SM values $R^{\nu} = 0.3950$ and $R^{\overline{\nu}} = 0.4066$. We simply rescale our naive SM calculations to the more accurate ones. We apply the same rescaling to the new physics contributions to set the 90% C.L. bounds,

$$\mid \epsilon^{\alpha\mu 11}_{S,q} \mid , \mid \epsilon^{\alpha\mu 11}_{P,q} \mid < 0.19 \, , \quad \mid \epsilon^{\alpha\mu 11}_{T,q} \mid < 0.013 \, . \tag{4.61}$$

The degeneracies between the three SMNEFT WCs can be broken by the R^{ν} and $R^{\overline{\nu}}$ measurements. By plugging the numerical relations in Eq. (4.15) into Eqs. (4.59) and (4.60), the bounds on the three SMNEFT WCs, allowing all of them to be nonzero simultaneously, are

$$\mid C^{\alpha\mu 11}_{NLQu} \mid < 0.078 \, , \quad \mid C^{\alpha\mu 11}_{NLdQ} \mid < 0.076 \, , \quad \mid C'^{\alpha\mu 11}_{NLdQ} \mid < 0.015 \, . \tag{4.62}$$

4.6 CEνNS

Coherent elastic neutrino-nucleus scattering occurs when the momentum exchanged is smaller than the inverse of the nucleus size, which typically requires neutrino energies of $\mathcal{O}(10$ MeV$)$. The cross section is enhanced by the square of the number of nucleons, thus providing an excellent tool to investigate GNI at low energies. The COHERENT experiment has recently observed CEνNS in a low-threshold CsI detector at the 6.7σ level. This is consistent with the SM at 1σ [70]. As we have discussed in section 2.2, the neutrino flux from the Spallation Neutron Source (SNS) is comprised of prompt, monoenergetic ν_μ from stopped pion decays, $\pi^+ \to \mu^+ + \nu_\mu$, and $\overline{\nu}_\mu$ and ν_e from the subsequent muon decays, $\mu^+ \to e^+ + \overline{\nu}_\mu + \nu_e$. The ν_μ energy is fixed at $(m_\pi^2 - m_\mu^2)/(2m_\pi) \approx 30$ MeV due to the two-body pion decay. The ν_e and $\overline{\nu}_\mu$ energies have a kinematic upper bound, $m_\mu/2 \approx 50$ MeV.

The differential cross section including scalar, vector, and tensor contributions reads [27]

$$\frac{d\sigma_a^\beta}{dE_r} = \frac{G_F^2}{4\pi} M_a N_a^2 [(\xi_S^\beta)^2 \frac{E_r}{E_{r,\max}} + (\xi_V^\beta)^2 (1 - \frac{E_r}{E_{r,\max}} - \frac{E_r}{E_\nu}) + (\xi_T^\beta)^2 (1 - \frac{E_r}{2E_{r,\max}} - \frac{E_r}{E_\nu})] F^2(q^2) \,, \tag{4.63}$$

where a denotes the target material and α denotes the neutrino flavor. M_a and N_a are the molar mass of the target nucleus and neutron number of the target, respectively. The flavor index $\beta = \mu$ includes both ν_μ and $\overline{\nu}_\mu$. $F(q^2)$ is the nuclear form factor [69]. The maximum recoil energy $E_{r,\max} = \frac{2E_\nu^2}{M_a + 2E_\nu} \approx \frac{2E_\nu^2}{M_a}$. Since the typical recoil energy E_r is $\mathcal{O}(10)$ keV, and the neutrino energy E_ν is $\mathcal{O}(10)$ MeV, we can safely ignore the interference term between scalar and tensor interactions, which is proportional to E_r/E_ν. The ξ_S, ξ_V, and ξ_T collect the contributions from scalar, vector, and tensor interactions, respectively, and are defined as

$$\begin{aligned}
(\xi_S^\beta)^2 &= \frac{1}{N_a^2} \{ (\sum_{q=u,d} 2\mathrm{Re}(\epsilon_{S,q}^{\alpha\beta 11}) [N \frac{m_n}{m_q} f_{Tq}^n + Z \frac{m_p}{m_q} f_{Tq}^p])^2 \\
&\quad + (\sum_{q=u,d} 2\mathrm{Im}(\epsilon_{S,q}^{\alpha\beta 11}) [N \frac{m_n}{m_q} f_{Tq}^n + Z \frac{m_p}{m_q} f_{Tq}^p])^2 \} \,, \\
(\xi_V^\beta)^2 &= \frac{2}{N_a^2} (Z(2g_{V,u} + g_{V,d}) + N(g_{V,u} + 2g_{V,d}))^2 \,, \\
(\xi_T^\beta)^2 &= \frac{8}{N_a^2} (\sum_{q=u,d} 4\,\mathrm{Re}(\epsilon_{T,q}^{\alpha\beta 11}) [Z\delta_q^p + N\delta_q^n])^2 \,,
\end{aligned} \tag{4.64}$$

where f_{Tq}^p and f_{Tq}^n are the mass fractions of quark q in the respective nucleon, and the δ_q's are the corresponding nucleon tensor charges. The effective vector coupling $g_{V,q}$ is

$$g_{V,q} \equiv g_{L,q} + g_{R,q} \,. \tag{4.65}$$

The expected number of events per day with recoil energy in the energy range $[E_r,\, E_r + \Delta E_r]$ and arrival time in the time interval $[t,\, t + \Delta t]$ is given by

$$N_{th}(t, E_r, \epsilon) = \sum_{\beta=e,\mu} \frac{m_{\det} N_A}{M_a} \int_{\Delta E_r} dE_r \int_{\Delta t} dt \rho_\alpha(t) \int_{E_\nu^{\min}}^{E_\nu^{\max}} dE_\nu \, \phi_\beta(E_\nu) \, \frac{d\sigma_a^\beta(\epsilon)}{dE_r} \,, \tag{4.66}$$

where $m_{\det}$ is the detector mass, $N_A = 6.022 \times 10^{23}\,\mathrm{mol}^{-1}$, and $\rho_\alpha(t)$ is the arrival time probability density function. To calculate the differential neutrino-nucleus scattering cross section, we need to evaluate the matrix elements of the operators between nuclear states. We adopt the following numerical values of the nuclear matrix elements [129, 130]

$$\begin{aligned} &f^p_{Tu} = 0.0208\,, \quad f^p_{Td} = 0.0411\,, \quad f^n_{Tu} = 0.0189\,, \quad f^n_{Td} = 0.0451\,, \\ &\delta^p_u = 0.792\,, \quad \delta^p_d = -0.194\,, \quad \delta^n_u = -0.194\,, \quad \delta^n_d = 0.792\,. \end{aligned} \tag{4.67}$$

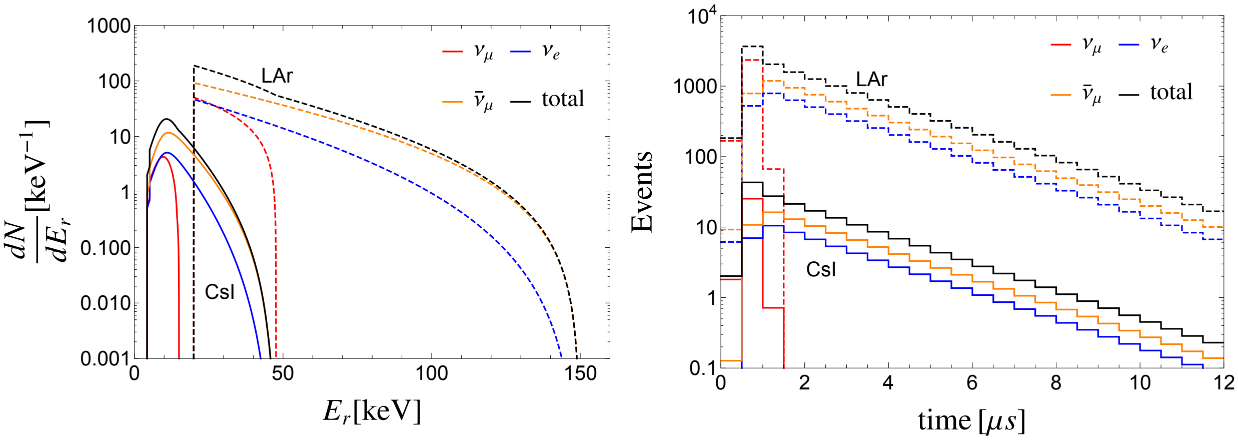

Figure 13: The SM recoil energy (left) and temporal (right) distributions in the current COHERENT CsI detector (solid lines) and a future COHERENT LAr detector (dashed curves). Threshold effects are included. The red (blue) [orange] curves correspond to the contribution from muon (electron) [anti-muon] neutrinos. The black lines correspond to the sum of all the flavor contributions.

Following Ref. [51], we study the current and projected constraints on the three GNI from the COHERENT experiment. Several COHERENT experiments with multiple targets have been proposed. In this study, we consider a future 750 kg liquid argon (LAr) detector with a 610 kg fiducial mass taking data for four years. The energy threshold is around 20 keV, which is higher than the 6.5 keV CsI energy threshold. The observed event distributions based on the SM simulations are shown in Fig. 13. The future LAr experiment will provide much more statistics even though it has a higher threshold of nuclear recoil energy. GNI can modify the shape of the recoil energy and temporal distributions. The scalar and tensor GNI distributions comparing to the SM are shown in Fig. 14. The muon flavor contributions dominate over the electron flavor as there are twice as many muon flavor neutrinos as electron flavor neutrinos. Since the $\overline{\nu}_\mu$ energy distribution peaks at the end point $m_\mu/2$, there are more events in the tail of the energy spectrum for GNI involving the muon flavor. Another observation from Fig. 14 is that COHERENT experiment is much more sensitive to the scalar interactions than tensor interactions. By using the energy spectrum of the current COHERENT data, we find that the current 90% C.L. bounds on the scalar or tensor interactions, allowing only a single nonzero parameter, are

$$(\xi_S^\mu)^2 < 0.60\,, \quad (\xi_T^\mu)^2 < 0.73\,, \quad (\xi_S^e)^2 < 1.5\,, \quad (\xi_T^e)^2 < 1.6\,. \tag{4.68}$$

Also, the projected 90% C.L. bounds from future COHERENT data by using both the spectral and temporal information are

$$(\xi_S^\mu)^2 < 0.012\,, \quad (\xi_T^\mu)^2 < 0.013\,, \quad (\xi_S^e)^2 < 0.030\,, \quad (\xi_T^e)^2 < 0.027\,, \tag{4.69}$$

which is an order of magnitude improvement. Again, the bounds are set based on only one of them being nonzero. The projected 90% C.L. bounds in the $(\xi_S^\alpha)^2$-$(\xi_T^\alpha)^2$ plane are shown in Fig. 15. Because of degeneracies between the SMNEFT WCs in Eq. (4.15), bounds on individual parameters cannot be placed if all the parameters are allowed to float. The bounds on the individual can be derived after running and matching. The current (projected) 90% C.L. bounds on SMNEFT WCs, after setting the others to zero, are

$$\begin{aligned}
&|\, C_{NLQu}^{\alpha e11} \,| < 8.1\times10^{-2}\,(3.2\times10^{-3})\,, \quad |\, C_{NLQu}^{\alpha\mu11} \,| < 5.1\times10^{-2}\,(2.0\times10^{-3}),\\
&|\, C_{NLdQ}^{\alpha e11} \,| < 7.7\times10^{-2}(3.1\times10^{-3})\,, \quad |\, C_{NLdQ}^{\alpha\mu11} \,| < 4.9\times10^{-2}\,(1.9\times10^{-3}),\\
&|\, C_{NLdQ}^{\prime\alpha e11} \,| < 2.0\times10^{-1}\,(2.1\times10^{-2})\,, \quad |\, C_{NLdQ}^{\prime\alpha\mu11} \,| < 1.4\times10^{-1}\,(1.4\times10^{-2})\,.
\end{aligned} \tag{4.70}$$

The projected 90% C.L. bounds in the C_{NLQu}-C_{NLdQ} (C_{NLdQ}-C'_{NLdQ}) planes, are shown by the brown dashed contours in the upper (lower) panels of Fig. 12. We have set $C_{NLQu} = 0$ in the C_{NLdQ}-C'_{NLdQ} planes, because otherwise the bounds are too weak to display. The current COHERENT bounds are not shown as they are irrelevant in comparison.

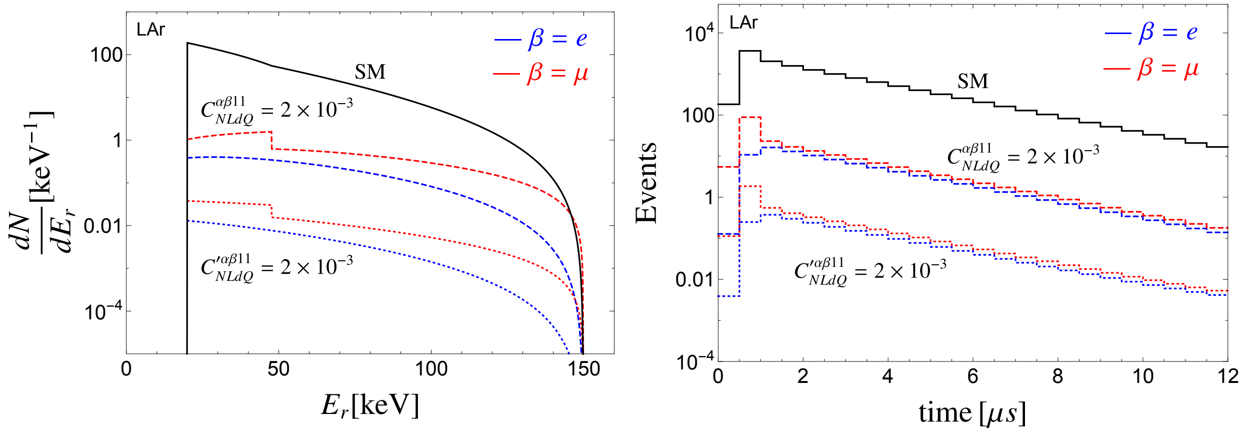

(a) (b)

Figure 14: The recoil energy (left) and temporal (right) distributions in a future COHERENT LAr detector. Threshold effects are included. The black solid lines are the SM case including all flavors. The blue (red) curves correspond to the electron (muon+antimuon) flavor contributions. The dashed (dotted) curves correspond to the contributions from the scalar (tensor) interactions with $C_{NLdQ}\,(C'_{NLdQ}) = 2\times10^{-3}$.

4.7 Collider Constraints

High-energy colliders can set strong bounds on the Wilson coefficients of scalar, pseudoscalar, and tensor interactions. In this section, we study the sensitivity to the WCs at proton-proton and electron-proton colliders. We set bounds using the LHC and evaluate the potential of the HL-LHC and LHeC to probe GNI. By integrating over the full phase space, we find the partonic cross sections of the SM mediated by the W boson and of the contact scalar and tensor interactions to be [131]

$$\text{LHC}: \qquad \hat{\sigma}_S = \frac{G_F^2 \hat{s}}{24\pi} C_S^2\,, \hat{\sigma}_T = \frac{2G_F^2 \hat{s}}{9\pi} C_T^2\,, \hat{\sigma}_{SM}(u\bar{d} \to W^* \to \mu^+\nu_\mu) = \frac{G_F^2 \hat{s}}{18\pi} \frac{M_W^4}{(\hat{s} - M_W^2)^2}\,, \tag{4.71}$$

$$\text{LHeC}: \qquad \hat{\sigma}_S = \frac{G_F^2 \hat{s}}{24\pi} C_S^2\,, \quad \hat{\sigma}_T = \frac{14G_F^2 \hat{s}}{3\pi} C_T^2\,, \quad \hat{\sigma}_{SM}(eq \to \nu_e q') = \frac{G_F^2 \hat{s}}{2\pi} \frac{M_W^2}{\hat{s} + M_W^2}\,, \tag{4.72}$$

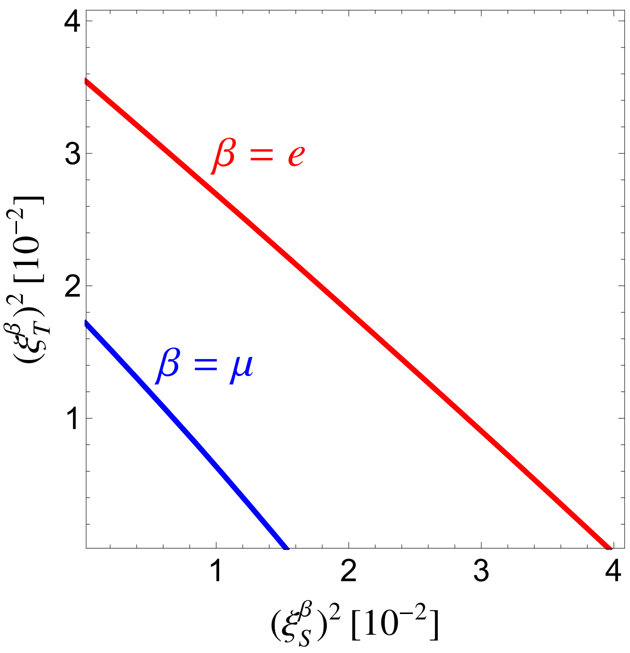

Figure 15: Projected 90% C.L. upper bounds from the future COHERENT experiment with a 610 kg fiducial mass of LAr.

where $C_S \in \{C_{NLQu}, C_{NLdQ}\}$, $C_T = C'_{NLdQ}$. Note that the ratios of the tensor to scalar cross sections, $\hat{\sigma}_T/\hat{\sigma}_S$, are 16/3 at the LHC and 112 at the LHeC. Clearly, the LHeC is much more sensitive to tensor interactions than scalar interactions. Owing to its lower center-of-mass energy, we expect bounds derived from the LHeC to be weaker than those from the LHC, given the $\hat{s}$-dependence of the higher-dimensional operators.

The interference between chirality-flipped operators and SM operators are helicity suppressed, and the interference between the scalar (O_{NLdQ}) and tensor (O'_{NLdQ}) interactions is generally nonzero. The differential distributions for the interference of the latter operators in the center-of-mass frame are found to be

$$\begin{aligned} \text{LHC:} \quad & \frac{d\hat{\sigma}_{ST}}{d\cos\theta^*} = \frac{G_F^2 \hat{s}}{12\pi}(C_S^* C_T + C_T^* C_S)\cos\theta^*\,, \\ \text{LHeC:} \quad & \frac{d\hat{\sigma}_{ST}}{d\cos\theta^*} = \frac{G_F^2 \hat{s}}{16\pi}(C_S^* C_T + C_T^* C_S)(\cos^2\theta^* - 2\cos\theta^* - 3)\,. \end{aligned} \tag{4.73}$$

The interference leads to a linear asymmetry at the LHC and the integrated rate vanishes, while the integrated rate at the LHeC is $\hat{\sigma}_{ST} = -G_F^2 \hat{s}/3\pi(C_S^* C_T + C_T^* C_S)$.

The hadronic cross sections can be obtained by convolving with the parton distribution functions,

$$\sigma_{LHC} = \sum_{q,q'} \int_{\tau_{min}}^{\tau_{max}} d\tau \int_{\tau}^{1} \frac{dx}{x} f_q(x, \mu_F) f_{q'}(\tau/x, \mu_F) \hat{\sigma}(\tau s)\,, \tag{4.74}$$

$$\sigma_{LHeC} = \sum_{q} \int_{x_{min}}^{x_{max}} dx f_q(x, \mu_F) \hat{\sigma}(xs)\,. \tag{4.75}$$

In the following, we use the Monte Carlo event generator MadGraph5_aMC@NLO [76] to generate signal and background samples at the LHC and LHeC. The GNI Lagrangian is implemented in the FeynRules 2.0 [78] framework. PYTHIA8 [132] (PYTHIA6 [80]) is used for parton showering and hadronization at the LHC (LHeC). We perform the detector simulations using Delphes 3.4.1 [82].

Before evaluating the collider sensitivity to the Wilson coefficients, we note that our EFT description is valid only for $\sqrt{\hat{s}} < \Lambda$, which calls for an assumption about the energy scale of the new physics. We consider two representative scenarios of the new physics scale, which we call low-scale new physics (LNP) with $\Lambda \sim 1$ TeV, and high-scale new physics (HNP) with $\Lambda \gg 1$ TeV. In the HNP case, we assume the EFT method to be valid for the entire energy scale relevant to LHC data. In the LNP case, however, we limit our analysis to a subset of the LHC data below 1 TeV.

4.7.1 Proton-proton colliders

Both scalar and tensor CC contact interactions can be probed at high-energy proton-proton colliders, under the assumption that the energy scale of the new dynamics is not kinematically accessible. The signal channel is the Drell-Yan (DY) process, $pp \to \ell\nu + X$. Due to the missing neutrino in the final state, our analysis is based on the distribution of the transverse mass, which is reconstructed by the charged lepton transverse momentum (p_T^ℓ) and the missing transverse momentum ($E_T^{\rm miss}$)

$$m_T = \sqrt{2 p_T^\ell E_T^{\rm miss} (1 - \cos\Delta\phi(p_T^\ell, E_T^{\rm miss}))}\,. \tag{4.76}$$

The main background for large values of m_T is DY production of W bosons. The latest analysis for charged lepton and missing transverse momentum events conducted by ATLAS used 139 fb^{-1} of data collected at $\sqrt{s} = 13$ TeV [133]. In the rest of our study, we only use the m_T distributions below 800 GeV for the LNP scenario, and the full range of m_T for the HNP scenario. For our analyses, we define the statistical significance in terms of

$$\chi^2 = \sum_i \frac{(n_{b,i} + n_{s,i} - n_{\text{data},i})^2}{n_{\text{data},i} + (\sigma_i n_{\text{data},i})^2}\,, \tag{4.77}$$

where $n_{b(\text{data}),i}$ is the number of background (observed) events in the i^{th} bin, which is obtained directly from Ref. [133]. $n_{s,i}$ is the number of signal events simulated in Madgraph at LO. σ_i is the total systematic uncertainty, which is chosen according to Ref. [133]:

electron channel: $\sigma_e \sim 10\%\,(12\%)$ for $m_T = 300\,(2000)$ GeV;
muon channel: $\sigma_\mu \sim 10\%\,(17\%)$ for $m_T = 300\,(2000)$ GeV.

The current 90% C.L. bounds, defined by $\Delta\chi^2 < 2.71$, on the LNP (HNP) scalar and tensor operators are

$$\mid C_{NLQu}^{\alpha e11} \mid < 2.5\,(0.44) \times 10^{-3}\,, \mid C_{NLdQ}^{\alpha e11} \mid < 2.6\,(0.46) \times 10^{-3}\,, \mid C_{NLdQ}^{\prime \alpha e11} \mid < 1.2\,(0.24) \times 10^{-3}\,, \tag{4.78}$$

$$\mid C_{NLQu}^{\alpha \mu 11} \mid < 2.9\,(0.66) \times 10^{-3}\,, \mid C_{NLdQ}^{\alpha \mu 11} \mid < 3.0\,(0.68) \times 10^{-3}\,, \mid C_{NLdQ}^{\prime \alpha \mu 11} \mid < 1.4\,(0.40) \times 10^{-3}\,. \tag{4.79}$$

The bounds on C_{NLQu} are slightly stronger than for C_{NLdQ} because of the size of the CKM matrix element V_{ud}. These bounds are consistent with those in Ref. [133]. The 90% C.L. allowed regions in the C_{NLdQ}-C_{NLQu} and C_{NLdQ}-C'_{NLdQ} planes are shown in the Fig. 12. The solid red (blue) contours correspond to the LNP (HNP) case. We have checked numerically using Madgraph that the interference between scalar operator O_{NLdQ} and tensor operator O'_{NLdQ} can be ignored.

To assess the future potential of the LHC, we assume an integrated luminosity of $L = 3$ ab^{-1} and $\sqrt{s} = 14$ TeV at the HL-LHC. In this analysis, we simulate the DY W background at LO multiplied by a scale factor obtained from Ref. [133], to include other smaller backgrounds including top pairs, single top, $W \to \tau\nu$, DY Z, and di-bosons. The signals are also generated at tree level. We do not include a K factor as it applies to both signal and background, so the significance is simply scaled by $\sqrt{K}$ after including higher-order corrections. The selection rules applied in this analysis are slightly different between the electron and muon final states. For the muon (electron) final states, we require

- $p_T^{\mu(e)} > 55\,(65)\,\text{GeV}$ and $|\eta_\ell| < 2.4$,
- veto b-tagged jets,
- discard additional electron or muon with $p_T > 20\,\text{GeV}$ and $|\eta_\ell| < 2.4$,
- $m_T > 300$ GeV,

(4.80)

in which, the electron p_T cut is slightly stronger than the muon p_T cut, in order to suppress the non-prompt backgrounds. The distributions of m_T above 300 GeV after applying the cuts are shown in Fig 16a. Deviations from the SM arise in the tails of the m_T distributions because the sub-process cross sections for a dim-6 operator scale as $\hat{s}$; see Eq. (4.71). For the same size WC, tensor interactions have a larger cross section than scalar interactions. The χ^2 used in this analysis is defined in Eq. (4.77), with n_{data} replaced by the values from SM simulations. The projected 90% C.L. bounds on the LNP (HNP) scalar and tensor operators are

$$| \, C_{NLQu}^{\alpha e11} \, |< 2.3\,(0.28) \times 10^{-3} \,, | \, C_{NLdQ}^{\alpha e11} \, |< 2.4\,(0.28) \times 10^{-3} \,, | \, C_{NLdQ}^{\prime\alpha e11} \, |< 1.1\,(0.18) \times 10^{-3} \,, \tag{4.81}$$

$$| \, C_{NLQu}^{\alpha\mu11} \, |< 2.7\,(0.28) \times 10^{-3} \,, | \, C_{NLdQ}^{\alpha\mu11} \, |< 2.8\,(0.29) \times 10^{-3} \,, | \, C_{NLdQ}^{\prime\alpha\mu11} \, |< 1.3\,(0.18) \times 10^{-3} \,. \tag{4.82}$$

The bounds from HL-LHC on scalar (tensor) interactions with the assumption of LNP are comparable with (much stronger than) the ones we obtained for the future COHERENT experiment. The dashed red (blue) contours in Fig. 12 show the 90% C.L. projections for the HL-LHC with the LNP (HNP) assumption. The bounds on the WCs are stronger for HNP than for LNP, because the signals in the high-energy tails of the m_T distributions are not buried in the SM background. These bounds can be converted into limits on the effective couplings $\kappa = \sqrt{|C|}(\Lambda/v)$ for fixed values of the new physics scale Λ. The 90% C.L. bounds on κ are provided in Table 6 for LNP (with $\Lambda = 1$ TeV) and HNP (with $\Lambda = 10$ TeV).

As expected, bounds on κ are stronger in the LNP case than the HNP case. Alternatively, if we assume that $\kappa \approx 1$, then HL-LHC bounds on the WCs for HNP imply a sensitivity to $\Lambda \sim 20$ TeV. This is comparable to the expected sensitivity of W' searches at the HL-LHC [134].

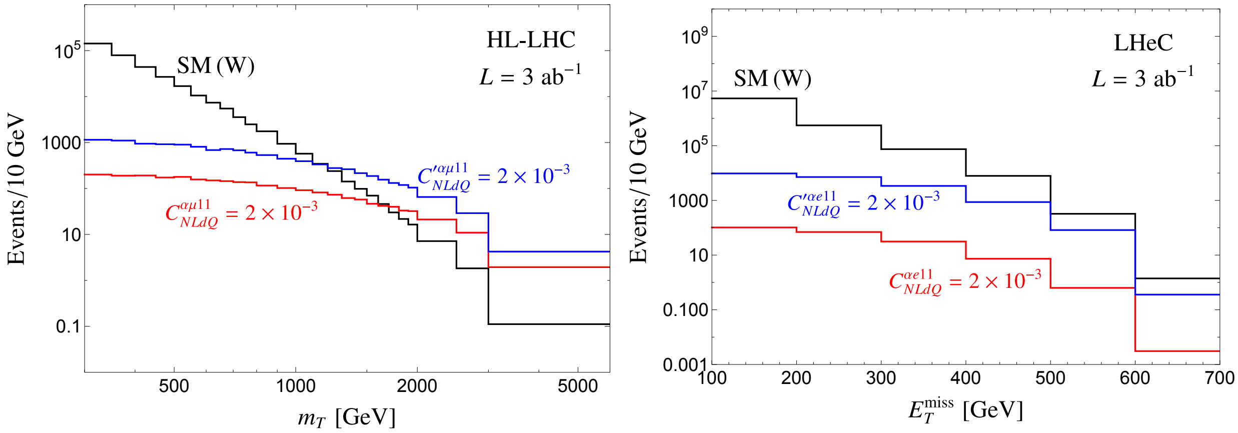

(a)

(b)

Figure 16: Left: Distribution of m_T at the HL-LHC with an integrated luminosity of $3\ \mathrm{ab}^{-1}$. Right: Distribution of E_T^{miss} at the LHeC with $3\ \mathrm{ab}^{-1}$ and a 1.3 TeV center-of-mass energy. The black histograms corresponds to the SM. The red (blue) histograms correspond to scalar (tensor) interactions with C_{NLdQ} (C'_{NLdQ}) $= 2 \times 10^{-3}$.

Coupling	$\kappa^{\alpha e 11}_{NLQu}$	$\kappa^{\alpha e 11}_{NLdQ}$	$\kappa'^{\alpha e 11}_{NLdQ}$	$\kappa^{\alpha\mu 11}_{NLQu}$	$\kappa^{\alpha\mu 11}_{NLQu}$	$\kappa'^{\alpha\mu 11}_{NLQu}$
LHC: LNP (HNP)	0.20 (0.85)	0.21 (0.87)	0.14 (0.63)	0.22 (1.0)	0.22 (1.1)	0.15 (0.81)
HL-LHC: LNP (HNP)	0.19 (0.68)	0.20 (0.68)	0.13 (0.55)	0.21 (0.68)	0.22 (0.69)	0.15 (0.55)

Table 6: Current and projected 90% C.L. bounds on the new physics coupling κ from LHC and HL-LHC data, respectively, for the LNP ($\Lambda = 1$ TeV) and HNP ($\Lambda = 10$ TeV) cases.

4.7.2 Electron-proton colliders

The HERA collaboration set bounds on the contact interaction $e\nu qq'$ using the charged current process, $e^{\pm}p \to \overset{(-)}{\nu} X$, from the Q^2 and x distributions [135]. The lower bound on the mass scale of the contact term is around 1 TeV with the strong coupling $\sim 4\pi$. This bound can be translated to our scenario:

$$| C_{NLQu}^{\alpha e11} |, | C_{NLdQ}^{\alpha e11} |, | C_{NLdQ}^{\prime\alpha e11} | \lesssim 5 \,, \tag{4.83}$$

which is very weak compared to bounds from high-energy colliders.

Next, we consider the future ep collider, LHeC, with $\sqrt{s} = 1.3$ TeV ($E_e = 60$ GeV, $E_p = 7$ TeV) and $L = 3$ ab^{-1}. The signal channel is mono-jet, $ep \to j\nu + X$, through the t-channel. The main background is mediated by SM W bosons. For the analysis we use the following set of basic cuts:

- leading jet should have $p_T^j > 20\,\text{GeV}$ and $|\eta_j| < 2.5$,
- veto any electrons with $p_T^e > 20\,\text{GeV}$ and $|\eta_e| < 2.5$,
- the angular distance between jet and missing E_T should be bigger than 0.4.

The distributions of the missing transverse energy above 100 GeV after applying the cuts are shown in Fig 16b. To maximize our $\chi^2 = S^2/B$, in which we do not include systematic uncertainties, we select the cut on the missing transverse energy as $E_T^{\text{miss}} > 300$ GeV. The projected 90% C.L. bounds on the individual SMNEFT WCs are

$$| C_{NLQu}^{\alpha e11} | < 3.9 \times 10^{-3} \,, \quad | C_{NLdQ}^{\alpha e11} | < 4.0 \times 10^{-3} \,, \quad | C_{NLdQ}^{\prime\alpha e11} | < 0.38 \times 10^{-3} \,, \tag{4.84}$$

with only one WC taken to be nonzero. If all parameters are allowed to be nonzero, the bounds weaken slightly due to the mixing between O_{NLdQ} and O'_{NLdQ}:

$$| C_{NLQu}^{\alpha e11} | < 3.9 \times 10^{-3} \,, \quad | C_{NLdQ}^{\alpha e11} | < 6.1 \times 10^{-3} \,, \quad | C_{NLdQ}^{\prime\alpha e11} | < 0.58 \times 10^{-3} \,. \tag{4.85}$$

The projected 90% C.L. bounds on the C_{NLdQ}-C_{NLQu} and C_{NLdQ}-C'_{NLdQ} are shown in Fig. 12 by the purple dashed contours. Due to the smaller center-of-mass energy, the bounds on the scalar interactions from LHeC are weaker than the ones from HL-LHC. However, for tensor interactions, the bounds from LHeC are stronger than HL-LHC for the LNP case. We compiled all the bouns in Table 7 and 8.

WC	π^+ decay	β decay	ν DIS	CEνNS	HERA	LHC: LNP(HNP)
$C_{NLQu}^{\alpha e11}$	3.3×10^{-6}	3.4×10^{-2}	0.77	8.1×10^{-2}	$\boldsymbol{\sim 5}$	$\mathbf{2.5\,(0.44) \times 10^{-3}}$
$C_{NLdQ}^{\alpha e11}$	3.4×10^{-6}	3.5×10^{-2}	0.75	7.7×10^{-2}	$\boldsymbol{\sim 5}$	$\mathbf{2.6\,(0.46) \times 10^{-3}}$
$C_{NLdQ}^{\prime\alpha e11}$	3.9×10^{-5}	2.8×10^{-2}	0.15	0.20	$\boldsymbol{\sim 5}$	$\mathbf{1.2\,(0.24) \times 10^{-3}}$
$C_{NLQu}^{\alpha\mu11}$	1.5×10^{-3}	-	$\mathbf{7.8 \times 10^{-2}}$	5.1×10^{-2}	-	$\mathbf{2.9\,(0.66) \times 10^{-3}}$
$C_{NLdQ}^{\alpha\mu11}$	1.5×10^{-3}	-	$\mathbf{7.6 \times 10^{-2}}$	4.9×10^{-2}	-	$\mathbf{3.0\,(0.68) \times 10^{-3}}$
$C_{NLdQ}^{\prime\alpha\mu11}$	1.7×10^{-2}	-	$\mathbf{1.5 \times 10^{-2}}$	0.14	-	$\mathbf{1.4\,(0.40) \times 10^{-3}}$

Table 7: Current 90% C.L. bounds on the three SMNEFT WCs C_{NLQu}, C_{NLdQ}, and C'_{NLdQ}, for the electron and muon flavors at a 1 TeV energy scale. The constraints obtained by allowing all WCs to simultaneously vary are in boldface.

WC	CEνNS-LAr	LHeC	HL-LHC: LNP(HNP)
$C_{NLQu}^{\alpha e11}$	3.2×10^{-3}	$\mathbf{3.9 \times 10^{-3}}$	$\mathbf{2.3\,(0.28) \times 10^{-3}}$
$C_{NLdQ}^{\alpha e11}$	3.1×10^{-3}	$\mathbf{6.1 \times 10^{-3}}$	$\mathbf{2.4\,(0.28) \times 10^{-3}}$
$C_{NLdQ}^{\prime\alpha e11}$	2.1×10^{-2}	$\mathbf{0.58 \times 10^{-3}}$	$\mathbf{1.1\,(0.18) \times 10^{-3}}$
$C_{NLQu}^{\alpha\mu11}$	2.0×10^{-3}	-	$\mathbf{2.7\,(0.28) \times 10^{-3}}$
$C_{NLdQ}^{\alpha\mu11}$	1.9×10^{-3}	-	$\mathbf{2.8\,(0.29) \times 10^{-3}}$
$C_{NLdQ}^{\prime\alpha\mu11}$	1.4×10^{-2}	-	$\mathbf{1.3\,(0.18) \times 10^{-3}}$

Table 8: Projected 90% C.L. bounds on the three SMNEFT WCs C_{NLQu}, C_{NLdQ}, and C'_{NLdQ}, with electron and muon flavor, at 1 TeV energy scale. The constraints obtained by allowing all WCs to simultaneously vary are in boldface.

5.0 Dark Matter Blind Spots at One-Loop

The current level of experimental sensitivity therefore calls for increased accuracy of the theoretical predictions as well, in order to thoroughly probe interesting and well-motivated WIMP scenarios. This becomes especially important if the leading order predictions for these scattering cross-sections are negligibly small or even exactly zero either due to symmetry reasons or due to cancellations among different contributions to the relevant DM effective couplings. Next-to-leading order corrections then become important, and would constitute a benchmark for the near-future multi-ton scale liquid Xenon-based direct detection experiments, targeting at a DM-nucleon scattering cross-section below 10^{-47}cm^2.

A well-studied example of the above scenario where the one-loop contributions to the DM-nucleon scattering rate become important is DM belonging to a multiplet of the SM weak interaction group $\mathrm{SU(2)_L}$ [136, 137]. For both real $\mathrm{SU(2)_L}$ triplets with zero hypercharge (e.g., the wino in the minimal supersymmetric standard model, MSSM) and Majorana $\mathrm{SU(2)_L}$ doublets (e.g., the Higgsino in the MSSM) the leading contribution to spin-independent (SI) scattering with nucleons appears at one-loop. In the former case, the SI cross-section with nucleon is only mildly sensitive to the DM mass and is obtained to be around $2.3 \times 10^{-47}\text{cm}^2$ in the limit $M_{\text{DM}} \gg M_W$, including higher order corrections at next-to-leading order in α_s [138, 139]. Therefore, these DM candidates are natural benchmark targets for multi-ton scale detectors. For Higgsino-like $\mathrm{SU(2)_L}$ doublet Majorana fermions, the rate is further suppressed by two orders of magnitude, and the SI cross-section is around 10^{-49}cm^2. Such cross-sections are below the irreducible neutrino floor [140, 141], thereby making necessary larger detector volumes and exposure time, as well as the development of directional detection methods [142, 143].

While for the pure $\mathrm{SU(2)_L}$ multiplets discussed above the tree-level SI scattering rates are absent due to symmetry reasons, there are other scenarios in which very small tree-level rates are obtained due to cancellations of different contributions to the relevant effective couplings. For example, if the neutral components of different $\mathrm{SU(2)_L}$ multiplets mix after electroweak symmetry breaking, generically there are regions of parameter space where the effective coupling to the Higgs boson(s), which determines the leading contribution to the SI scattering rate, either becomes small or even vanishes, a scenario dubbed as "blind spots" for DM direct detection [144, 145, 146, 147, 148, 149, 150, 151]. While the particular values and relations of the theory parameters that result in the blind spots may not have any deeper theoretical implications, or may even be viewed as a fine-tuning to a special hypersurface within the parameter space, they do characterize a distinctive class of phenomena that need to be scrutinized. Such blind spots for DM-nucleon scattering therefore present us with another context in which the higher-order electroweak corrections, involving states from both the DM and the SM sectors in the loop amplitudes, are important to evaluate in order to quantify its detectability. In this chapter, we compute the one-loop corrections to DM-nucleon scattering processes near such blind spots, and assess their implications for different direct detection probes.

As an example scenario, which represents all the features of more involved models such as the bino-Higgsino mixed DM in the MSSM [28], we begin by studying a DM model with mixing between an $\mathrm{SU(2)_L \times U(1)_Y}$ singlet fermion and the neutral components of two $\mathrm{SU(2)_L}$ doublet fermions [152, 153, 149, 154]. The details of this simplified model and the appearance of tree-level blind spots are reviewed in Section 5.1. We then systematically evaluate the impact of the one-loop corrections for the SI scattering rates near the blind spots in the singlet-doublet model, after defining an on-shell renormalization procedure for the DM sector. The computational framework and the results of the one-loop corrections are discussed in Section 5.2, while the details of the on-shell renormalization scheme adopted are summarized in Appendix A. In Section 5.3 we utilize these one-loop results to find out the prospects of observing DM-nucleon scattering near the tree-level blind spots. In this section, we also compare the prospects for probing the one-loop SI rates with the reach from the tree-level spin-dependent (SD) DM-nucleon scattering searches. We also briefly review the computational framework adopted in this chapter for SI and SD DM-nucleon scattering in Appendix B, and the mapping of the singlet-doublet model parameters to the case for MSSM bino-Higgsino mixed DM scenario in Appendix C.

5.1 Singlet-doublet Dark Matter and Tree-level Blind Spot

To understand the appearance of blind spots for DM direct detection, it is instructive to consider a simple model, in which the DM candidate is a linear combination of an electroweak singlet Majorana fermion χ_S, and the neutral components of two $\mathrm{SU(2)_L}$ doublet states χ_{D1} and χ_{D2}, with hypercharge $+1/2$ and $-1/2$, respectively [144, 149],

$$\chi_{D1} = (\chi_1^+, \chi_1^0)^\top \quad \text{and} \quad \chi_{D2} = (\chi_2^0, \chi_2^-)^\top. \tag{5.1}$$

The mixing between the singlet and the neutral components of the doublet states occurs after electroweak symmetry breaking. Such a scenario can appear in beyond-the-standard-model constructions such as the MSSM, in which the singlet state is the bino, and the two doublet states correspond to the two Higgsinos. In the MSSM some of the couplings of these states with the SM sector are determined by gauge symmetry and supersymmetry, and therefore the results of the singlet-doublet model can be mapped to the MSSM case, as long as all the sfermions, heavy scalars and wino are decoupled.

In order to have a stable DM candidate, we impose an additional Z_2 symmetry, under which the DM sector states are odd, and all the SM sector states are even. Thus, the lightest neutral state in the dark sector is the DM candidate, where the mass spectrum and Yukawa couplings of the dark sector particles are determined by the following Lagrangian

$$\mathscr{L}_Y = -\left(\frac{1}{2}M_S\chi_S\chi_S + M_D\chi_{D1}\cdot\chi_{D2} - y_1\chi_S\chi_{D1}\cdot\widetilde{H} - y_2\chi_S\chi_{D2}\cdot H\right) + \text{h.c.}, \tag{5.2}$$

where $H = \left(\phi^+, (v+h+i\eta)/\sqrt{2}\right)^\top$ is the SM Higgs doublet, with a vacuum expectation value $v = 246$ GeV, while $\widetilde{H} = i\sigma_2 H^*$. The dot products in Eq. (5.2) indicate the contraction of $\mathrm{SU(2)_L}$ indices to form a singlet.

We see that the mass spectrum is determined by four free parameters, namely, M_D, M_S, y_1 and y_2. By re-defining the fields χ_{D1}, χ_{D2}, and χ_S, we can make three of them positive, chosen to be y_1, y_2, and M_S. For simplicity, we do not include any possible CP violation in the DM sector, and restrict to real values of M_D only. After electroweak symmetry breaking, the neutral components of the doublet and singlet dark fermions mix, and the mass matrix of neutral dark sector in the gauge basis $\chi^0 = (\chi_S, -\chi_2^0, \chi_1^0)^\top$ is given by

$$\mathbf{M_N} = \begin{pmatrix} M_S & \frac{yv\cos\beta}{\sqrt{2}} & \frac{yv\sin\beta}{\sqrt{2}} \\ \frac{yv\cos\beta}{\sqrt{2}} & 0 & M_D \\ \frac{yv\sin\beta}{\sqrt{2}} & M_D & 0 \end{pmatrix} , \tag{5.3}$$

where $\tan\beta = y_1/y_2$, with $y_1 = y\sin\beta$ and $y_2 = y\cos\beta$.

5.1.1 Spin-independent interaction

The dominant contribution to SI direct detection cross-section stems from the Higgs boson exchange diagram, and we obtain the tree-level DM-Higgs coupling using the low energy theorem

$$C^0_{h\widetilde{\chi}_1^0\widetilde{\chi}_1^0} = \frac{1}{2}\frac{\partial M_{\widetilde{\chi}_1^0}(v)}{\partial v} = \frac{y^2 v[M_D\sin(2\beta) + M_{\widetilde{\chi}_1^0}]}{6M^2_{\widetilde{\chi}_1^0} - 4M_{\widetilde{\chi}_1^0}M_S - 2M_D^2 - y^2v^2} , \tag{5.4}$$

where $\widetilde{\chi}_1^0$ is the lightest neutral mass eigenstate. In the limit of vanishing momentum transfer relevant for nuclear-recoil experiments, the SI direct detection rate is fixed by the Wilson coefficient f_q of the operator $m_q\overline{\widetilde{\chi}_1^0}\widetilde{\chi}_1^0\overline{q}q$. The t-channel Higgs exchange process leads to the following isospin-conserving Wilson coefficient for interactions with up-type and down-type quarks

$$f_u = f_d = -\frac{C^0_{h\widetilde{\chi}_1^0\widetilde{\chi}_1^0}}{vm_h^2} . \tag{5.5}$$

There is an additional effective coupling to a pair of gluons in the nucleon, which is obtained on integrating out the heavy quarks coupled to the Higgs propagator, and the corresponding Wilson coefficient is given as [28]

$$f_G = -\frac{1}{12}\sum_{q=c,b,t} f_q . \tag{5.6}$$

Combining the quark and the gluon contributions, we obtain the effective coupling of the DM state to nucleons, $f_N\overline{\widetilde{\chi}_1^0}\widetilde{\chi}_1^0\overline{N}N$, with

$$f_N/m_N = \sum_{q=u,d,s} f_q f^N_{Tq} + \frac{2}{27}\sum_{q=c,b,t} f_q f^N_{TG} = -\frac{C^0_{h\widetilde{\chi}_1^0\widetilde{\chi}_1^0}}{vm_h^2}\left[\sum_{q=u,d,s} f^N_{Tq} + \frac{2}{9}f^N_{TG}\right] , \tag{5.7}$$

where f^N_{Tq} and f^N_{TG} are the mass-fraction parameters of the quarks and the gluon in the nucleon N, respectively, and $f^N_{TG} \equiv 1 - \sum_{q=u,d,s} f^N_{Tq}$. We have summarized the additional details in the computation of DM-nucleon scattering in Appendix B.

Thus, we see from the above discussion that at the leading order, the SI DM-nucleon scattering rate via the Higgs boson exchange would vanish if the mass and Yukawa coupling parameters satisfy the following blind-spot condition [144, 155, 149]

$$M_D \sin(2\beta) + M_{\widetilde{\chi}^0_1} = 0. \tag{5.8}$$

For our choice of the phases of the mass and Yukawa coupling parameters, we see that the blind-spot condition can be satisfied for $M_D < 0$. For the specific choice of parameters that satisfy the blind-spot condition, since the coupling of the DM mass eigenstate to the Higgs boson is zero, the physical mass of the DM state is either M_S or M_D, depending upon the hierarchy. Thus the two possibilities are

1. $M_{\widetilde{\chi}^0_1} = M_S$, $-M_D > M_S$, $\sin(2\beta) = M_S/(-M_D)$,
2. $M_{\widetilde{\chi}^0_1} = -M_D$, $-M_D < \left(M_S + \sqrt{M_S^2 + (yv)^2}\right)/2$, $\tan\beta = 1$.

While the first possibility leads to an SI blind spot, the second one implies a blind spot for both SI and SD scattering. For our subsequent analyses, we take up the first case as an illustration.

5.1.2 Spin-dependent interaction

In the singlet-doublet model, the spin-dependent interaction of DM with the nucleon is determined by the gauge interaction of the doublet components with the Z-boson. The relevant interaction Lagrangian is given in terms of the gauge eigenstates by

$$\mathscr{L}_{int} = -\frac{e}{2\cos\theta_W \sin\theta_W} \left[(\chi^0_1)^\dagger \sigma^\mu_- \chi^0_1 - (\chi^0_2)^\dagger \sigma^\mu_- \chi^0_2\right] Z_\mu, \tag{5.9}$$

where θ_W is the Weinberg angle. Thus the axial-vector coupling of the DM state to the Z-boson, which leads to the spin-dependent interaction with nucleons is obtained to be

$$C^0_{Z\widetilde{\chi}^0_1\widetilde{\chi}^0_1} = \frac{e}{2s_W c_W}(U^2_{21} - U^2_{31}), \tag{5.10}$$

where $s_W = \sin\theta_W,\ c_W = \cos\theta_W$, and the mixing matrix in the neutral dark sector is defined by

$$\widetilde{\chi}^0 = U^\dagger \chi^0, \tag{5.11}$$

with the mass eigenstates $\widetilde{\chi}^0 = (\widetilde{\chi}^0_1, \widetilde{\chi}^0_2, \widetilde{\chi}^0_3)^\top$. Therefore, the Wilson coefficient of the relevant low-energy effective interaction $\overline{\widetilde{\chi}^0_1}\gamma^\mu\gamma^5\widetilde{\chi}^0_1\bar{q}\gamma_\mu\gamma^5 q$ is found to be (please see Appendix B for further details on the standard formalism adopted)

$$d_u = \frac{-e^2(U_{21}^2 - U_{31}^2)}{8M_Z^2 s_W^2 c_W^2} = -d_d\ . \tag{5.12}$$

5.2 Radiative Corrections to DM-nucleon Scattering

We now turn to the electroweak radiative corrections to the spin-independent DM direct detection rate near the tree-level blind spots. Since the SI scattering rates are vanishingly small around this region of mass and coupling parameters, the next-to-leading order (NLO) corrections are expected to play an important role in determining the detectability of such DM model-space. Furthermore, as we will see in the following, there also appears a new blind spot at NLO order, at a shifted parameter region compared to the tree-level one.

5.2.1 Computational framework

In addition to the interaction Lagrangians described in Eqs. (5.2) and (5.9), the following additional interaction terms (in the gauge basis) involving the charged components of the DM doublets and the weak bosons enter the computation of the radiative corrections

$$\mathscr{L}_{int} = \frac{e}{\sqrt{2}\ s_W}\left[\left((\chi_1^0)^\dagger\sigma_-^\mu\chi_1^+ + (\chi_2^-)^\dagger\sigma_-^\mu\chi_2^0\right)W_\mu^- + \text{ h.c.}\right]. \tag{5.13}$$

There are two different amplitudes contributing to the NLO electroweak corrections to DM-nucleon scattering, with representative Feynman diagrams depicted in Fig. 17. The first one stems from the one-loop vertex corrections to the Higgs-DM coupling, as shown in Fig. 17a, while the second one is given by the box diagrams shown in Fig. 17b. Since the triangle diagrams are ultraviolet (UV) divergent, we need to renormalize the relevant mass, mixing and coupling parameters. We have adopted the on-shell renormalization scheme for the DM sector, the details of which are described in Appendix A.

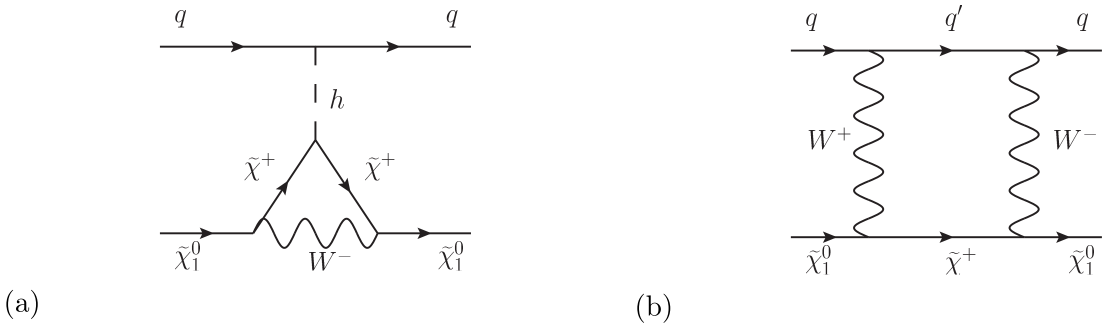

Figure 17: Representative Feynman diagrams contributing to DM-quark spin-independent scattering.

In addition to the class of diagrams represented in Fig. 17, there are other sets of diagrams entering the NLO electroweak corrections to the same process. These involve the Higgs self-energy corrections and the vertex corrections to the quark Yukawa couplings. However, the contribution of these latter diagrams to the DM-quark effective vertex is proportional to the tree-level DM-Higgs coupling, which is vanishingly small near the tree-level blind-spot region of our interest. We therefore focus on the diagrams in Fig. 17 for our computation, which constitute a UV-finite subset.

We have generated the relevant Feynman diagrams and the corresponding matrix elements using *FeynArts* [156], which are then passed onto *FeynCalc* [157, 158] to perform the Passarino-Veltman reduction of the one-loop integrals. We have used Collier [159, 160, 161, 162] for the numerical evaluation of the one-loop scalar integrals. We have adopted the Feynman gauge for our computations.

5.2.2 Results

The contribution to the effective DM-quark interaction from the vertex corrections represented by the triangle diagrams in Fig. 17a, $f_N^{\rm tri}$, has the same form as the tree-level t-channel

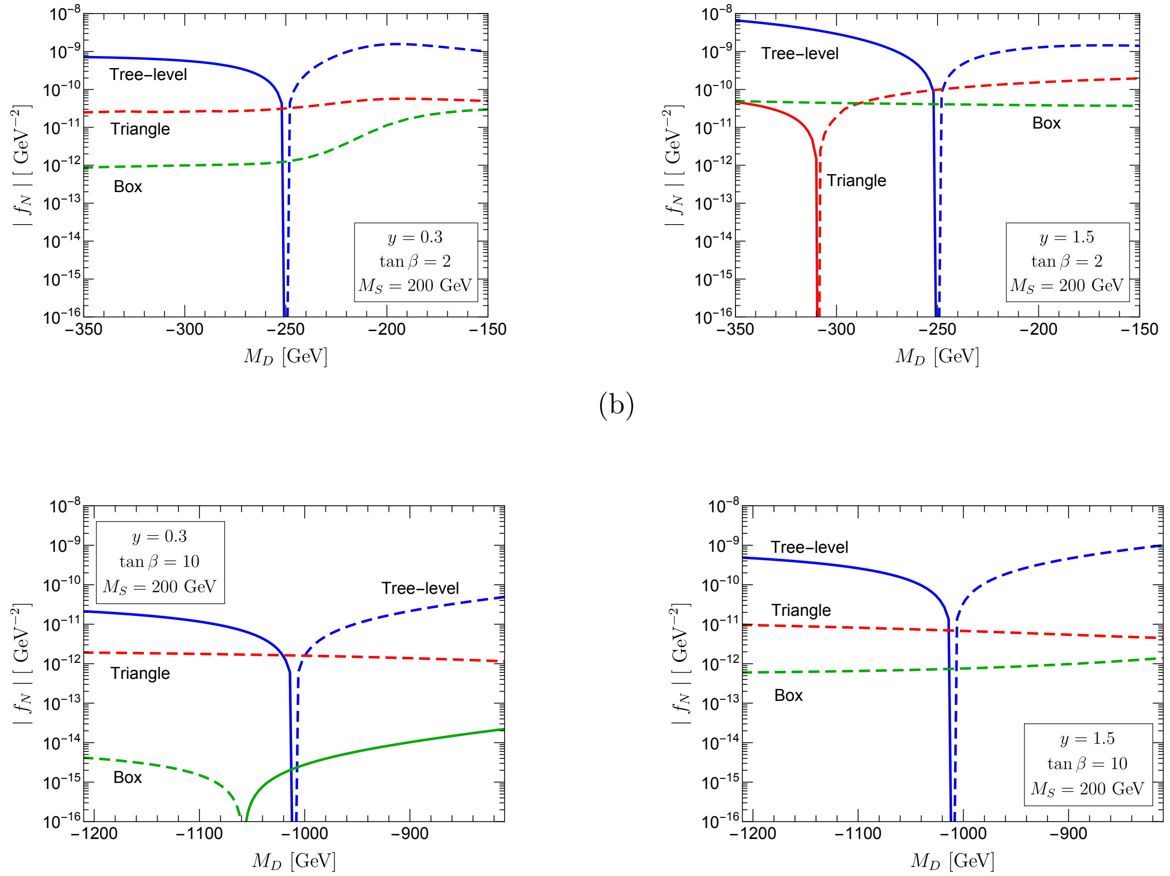

(a) (b)

(c) (d)

Figure 18: Contributions to the absolute value of f_N as a function of M_D, from tree-level diagrams (blue), one-loop triangle diagrams (red), and one-loop box diagrams (green). The dashed lines indicate negative values of f_N. The value of the singlet dark fermion mass is fixed as $M_S = 200$ GeV, with $\tan\beta = 2$ (upper panels) and $\tan\beta = 10$ (lower panels), for representative values of $y = 0.3$ (left columns) and $y = 1.5$ (right columns).

Higgs exchange vertex, with the Higgs-DM coupling $C^0_{h\widetilde{\chi}^0_1\widetilde{\chi}^0_1}$ replaced by its one-loop counterpart $C^{\rm tri}_{h\widetilde{\chi}^0_1\widetilde{\chi}^0_1}$

$$f_N^{\rm tri}/M_N = -\frac{C^{\rm tri}_{h\widetilde{\chi}^0_1\widetilde{\chi}^0_1}}{v m_h^2}\left(\sum_{q=u,d,s} f_{Tq} + \frac{2}{9} f_{TG}\right). \tag{5.14}$$

The box diagrams shown in Fig. 17b also induce corrections to the Wilson coefficient of the operator $\overline{\widetilde{\chi}_1^0}\widetilde{\chi}_1^0\overline{q}q$, denoted as $C_q^{\rm box}$, which are not universal for different flavors, and lead to the following corrections to the DM-nucleon effective scalar coupling:

$$f_N^{\rm box}/M_N = \sum_{q=u,d,s} \frac{C_q^{\rm box}}{m_q} f_{Tq} + \frac{2}{27} f_{TG} \sum_{q=c,b,t} \frac{C_q^{\rm box}}{m_q}, \tag{5.15}$$

The other possible structures for spin-independent operators generated by the radiative corrections are suppressed either by the small momentum transfer or by powers of small DM velocity [163].

We show the resulting magnitudes of the tree-level $f_N^{\rm tree}$, the triangle diagram $f_N^{\rm tri}$, and the box diagram $f_N^{\rm box}$ contributions as a function of M_D in Fig. 18, where we have adopted the Feynman gauge for our computations. The results are shown for $M_S = 200$ GeV with various values of y and $\tan\beta$. Here, dashed lines have been used to indicate negative values of the Wilson coefficients. We note several interesting features in Fig. 18. First of all, although the tree-level contribution naturally dominates in the parameter region away from the blind spot, near the blind spot it decreases dramatically. The one-loop contribution, especially from the triangle diagrams, therefore gives rise to the leading contribution in this region. Secondly, away from the blind spot, the one-loop electroweak effects are still appreciable. For example, we see in Figs. 18b and 18c that the contributions from the triangle diagrams considered can shift the tree-level results by up to 10%. Third, the box diagram contribution can be comparable to the triangles in certain regions of parameter space. Fourth, there are values of parameters around which the triangle and the box contributions can change sign individually, and therefore have their own blind spots, as seen in Figs. 18b and 18c.

Most importantly, the full amplitude, which is a coherent sum of all the diagrams, always shows a new blind spot at the NLO level, perturbatively shifted from the tree-level blind spot. We quantify this shift by introducing a mass parameter difference

$$\delta M_D = M_D^{(0)} - M_D^{(1)}, \tag{5.16}$$

which is the difference between the tree-level blind spot $M_D^{(0)} = -M_{\widetilde{\chi}_1^0}/\sin 2\beta$ and the new blind spot $M_D^{(1)}$ obtained at NLO, on including the one-loop corrections. This variation in δM_D is shown in Fig. 19 as a function of M_S. The amount of the shift in the values of M_D

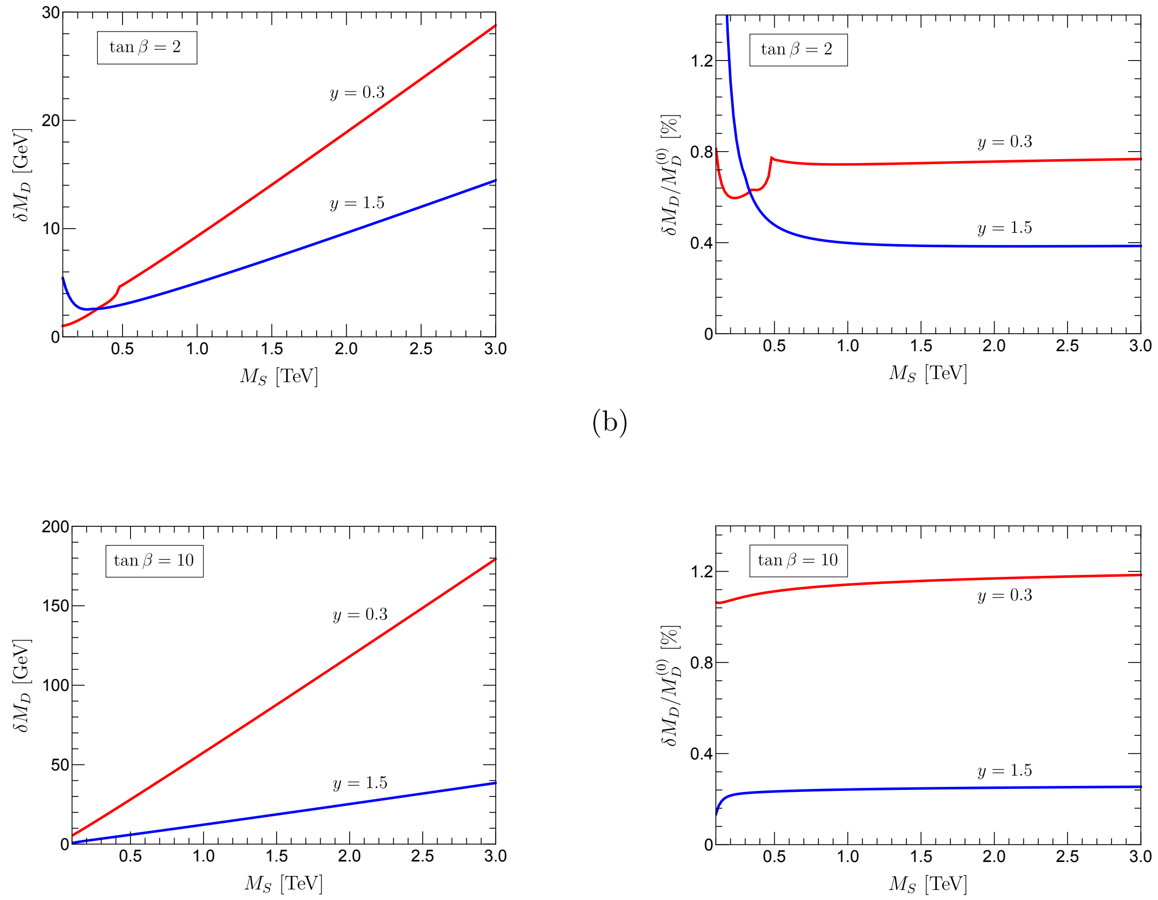

(a) (b) (c) (d)

Figure 19: Shift in the position of the blind spot δM_D versus M_S, with $\delta M_D = M_D^{(0)} - M_D^{(1)}$. The results are shown for two values of the coupling $y = 0.3$ (red) and $y = 1.5$ (blue), with $\tan\beta = 2$ (upper panels) and $\tan\beta = 10$ (lower panels). We also show the ratio $\delta M_D/M_D^{(0)}$ in the right panels.

is almost linearly proportional to the value of M_S as seen in Figs. 19a and 19c. The results are shown for two values of the coupling $y = 0.3$ (red) and $y = 1.5$ (blue), with $\tan\beta = 2$ (upper panels) and $\tan\beta = 10$ (lower panels). As we can see from this figure, the shift is larger for large values of $\tan\beta$ and small values of y. We also show the ratio $\delta M_D/M_D^{(0)}$ in Figs. 19b and 19d (the right panels), and it can be around $\mathcal{O}(1\%)$ for small values of y.

We note that the red curves in Figs. 19a and 19b, with $y = 0.3$ and $\tan\beta = 2$, exhibit two cusps at $M_S \simeq 330$ GeV and 470 GeV. These are due to the opening of new thresholds where the decays $\widetilde{\chi}^0_{2,3} \to \widetilde{\chi}^0_1 Z$ and $\widetilde{\chi}^0_{2,3} \to \widetilde{\chi}^0_1 h$, respectively, become kinematically accessible[1]. On the other hand, the blue curves in Figs. 19a and 19b, and all the curves in Figs. 19c and 19d do not have such cusps, as the decay channels $\widetilde{\chi}^0_{2,3} \to \widetilde{\chi}^0_1 Z$ and $\widetilde{\chi}^0_{2,3} \to \widetilde{\chi}^0_1 h$ are always allowed in the relevant parameter regions.

5.3 Direct Detection: Current Constraints and Future Prospects

We now apply the results of the previous section to estimate the reach of ongoing and future direct detection experiments in the singlet-doublet model parameter space near the tree-level blind spot region. After discussing the NLO contribution to the spin-independent scattering, we also show the LO estimate for the reach of spin-dependent scattering experiments for comparison.

5.3.1 Spin-independent scattering cross-sections at one-loop

In this section, we focus on the parameter region for the tree-level SI blind spot, where the NLO corrections are most impactful in extending the reach of SI direct detection probes. For a fixed value of $\tan\beta$, this then leads to a two-dimensional parameter space of interest, that of the DM mass ($M_{\widetilde{\chi}^0_1}$) and Yukawa coupling y plane. The value of M_D, for each $M_{\widetilde{\chi}^0_1}$, is fixed to be $-M_{\widetilde{\chi}^0_1}/\sin(2\beta)$ as given by the blind-spot condition in Eq. (5.8).

In Fig. 20, we show the contours of SI DM-nucleon scattering cross-section, $\sigma_{\rm SI}$, in the $y - M_{\widetilde{\chi}^0_1}$ plane, for values of $\tan\beta = 2$ (left) and $\tan\beta = 10$ (right). As we can see, for $\tan\beta = 2$, $\sigma_{\rm SI}$ takes values in the range of about 10^{-47} cm^2 to 10^{-50} cm^2, for $M_{\widetilde{\chi}^0_1}$ values in the interval 100 GeV $-$ 2 TeV, and coupling coefficient y in the range $0.3 - 1.5$. For a given coupling, the cross-section decreases with increasing DM mass, and the future projection from the LZ experiment [2] (blue shaded region) is expected to probe a DM mass upto

---

[1] The masses of $\widetilde{\chi}^0_2$ and $\widetilde{\chi}^0_3$ are nearly degenerate close to the tree-level blind spot parameter region.

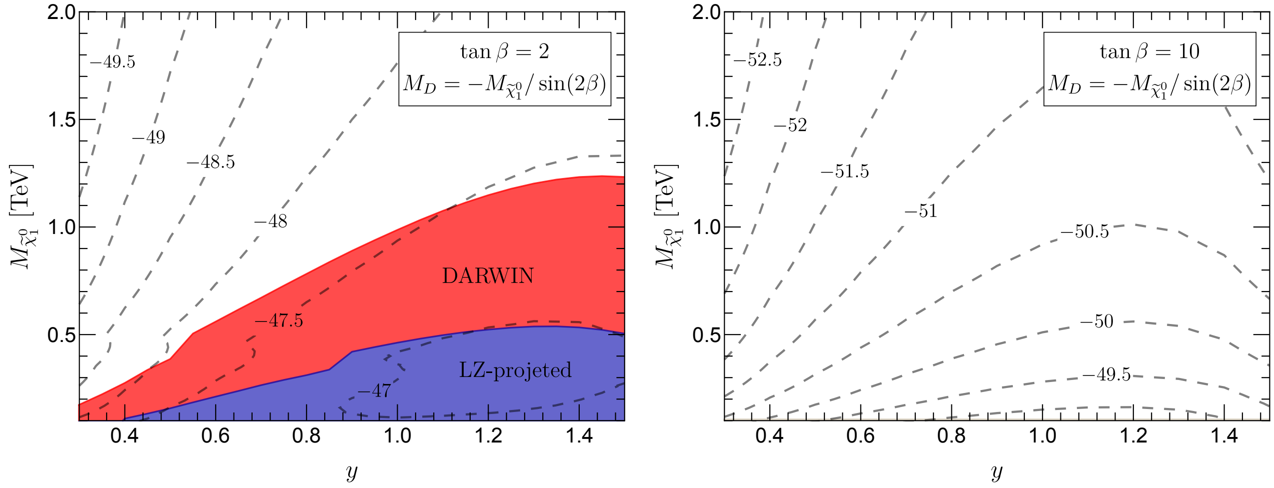

(a) (b)

Figure 20: Spin-independent DM-nucleon scattering cross-section ($\sigma_{\rm SI}$) in the DM mass ($M_{\widetilde{\chi}_1^0}$)–Yukawa coupling (y) plane, with M_D fixed by the blind-spot condition. The results are shown for $\tan\beta = 2$ (left panel) and $\tan\beta = 10$ (right panel). The contours represent lines with fixed values of $\log_{10}\sigma^{\rm SI}$, with $\sigma_{\rm SI}$ expressed in cm^2 units. The projected reach of the LZ [2] (blue shaded) and DARWIN [3] (red shaded) experiments are also shown.

about 500 GeV (blue shaded region in Fig. 20), for the above range of y. This reach can be further extended by the DARWIN experiment [3] (red shaded region), which can probe DM masses of upto 1250 GeV for the same range of coupling values. For higher values of $\tan\beta$, as seen with $\tan\beta = 10$ in the right panel of Fig. 20, the expected cross-section is smaller due to the suppression from smaller mixing angles, with a maximum of around 10^{-49} cm^2, which may not be accessible to DARWIN. Thus, the small $\tan\beta$ scenario leads to similar $\sigma_{\rm SI}$ as in the case of wino-like real triplet DM, as discussed in the introduction, while the intermediate $\tan\beta$ scenario predicts cross-sections similar to the case of Majorana Higgsino-like doublets.

5.3.2 Tree-level spin-dependent scattering cross-sections

In the spin-independent (SI) blind-spot region considered above, the effective coupling of the DM mass eigenstate to the Higgs boson vanishes. On the other hand, the spin-dependent (SD) scattering rate, which is determined at the tree level by the DM-Z-boson coupling, can have an appreciable rate for the same set of model parameters. In general, though the experimental sensitivity of SD scattering is weaker than that of SI scattering, near the blind spot they might have comparable reach [150], since the SI rates appear only at NLO.

We show the spin-dependent scattering cross-sections, $\sigma_{\rm SD}^{p}$ for proton and $\sigma_{\rm SD}^{n}$ for neutron, in Fig. 21 in the $y - M_{\widetilde{\chi}_1^0}$ plane, with all other parameters and conditions being the same as in Fig. 20. The corresponding cross-sections are in the range of $10^{-38} - 10^{-43}$ cm^2 for $\tan\beta = 2$, and around an order of magnitude lower for $\tan\beta = 10$, in the parameter space studied. The reach from the current PICO-60 experiment [164, 165, 166] (blue shaded region) and the future projections from the LZ experiment [2] (red shaded region) are also shown. For $\tan\beta = 2$, the reach from PICO-60 is upto about $M_{\widetilde{\chi}_1^0} = 840$ GeV, while the future projection from LZ can probe DM masses upto 1560 GeV. For $\tan\beta = 10$, the reach from PICO-60 is reduced to 230 GeV and that of LZ to around 350 GeV.

Thus in the particular simple model adopted in this study the tree-level SD scattering has somewhat better prospects in probing the model parameter space, compared to the one-loop SI scattering rates. However, since the SI and SD rates probe the coupling of the DM particle to different sets of SM particles, both of them are necessary probes of the model, with combined experimental observations leading to a unified picture of the DM-nucleon effective couplings.

Before concluding, a special remark is in order. The search for missing particles, the potential DM candidates, at high-energy colliders is complementary to the DM direct detection. The charged and neutral dark sector states can be pair-produced in quark-antiquark annihilation via the s-channel $W^{\pm}, Z$-boson exchange in the Drell-Yan process. These states, apart from the lightest neutral DM particle, would decay via electroweak interactions to final states containing W and Z bosons. Thus, multiple leptons and missing transverse momenta are the most promising channels to search for at hadron colliders, such as the LHC [167, 168],

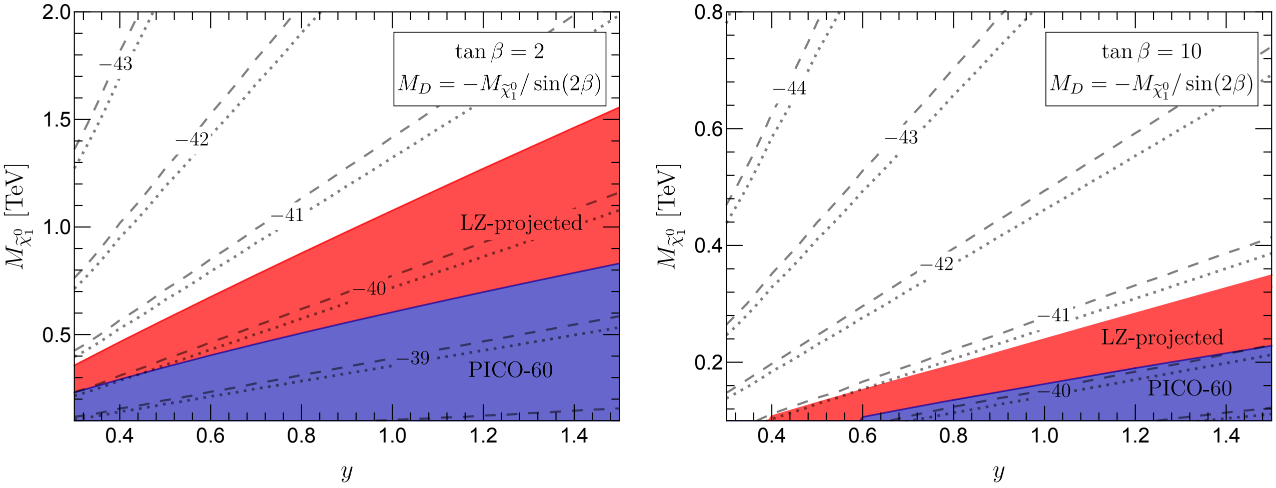

(a)

(b)

Figure 21: Spin-dependent DM-nucleon scattering cross-sections ($\sigma_{\rm SD}^{p,n}$) in the DM mass ($M_{\tilde{\chi}_1^0}$)–Yukawa coupling (y) plane, with all other parameters and conditions being the same as in Fig. 20. The contours represent lines with fixed values of $\log_{10}\sigma_{\rm SD}^{p}$ (dashed) and $\log_{10}\sigma_{\rm SD}^{n}$ (dotted), with $\sigma_{\rm SD}^{p,n}$ expressed in cm^2 units. The reach of the ongoing PICO-60 experiment (blue shaded) and the projected reach of the LZ experiment (red shaded) are also shown.

including its luminosity (HL-LHC) [169, 170], and possibly energy (HE-LHC) upgrades [171]. For small mass gaps between the charged and neutral dark sector particles, a likely scenario under our consideration, searches for disappearing tracks and displaced vertices are relevant [172]. For a detailed discussion of the LHC complementarity for DM search near the blind-spot region, we refer the reader to Ref. [150]. On the other hand, the situation could be more optimistic if there are relatively light colored states (such as gluinos and squarks in SUSY), that could be copiously produced at hadron colliders and that could subsequently decay to the DM states resulting in large missing transverse momentum and multiple jets in the final state [173].

6.0 Dark Matter and Electroweak Phase Transition with an SU(2) Dark Sector

There is mounting evidence for the existence of DM through its gravitational effects. However, the null results of the last fifty years of searches challenge the most theoretically attractive candidates, namely, the standard weakly interacting massive particles (WIMPs), that are charged under the SM weak interactions (see Ref. [28] for review). On the other hand, it is quite conceivable that the DM particles live in a dark sector that are not charged under the SM gauge group. Furthermore, the dark sector may have a rich particle spectrum, leading to other observable consequences [33]. A massless dark gauge field, dubbed as the dark radiation (DR), is one of the quite interesting extensions that could help to alleviate the tension between Planck and HST measurements of the Hubble constant [34]. DM-DR interactions and DM self-interactions can provide solutions to the small-scale structure problems which challenge the cold dark matter (CDM) paradigm [35, 36, 37].

In this chapter, we would like to explore the potentially observable effects beyond the gravitational interactions from a hypothetical dark sector [174]. We assume that the dark sector interacts with the SM particles only through the Higgs portal [38]. An immediate consequence of this would be the modification of the Higgs boson properties that will be probed in the on-going and future high energy experiments [39, 40]. The DM searches from the direct and indirect detection experiments will provide additional tests for the theory [28]. Perhaps, an even more significant impact would be on the nature of the electroweak phase transition (EWPT) at the early Universe (see, e.g., [41, 42, 43] for recent reviews), which could shed light on another profound mystery: the origin of baryon asymmetry in the Universe. Indeed, one of the best-motivated solutions to this mystery is the electroweak baryogenesis (EWBG) [44, 45, 46, 47] (see also [48, 49] for pedagogical introductions). For a successful generation of the baryon asymmetry during the EWPT, all of the three Sakharov conditions [50] have to be satisfied. One of the three Sakharov conditions is to assure a strong first-order phase transition (FOPT), that is absent within the minimal SM, but could be achieved by the Higgs portal to a sector beyond the SM. It is important to note that many well-motivated extensions of the SM predict gravitational wave (GW) signals through a strong FOPT, that are potentially detectable at LIGO and future LISA-like space-based GW detectors.

Given the rich physics associated with a dark sector, there have been significant activities in the literature dealing with many different aspects of the theory and phenomenology. In the dark sector, both Abelian ($\mathrm{U(1)_D}$) and non-Abelian ($\mathrm{SU(2)_D}$, $\mathrm{SU(3)_D}$) gauge sectors have been studied with different symmetry breaking patterns induced by various scalar scenarios. Building upon the existing literature, in this chapter, we will focus on a dark $\mathrm{SU(2)_D}$ model un-charged under the SM gauge group. Some early exploration and the phenomenology associated with the model have been examined [175, 176, 177, 178, 179, 180, 181, 182, 183, 184, 185]. The previous works mainly focused on the DM studies. In this work, we will study the EWPT and GW with this well-motivated DM model. In this class of models, it remains largely unconstrained on the choice of the dark scalar sector. With just one real scalar triplet, we could achieve a FOPT at the early Universe by transitioning from an electroweak symmetric vacuum that breaks the $\mathrm{SU(2)_D}$ symmetry to an electroweak broken vacuum that preserves the $\mathrm{SU(2)_D}$ symmetry [186]. As such, all the dark sector particles would remain massless, and there would be no cold DM candidate in this simplest scenario. Alternatively, we would like to explore the following two cases to facilitate a strong FOPT in the early Universe and to have viable cold DM candidates

1. one real scalar triplet and one real scalar singlet;
2. two real scalar triplets.

For both cases, at zero temperature, only one scalar triplet gets a nonzero vacuum expectation value (VEV) and partially breaks the $\mathrm{SU(2)_D}$ into $\mathrm{U(1)_D}$. The massless vector gauge boson associated with the unbroken $\mathrm{U(1)_D}$ symmetry can serve as a dark radiation (DR). The other two massive gauge bosons associated with the symmetry breaking are our vector DM candidates. Due to the presence of the non-Abelian gauge boson couplings, the DM-DR and DM-DM interactions can be naturally introduced. The other scalar triplet or singlet can develop a non-zero VEV at a finite temperature and can thus trigger a strong FOPT, besides providing the scalar DM candidates.

The rest of the chapter is organized as follows. In section 6.1, we introduce our model and particle spectrum, with the phenomenological constraints presented in section 6.2 and DM phenomenology in section 6.3. In section 6.4, we perform the study of EWPT and the GWs spectrum with two benchmark points (BMs) as shown in Table 9.

6.1 Theoretical Framework

In addition to the SM, we include a non-Abelian $\mathrm{SU(2)_D}$ dark sector. We consider two scenarios for the dark scalar sector, a real singlet plus a real triplet (ST), or two real triplets (TT) under the dark gauge group $\mathrm{SU(2)_D}$:

$$\Phi_1 = \begin{cases} \mathrm{ST} & \frac{1}{\sqrt{2}}(v_1 + \omega) \\ \mathrm{TT} & \frac{1}{\sqrt{2}}(\omega_1,\, \omega_2,\, v_1 + \omega_3)^{\mathrm{T}} \end{cases}, \quad \Phi_2 = \frac{1}{\sqrt{2}}(\varphi_1,\, v_2 + \varphi_2,\, \varphi_3)^{\mathrm{T}}. \tag{6.1}$$

We assume that the dark sector does not carry SM charges but rather interacts with the SM particles through the Higgs portal interactions. Therefore, the Lagrangian of the model consists of three parts

$$\begin{aligned} \mathscr{L} &= \mathscr{L}_{\mathrm{SM}} + \mathscr{L}_{\mathrm{portal}} + \mathscr{L}_{\mathrm{DS}}, & (6.2)\\ -\mathscr{L}_{\mathrm{SM}} &\supset V_{\mathrm{SM}} = m_H^2|H|^2 + \frac{\lambda_H}{2}|H|^4, & (6.3)\\ -\mathscr{L}_{\mathrm{portal}} &\supset V_{\mathrm{portal}} = \lambda_{H11}|H|^2|\Phi_1|^2 + \lambda_{H22}|H|^2|\Phi_2|^2, & (6.4)\\ \mathscr{L}_{\mathrm{DS}} &= -\frac{1}{4}\tilde{W}^a_{\mu\nu}\tilde{W}^{a\mu\nu} + |D_\mu\Phi_1|^2 + |D_\mu\Phi_2|^2 - V_{\mathrm{DS}}, & (6.5) \end{aligned}$$

where $\tilde{W}^a_{\mu\nu} = \partial_\mu \tilde{W}^a_\nu - \partial_\nu \tilde{W}^a_\mu + \tilde{g} f^{abc}\tilde{W}^b_\mu \tilde{W}^c_\nu$ is the dark gauge field strength tensor; $D_\mu = \partial_\mu - i\tilde{g}T^a\tilde{W}^a_\mu$ is the covariant derivative in the dark sector with T^a being the $\mathrm{SU(2)_D}$ generators, which is given in the 3-dimensional representation by

$$T_1 = \begin{pmatrix} 0 & 0 & 0 \\ 0 & 0 & -i \\ 0 & i & 0 \end{pmatrix}, T_2 = \begin{pmatrix} 0 & 0 & i \\ 0 & 0 & 0 \\ -i & 0 & 0 \end{pmatrix}, T_3 = \begin{pmatrix} 0 & -i & 0 \\ i & 0 & 0 \\ 0 & 0 & 0 \end{pmatrix}; \tag{6.6}$$

and $H^{\mathrm{T}} = (G^{+}, (v_h + h_0 + iG_0)/\sqrt{2})$, being the SM Higgs doublet. The most general renormalizable hidden sector potential with an assumed Z_2 symmetry is given by

$$V_{\mathrm{DS}} = m_{11}^2|\Phi_1|^2 + m_{22}^2|\Phi_2|^2 + \frac{\lambda_1}{2}|\Phi_1|^4 + \frac{\lambda_2}{2}|\Phi_2|^4 + \lambda_3|\Phi_1|^2|\Phi_2|^2 + \lambda_4|\Phi_1^\dagger\Phi_2|^2, \tag{6.7}$$

where $\lambda_4 = 0$ in the ST model. In principle, there can be cubic terms for the singlet scalar, which can change the phase transition dramatically. However, we will not consider breaking the Z_2 symmetry in this work.[1]

In our phenomenological analyses in the following sections, we choose $v_1 = 0$ at the zero temperature. An important consequence of this choice is to leave the dark $\mathrm{U(1)_D}$ unbroken so that there will be a massless dark gauge field, DR, which would have observational implications.

6.1.1 Mass spectrum

With the choice of $v_1 = 0$, the SM Higgs boson mixes only with the $\mathrm{SU(2)_D}$ dark scalar φ_2. In the TT scenario, the mass terms for the scalar bosons are

$$-\mathscr{L}_{\mathrm{scalar}}^{\mathrm{mass}} \supset \frac{1}{2}\mathbf{h}^T\mathbf{M_h}\mathbf{h} + \frac{1}{2}m_{\omega_2}^2\omega_2^2 + m_{\omega^\pm}^2\omega^+\omega^-, \tag{6.8}$$

where $\mathbf{h} = \{h_0, \varphi_2\}$ are two neutral scalars with the mass matrix

$$\mathbf{M_h} = \begin{pmatrix} \lambda_H v_h^2 & \lambda_{H22}v_2v_h \\ \lambda_{H22}v_2v_h & \lambda_2 v_2^2 \end{pmatrix}, \tag{6.9}$$

and $m_{\omega^\pm}^2 = \frac{1}{2}(\lambda_3 v_2^2 + 2m_{11}^2 + \lambda_{H11}v_h^2)$ is the mass of the $\mathrm{SU(2)_D}$ charged scalars. The mass for another neutral scalar ω_2 is $m_{\omega_2}^2 = \frac{1}{2}((\lambda_3+\lambda_4)v_2^2 + 2m_{11}^2 + \lambda_{H11}v_h^2)$. The scalar fields $\omega^\pm$ are defined as

$$\omega^+ \equiv \frac{\omega_1 - i\omega_3}{\sqrt{2}}, \quad \omega^- \equiv \frac{\omega_1 + i\omega_3}{\sqrt{2}}. \tag{6.10}$$

---

[1] In doing so, there could be the formation of domain walls during the phase transition when the field acquires a non-zero VEV, which serves as another source for GW production when they annihilate (see, e.g., [187]). If they persist and still exist today, that might be problematic. These are interesting questions and needs a dedicated analysis of their formation, evolution and annihilation in a specified cosmological context, which however is beyond the scope of the current study and will be left to a future investigation.

In the ST scenario, there is only one massive scalar with mass

$$m_\omega^2 = m_{\omega^\pm}^2. \tag{6.11}$$

Please note that the sign ± refers to the dark $\mathrm{SU}(2)_\mathrm{D}$ charge. The neutral scalars h_0 and φ_2 are mixed. The mass eigenstates $\mathbf{h'} = \{h_1, h_2\}$ can be obtained from a rotation on $\mathbf{h}$

$$\begin{pmatrix} h_1 \\ h_2 \end{pmatrix} = \mathcal{R}(\theta) \begin{pmatrix} h_0 \\ \varphi_2 \end{pmatrix}. \tag{6.12}$$

The rotation matrix can be parametrized by one mixing angle θ as

$$\mathcal{R}(\theta) = \begin{pmatrix} \cos\theta & \sin\theta \\ -\sin\theta & \cos\theta \end{pmatrix}. \tag{6.13}$$

The mass eigenvalues are

$$\mathcal{R}\mathbf{M_h}\mathcal{R}^T = \begin{pmatrix} m_{h_1}^2 & 0 \\ 0 & m_{h_2}^2 \end{pmatrix}. \tag{6.14}$$

Here and henceforth, we identify h_1 as the SM-like Higgs boson with $m_{h_1} = 125$ GeV, and h_2 is a heavier scalar in the model.

The scalar fields φ_1 and φ_3 are the Nambu-Goldstone (NG) bosons absorbed by two of the $\mathrm{SU}(2)_\mathrm{D}$ gauge bosons $\tilde{W}_1$ and $\tilde{W}_3$. The mass terms of dark gauge bosons are contained in $(D_\mu\Phi_1)^2$ and $(D_\mu\Phi_2)^2$ in Eq. (6.5)

$$-\mathscr{L}_{\text{vector}}^{\text{mass}} \supset \frac{1}{2} M_{\tilde{W}}^2 \sum_{i=1,3} \tilde{W}_i^2 = m_{\tilde{W}^\pm}^2 \tilde{W}^+ \tilde{W}^-, \tag{6.15}$$

where

$$\tilde{W}^+ \equiv \frac{\tilde{W}_1 - i\tilde{W}_3}{\sqrt{2}},\ \tilde{W}^- \equiv \frac{\tilde{W}_1 + i\tilde{W}_3}{\sqrt{2}},\ m_{\tilde{W}^\pm} = \tilde{g} v_2, \tag{6.16}$$

and $\tilde{W}_2$ remains massless.

6.1.2 Interactions

The interactions between the SM and the dark sector are generated through the Higgs portal as in Eq. (6.4), specifically

$$\begin{aligned}\mathscr{L}^{\text{int}}_{\text{DS-SM}} \supset\ & 2\tilde{g}^2 v_2(\sin\theta h_1 + \cos\theta h_2)\tilde{W}^+\tilde{W}^- + \tilde{g}^2(\sin\theta h_1 + \cos\theta h_2)^2\tilde{W}^+\tilde{W}^- \\ & - \sum_{i=1,2}(c_i h_i \omega^+\omega^- - d_i h_i \omega_2^2) - \sum_{\substack{i,j=1,2 \\ i<j}}(c_{ij} h_i h_j \omega^+\omega^- - d_{ij} h_i h_j \omega_2^2) \qquad ,\end{aligned} \tag{6.17}$$

where the scalar couplings are given in terms of the mixing angle and the other model parameters

$$c_1 = \lambda_3 v_2 \sin\theta + \lambda_{H11} v_h \cos\theta, \quad d_1 = \frac{1}{2}((\lambda_3+\lambda_4)v_2\sin\theta + \lambda_{H11} v_h \cos\theta), \tag{6.18}$$

$$c_2 = \lambda_3 v_2 \cos\theta - \lambda_{H11} v_h \sin\theta, \quad d_2 = \frac{1}{2}((\lambda_3+\lambda_4)v_2\cos\theta - \lambda_{H11} v_h \sin\theta), \tag{6.19}$$

$$c_{11} = \frac{1}{2}(\lambda_3 \sin^2\theta + \lambda_{H11}\cos^2\theta), \quad d_{11} = \frac{1}{4}((\lambda_3+\lambda_4)\sin^2\theta + \lambda_{H11}\cos^2\theta), \tag{6.20}$$

$$c_{12} = \frac{1}{2}(\lambda_3 - \lambda_{H11})\sin 2\theta, \quad d_{12} = \frac{1}{4}(\lambda_3 + \lambda_4 - \lambda_{H11})\sin 2\theta, \tag{6.21}$$

$$c_{22} = \frac{1}{2}(\lambda_3 \cos^2\theta + \lambda_{H11}\sin^2\theta), \quad d_{22} = \frac{1}{4}((\lambda_3+\lambda_4)\cos^2\theta + \lambda_{H11}\sin^2\theta). \tag{6.22}$$

In the ST scenario, c_i, c_{ij}, and λ_4 are zero. The above interactions govern the phenomenology relevant for the potential experimental observations, such as the Higgs properties, the DM relic density and direct detections, and EWPT at the early Universe, as we will explore in the following sections.

6.2 Phenomenological Constraints

The scalar potential of the model is

$$V_S = \frac{m_H^2}{2}h_0^2 + \frac{\lambda_H}{8}h_0^4 + \frac{m_{11}^2}{2}\omega_3^2 + \frac{\lambda_1}{8}\omega_3^4 + \frac{m_{22}^2}{2}\varphi_2^2 + \frac{\lambda_2}{8}\varphi_2^4 + \frac{\lambda_{H11}}{4}h_0^2\omega_3^2 + \frac{\lambda_{H22}}{4}h_0^2\varphi_2^2 + \frac{\lambda_3}{4}\omega_3^2\varphi_2^2. \tag{6.23}$$

The two minima conditions $\frac{\partial V_S}{\partial h_0} = 0$ and $\frac{\partial V_S}{\partial \varphi_2} = 0$ evaluated at the VEVs are

$$v_h(2m_H^2 + \lambda_H v_h^2 + \lambda_{H11} v_1^2 + \lambda_{H22} v_2^2) = 0\,, \tag{6.24}$$

$$v_2(2m_{22}^2 + \lambda_{H22} v_h^2 + \lambda_3 v_1^2 + \lambda_2 v_2^2) = 0\,. \tag{6.25}$$

The mass parameters m_H and m_{22} can be solved by using these two minima conditions

$$m_H^2 = -\frac{1}{2}(\lambda_H v_h^2 + \lambda_{H11} v_1^2 + \lambda_{H22} v_2^2), \tag{6.26}$$

$$m_{22}^2 = -\frac{1}{2}(\lambda_{H22} v_h^2 + \lambda_3 v_1^2 + \lambda_2 v_2^2). \tag{6.27}$$

In the TT model as described in the last section, there are fourteen parameters

$$\tilde{g},\, v_h,\, v_1,\, v_2,\, m_H^2,\, m_{11}^2,\, m_{22}^2,\, \lambda_H,\, \lambda_{H11},\, \lambda_{H22},\, \lambda_1,\, \lambda_2,\, \lambda_3,\, \lambda_4.$$

By applying the two extrema conditions in Eqs. (6.24) and (6.25) for the scalar potential and $v_1 = 0$, we can get rid of three parameters. Adopting the SM values $m_{h_1} = 125$ GeV, $v_h = 246$ GeV, we are left with nine independent parameters, which can be chosen as

$$\sin\theta,\, \tilde{g},\, m_{\tilde{W}^+},\, m_{h_2},\, m_{\omega^+},\, m_{\omega_2},\, \lambda_1,\, \lambda_{H11},\, \lambda_3. \tag{6.28}$$

In the ST model, we have one less free parameter as m_{ω^+} and m_{ω_2} are replaced by one parameter m_ω.

We wish to have observable imprints from the dark sector in the current and future experiments. We thus take the $\mathrm{SU}(2)_\mathrm{D}$ symmetry breaking not too far from the electroweak scale in the SM, and vary the mass of the second Higgs boson m_{h_2} in the range of 200 GeV−1 TeV. We will not consider $m_{h_2} > 1$ TeV, as the perturbative GW calculations are not reliable. We examine the possible bounds on the other model parameters from the existing experiments in the following sessions. For the purpose of illustration, we choose two benchmark points (BMs) for the input parameters as shown in Table 9. Some other calculated physical quantities are also summarized in the table.

Parameters	BM1	BM2
$\sin\theta$	-0.25	-0.12
$\tilde{g}$	0.094	0.133
$m_{\tilde{W}^\pm}$	94 GeV	133 GeV
m_{h_2}	200 GeV	290 GeV
$m_{\omega^\pm}$	1.2 TeV	1.3 TeV
m_{ω_2}	2.0 TeV	1.9 TeV
λ_1	3.5	3.5
λ_{H11}	2.0	2.0
λ_3	3.0	3.5
λ_H	0.28	0.27
λ_2	3.8×10^{-2}	8.3×10^{-2}
λ_{H22}	2.4×10^{-2}	3.2×10^{-2}
λ_4	5.0	4.0
v_2	1 TeV	1 TeV
$\Omega_{\tilde{W}^\pm} h^2$	0.096	0.12
$\sigma_{\rm SI}$ (cm^2)	7.8×10^{-47}	8.0×10^{-47}
T_c (GeV)	177	252
T_n (GeV)	147	234
β/H_n	297	760
α	0.32	5.1×10^{-2}
phase transition pattern	2-step (6.85)	3-step (6.86)

Table 9: Model parameters and calculated physical quantities with two benchmark points, BM1 and BM2. The independent model parameters in Eq. (6.28) are listed in the upper part of the table.

6.2.1 Vacuum stability

A stable physical vacuum has to be bounded from below keeping the scalar fields from running away. The behavior of the scalar potential is dominant by the quartic part when the field strength approaches infinity. The conditions of vacuum stability are given in Ref. [188, 189]. Following their procedure, we find the following conditions

$$\lambda_H > 0, \quad \lambda_1 > 0, \quad \lambda_2 > 0, \tag{6.29}$$

$$\lambda_3 + \lambda_4 + \sqrt{\lambda_1 \lambda_2} > 0, \tag{6.30}$$

$$\lambda_{H11} + \sqrt{\lambda_H \lambda_1} > 0, \quad \lambda_{H22} + \sqrt{\lambda_H \lambda_2} > 0. \tag{6.31}$$

6.2.2 Partial wave unitarity

The scattering amplitudes for spin-less 2 → 2 processes can be decomposed into a sum over the partial waves a_j as

$$\mathcal{A}(\alpha) = 16\pi \sum_{j=0}^{\infty} a_j (2j+1) P_j(\cos\alpha), \tag{6.32}$$

where $P_j(\cos\alpha)$ are the Legendre polynomials in terms of the scattering angle α. The perturbative unitarity requires $\mathrm{Im}(a_j) = |a_j|^2$, which implies

$$|a_j| \leq 1, \quad |\mathrm{Re}(a_j)| \leq \frac{1}{2}. \tag{6.33}$$

We will adopt the second condition as it turns out to be more constraint. The s-wave amplitude can be computed by

$$a_0 = \frac{1}{32\pi} \int_{-1}^{1} \mathcal{A}(\alpha) d\cos\alpha, \quad a_j = 0\,(j > 0). \tag{6.34}$$

For a spin-less 2 → 2 elastic scattering process, the unitarity bound can be rephrased as

$$|\mathcal{A}| < 8\pi. \tag{6.35}$$

Owing to the Goldstone-boson equivalence theorem, the scattering of the longitudinal gauge bosons can be approximated by the pseudo-Goldstone boson scattering in the high-energy limit. Given the fact that the high energy scattering is dominated by the four-scalar contact interactions, we only need to evaluate the quartic or bi-quadratic terms. There are ten scalar fields in the TT scenario, namely, $\omega_i\,(i = 1 \text{ to } 3), \varphi_j\,(j = 1 \text{ to } 3)$, $G_k\,(k = 0 \text{ to } 2)$, and h_0. So there are 55 pair combinations and 1540 scattering channels. An additional symmetric factor $1/\sqrt{2}$ needs to be included for each pair of identical particles in the initial or final states. The unitarity bounds from scattering amplitude matrix $\mathbf{A_{55\times55}}$ are

$$\begin{aligned}
|\lambda_H| &< 8\pi, \quad |\lambda_{H11}| < 8\pi, \quad |\lambda_{H22}| < 8\pi, \\
|\lambda_3 - \frac{1}{2}\lambda_4| &< 8\pi, \quad |\lambda_3 + \frac{1}{2}\lambda_4| < 8\pi, \quad |\lambda_3 + 2\lambda_4| < 8\pi, \qquad (6.36) \\
|\lambda_1 + \lambda_2 - \sqrt{(\lambda_1-\lambda_2)^2 + \lambda_4^2}| &< 16\pi, \quad |\lambda_1 + \lambda_2 + \sqrt{(\lambda_1-\lambda_2)^2 + \lambda_4^2}| < 16\pi, \\
&|\text{Eigenvalues}[\mathcal{P}]| < 8\pi,
\end{aligned}$$

where

$$\mathcal{P} = \frac{1}{2}\begin{pmatrix} 5\lambda_1 & 3\lambda_3 + \lambda_4 & 2\sqrt{3}\lambda_{H11} \\ 3\lambda_3 + \lambda_4 & 5\lambda_2 & 2\sqrt{3}\lambda_{H22} \\ 2\sqrt{3}\lambda_{H11} & 2\sqrt{3}\lambda_{H22} & 6\lambda_H \end{pmatrix}. \qquad (6.37)$$

Similarly, for the ST case, there are a total of eight scalar fields and therefore 36 pair combinations. The unitarity bounds from scattering amplitude matrix $\mathbf{A_{36\times36}}$ are

$$|\lambda_H| < 8\pi, \quad |\lambda_{H11}| < 8\pi, \quad |\lambda_{H22}| < 8\pi, \qquad (6.38)$$

$$|\lambda_2| < 8\pi, \quad |\lambda_3| < 8\pi, \quad |\text{Eigenvalues}[\mathcal{P}']| < 8\pi, \qquad (6.39)$$

where

$$\mathcal{P}' = \frac{1}{2}\begin{pmatrix} 3\lambda_1 & 3\lambda_3 & 2\lambda_{H11} \\ \lambda_3 & 5\lambda_2 & 2\sqrt{3}\lambda_{H22} \\ 2\lambda_{H11} & 2\sqrt{3}\lambda_{H22} & 6\lambda_H \end{pmatrix}. \qquad (6.40)$$

6.2.3 Electroweak precision observables

Quantum corrections to the W boson mass [7] and the electroweak oblique parameters [190], from the mixing between SM Higgs and the dark massive eigenstates, can put constraints on the model parameters $\sin\theta$ and m_{h_2}. The bound from W boson mass constraint, which is shown by the gray shaded region in Fig. 22, turns out to be more stringent than that from the oblique parameters [7, 191]. The bound from oblique parameters are shown by the dashed brown line in Fig. 22 for comparison.

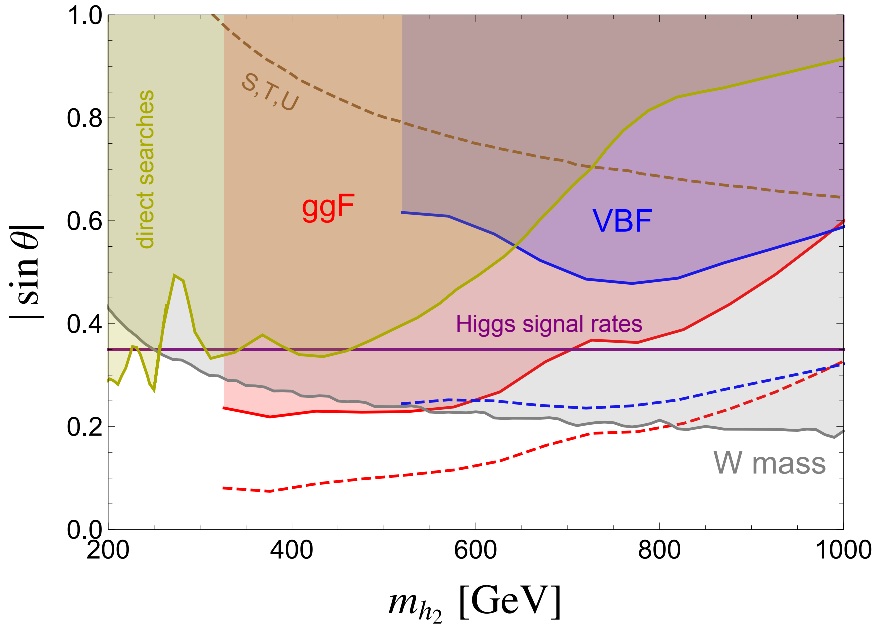

Figure 22: Upper bounds on the mixing angle $|\sin\theta|$ versus the heavy Higgs mass m_{h_2}. The horizontal purple line is from the Higgs signal rate measurement [4]. The yellow shaded region shows the upper bound from the direct searches for the heavy Higgs at LEP and LHC ($\sqrt{s} = 7$ TeV) [5]. The blue (red) shaded regions are excluded by the LHC di-boson searches with VBF (ggF) channels. The blue and red dashed lines correspond to the HL-LHC projection for these two channels, respectively [6]. The grey shaded area labelled by W mass, and the area above the brown dashed line labelled by S, T, U are excluded by the electroweak precision observables [7].

6.2.4 Higgs phenomenology

The scalar state h_0 mixes with φ_2 after the electroweak symmetry breaking. We identify that the lighter mass eigenstate h_1 is the observed SM-like Higgs boson with a mass of 125 GeV. The couplings of the physical scalars h_1 and h_2 to the SM particles are

$$\mathscr{L} \supset \frac{h_1 \cos\theta - h_2 \sin\theta}{v_h}(2m_W^2 W_\mu^+ W^{\mu-} + m_Z^2 Z_\mu Z^\mu - \sum_f m_f \bar{f} f). \tag{6.41}$$

The SM-like Higgs boson coupling to the SM particles are modified by a universal factor $\cos\theta$. The relevant Higgs self-interactions in the scalar sector are

$$\begin{aligned}
&\mathscr{L} \supset -\kappa_{111}h_1^3 - \kappa_{112}h_1^2h_2 - \kappa_{122}h_1h_2^2 - \kappa_{222}h_2^3, \qquad (6.42)\\
&\kappa_{111} = \frac{m_{h_1}^2(v_2\cos^3\theta + v_h\sin^3\theta)}{2v_2v_h}, \quad \kappa_{112} = -\frac{\sin 2\theta(2m_{h_1}^2 + m_{h_2}^2)(v_2\cos\theta - v_h\sin\theta)}{4v_2v_h},\\
&\kappa_{122} = \frac{\sin 2\theta(m_{h_1}^2 + 2m_{h_2}^2)(v_2\sin\theta + v_h\cos\theta)}{4v_2v_h}, \quad \kappa_{222} = \frac{m_{h_2}^2(v_h\cos^3\theta - v_2\sin^3\theta)}{2v_2v_h},
\end{aligned}$$

where $v_2 = m_{\tilde{W}^+}/\tilde{g}$. These couplings are important for the DM annihilation at the early Universe through the Higgs portal. The Higgs phenomenology at colliders is similar to that of one real singlet scalar extension of the SM, which has been extensively studied (see [192, 193, 194, 195] and references therein). The most relevant parameters are the mixing angle θ and the mass of the second Higgs m_{h_2} as shown in Eq. (6.41). The current bounds on $\sin\theta$ and m_{h_2} from the Higgs phenomenology are shown in Fig. 22. We will discuss the details of each bound in the following subsections.

6.2.4.1 Higgs invisible decay In the case that DM masses are larger than the half of the Higgs boson mass, the invisible decay of the Higgs boson is to the DR $\tilde{W}_2$ through the $\mathrm{SU(2)_D}$ charged scalar and gauge bosons loops as shown in Fig. 23. The decay width through dark gauge bosons can be calculated as

$$\Gamma_{\tilde{W}}(h_1 \to \tilde{W}_2\tilde{W}_2) = \frac{\tilde{\alpha}^3\sin^2\theta m_{h_1}^3}{64\pi^2 m_{\tilde{W}^+}^2}(2 + 3\tau^{-1} + 3\tau^{-1}(2-\tau^{-1})f(\tau))^2, \qquad (6.43)$$

where

$$\tilde{\alpha} = \frac{\tilde{g}^2}{4\pi}, \quad \tau = \frac{m_{h_1}^2}{4m_{\tilde{W}^+}^2}, \quad \text{and} \quad f(\tau) = \begin{cases} \arcsin^{-1}(\sqrt{\tau}) & \text{for } \tau \leq 1, \\ -\frac{1}{4}[\ln\frac{1+\sqrt{1-\tau^{-1}}}{1-\sqrt{1-\tau^{-1}}} - i\pi]^2 & \text{for } \tau > 1. \end{cases} \qquad (6.44)$$

In the limit $m_{h_1} \ll m_{\omega^+}$, the decay width through dark scalars can be calculated as

$$\Gamma_\omega(h_1 \to \tilde{W}_2\tilde{W}_2) = \frac{5\tilde{\alpha}^2c_1^2}{\pi^3 m_{h_1}}(\frac{m_{h_1}}{8\sqrt{3}m_{\omega^+}})^4, \qquad (6.45)$$

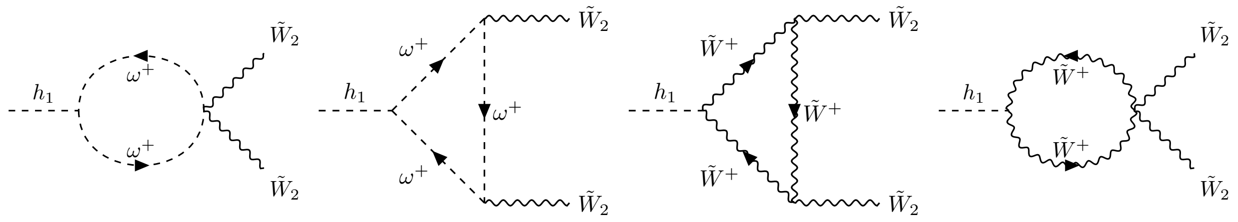

Figure 23: Feynman diagrams for the Higgs invisible decay to the dark radiation.

where c_1 is the coupling of vertex $h_1\omega^+\omega^-$ given in Eq. (6.18). The Higgs invisible decay width for our benchmark points shown in Table 9 are

$$\text{BM1:} \quad \Gamma(h_1 \to \tilde{W}_2\tilde{W}_2) = 3.1 \times 10^{-7}\ \text{MeV}, \tag{6.46}$$

$$\text{BM2:} \quad \Gamma(h_1 \to \tilde{W}_2\tilde{W}_2) = 2.1 \times 10^{-5}\ \text{MeV}, \tag{6.47}$$

which are dominated by the last two diagrams in Fig. 23. The Higgs invisible decay is highly suppressed by the small mixing angle, dark-sector gauge coupling, and the one-loop suppression. The branching fractions of the invisible Higgs decay are far beyond the reach of current and future experiments.

6.2.4.2 Higgs coupling measurements

Higgs couplings with SM particles have been measured with good precisions at the LHC. The Higgs signal strength is defined as [196]

$$\mu_{h_1} \equiv \frac{\sigma_{h_1}\ \text{BR}(h_1 \to \text{SM})}{\sigma_{h_1}^{\text{SM}}\ \text{BR}^{\text{SM}}(h_1 \to \text{SM})}, \tag{6.48}$$

where $\sigma_{h_1} = \cos^2\theta\sigma_{h_1}^{\text{SM}}$, $\text{BR}(h_1 \to \text{SM}) = \frac{\Gamma_{h_1}^{\text{SM}}\cos^2\theta}{\Gamma_{h_1}^{\text{SM}}\cos^2\theta+\Gamma_{h_1}^{\text{DS}}}$, and by definition $\text{BR}^{\text{SM}}(h_1 \to \text{SM}) \equiv 1$. Therefore, the signal strength can be written as

$$\mu_{h_1} = \frac{\Gamma_{h_1}^{\text{SM}}\cos^4\theta}{\Gamma_{h_1}^{\text{SM}}\cos^2\theta + \Gamma_{h_1}^{\text{DS}}}. \tag{6.49}$$

As we learned from the previous section, $\Gamma_{h_1}^{\text{DS}}$ are highly suppressed, as the SM-like Higgs h_1 can only decay to DR through one-loop diagrams in Fig. 23. The signal strength simply scales as $\cos^2\theta$. The bound on the mixing angle, from the Higgs couplings measurement by ATLAS [4], is $|\sin\theta| \lesssim 0.35$, which is shown by the purple line in Fig. 22.

Of special interest is the SM-like Higgs triple coupling κ_{111} as in Eq. (6.42) because of its sensitivity to the BSM new physics and its crucial role in EWPT. We write the derivation from the SM prediction as

$$\Delta\kappa_3 = \frac{\kappa_{111} - \kappa_{111}^{\rm SM}}{\kappa_{111}^{\rm SM}} = -1 + \cos^3\theta + \frac{v_h}{v_2}\sin^3\theta. \tag{6.50}$$

We depict the resultant deviation of $\Delta\kappa_3$ in the v_2-$\sin\theta$ plane in Fig. 24 by the gray solid lines. For most of the viable parameter space, the magnitude of $\Delta\kappa_3$ is less than 25%. We also mark the predictions of our benchmark points BM1 for about −10% by the red-cross and MB2 for about −2% by the blue-star, respectively. The achievable sensitivity to probe $\Delta\kappa_3$ in the future collider experiments has been extensively studied. While the HL-LHC will only have a moderate sensitivity to κ_3 [197, 198], future improvements are highly anticipated, reaching a 1σ sensitivity of 13% at a 1-TeV ILC [199] and 10% at CLIC [200], and 2σ sensitivity of 5% at FCC$_{hh}$/SPPC [201], 2% at a multi-TeV muon collider [202]. The precision measurement for κ_3 would provide important indirect test of the model as well as BSM theories in general.

6.2.4.3 Direct searches for the heavy Higgs boson

The heavy Higgs boson in the model, h_2, can interact with the SM particles via the mixing as shown in Eq. (6.13). The coupling strength is proportional to $\sin\theta$. The heavy Higgs searches at the high-energy colliders can put strong constraints in this scenario. Heavy Higgs h_2 mainly decay to heavy particles when they are kinematically allowed, such as $b\bar{b}$, top quarks, massive gauge bosons, and the dark gauge bosons. The branching fractions of the heavy Higgs decay versus m_{h_2} are shown in Fig. 25, where the other parameters are fixed as BM1 in Table 9 for illustration. The heavy Higgs decay channels are to di-bosons $WW + ZZ$ until the threshold for $\tilde{W}^+\tilde{W}^-$ is open, as shown in Fig. 25.

The LHC di-boson resonance search in gluon-gluon fusion (ggF) and vector boson fusion (VBF) [6] can put strong bounds on the mixing angle θ and the heavy Higgs mass m_{h_2}. We

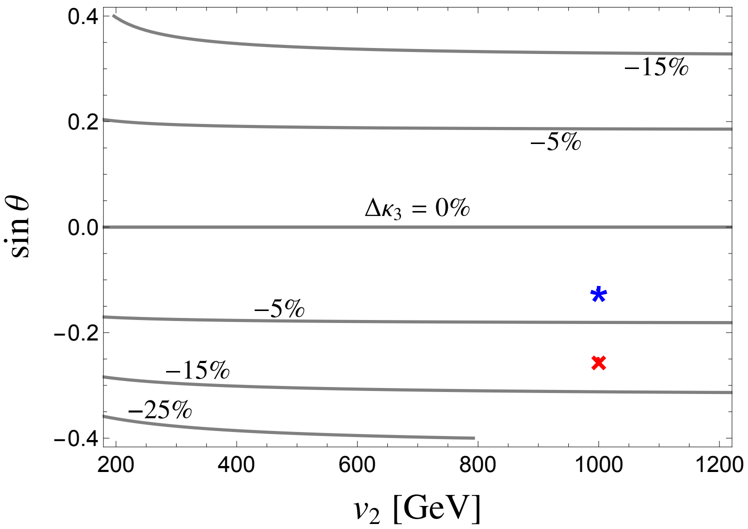

Figure 24: Predicted deviation of $\Delta\kappa_3$ in the v_2-$\sin\theta$ plane as defined in Eq. (6.50). The red-cross and blue-star indicate the predictions for our BM1 and BM2 points, respectively.

evaluate the resonance production rate as

$$\sigma(pp \to VV) = \sigma(pp \to h_2)\ \mathrm{BR}(h_2 \to VV). \tag{6.51}$$

The bounds on the plane in m_{h_2}-$\sin\theta$ with $v_2 = 1000$ GeV are shown by the red (ggF) and blue (VBF) shaded regions in Fig. 22. The dashed lines with the same color scheme are the projected limit from HL-LHC with 3 ab^{-1} integrated luminosity, obtained by rescaling the current bounds by the square root of luminosity ratio $\sqrt{3000/36.1}$. For the mass below 350 GeV, we adopted the bounds provided in Ref. [5] from a combination of various decay channels at LEP and LHC with $\sqrt{s} = 7$ TeV. The bounds are shown by the yellow shaded region.

6.3 Dark Radiation and Dark Matter Phenomenology

The dark sector in our model possesses rich phenomenology. There are two self-interacting vector DM candidates $\tilde{W}^{\pm}$. The massless state $\tilde{W}_2$ is the DR. In addition, there is one scalar

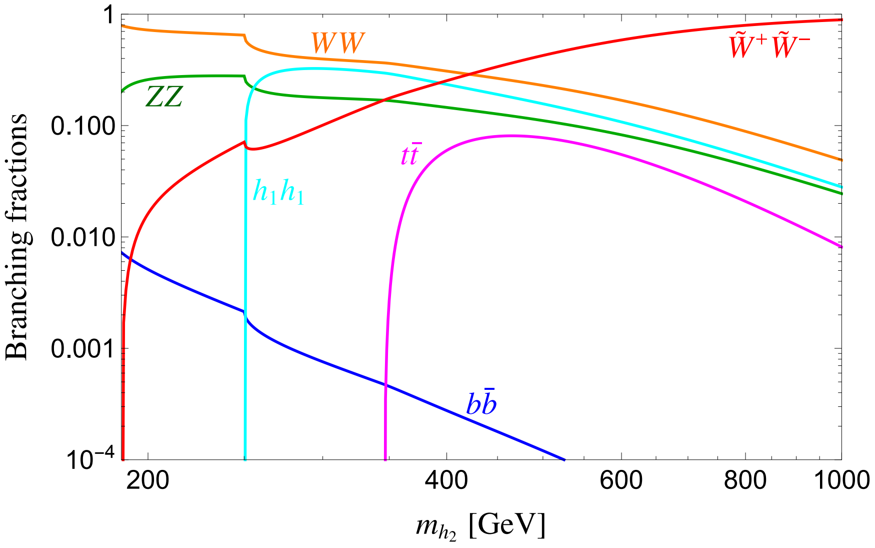

Figure 25: Branching fractions of heavy Higgs h_2 decay versus m_{h_2}. The other parameters are fixed as BM1 in Table 9.

DM ω in the ST scenario, or there are three self-interacting scalar DM candidates $\omega^\pm$ and ω_2 in the TT scenario. The DM interactions with SM particles are through the mixing between φ_2 and h_0. The relevant Lagrangian of DM-SM interactions are shown in Eq. (6.17). Due to the non-Abelian nature of the dark sector, there exist nontrivial self-interactions inside the dark sector among scalar DM, vector DM, and DR, which are from the dark gauge couplings and the scalar potential. For simplicity we decoupled the scalar DM by assuming the mass hierarchy to be $m_{\tilde{W}^+} \ll m_\omega$ in ST, or $m_{\tilde{W}^+} \ll m_{\omega^+} \lesssim m_{\omega_2}$ in TT.

6.3.1 Dark radiation

The massless DR $\tilde{W}_2$ associated with the unbroken $\mathrm{U(1)_D}$ can contribute to the energy density of the Universe, regulating the Universe expansion rate. In the radiation-dominated era, the expansion rate of the Universe depends on the relativistic energy density

$$\rho = g_*(T)\frac{\pi^2}{30}T^4, \tag{6.52}$$

where g_* is the total relativistic degrees of freedom defined as

$$g_*(T) \equiv \sum_{m_i<T} C_i g_i (\frac{T_i}{T})^4, \tag{6.53}$$

where the coefficients are C_i=1 (7/8) for bosons (fermions), and g_i is the internal degrees of freedom for particle i. $\tilde{W}_2$ can contributes to g_* and it is conventional to define this extra energy density by

$$\Delta N_{\text{eff}} \equiv \frac{\rho_{\tilde{W}_2}}{\rho_\nu} = \frac{8}{7}(\frac{\tilde{T}}{T_\nu})^4, \tag{6.54}$$

where $\tilde{T}$ is the dark sector's temperature, T_ν is the SM neutrinos' temperature. After neutrinos decouple from the thermal bath, the ratio $\tilde{T}/T_\nu$ is fixed as they evolve in the same way. We thus evaluate this temperature ratio at the epoch of neutrino decoupling. Before the DM decouples, the dark sector and visible sector are in thermal equilibrium, $\tilde{T}_{\text{dec},\chi} = T_{\text{dec},\chi}$. After decoupling of DM, the dark sector and visible sector lost thermal contact, the entropy is conserved in each sector separately. So we have [203]

$$\frac{g_{*s}^{\text{DS}}(\tilde{T}_{\text{dec},\nu})\tilde{T}^3_{\text{dec},\nu}}{g_{*s}^{\text{DS}}(\tilde{T}_{\text{dec},\chi})\tilde{T}^3_{\text{dec},\chi}} = \frac{g_{*s}^{\text{SM}}(T_{\text{dec},\nu})T^3_{\text{dec},\nu}}{g_{*s}^{\text{SM}}(T_{\text{dec},\chi})T^3_{\text{dec},\chi}}, \tag{6.55}$$

where g_{*s} is the relativistic degrees of freedom for entropy

$$g_{*s}(T) \equiv \sum_{m_i<T} C_i g_i (\frac{T_i}{T})^3. \tag{6.56}$$

At the DM decoupling, $T_{\text{dec},\chi} \ll m_\chi$. The only relativistic particle is the DR. So that $g_{*s}^{\text{DS}}(\tilde{T}_{\text{dec},\chi}) = g_{*s}^{\text{DS}}(\tilde{T}_{\text{dec},\nu}) = 2$. In the visible sector, $g_{*s}^{\text{SM}}(T_{\text{dec},\chi}) = 106.75$, $g_{*s}^{\text{SM}}(T_{\text{dec},\nu}) = 10.75$. Combining Eqs. (6.54) and (6.55), ΔN_{eff} can be evaluated as

$$\Delta N_{\text{eff}} = \frac{8}{7}(\frac{10.75}{106.75})^{4/3} \approx 0.054. \tag{6.57}$$

Currently, the strongest bounds on N_{eff} come from the Planck satellite [204, 205] which measured $N_{\text{eff}} = 2.99 \pm 0.17$ including baryon acoustic oscillation data. The projected limit of CMB Stage IV experiments is $\Delta N_{\text{eff}} = 0.03$ [206], which has sufficient sensitivity to explore this scenario.

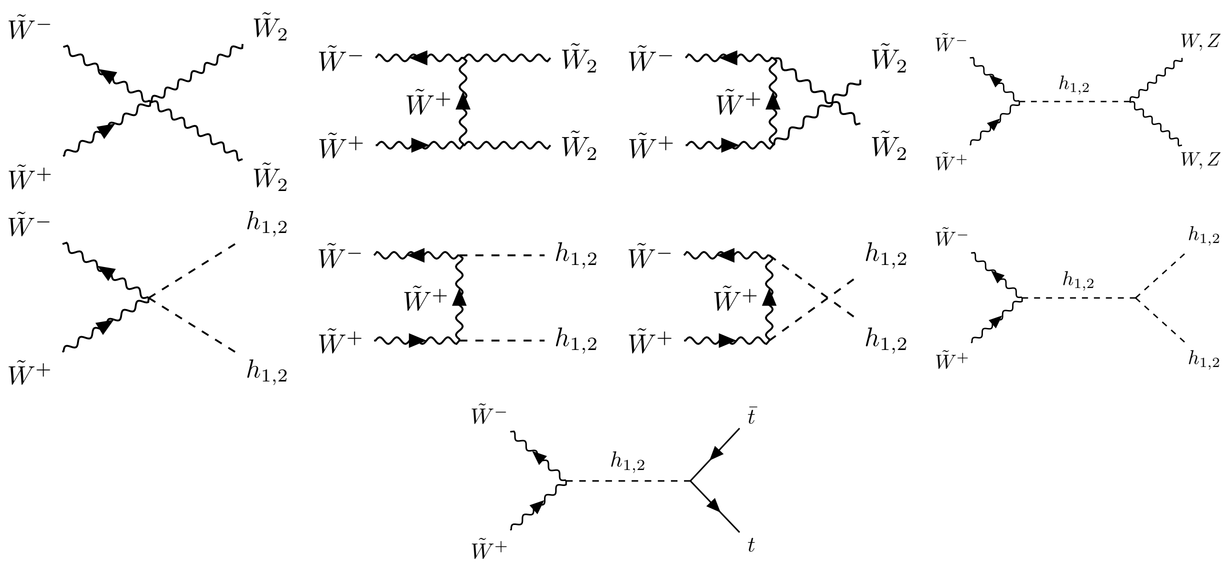

Figure 26: Representative Feynman diagrams for vector DM $\tilde{W}^+\tilde{W}^-$ pair annihilation.

6.3.2 Relic density

The observed value of the DM relic density $\Omega_{\text{obs}}h^2 \simeq 0.12$ inferred by the Planck collaboration from the analysis of Cosmic Microwave Background (CMB) [207]. The vector DM candidates $\tilde{W}^{\pm}$ and scalar DM candidates ω ($\omega^{\pm}$ and ω_2) in the ST (TT) model can account for the DM relic density we observed today.[2] By solving the Boltzmann equation in the standard freeze-out scenario, the relic density of our DM candidates can be estimated by [208]

$$\Omega_{\text{DM}}h^2 = 1.07 \times 10^9 \frac{x_f \ \text{GeV}^{-1}}{(g_{*S}/\sqrt{g_*})M_{pl}\langle\sigma v_{\text{rel}}\rangle}, \tag{6.58}$$

where $x_f \equiv m_\chi/T_f$, which can be estimated by

$$x_f = \ln\left[0.038\frac{g}{\sqrt{g_*}}M_{pl}m_\chi\langle\sigma v_{\text{rel}}\rangle\right] - \frac{1}{2}\ln\ln\left[0.038\frac{g}{\sqrt{g_*}}M_{pl}m_\chi\langle\sigma v_{\text{rel}}\rangle\right]. \tag{6.59}$$

Here g_* (g_{*S}) is the effective degree of freedom in energy density (entropy) at freeze-out defined in Eq. (6.53) ((6.56)). We evaluate the s-wave annihilation cross section at the

---

[2] An $SU(2)_{\text{D}}$ theory broken down to $U(1)_{\text{D}}$ by an adjoint scalar gives rise to dark magnetic monopoles, which may also contribute to the relic density calculation [178]. However, for our choices of triplet VEVs and $\tilde{g}$, it is unlikely that monopoles will contribute significantly to the observed relic density (see Fig. 3 of Ref. [178]). Hence, for simplicity we do not include monopoles in our consideration.

leading order [209]

$$\langle \sigma v_{\rm rel} \rangle = \frac{1}{32\pi} \frac{\sqrt{1-4M_W^2/s}}{m_\chi^2} |M_{\rm annihilation}(s)|^2. \tag{6.60}$$

The attractive longe-range force between the vector DM $\tilde{W}^\pm$ introduced by the exchange of massless DR $\tilde{W}_2$ can increase the annihilation cross section, which is the so-called Sommerfeld enhancement. The Sommerfeld factor is given by [137]

$$\hat{S} = \frac{\tilde{\alpha}\pi}{v} \frac{1}{1-\exp[-\tilde{\alpha}\pi/v]}. \tag{6.61}$$

When the DM freezes out, $x_f \approx 25$, $v = 1/\sqrt{x_f} \approx 0.2$. With $g \sim 0.3$, $\hat{S} - 1 \sim 6 \times 10^{-2}$. So, we can safely ignore the effects of the Sommerfeld enhancement in this work for the relic density calculation. We calculated the annihilation cross section of the process

$\tilde{W}^+\tilde{W}^- \to W^+W^-,\ ZZ,\ \bar{t}t,\ h_1h_1,\ h_1h_2,\ h_2h_2,\ \tilde{W}_2\tilde{W}_2,$

$\omega^+\omega^- \to W^+W^-,\ ZZ,\ \bar{t}t,\ h_1h_1,\ h_1h_2,\ h_2h_2,\ \tilde{W}^+\tilde{W}^-, \tilde{W}_2\tilde{W}_2,$

$\omega_2\omega_2 \to W^+W^-,\ ZZ,\ \bar{t}t,\ h_1h_1,\ h_1h_2,\ h_2h_2,\ \tilde{W}^+\tilde{W}^-,\ \omega^+\omega^-.$

The representative Feynman diagrams for the vector DM $\tilde{W}^\pm$ pair annihilation are shown in Fig. 26. Scalar DM pair annihilations have similar diagrams.

Since we choose $m_{\omega^\pm}, m_{\omega_2} \gg m_{\tilde{W}^\pm}$, scalar DM candidates $\omega^\pm$ and ω_2 will be decoupled much earlier than vector DM $\tilde{W}^\pm$. The scalar DM states in the TT model annihilate dominantly into the vector DM $\tilde{W}^\pm$. While, in the ST model, the scalar DM annihilation channel is dominated by $\omega\omega \to h_2h_2$ as it does not carry any charge. At the decoupling of $\omega^\pm$ and ω_2, $n_{\tilde{W}^\pm} = n^{\rm eq}_{\tilde{W}^\pm}$. Therefore, including the DM self-interacting processes can further reduce the relic density of $\omega^\pm$ and ω_2. The number densities of $\omega^\pm$ and ω_2 are much less than $\tilde{W}^\pm$ at the decoupling of $\tilde{W}^\pm$. Therefore, we ignore the processes $\omega^+\omega^- \to \tilde{W}^+\tilde{W}^-$ and $\omega_2\omega_2 \to \tilde{W}^+\tilde{W}^-$ when we evaluate the number density of $\tilde{W}^\pm$. The vector DM mainly annihilates into the DR $\tilde{W}_2$ except in the resonance region $m_{\tilde{W}^\pm} \approx m_{h_2}/2$. The branching fractions to a specific final state from an initial state annihilation of both vector and scalar DM pairs are shown in Fig. 27.

The relic densities for some benchmark points are shown in the left panel of Fig. 28 as functions of heavy Higgs mass m_{h_2}. The vector DM relic density is highly suppressed at the

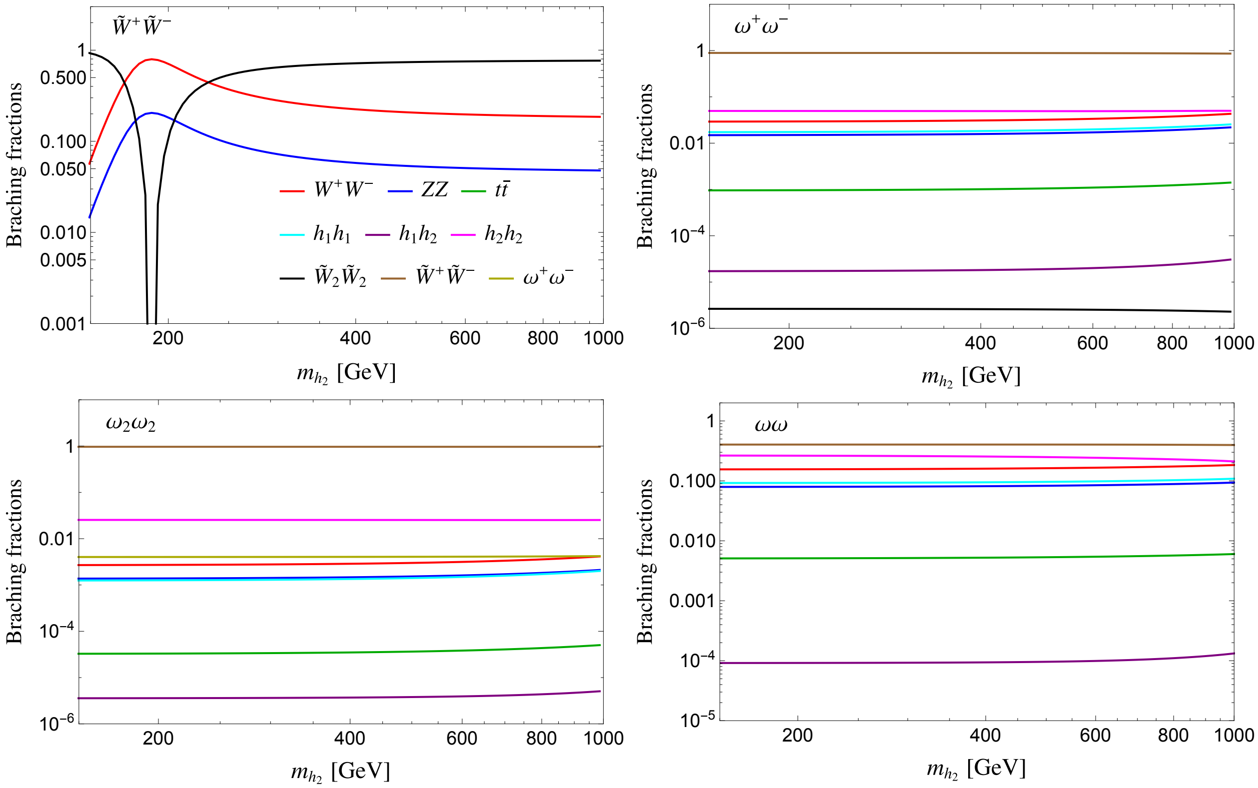

Figure 27: Annihilation branching fractions of vector DM pair $\tilde{W}^+\tilde{W}^-$ (upper left), scalar DM pair $\omega^+\omega^-$ (upper right), $\omega_2\omega_2$ (lower left), and $\omega\omega$ (lower right). The other parameters are fixed as BM1 in Table 9.

resonance region. The scalar DM contributions to the total relic density are negligible. The dashed green lines are the scalar DM from the ST scenario, which mostly overlaps with $\omega^\pm$ as they have the same masses and similar annihilation channel as shown in Fig. 27. We require the DM not to be overly produced $\Omega_{\rm DM}h^2 \lesssim 0.12$. The dashed horizontal line in the left panel of Fig. 28 indicates the current relic density bound from PLANCK. In the resonance region $m_{\tilde{W}^\pm} \approx m_{h_2}/2$, the annihilation cross sections via an s-channel h_2 are enhanced, and the relic density is much less than the observed value. Away from the resonant region, $\tilde{W}^\pm$ could be adequate as a CDM candidate.

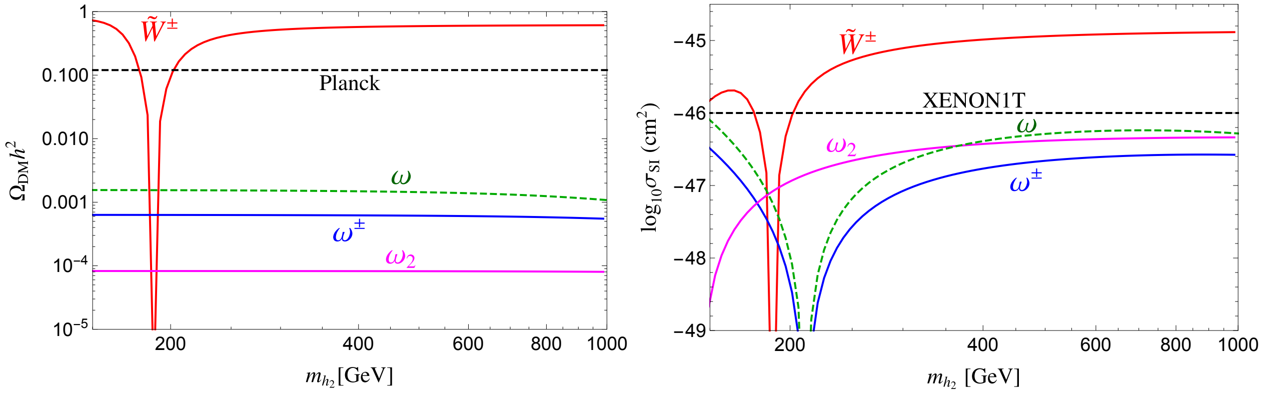

Figure 28: DM relic densities $\Omega_{\rm DM}h^2$ (left) and the SI cross section $\sigma_{\rm SI}$ (right) for the vector and scalar DM candidates versus m_{h_2}. The dashed green lines are the scalar DM ω from the ST model. The solid blue and magenta lines are the scalar DM $\omega^{\pm}, \omega_2$ from the TT model, respectively. The solid red lines are from the vector DM $\tilde{W}^{\pm}$. The dashed horizontal lines indicate the current bounds from PLANCK (left) and XERNON1T (right), respectively. The other parameters are fixed as BM1 in Table 9.

6.3.3 Direct detection

The null results of direct detection experiments can set strong bounds on our dark sector parameter space. In this model, the DM candidates χ couple to the dark scalar φ_2. φ_2 couples to the SM particles through the Higgs portal. The dominant contributions to the spin-independent (SI) scattering cross section come from the exchange of the SM-like Higgs bosons h_1 and the heavy Higgs bosons h_2. The effective interactions of DM ($\chi = \tilde{W}^{\pm}, \omega^{\pm}, \omega_2, \omega$) with light quarks and gluons are given as [28]

$$\mathscr{L}^{\rm eff}_{q,g} = \sum_{q=u,d,s} f^{\chi}_q m_q \chi\chi\bar{q}q + f^{\chi}_G \chi\chi \frac{\alpha_s}{\pi} G^{a\mu\nu} G^a_{\mu\nu}, \tag{6.62}$$

where $G^a_{\mu\nu}$ is the field strength tensor of gluon and α_s is the strong coupling constant. f_q^χ is the effective couplings between DM χ and light quarks, which, in our model, are

$$\begin{aligned} f_q^{\tilde{W}^\pm} &= \tilde{g}^2 \frac{v_2}{v_h} \sin\theta\cos\theta(\frac{1}{m_{h_2}^2} - \frac{1}{m_{h_1}^2}), & (6.63)\\ f_q^{\omega^\pm} &= \frac{1}{v_h}(\frac{c_2\cos\theta}{m_{h_2}^2} - \frac{c_1\sin\theta}{m_{h_1}^2}), & (6.64)\\ f_q^{\omega_2} &= \frac{1}{v_h}(\frac{d_2\cos\theta}{m_{h_2}^2} - \frac{d_1\sin\theta}{m_{h_1}^2}). & (6.65)\end{aligned}$$

The coupling between DM and gluon comes from the effective coupling after integrating-out of heavy quarks

$$f_G^\chi = -\frac{1}{12}\sum_{Q=c,b,t} f_Q^\chi = -\frac{1}{4} f_q^\chi. \tag{6.66}$$

The interactions between DM and nucleon can be evaluated by using the nucleon matrix elements

$$\langle N|m_q\bar{q}q|N\rangle \equiv f_{Tq}^N m_N,\ \langle N|\frac{\alpha_s}{\pi}GG|N\rangle = -\frac{8}{9}m_N f_{TG}^N, \tag{6.67}$$

where f_{Tq}^N and f_{TG}^N are the mass-fraction parameters of the quarks and the gluon in the nucleon N,respectively. In our numerical calculations, we adopt $f_{Td}^p = 0.0191$, $f_{Tu}^p = 0.0153$, $f_{Ts}^p = 0.0447$, and $f_{TG}^p \equiv 1 - \sum_{q=u,d,s} f_{Tq}^p = 0.925$ [210]. The effective interactions of DM and nucleon can be expressed as

$$\mathscr{L}_N^{\text{eff}} = f_N^\chi \chi\chi\bar{N}N, \tag{6.68}$$

where the effective coupling f_N can be calculated by

$$f_N^\chi = m_N(\sum_{q=u,d,s} f_{Tq}^N f_q^\chi - \frac{8}{9} f_{TG}^N f_G^\chi). \tag{6.69}$$

The SI cross section of DM with nucleon can be calculated with [211]

$$\hat{\sigma}_{\text{SI}}^\chi = \frac{1}{\pi}\left(\frac{m_N}{m_\chi + m_N}\right)^2 (f_N^\chi)^2, \tag{6.70}$$

where m_N is the mass of nucleon and m_χ is the mass of DM candidate. To derive the experimental upper bound, we scale the SI cross sections with the density fractions

$$\sigma_{\text{SI}} = \left(\frac{\Omega_\chi h^2}{\Omega_{\text{obs}} h^2}\right)\hat{\sigma}_{\text{SI}}^\chi. \tag{6.71}$$

The XENON1T [30] and the SI cross sections are shown in the right panel of Fig. 28. In the resonance region $m_{\tilde{W}^\pm} \approx m_{h_2}/2$, the relic density is much less than the observed value, hence the direct detection bound can be easily evaded. Away from the resonant region however, $\tilde{W}^\pm$ could lead to a detectable cross section.

6.3.4 Dark matter self-interactions

The collision-less and cold DM can successfully describe the large scale structure of the Universe [212]. There are, however, some challenges for the cold and collision-less DM model at the small-scale (see Ref. [213] for a review). Rather than going to the warm DM scenario, there are generally two mechanisms which can alleviate the CDM challenges: (i) DM-DR interactions [36]; (ii) DM self-interactions [35].

In our model, the leading DM self-interaction is mediated by the massless DR. This scenario has been studied carefully in Ref. [214, 215]. The most relevant DM self-interactions are through t/u-channel mediated by the massless DR. The differential cross section of t- and u-channel in the center-of-mass (CM) frame is

$$\frac{d\sigma}{d\Omega} \propto \frac{\tilde{\alpha}^2}{16 m_{\tilde{W}^\pm}^2 v_r^4 \sin^4 \frac{\theta_{\rm cm}}{2}}, \tag{6.72}$$

leading to $\sigma \sim \pi\tilde{\alpha}^2/(m_{\tilde{W}^\pm}^2 v_r^4)$, where v_r is the relative velocity of the two colliding DM particles in the CM frame. The cross sections of the DM self-interactions quickly drop at higher velocities to evade impacts on the large scale structure, hence, maintain the effective collision-less descriptions. From the observed ellipticity of galactic DM halos [214, 215], a bound on the dark gauge couplings can be estimated as

$$(\frac{\tilde{g}}{0.1})^4(\frac{200 \text{ GeV}}{m_{\tilde{W}^\pm}})^3 \lesssim 50. \tag{6.73}$$

This constraint can potentially be overly strong and depends on the assumptions of DM relic density [215]. The constraints from the Bullet Cluster are much weaker [214, 215]. To solve the small-scale structure problems, we need $\sigma/m_{\tilde{W}} \sim 0.1 - 10 \text{ cm}^2/g$ at dwarf galaxies [216, 178], which gives

$$(\frac{\tilde{g}}{0.1})^4(\frac{200 \text{ GeV}}{m_{\tilde{W}^\pm}})^3 \sim 0.01 - 1. \tag{6.74}$$

DM can also interact with themselves through four-gauge-boson contact and s-channel interactions. The cross sections of contact interactions are $\sigma \sim \pi\tilde{\alpha}^2/m^2_{\tilde{W}^\pm}$; the s-channel cross sections are $\sigma \sim \pi\tilde{\alpha}^2 v_r^4/m^2_{\tilde{W}^\pm}$. Therefore they are irrelevant compared to the contributions of u/t-channel for the DM self-interactions for low-velocity systems such as dwarf galaxies. It is evident from the discussion above that the DM-DR interaction cross sections are suppressed by the DM mass. So, for the parameter space of our interest in this work, DM and DR are decoupled very early and cannot significantly change the small-scale structures of the Universe. Before closing the DM section, we would like to mention that we will not study the indirect detection aspects of this model due to the complication with the Sommerfeld enhancement in low-velocity systems.

6.4 Electroweak Phase Transition and Gravitational Waves

6.4.1 Electroweak phase transition

The dynamics of the phase transition is determined by the effective potential at the finite temperature (see, *e.g.*, Ref. [217] for a recent review), which can be calculated perturbatively or non-perturbatively on the lattice with dimensional reduction [218, 219, 220]. While the latter approach provides a gauge independent result and is free of the infrared problem [221], it is computationally expensive and so far has been adopted for only a few models with a simple extended Higgs sector [222, 223, 224, 225, 226, 227]. Therefore the perturbative method was predominant in the literature on the analysis of a thermal phase transition. In the standard perturbative approach, the effective potential receives contributions from the tree-level potential, the one-loop Coleman-Weinberg correction and its finite-temperature counterpart, as well as Daisy resummations, which together leads to a gauge dependent result (see, *e.g.*, Refs. [228, 229] for a study of the uncertainties with this approach). A gauge independent result nevertheless can still be obtained if only the leading order thermal correction at the high temperature is kept [230]. This also makes an analytical understanding of the otherwise complicated effective potential possible and can better guide the exploration of the phase history. Thus we follow this gauge independent perturbative approach. The finite temperature effective potential can thus be written in the following simplified form

$$V^{(1)}(T) = V_{\rm tree} + \Delta V^{(1)}(T), \tag{6.75}$$

where $V_{\rm tree}$ is given in Eq (6.23) and $\Delta V^{(1)}(T)$ is the leading thermal correction given by [231]

$$\Delta V^{(1)}(T) = \frac{T^4}{2\pi^2}\left\{\sum_b n_b J_B[\frac{m_b^2(\phi_i)}{T^2}] - \sum_f n_f J_F[\frac{m_f^2(\phi_i)}{T^2}]\right\}, \tag{6.76}$$

where $\phi_i (i = 1, 2, 3)$ indicates any of the three fields. Here the functions J_B and J_F have the following high-temperature limit, *i.e.,* for $y \equiv m/T \ll 1$,

$$J_B(y^2) \simeq \frac{-\pi^4}{45} + \frac{\pi^2}{12}y^2 - \frac{\pi}{6}y^3 + O(y^4), \quad J_F(y^2) \simeq \frac{7\pi^4}{360} - \frac{\pi^2}{24}y^2 + O(y^4). \tag{6.77}$$

Therefore at order y^2, the thermal corrections reduce to a simpler polynomial form

$$\Delta V^{(1)}(T) = \frac{T^2}{24}[n_s {\rm Tr}(\mathbf{M_S}^2) + n_{\tilde{W}} {\rm Tr}(\mathbf{M_V}^2) + n_W m_W^2 + n_Z m_Z^2 + \frac{n_t}{2} m_t^2], \tag{6.78}$$

where $\mathbf{M_S}$ and $\mathbf{M_V}$ are the field-dependent masses for scalar and dark gauge bosons, which are given in Appendix D. From the finite temperature effective potential, the details of the phase transition can be studied. In particular, one can determine the thermal mass terms. For the TT model, they are given by

$$\begin{aligned} m_H^2(T) &= m_H^2 + \frac{T^2}{16}(g_1^2 + 3g_2^2 + 2(2\lambda_H + \lambda_{H11} + \lambda_{H22} + 2y_t^2)), & (6.79)\\ m_{11}^2(T) &= m_{11}^2 + \frac{T^2}{24}(12\tilde{g}^2 + 5\lambda_1 + 3\lambda_3 + \lambda_4 + 4\lambda_{H11}), & (6.80)\\ m_{22}^2(T) &= m_{22}^2 + \frac{T^2}{24}(12\tilde{g}^2 + 5\lambda_1 + 3\lambda_3 + \lambda_4 + 4\lambda_{H22}). & (6.81)\end{aligned}$$

In the ST model, the thermal mass terms are

$$\begin{aligned} m_H^2(T) &= m_H^2 + \frac{T^2}{16}(g_1^2 + 3g_2^2 + 2(2\lambda_H + \frac{1}{3}\lambda_{H11} + \lambda_{H22} + 2y_t^2)), & (6.82)\\ m_{11}^2(T) &= m_{11}^2 + \frac{T^2}{24}(3\lambda_1 + 3\lambda_3 + 4\lambda_{H11}), & (6.83)\\ m_{22}^2(T) &= m_{22}^2 + \frac{T^2}{24}(12\tilde{g}^2 + 5\lambda_1 + 3\lambda_3 + 4\lambda_{H22}). & (6.84)\end{aligned}$$

Extrema Type	h_0	ω_3 or ω	φ_2	potential value $V_{\min}$	stableness
Type-1	0	0	0	0	condition (E.1)
Type-2	v_h	0	0	$-\frac{m_H^4}{2\lambda_H}$	condition (E.2)
Type-3	0	v_1	0	$-\frac{m_{11}^4}{2\lambda_1}$	condition (E.3)
Type-4	0	0	v_2	$-\frac{m_{22}^4}{2\lambda_2}$	condition (E.4)
Type-5	v_h	v_1	0	$-\frac{\lambda_H m_{11}^4 - 2\lambda_{H11} m_{11}^2 m_H^2 + \lambda_1 m_H^4}{2\lambda_1\lambda_H - 2\lambda_{H11}^2}$	condition (E.5)
Type-6	0	v_1	v_2	$-\frac{\lambda_1 m_{22}^4 - 2\lambda_3 m_{11}^2 m_{22}^2 + \lambda_2 m_{11}^4}{2\lambda_1\lambda_2 - 2\lambda_3^2}$	condition (E.6)
Type-7	v_h	0	v_2	$-\frac{\lambda_H m_{22}^4 - 2\lambda_{H22} m_{22}^2 m_H^2 + \lambda_2 m_H^4}{2\lambda_2\lambda_H - 2\lambda_{H22}^2}$	condition (E.7)
Type-8	v_h	v_1	v_2	see details in Ref. [232]	Ref. [232]

Table 10: Eight possible types of stable vacuum extrema in the three VEVs scenario.

Even though those two scenarios have the same zero-temperature potential in Eq. (6.23), the mass parameters evolve differently with temperature as shown in Eqs. (6.79) to (6.84). The parameter space for FOPT in those two scenarios is not the same, though the phase transition pattern should not be qualitatively different. For the rest of this chapter, we will focus on the two BMs in Table 9 in the TT scenario as an illustration for the phase transition and GW generation. Given the three possible non-zero VEVs (v_h, v_1, v_2), there are eight combinations of possible extrema. Those and their stable conditions are listed in Appendix B and summarized in Table 10. With the desirable features from the extra DR, we require that at $T = 0$, the stable vacuum be in Type-7: $(v_h, 0, v_2)$. From the scanning, we found mainly two possible paths of the phase transitions to achieve this pattern

$$\text{two-step: } (v_h, v_1, v_2): \quad (0,0,0) \;\; \rightarrow (0, v_1, 0) \Rightarrow (v_h, 0, v_2), \tag{6.85}$$

$$\text{three-step: } (v_h, v_1, v_2): \quad (0,0,0) \;\; \rightarrow (0, v_1, 0) \Rightarrow (0, 0, v_2) \rightarrow (v_h, 0, v_2), \tag{6.86}$$

where "⇒" indicates a first-order phase transition and "→" for a continuous transition.[3]

---

[3] See a remark on this in Appendix F.

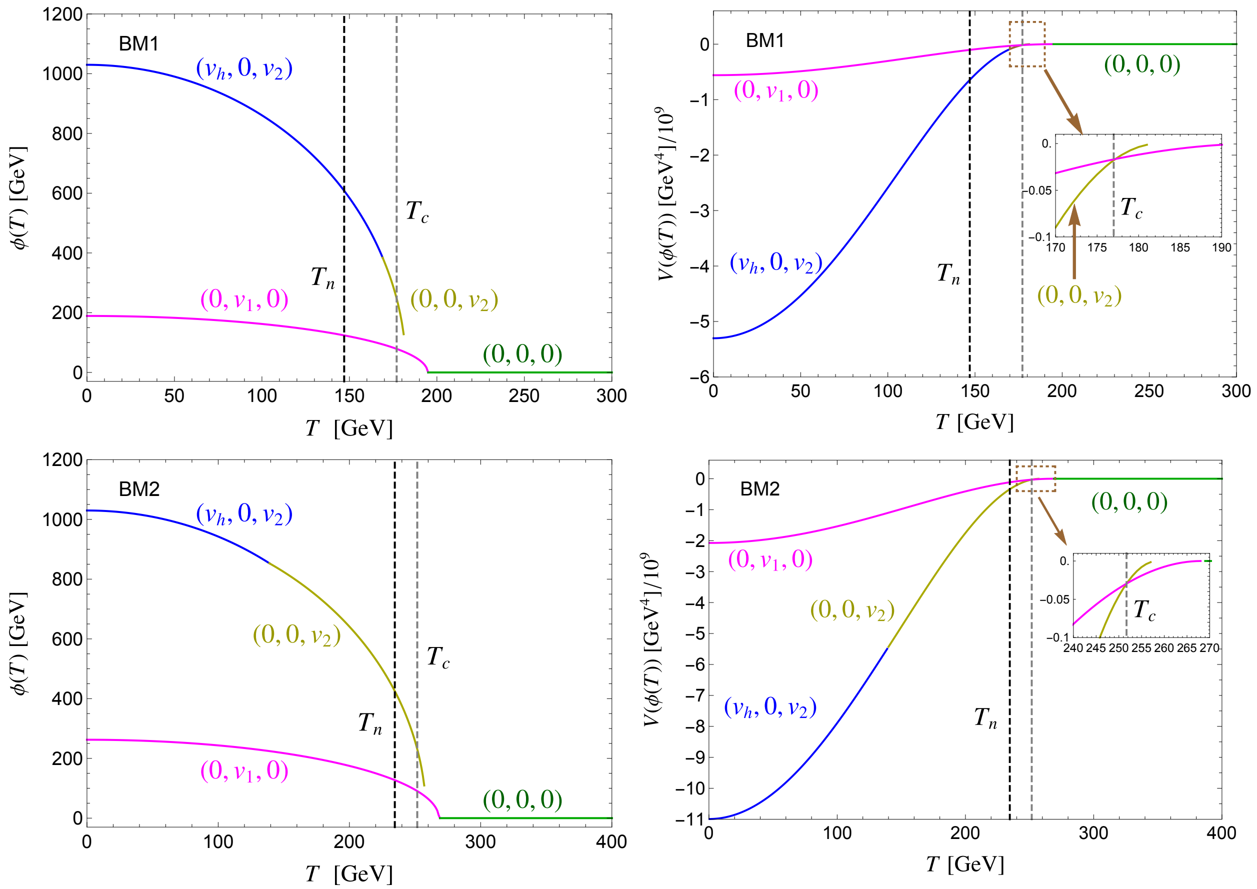

Figure 29: The evolution of the vacuum ($\phi \equiv \sqrt{v_h^2 + v_1^2 + v_2^2}$, left) as a function of the temperature T, and their corresponding potential values (right) are shown for BM1 (upper panels) and BM2 (lower panels). Here the critical and nucleation temperatures are denoted by the dashed vertical lines, respectively.

The two-step transition as in Eq. (6.85) can yield an electroweak FOPT [233], while the second path in Eq. (6.86) would not lead to an electroweak FOPT and can wash out any previously existing baryon asymmetry. To give a clearer picture of the above transitions, we illustrate the vacuum evolution in detail for the case of BM1 as defined in Table 9. In this case, the phase transition is a two-step process as shown in Eq. (6.85). The evolution of the vacuum and the corresponding potential values in BM1 are shown in the upper panel of Fig. 29. We see that at high temperatures, the stable vacuum is in a symmetric phase of Type-1: $(0,0,0)$. At $T \approx 200$ GeV, the field Φ_1 develops a VEV and the stable phase becomes of Type-3: $(0,v_1,0)$ through a continuous transition, where the order parameter, the VEV v_1, undergoes a continuous change. As the temperature further decreases, another minimum appears via Φ_2 at $(0,0,v_2)$, which eventually evolves into a minimum of Type-7 $(v_h,0,v_2)$ continuously. At $T = T_c$, corresponding to the right of the vertical dashed line in the left panel of Fig. 29, these two types of vacua $(0,v_1,0)$ and $(0,0,v_2)$ are degenerate, and are separated by a barrier, characteristic for a FOPT. At $T < T_c$, the initially stable vacuum at $(0,v_1,0)$ now becomes metastable while the phase corresponding to $(0,0,v_2)$ becomes energetically preferable, and the Universe becomes supercooled as T decreases. During the coexistence of these two phases, while the probability for the Universe to make a transition from the former to the latter becomes increasingly higher, it remains significantly small during this period. The temperature at which the phase transition happens can be quantified by the temperature when there is about one bubble per Hubble volume, and is called the nucleation temperature T_n, corresponding to the left of the vertical dashed line in Fig. 29. As T decreases towards T_n, the minimum at $(0,0,v_2)$ evolves into $(v_h,0,v_2)$. At $T \approx T_n$, the transition then proceeds through the formation of bubbles, with the vacuum inside being the more stable one $(v_h,0,v_2)$, and that outside the metastable one $(0,v_1,0)$. Thus the VEV changes non-continuously. The BM2 has a three-step phase transition shown in Eq. (6.86) and the lower panels of Fig. 29. It is similar to BM1 but different in that it has a prolonged phase at $(0,0,v_2)$ coexisting with the metastable $(0,v_1,0)$. The tunneling probability is thus high enough for a FOPT from $(0,v_1,0)$ to $(0,0,v_2)$ before the latter evolves into $(v_h,0,v_2)$. After this step, the vacuum at $(0,0,v_2)$ makes a further continuous electroweak transition to $(v_h,0,v_2)$. Further description of the process is provided in an Appendix F.

6.4.2 Gravitational waves

From studies of the above phase transition and its evolution at different temperatures, one can determine a set of portal parameters that determine the resulting GW signals [234]

$$T_n, \quad \alpha, \quad \beta/H_n, \quad v_w, \tag{6.87}$$

where T_n, as introduced previously, is the nucleation temperature denoting roughly the time for the onset of phase transition when there is one bubble per Hubble volume; α is a dimensionless quantity characterizing the energy fraction released from the phase transition in the unit of the total radiation energy density at T_n; β is roughly the inverse time duration of the phase transition determining the peak frequency of the GWs and H_n is the Hubble rate H at T_n; v_w is the wall velocity.

The calculations start with the determination of the tunneling probability per unit time per unit volume given by [235]

$$\Gamma(T) \simeq T^4 \left(\frac{S_3}{2\pi T}\right)^{3/2} e^{-S_3/T}, \tag{6.88}$$

where S_3 is the three-dimensional Euclidean action corresponding to the critical bubble:

$$S_3 = \int_0^\infty dr\ r^2 \left[\frac{1}{2}(\frac{d\phi(r)}{dr})^2 + V(\phi, T)\right], \tag{6.89}$$

with the scalar field minimizing the action and corresponding to the solution of the following equation of motion:

$$\frac{d^2\phi}{dr^2} + \frac{2}{r}\frac{d\phi}{dr} = \frac{dV(\phi, T)}{dr}, \tag{6.90}$$

subjected to the bounce boundary conditions

$$\lim_{r\to\infty} \phi(r) = 0, \quad \left.\frac{d\phi}{dr}\right|_{r=0} = 0. \tag{6.91}$$

In this work, we employ the **CosmoTransitions** [236] to solve the above bounce equation and thus compute the Euclidean action S_3. From the nucleation rate, the nucleation temperature is usually determined by solving the following equation,[4]

$$\int_{T_n}^\infty \frac{dT}{T}\frac{\Gamma(T)}{H(T)^4} = 1, \tag{6.92}$$

which says that there is about one bubble in a Hubble volume. A rough estimation of nucleation temperature T_n is usually obtained using the condition $S_3(T_n)/T_n = 140$ [238]. One can further calculate the parameter β where

$$\beta = H_* T_* \left.\frac{d(S_3/T)}{dT}\right|_{T_*}, \tag{6.93}$$

---

[4] It can be more precisely determined by directly calculating the number of bubbles in a generic expanding Universe as shown in Ref. [237].

where T_* is the GW generation temperature and is approximately equal to the nucleation temperature T_n. Similar to the definition of H_n, H_* is the Hubble rate H at T_*. The dimension of β is hertz and it is related to the mean bubble separation at the phase transition(see, e.g., [239, 237] for the derivation in Minkowski and FLRW spacetimes), which in turn gives the typical scale for GW production and thus its peak frequency. Moreover, α is the vacuum energy released from the EWPT normalized by the total radiation energy density

$$\alpha = \frac{\rho_{\text{vac}}}{\rho^*_{\text{rad}}} = \frac{1}{\rho^*_{\text{rad}}}\left[T\frac{\partial \Delta V(T)}{\partial T} - \Delta V(T)\right]\Big|_{T_*}, \tag{6.94}$$

where $\Delta V(T) = V_{\text{low}}(T) - V_{\text{high}}(T)$ is the difference between lower and higher phases, and $\rho^*_{\text{rad}} = g_*\pi^2 T^4/30$, g_* is the relativistic degrees of freedom at $T = T_*$. For a phase transition in a thermal plasma, as is considered here, the energy released goes in part into the kinetic energy of the plasma, with energy fraction κ_v, which sources gravitational waves, and into the heat of the plasma. The flow can also go turbulent, with energy fraction κ_{turb}, which becomes another source for GW production. A fraction of released energy can also go into the gradient of the scalar fields, which however is believed to be of negligible fraction [240] and we will not consider it here.

With these portal parameters, we are ready to calculate the GW energy density spectrum. The GW from a FOPT, as in most cosmic processes, is a stochastic background and can be searched for using the cross correlation method − see recent reviews on theories [234, 241, 242] and on detection methods [243, 244]. It is now generally accepted that there are mainly three sources for GW production during a cosmological FOPT: bubble wall collisions, sound waves, and magnetohydrodynamic (MHD) turbulence. For bubble collisions, the GW is sourced by the stress energy located at the wall and can be understood very well both analytically [245] and numerically [246] under the envelope approximation [247, 248, 249], where the wall is assumed to be thin and contribution from the overlapped regions is neglected. There has also been recent progress for simulations going beyond the envelope approximation [250, 251, 252]. However, for a phase transition proceeding in a thermal plasma, it is believed to be of negligible contribution [240]. A significant fraction of the energy released from the phase transition goes to the kinetic energy of the plasma, while the rest heats up the plasma. The kinetic energy of the plasma corresponds to the velocity perturbations of the plasma, which are sound waves in a medium consisting of relativistic particles. This relatively long-living acoustic production of GW is generally accepted to be the dominant one. GW spectrum from this source typically relies on large scale lattice simulations [253, 254, 255, 256]. However, an analytical modeling reproduces the spectra from simulations reasonably well based on the sound shell model [257, 239] (see Ref. [237] for the generalization to an expanding Universe), which assumes the plasma velocity field is a linear superposition of the sound shells from all bubbles. The fully ionized fluid can go turbulent for a sufficiently large Reynolds number and corresponds to the third source [253, 254]. We will thus include only the contributions from the sound waves and the MHD turbulence, with the present dimensionless GW energy fraction spectrum given by

$$\Omega_{\mathrm{GW}} h^2 \simeq \Omega_{\mathrm{sw}} h^2 + \Omega_{\mathrm{turb}} h^2, \tag{6.95}$$

where $h \approx 0.673$, the Hubble rate today H_0 in unit of 100 $\mathrm{kms^{-1}Mpc^{-1}}$. The sound wave's contribution is [258, 234]

$$\Omega_{\mathrm{sw}} h^2 = 2.65 \times 10^{-6} \left(\frac{H_*}{\beta}\right) \left(\frac{\kappa_v \alpha}{1+\alpha}\right)^2 \left(\frac{100}{g_s}\right)^{\frac{1}{3}} v_w \left(\frac{f}{f_{\mathrm{sw}}}\right)^3 \left[\frac{7}{4+3(f/f_{\mathrm{sw}})^2}\right]^{\frac{7}{2}} \times \Upsilon(\tau_{\mathrm{sw}}). \tag{6.96}$$

Here g_s is the relativistic degrees of freedom for entropy; T_* is the temperature right after GW production stops; f_{sw} is the present peak frequency:

$$f_{\mathrm{sw}} = 1.9 \times 10^{-2}\ \mathrm{mHz} \frac{1}{v_w} \left(\frac{\beta}{H_*}\right) \left(\frac{T_*}{100\ \mathrm{GeV}}\right) \left(\frac{g_s}{100}\right)^{\frac{1}{6}}. \tag{6.97}$$

Here, κ_v can be calculated from a semi-analytical hydrodynamic analysis of the velocity profile of a single bubble for given v_w and α [259]. This determination gives a good estimate of κ_v for relatively weak transitions, i.e., $\alpha \ll 1$. However, for strong transitions and for small v_w, a recent simulation found that κ_v as determined this way gives an overestimation [256]. Therefore care should be taken when calculating κ_v from the hydrodynamic analysis. Moreover, the multiplication factor Υ was only discovered in a recent study [237] (which was also adopted in Ref. [217]), and originates from the finite lifetime of the source.

$$\Upsilon = 1 - \frac{1}{\sqrt{1 + 2\tau_{\mathrm{sw}} H_*}}, \tag{6.98}$$

and the usually adopted spectrum corresponds to $\tau_{\rm sw} \to \infty$ for which Υ takes the asymptotic value 1. However, the lifetime of the sound waves is certainly finite which leads to a suppression of the spectrum. We note that before the discovery of Υ, a similar suppression factor $\min(1, \tau_{\rm sw} H_*)$ was adopted [260, 261, 262] based on a Minkowski derivation of the spectrum [254], which corresponds to the limit of Υ when $\tau_{\rm sw} H_* \ll 1$. The lifetime $\tau_{\rm sw}$ can be taken as the time scale when the turbulence develops, roughly given by [263, 255]:

$$\tau_{\rm sw} \sim \frac{R_*}{\bar{U}_f}, \tag{6.99}$$

where R_* is the mean bubble separation and is related to β through the relation $R_* = (8\pi)^{1/3} v_w/\beta$ for an exponential nucleation of the bubbles (see, *e.g.*, Ref. [239] for a derivation in Minkowski spacetime and see Ref. [237] for an analysis in the expanding Universe); $\bar{U}_f$ is the root-mean-squared fluid velocity and can be determined from the hydrodynamic analysis, with the result $\bar{U}_f = \sqrt{(}3\kappa_v \alpha/4)$ [239, 258].

The contributions from MHD turbulence can be modeled as [234]

$$\Omega_{\rm turb} h^2 = 3.35 \times 10^{-4} \left(\frac{H_*}{\beta}\right) \left(\frac{\kappa_{\rm turb}\alpha}{1+\alpha}\right)^{\frac{3}{2}} \left(\frac{100}{g_s}\right)^{\frac{1}{3}} v_w \frac{(f/f_{\rm turb})^3}{[1+(f/f_{\rm turb})]^{\frac{11}{3}}(1+8\pi f/H_0)}, \tag{6.100}$$

where $\kappa_{\rm turb}$ is the energy going to turbulence and $f_{\rm turb}$ is the present day peak frequency:

$$f_{\rm turb} = 2.7 \times 10^{-2}\ \text{mHz} \frac{1}{v_w} \left(\frac{\beta}{H_*}\right) \left(\frac{T_*}{100\ \text{GeV}}\right) \left(\frac{g_s}{100}\right)^{\frac{1}{6}}. \tag{6.101}$$

We note that the contribution from MHD is currently the least understood and might witness significant changes in the future. Indeed recent direct numerical simulations show significantly different result [264]. Also the value of $\kappa_{\rm turb}$ is unknown and we take tentatively $\kappa_{\rm turb} \approx (5 \sim 10)\% \kappa_v$ [254] . For both contributions, while in principle the wall velocity v_w can be calculated from micro-dynamics of particle interactions with the Higgs condensate, its precise value remains undetermined due to the theoretical uncertainties in the calculations. On the other hand, if baryon asymmetry were to be generated during the phase transition, then a subsonic value is needed. However a supersonic value of v_w might still be compatible with EWBG due to the outflowing fluid around the wall [265], as adopted in [266, 267, 194, 268], though a definitive justification of this argument is still missing, which would require a thorough scrutiny of the particle transport near the wall. So we choose ten-

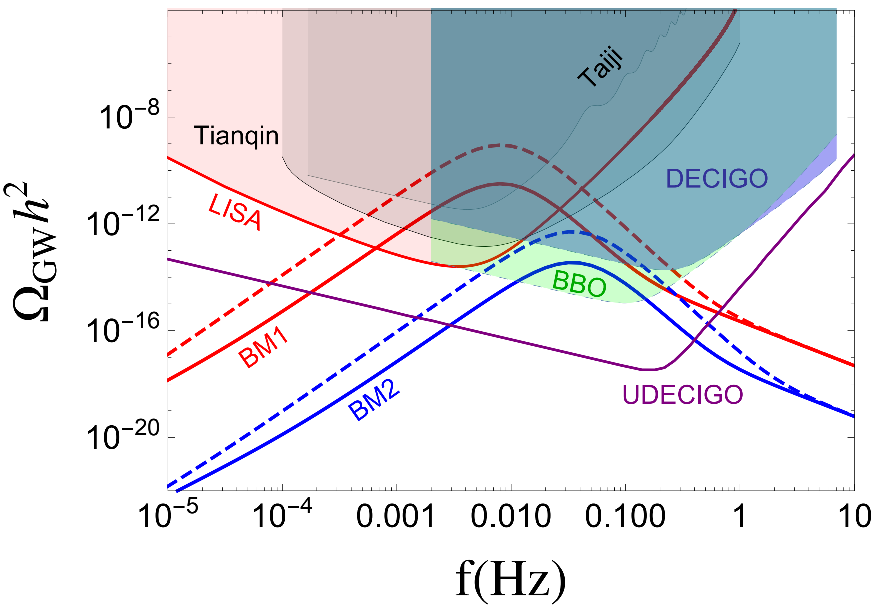

Figure 30: Gravitational wave energy spectrum versus the frequency for our two benchmark points and experimental sensitivities of some GW detectors. The dashed color lines indicate the corresponding spectrum without the suppression factor Υ.

tatively a value $v_w = 1$. For the benchmark points in Table 9, the GW spectrum are shown in Fig. 30. To illustrate the suppression effect of Υ, We present the results without considering it by the dashed lines. Some space-based interferometers sensitivities: LISA [269], Taiji [270], TianQin [271], Big Bang Observer (BBO), DECi-hertz Interferometer GW Observatory (DECIGO) and Ultimate-DECIGO [272] are overlaid in Fig. 30. To quantify the detectability of the signals, we define the signal-to-noise ratio (SNR) [234]:

$$\mathrm{SNR} = \sqrt{\delta \times \mathcal{T} \int_{f_{min}}^{f_{max}} df \left[\frac{h^2\Omega_{\mathrm{GW}}(f)}{h^2\Omega_{\mathrm{exp}}(f)}\right]^2}, \tag{6.102}$$

where $\mathcal{T}$ is the duration of the mission in years. Here we adopt $\mathcal{T} = 5$. $h^2\Omega_{\mathrm{exp}}(f)$ denotes the experimental sensitivities as shown in Fig. 30. $\delta = 2$ for BBO and UDECIGO, and $\delta = 1$ for the rest, indicating the number of independent channels for the GWs detector. The values of SNR with LISA and BBO configuration yield

$$\text{BM1:} \quad \text{SNR} = 1.08 \times 10^2 \text{ (LISA)}, \ \text{SNR} = 8.56 \times 10^2 \text{ (BBO)}, \tag{6.103}$$

$$\text{BM2:} \quad \text{SNR} = 9.95 \times 10^{-3} \text{ (LISA)}, \ \text{SNR} = 8.25 \text{ (BBO)}. \tag{6.104}$$

The threshold value of SNR for detection is 10 or 50 [234], and thus the BM1 can produce strong GW signal which can be detectable at both LISA and BBO.

We summarize our results on the m_{h_2}-$\sin\theta$ plane in Fig. 31, fixing the other parameters according to our BM1 (left panel) and BM2 (right panel). The orange shaded regions are allowed by the DM direct detections. Outside the cyan shaded regions, DM would over-close our Universe. The black points are the viable FOPT points which can enable GW production. The gray solid lines show the predicted deviation of the SM triple Higgs coupling. Our BM1 and BM2 points sit in the red-cross and blue-star symbols, respectively.

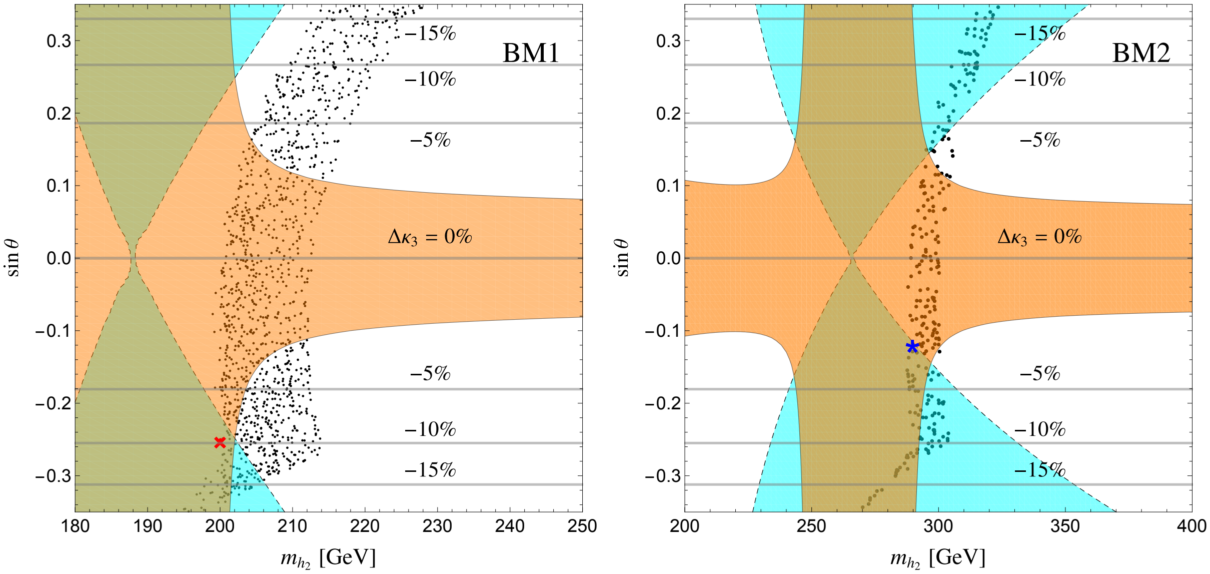

Figure 31: Contour plot on $\sin\theta$ - m_{h_2} plane. The orange (cyan) shaded regions are allowed by DM direct detection (relic density). The dashed lines indicate the value of $\Delta\kappa_3$ defined in Eq. (6.50). The black points give strong FOPT. The red cross at left panel and blue star at right panel are our BM1 and BM2 points, respectively.

7.0 Conclusions

7.1 Conclusions in the GNI Studies

Next generation neutrino oscillation and CEνNS experiments will reach the sensitivity to discover new physics parameterized in the form of GNI. We have considered two different approaches to the GNI. One is in a UV-complet Z' model, which is discussed in chapter 2. In chapter 3, we presented the ADMs of SMNEFT operators with gauge and Yukawa dependence. In chapter 4, we studied new physics associated with neutrinos without theoretical prejudice, with allowance for scalar, pseudoscalar, vector, axial-vector and tensor interactions of neutrinos with SM fermions within SMNEFT framework. If the new physics scale is much higher than the electroweak scale, it is appropriate to work in a model-independent EFT framework below the new physics scale. GNI operators below the electroweak scale are generated by EFT operators that respect the SM gauge symmetry.

In chapter 2, We considered three scenarios: $B - 3L_\mu$ (case A), $B - \frac{3}{2}(L_\mu + L_\tau)$ (case B), and $B - 3L_\tau$ (case C). The Z' decay branching fractions are shown in Fig. 1. Our main results are shown in Fig. 2. In Cases A and B, we mainly use neutrino oscillation, CEνNS, and collider experiments to put constraints on the coupling g' in the mass range, 5 MeV$< M_{Z'} <$ 6 TeV. We found that neutrino oscillation and CEνNS experiments give the most stringent bounds for masses below the dimuon threshold which is around 200 MeV. Above the dimuon threshold up to 70 GeV, LHCb prompt-like dark photon searches provide the strongest constraints except near the J/ψ, Υ resonances and in the vicinity of the Z-pole. ATLAS dimuon searches give the strongest bounds in the mass range, 250 GeV $\leq M_{Z'} \leq$ 6 TeV. The $(g-2)_\mu$ favored region is excluded by a combination of the experiments in the mass range considered. Our Case C is unconstrained by the COHERENT experiment. Neutrino oscillation experiments set the strongest constraints up to 200 GeV. The LHC gives the strongest constraints for 200 GeV $\leq M_{Z'} \leq$ 4 TeV. We estimated the sensitivity of the high luminosity LHC with an integrated luminosity of 3 ab^{-1} and find the that the reach of the $Z' \to \mu^+\mu^-$ channel is significantly improved in all of three scenarios; see Fig. 2. If the new gauge boson couples to first and second generation leptons, future CEνNS data can set stronger bounds than next-generation neutrino oscillation experiments in almost the entire mass range. DUNE and T2HK have the best sensitivity for Z' masses between $5-20$ MeV and $5-10$ MeV for Cases A and B, respectively. DUNE and T2HK have the best sensitivity for Z' masses between $5-20$ MeV and $5-10$ MeV for Cases A and B, respectively. Combining CEνNS and collider data will help to limit $M_{Z'}$ from above; see Fig. 4.

In chapter 3, we presented the Yukawa coupling contributions to the one-loop RGE for all fourfermion SMNEFT operators, and the new RGE terms for the four-fermion SMEFT operators due to the mixing between SMEFT and SMNEFT operators via the right-handed neutrino Yukawa couplings Y_n. The contributions from the fermionic operators come from the Feynman diagrams in Figs. 8a to 8d, with contributions from Fig. 8d given by the ξ parameters. We also presented the gauge terms of the one-loop anomalous dimension matrix for the dimension-six operators of SMNEFT; see Eqs. (3.65) to (3.69). We found that renormalization group evolution introduces interesting correlations among observables in different sectors. We discussed a few phenomenological implications of our results. To make contact with low energy observables we also included the matching of SMNEFT to LNEFT at the weak scale and RGE below the weak scale. However, to be confident that cancellations of terms between independent operators are absent, the full one-loop RGE must be calculated.

In chapter 4, we studied scalar, pseudoscalar and tensor neutrino interactions in the framework of SMNEFT, which extends SMEFT with right-handed neutrinos. At the dim-6 level, these interactions are produced by three less constrained and phenomenologically interesting operators, namely O_{NLQu}, O_{NLdQ}, and O'_{NLdQ}. Both neutral current and charged current interactions can be induced by a single operator, which can be explored in various experiments. To compare constraints from experiments at different energy scales, we perform the RG running above and below the weak scale, and map all the bounds into the parameter space of three WCs C_{NLQu}, C_{NLdQ}, and C'_{NLdQ} at 1 TeV. The full gauge and Yukawa terms of the one-loop anomalous dimension matrix for the dimension-six operators of SMNEFT are presented in chapter 3. We summarize the current and projected experimental bounds on the three WCs in Tables 7 and 8. The correlations between the three operators are shown in Fig. 12. Our main conclusions are as follows. Neutrino mass bounds indicate that the SMNEFT operators involving the second and third families of quarks are highly constrained, while the parameter space for neutrino interactions with the first quark generation is relatively unconstrained. This conclusion, however, is model-dependent and can be evaded. Bounds on the SMNEFT WCs from low-energy probes generally suffer from degeneracies, which are induced by RG running and matching, as is evident from Eq. (4.15). The high-energy probes set bounds directly on the SMNEFT WCs, and so are not subject to degeneracies. Low-energy probes and high-energy colliders are complementary. Charged pion decay is extremely sensitive to the LEFT pseudoscalar operators. But, there are degeneracies when the bounds are mapped into the SMNEFT WCs. With the assumption of only one nonzero operator at a time, the bounds on the electron flavor are at the 10^{-6} level. The strongest current bounds on the three SMNEFT operators are from LHC charged lepton $+E_T^{\rm miss}$ searches, and are at the $10^{-4}-10^{-3}$ level depending on the energy range of validity of the EFT. HL-LHC can improve the bounds by a factor of a few and reach 10^{-4} in the HNP case. For LNP, the improvement is minor because systematic uncertainties dominate for low m_T. Current LHC data can exclude $\kappa \gtrsim 0.14$ for $\Lambda = 1$ TeV and $\kappa \gtrsim 0.63$ for $\Lambda = 10$ TeV. Future HL-LHC data can exclude $\kappa \gtrsim 0.13$ for $\Lambda = 1$ TeV and $\kappa \gtrsim 0.55$ for $\Lambda = 10$ TeV. For strong interactions with $\kappa = 4\pi$, the new physics scale can be excluded up to 200 TeV. A future COHERENT experiment with LAr can set strong bounds on the scalar operators, comparable with that from the HL-LHC with the LNP assumption, especially when the muon flavor is involved. LHeC will be important to study tensor interactions involving the electron flavor, and can place bounds at the 10^{-4} level.

7.2 Conclusions in the WIMP Studies

The next research topics in PhD study are related to DM and electroweak phase transition. We considered two different WIMP models in chapter 5 and chapter 6, in which DM candidates carry $\rm SU(2)_L$ and dark $\rm SU(2)_D$ charges, respectivily.

In chapter 5, we studied the NLO electroweak corrections to spin-independent DM nucleon scattering, in scenarios where the tree-level predictions for these rates are very small. Such small leading order rates are obtained generically in DM models where the DM state results from the mixing of electroweak singlet and doublet states, due to cancellations in DM coupling to the Higgs boson, which is the primary mediator of SI interactions for Majorana fermion WIMPs. A well-known example of these DM blind spots is the case of bino-Higgsino mixed DM in the MSSM. To understand the impact of radiative corrections to DM-nucleon scattering in such a setup, we adopted a simple model for DM with one Majorana fermion singlet, and two electroweak doublets with opposite hypercharge, the neutral components of which mix after electroweak symmetry breaking. This corresponds to the MSSM neutralino sector with all the sfermions, heavy scalars and wino decoupled. We evaluated, adopting an on-shell renormalization scheme for the DM sector, the set of triangle and box diagrams for the radiative corrections to the DM-quark scalar effective operator, that could directly modify the predictions near the blind spots. We observed that the contribution to the DM-nucleon effective coupling f_N from the triangle diagrams dominates near the tree-level blind spot, as the leading order contribution is vanishingly small in this region. As expected, the one-loop contributions "unblind" the tree-level blind spots, as seen in Fig. 18. Away from the blind-spot region, the one-loop electroweak effects are still found to be appreciable. For example, the triangle diagrams considered can shift the tree-level value of f_N by upto 10%. We also find that the box diagram contribution can become comparable to the triangles in some parameter regions. There are values of parameters around which both the triangle and the box contributions can also change sign, and therefore have their own blind spots. Importantly, we always find a new blind spot at the NLO level where the sum of the tree-level and one-loop amplitudes go to zero. This leads to a shifted location for the blind-spot point, the amount of the shift in the values of the doublet mass mixing parameter M_D being almost linearly proportional to the value of the singlet mass M_S. This shift is found to be larger for large values of $\tan\beta$ (the ratio of the Yukawa couplings of the two doublets, y_1/y_2) and small values of y ($=\sqrt{y_1^2+y_2^2}$), and can be around $\mathcal{O}(1\%)$. These features are shown in Fig. 19. On taking into account the impact of the radiative corrections to SI scattering, the prospects of testing such tree-level blind-spot scenarios in future multi-ton scale liquid Xenon experiments improve considerably. In particular, we find that for smaller values of

$\tan\beta$, e.g., $\tan\beta = 2$, $\sigma_{\rm SI}$ takes values in the range of about 10^{-47} cm^2 to 10^{-50} cm^2, for $M_{\widetilde{\chi}_1^0}$ values in the interval 100 GeV $-$ 2 TeV, and coupling coefficient y in the range $0.3 - 1.5$. For this range of couplings, the future projection of the LZ experiment is expected to probe a DM mass upto about 500 GeV, while the reach can be further extended by the DARWIN experiment upto a DM mass of 1250 GeV. On the other hand, for higher values of $\tan\beta$, as seen with $\tan\beta = 10$, the expected cross-section is smaller, with a maximum of around 10^{-49} cm^2, which may not be accessible to DARWIN. Thus, the small $\tan\beta$ scenario leads to similar $\sigma_{\rm SI}$ as in the case of wino-like real triplet DM, while the intermediate $\tan\beta$ scenario predicts cross-sections similar to the case of Majorana Higgsino-like doublets. These results are presented in Fig. 20. On the other hand, as already examined in Ref. [150], the SD scattering cross-sections may be observable in certain SI blind-spot regions. Thus, combined tests of both the SI one-loop predictions and the tree-level SD cross-sections are feasible, thereby probing all the relevant effective operators for DM-nucleon interaction. With the increasing sensitivity of the DM direct detection experiments, resulting from the construction of bigger and ultra-low noise detectors, it is important to define benchmark targets for these near future multi-ton scale experiments. As we found in this study, higher order electroweak corrections to scenarios with mixed electroweak DM states present one such target, where the tree-level rates can be very small due to the vanishing of relevant DM effective couplings in certain parameter regions. In order to thoroughly probe interesting and well-motivated WIMP scenarios, it is therefore necessary to have theoretical predictions with increased accuracy that could match up to the future expected experimental precision.

In chapter 6, we extended the SM with a dark $\mathrm{SU(2)_D}$ gauge sector and a dark scalar sector. We imposed Z_2 symmetry in the dark scalar sector. We considered two different scalar scenarios under the dark $\mathrm{SU(2)_D}$ gauge charge, namely, a model with two scalar triplets (TT) and one with a scalar singlet plus a scalar triplet (ST). The dark sector couples to the SM through the Higgs portal $-$ the mixing between the SM Higgs boson and the dark scalars. We worked out the existing constraints on the dark sector model-parameters from the vacuum stability, perturbative unitarity, Higgs physics at the LHC, and the cosmological bounds from CMB measurements and the DM relic abundance and its direct detections. For illustration, we chose two representative benchmark points as shown in Table 9, which satisfy all the constraints, possess the desirable features, and could lead to observable effects. Via the Higgs portal, the properties of the SM Higgs boson would be modified, including the couplings and an invisible decay. It is particularly interesting to test the potentially large deviation of the Higgs boson triple-self coupling from the SM prediction. Direct searches for the heavy Higgs boson decaying to the SM heavy particles may also be fruitful. We showed those in Figs. 22, 24, and 25. Because of the existence of a massless DR associated with the unbroken subgroup $\mathrm{U(1)_D}$, it can introduce the velocity-dependent DM self-interaction, which would be desirable to resolve the small-scale structure problems. The two stable massive gauge bosons associated with the broken dark gauge group and the pseudo-Goldstone boson can serve as cold DM candidates. The acceptable relic densities were shown in the left panel of Fig. 28. We explored the prospects of their detection in the direct DM searches as shown in the right panel of Fig. 28. The nontrivial scalar potential has eight types of vacuum pattern for the vacuum structure as shown in Table 10. We have found both the two-step and three-step phase transitions with the cooling of the Universe. Due to the rich vacuum pattern, the scalar sectors can introduce a strong FOPT, as illustrated in Fig. 29 for the benchmark points BM1 with a successful EW FOPT, and BM2 with a FOPT in the dark sector. Our benchmark GW spectra are shown in Fig. 30. We found that the two-step EWPT in our BM1 can produce strong GW signals and can be detectable using the future space-based interferometers LISA and BBO, while the GW signal for BM2 may be difficult to observe at LISA due to the rather low signal-to-noise ratio. Given the outstanding puzzles we are facing now such as the identity of the DM and the nature of the EWPT, it is prudent to consider the possibility of a dark sector uncharged under the SM interactions. We demonstrated with a well-motivated example of a dark $\mathrm{SU(2)_D}$ sector, that rich physics may exist that is potentially observable with the current and future measurements at colliders, DM experiments, and GW interferometers.

Appendix A Details of On-shell Renormalization Scheme

The Lagrangian of the DM sector in the mass basis can be written as

$$\mathscr{L} = \overline{\widetilde{\chi}^+}\left(\not{p}P_L + \not{p}P_R - \eta\, M_D\right)\widetilde{\chi}_0^+ + \frac{1}{2}\overline{\widetilde{\chi}_i^0}\left(\not{p}P_L\delta_{ij} + \not{p}P_R\delta_{ij} - \left[\mathbf{U}^\top\mathbf{M_N}\mathbf{U}\right]_{ij}\right)\widetilde{\chi}_j^0, \tag{A.1}$$

where η is a phase factor and i, j are summed over 1 to 3. We specify the on-shell renormalization scheme adopted for the DM sector in the following.

According to the multiplicative renormalization procedure, we perform the following replacements of the parameters and the fields:

$$M_S \;\to\; M_S + \delta M_S, \qquad M_D \;\to\; M_D + \delta M_D, \tag{A.2}$$

$$y_1 \;\to\; y_1 + \delta y_1, \qquad y_2 \;\to\; y_2 + \delta y_2, \tag{A.3}$$

$$P_L\widetilde{\chi}^+ \;\to\; \left[1 + \frac{1}{2}\delta Z^L_{\widetilde{\chi}^+}\right]P_L\widetilde{\chi}^+, \qquad P_R\widetilde{\chi}^+ \;\to\; \left[1 + \frac{1}{2}\delta Z^R_{\widetilde{\chi}^+}\right]P_R\widetilde{\chi}^+, \tag{A.4}$$

$$P_L\widetilde{\chi}_i^0 \;\to\; \left[\mathbb{1} + \frac{1}{2}\delta\mathbf{Z}_{\widetilde{\chi}^0}\right]_{ij}P_L\widetilde{\chi}_j^0, \qquad P_R\widetilde{\chi}_i^0 \;\to\; \left[\mathbb{1} + \frac{1}{2}\delta\mathbf{Z}^*_{\widetilde{\chi}^0}\right]_{ij}P_R\widetilde{\chi}_j^0. \tag{A.5}$$

We note that the transformation matrix $\mathbf{U}$ is not renormalized in our scheme, so that, the mass matrix in the gauge basis $\mathbf{M_N}$ is replaced by

$$\mathbf{M_N} \;\to \mathbf{M_N} + \delta\mathbf{M_N} = \mathbf{M_N} + \begin{pmatrix} \delta M_S & \delta\Delta_2 & \delta\Delta_1 \\ \delta\Delta_2 & 0 & \delta M_D \\ \delta\Delta_1 & \delta M_D & 0 \end{pmatrix}, \tag{A.6}$$

where $\delta\Delta_{1,2} = \delta(y_{1,2}v/\sqrt{2})$. Then the mass matrix in the mass basis can be expressed as

$$\mathbf{M}_{\widetilde{\chi}^0} \;\to\; \mathbf{M}_{\widetilde{\chi}^0} + \delta\mathbf{M}_{\widetilde{\chi}^0} = \mathrm{diag}\left(M_{\widetilde{\chi}_1^0}, M_{\widetilde{\chi}_2^0}, M_{\widetilde{\chi}_3^0}\right) + \mathbf{U}^\top\delta\mathbf{M_N}\mathbf{U}. \tag{A.7}$$

In the following, we use Σ and $\hat{\Sigma}$ to denote un-renormalized and renormalized self-energies respectively. Decomposing into the following form

$$\hat{\Sigma}(p) = \hat{\Sigma}^L(p^2)\not{p}P_L + \hat{\Sigma}^R(p^2)\not{p}P_R + \hat{\Sigma}^{SL}(p^2)P_L + \hat{\Sigma}^{SR}(p^2)P_R, \tag{A.8}$$

the renormalized self-energies of the charged and neutral states are given by

$$\hat{\Sigma}^{L}_{\widetilde{\chi}^+}(p^2) = \Sigma^{L}_{\widetilde{\chi}^+}(p^2) + \frac{1}{2}(\delta Z^{L}_{\widetilde{\chi}^+} + \delta Z^{L*}_{\widetilde{\chi}^+}), \tag{A.9}$$

$$\hat{\Sigma}^{R}_{\widetilde{\chi}^+}(p^2) = \Sigma^{R}_{\widetilde{\chi}^+}(p^2) + \frac{1}{2}(\delta Z^{R}_{\widetilde{\chi}^+} + \delta Z^{R*}_{\widetilde{\chi}^+}), \tag{A.10}$$

$$\hat{\Sigma}^{SL}_{\widetilde{\chi}^+}(p^2) = \Sigma^{SL}_{\widetilde{\chi}^+}(p^2) - \frac{1}{2}(M_{\widetilde{\chi}^+}\delta Z^{L}_{\widetilde{\chi}^+} + \delta Z^{R*}_{\widetilde{\chi}^+} M_{\widetilde{\chi}^+} + 2\delta M_{\widetilde{\chi}^+}), \tag{A.11}$$

$$\hat{\Sigma}^{SR}_{\widetilde{\chi}^+}(p^2) = \Sigma^{SR}_{\widetilde{\chi}^+}(p^2) - \frac{1}{2}(M_{\widetilde{\chi}^+}\delta Z^{R}_{\widetilde{\chi}^+} + \delta Z^{L*}_{\widetilde{\chi}^+} M_{\widetilde{\chi}^+} + 2\delta M^{*}_{\widetilde{\chi}^+}), \tag{A.12}$$

$$\left[\hat{\Sigma}^{L}_{\widetilde{\chi}^0}(p^2)\right]_{ij} = \left[\Sigma^{L}_{\widetilde{\chi}^0}(p^2)\right]_{ij} + \frac{1}{2}\left[\delta \mathbf{Z}_{\widetilde{\chi}^0} + \delta \mathbf{Z}^{\dagger}_{\widetilde{\chi}^0}\right]_{ij}, \tag{A.13}$$

$$\left[\hat{\Sigma}^{R}_{\widetilde{\chi}^0}(p^2)\right]_{ij} = \left[\Sigma^{R}_{\widetilde{\chi}^0}(p^2)\right]_{ij} + \frac{1}{2}\left[\delta \mathbf{Z}^{*}_{\widetilde{\chi}^0} + \delta \mathbf{Z}^{\top}_{\widetilde{\chi}^0}\right]_{ij}, \tag{A.14}$$

$$\left[\hat{\Sigma}^{SL}_{\widetilde{\chi}^0}(p^2)\right]_{ij} = \left[\Sigma^{SL}_{\widetilde{\chi}^0}(p^2)\right]_{ij} - \frac{1}{2}\left[\mathbf{M}_{\widetilde{\chi}^0}\delta \mathbf{Z}_{\widetilde{\chi}^0} + \delta \mathbf{Z}^{\top}_{\widetilde{\chi}^0}\mathbf{M}_{\widetilde{\chi}^0} + 2\delta \mathbf{M}_{\widetilde{\chi}^0}\right]_{ij}, \tag{A.15}$$

$$\left[\hat{\Sigma}^{SR}_{\widetilde{\chi}^0}(p^2)\right]_{ij} = \left[\Sigma^{SR}_{\widetilde{\chi}^0}(p^2)\right]_{ij} - \frac{1}{2}\left[\mathbf{M}_{\widetilde{\chi}^0}\delta \mathbf{Z}^{*}_{\widetilde{\chi}^0} + \delta \mathbf{Z}^{\dagger}_{\widetilde{\chi}^0}\mathbf{M}_{\widetilde{\chi}^0} + 2\delta \mathbf{M}^{\dagger}_{\widetilde{\chi}^0}\right]_{ij}. \tag{A.16}$$

We choose the on-shell renormalization scheme by imposing (for $i, j = 1, 2, 3$)

$$\left[\widetilde{\mathrm{Re}}\hat{\Sigma}_{\widetilde{\chi}^+}(p)\right]\widetilde{\chi}^+(p)\Big|_{p^2=M^2_{\widetilde{\chi}^+}} = 0, \qquad \lim_{p^2\to M^2_{\widetilde{\chi}^+}} \frac{1}{\not{p} - M_{\widetilde{\chi}^+}}\left[\widetilde{\mathrm{Re}}\hat{\Sigma}_{\widetilde{\chi}^+}(p)\right]\widetilde{\chi}^+(p) = 0, \tag{A.17}$$

$$\left[\widetilde{\mathrm{Re}}\hat{\Sigma}_{\widetilde{\chi}^0}(p)\right]_{ij}\widetilde{\chi}^0_j(p)\Big|_{p^2=M^2_{\widetilde{\chi}^0_j}} = 0, \qquad \lim_{p^2\to M^2_{\widetilde{\chi}^0_i}} \frac{1}{\not{p} - M_{\widetilde{\chi}^0_i}}\left[\widetilde{\mathrm{Re}}\hat{\Sigma}_{\widetilde{\chi}^0}(p)\right]_{ii}\widetilde{\chi}^0_i(p) = 0, \tag{A.18}$$

where $\widetilde{\mathrm{Re}}$ takes only the real part of the loop integrals appearing in the self energies but not of the mixing matrix elements or couplings appearing therein. We further fix the imaginary parts of the wave-function renormalization constants by choosing

$$\mathrm{Im}\left[\delta Z^{L}_{\widetilde{\chi}^+}\right] = \mathrm{Im}\left[\delta Z^{R}_{\widetilde{\chi}^+}\right] = \mathrm{Im}\left[\delta \mathbf{Z}_{\widetilde{\chi}^0}\right]_{ii} = 0. \tag{A.19}$$

Thus, Eqs. (A.17− A.19) yield the counterterms

$$\begin{aligned}
\delta Z^L_{\widetilde{\chi}^+} =& -\Sigma^L_{\widetilde{\chi}^+}(M^2_{\widetilde{\chi}^+}) - M^2_{\widetilde{\chi}^+}\left[\Sigma^{L\prime}_{\widetilde{\chi}^+}(M^2_{\widetilde{\chi}^+}) + \Sigma^{R\prime}_{\widetilde{\chi}^+}(M^2_{\widetilde{\chi}^+})\right] \\
& - M_{\widetilde{\chi}^+}\left[\Sigma^{SL\prime}_{\widetilde{\chi}^+}(M^2_{\widetilde{\chi}^+}) + \Sigma^{SR\prime}_{\widetilde{\chi}^+}(M^2_{\widetilde{\chi}^+})\right],
\end{aligned} \tag{A.20}$$

$$\begin{aligned}
\delta Z^R_{\widetilde{\chi}^+} =& -\Sigma^R_{\widetilde{\chi}^+}(M^2_{\widetilde{\chi}^+}) - M^2_{\widetilde{\chi}^+}\left[\Sigma^{L\prime}_{\widetilde{\chi}^+}(M^2_{\widetilde{\chi}^+}) + \Sigma^{R\prime}_{\widetilde{\chi}^+}(M^2_{\widetilde{\chi}^+})\right] \\
& - M_{\widetilde{\chi}^+}\left[\Sigma^{SL\prime}_{\widetilde{\chi}^+}(M^2_{\widetilde{\chi}^+}) + \Sigma^{SR\prime}_{\widetilde{\chi}^+}(M^2_{\widetilde{\chi}^+})\right],
\end{aligned} \tag{A.21}$$

$$\delta M_D = \eta^*\delta M_{\widetilde{\chi}^+} = \frac{\eta^*}{2} M_{\widetilde{\chi}^+}\left[\Sigma^L_{\widetilde{\chi}^+}(M^2_{\widetilde{\chi}^+}) + \Sigma^R_{\widetilde{\chi}^+}(M^2_{\widetilde{\chi}^+})\right] + \eta^*\Sigma^{SL}_{\widetilde{\chi}^+}(M^2_{\widetilde{\chi}^+}), \tag{A.22}$$

$$\begin{aligned}
[\delta\mathbf{Z}_{\widetilde{\chi}^0}]_{ii} =& -\frac{1}{2}\left[\Sigma^L_{\widetilde{\chi}^0}(M^2_{\widetilde{\chi}^0_i}) + \Sigma^R_{\widetilde{\chi}^0_i}(M^2_{\widetilde{\chi}^0_i})\right]_{ii} \\
& - M^2_{\widetilde{\chi}^0_i}\left[\Sigma^{L\prime}_{\widetilde{\chi}^0}(M^2_{\widetilde{\chi}^0_i}) + \Sigma^{R\prime}_{\widetilde{\chi}^+}(M^2_{\widetilde{\chi}^0_i})\right]_{ii} - M_{\widetilde{\chi}^0_i}\left[\Sigma^{SL\prime}_{\widetilde{\chi}^0}(M^2_{\widetilde{\chi}^0_i}) + \Sigma^{SR\prime}_{\widetilde{\chi}^0}(M^2_{\widetilde{\chi}^0_i})\right]_{ii},
\end{aligned} \tag{A.23}$$

$$\begin{aligned}
[\delta\mathbf{Z}_{\widetilde{\chi}^0}]_{ij} =& \frac{2}{M^2_{\widetilde{\chi}^0_i} - M^2_{\widetilde{\chi}^0_j}}\Big[M^2_{\widetilde{\chi}^0_j}\Sigma^L_{\widetilde{\chi}^0}(M^2_{\widetilde{\chi}^0_j}) + M_{\widetilde{\chi}^0_i}M_{\widetilde{\chi}^0_j}\Sigma^R_{\widetilde{\chi}^0}(M^2_{\widetilde{\chi}^0_j}) + M_{\widetilde{\chi}^0_i}\Sigma^{SL}_{\widetilde{\chi}^0}(M^2_{\widetilde{\chi}^0_j}) \\
& + M_{\widetilde{\chi}^0_j}\Sigma^{SR}_{\widetilde{\chi}^0}(M^2_{\widetilde{\chi}^0_j}) - M_{\widetilde{\chi}^0_i}\delta\mathbf{M}_{\widetilde{\chi}^0} - M_{\widetilde{\chi}^0_j}\delta\mathbf{M}^\dagger_{\widetilde{\chi}^0}\Big]_{ij}, \quad \text{for } i \neq j,
\end{aligned} \tag{A.24}$$

$$[\delta\mathbf{M}_{\widetilde{\chi}^0}]_{ii} = \frac{1}{2}M_{\widetilde{\chi}^0_i}\left[\Sigma^L_{\widetilde{\chi}^0}(M^2_{\widetilde{\chi}^0_i}) + \Sigma^R_{\widetilde{\chi}^0}(M^2_{\widetilde{\chi}^0_i})\right]_{ii} + \left[\Sigma^{SL}_{\widetilde{\chi}^0}(M^2_{\widetilde{\chi}^0_i})\right]_{ii}, \tag{A.25}$$

where $\Sigma'(p^2)$ is the derivative of the self-energy $\Sigma'(p^2) = \partial\Sigma(p^2)/\partial p^2$. All the un-renormalized self-energies Σ in Eqs. (A.20− A.25) should be understood as $\widetilde{\mathrm{Re}}\Sigma$. The counterterms $\delta\Delta_1$, $\delta\Delta_2$ and δM_S in Eq. (A.6) are then fixed by solving the equations

$$[\delta\mathbf{M}_{\widetilde{\chi}^0}]_{ii} = \left[\mathbf{U}^\top\delta\mathbf{M_N}\mathbf{U}\right]_{ii}. \tag{A.26}$$

The relevant counterterms to the DM-Higgs coupling can be expressed as

$$\begin{aligned}
\delta\Gamma^{\mathrm{ct}}\left(\overline{\widetilde{\chi}^0_1}, \widetilde{\chi}^0_1, h\right) =& \left[\delta\mathbf{S}^L + \frac{1}{2}\delta\mathbf{Z}^\top_{\widetilde{\chi}^0}\mathbf{S}^L + \frac{1}{2}\mathbf{S}^L\delta\mathbf{Z}_{\widetilde{\chi}^0} + \frac{1}{2}\mathbf{S}^L\delta Z_h\right]_{11} P_L \\
& + \left[\delta\mathbf{S}^R + \frac{1}{2}\delta\mathbf{Z}^\dagger_{\widetilde{\chi}^0}\mathbf{S}^R + \frac{1}{2}\mathbf{S}^R\delta\mathbf{Z}^*_{\widetilde{\chi}^0} + \frac{1}{2}\mathbf{S}^R\delta Z_h\right]_{11} P_R.
\end{aligned} \tag{A.27}$$

where

$$\left[\mathbf{S}^L\right]_{ii} = -\frac{y_1}{\sqrt{2}}U_{3i}U_{1i} - \frac{y_2}{\sqrt{2}}U_{2i}U_{1i}, \tag{A.28}$$

$$\left[\mathbf{S}^L\right]_{ij} = -\frac{y_1}{\sqrt{2}}U_{3i}U_{1j} - \frac{y_2}{\sqrt{2}}U_{2i}U_{1j} + (i \leftrightarrow j), \quad \text{for } i \neq j, \tag{A.29}$$

$$\mathbf{S}_R = \mathbf{S}^\dagger_L. \tag{A.30}$$

The counterterms δy_1 and δy_2 are related to $\delta\Delta_1$ and $\delta\Delta_2$ through the relations

$$\delta y_1 = \sqrt{2}\frac{\delta\Delta_1}{v} - y_1\frac{\delta v}{v}, \qquad \delta y_2 = \sqrt{2}\frac{\delta\Delta_2}{v} - y_2\frac{\delta v}{v}, \tag{A.31}$$

with δv and δZ_h calculated in the on-shell scheme following the conventions in Ref. [273].

Appendix B DM-nucleon Scattering: Computational Framework

In this Appendix, we briefly review the formalism adopted for computing the DM-nucleon scattering cross-sections [28], and the values of the relevant nuclear matrix elements used. The effective interactions of a non-relativistic Majorana WIMP X with light quarks and gluons are given as

$$\mathscr{L}_{eff} = \sum_{q=u,d,s} \left(d_q \overline{X} \gamma^\mu \gamma^5 X \bar{q} \gamma_\mu \gamma^5 q + f_q m_q \overline{X} X \bar{q} q \right) + f_G \overline{X} X \frac{\alpha_s}{\pi} G^a_{\mu\nu} G^{a\mu\nu}, \tag{B.1}$$

where, $G^a_{\mu\nu}$ is the gluon field strength tensor and α_S is the strong coupling constant. Here, the operator involving axial-vector currents of the DM and the quark fields leads to spin-dependent interactions, while the other two operator structures lead to spin-independent scattering with nuclei.

To begin with, we define the matrix element (ME) of the scalar operator $\bar{q}q$ between nucleon states N (where N is either a proton or a neutron) as follows:

$$\langle N | m_q \bar{q} q | N \rangle \equiv f^N_{Tq} m_N. \tag{B.2}$$

The corresponding ME of the gluon operator can be obtained by using the trace of the energy momentum tensor T^μ_μ, which is given by

$$T^\mu_\mu = \sum_{q=u,d,s} m_q \bar{q} q + \sum_{Q=b,c,t} m_Q \bar{Q} Q - \frac{7\alpha_s}{8\pi} GG. \tag{B.3}$$

Here, we have used the shorthand GG to stand for $G^a_{\mu\nu} G^{a\mu\nu}$. Utilizing the fact that

$$\langle N | T^\mu_\mu | N \rangle \equiv m_N, \tag{B.4}$$

where, m_N is the nucleon mass, and by integrating out the heavy quarks using

$$\langle N | m_Q \bar{Q} Q | N \rangle = \langle N | - \frac{\alpha_s}{12\pi} GG | N \rangle, \tag{B.5}$$

we obtain the ME of the gluon operator

$$\langle N | \frac{\alpha_s}{\pi} GG | N \rangle = -\frac{8}{9} m_N f^N_{TG}. \tag{B.6}$$

Here, f_{TG}^{N} is related to f_{Tq}^{N} as

$$f_{TG}^{N} \equiv 1 - \sum_{q=u,d,s} f_{Tq}^{N}. \tag{B.7}$$

Similarly, the nucleon ME of the axial-vector quark current is defined as

$$\langle N|\bar{q}\gamma_\mu\gamma^5 q|N\rangle \equiv 2s_\mu \Delta q_N, \tag{B.8}$$

where s_μ is the nucleon spin. Combining these results, the effective interaction of Majorana WIMPs with nucleons is given by

$$\mathscr{L}_{eff} = \sum_{N=n,p} \left(f_N \overline{X} X \overline{N} N + a_N \overline{X} \gamma^\mu \gamma^5 X \overline{N} \gamma_\mu \gamma^5 N \right), \tag{B.9}$$

with the Wilson co-efficients,

$$f_N/m_N = \sum_{q=u,d,s} f_q f_{Tq}^{N} - \frac{8}{9} f_G f_{TG}^{N} \quad \text{and} \quad a_N = \sum_{q=u,d,s} d_q \Delta q_N. \tag{B.10}$$

For our computations, we adopt the following values of the nuclear matrix elements for proton: $f_{Tu}^{p} = 0.0153$, $f_{Td}^{p} = 0.0191$, and $f_{Ts}^{p} = 0.0447$, where we have used the lattice results for the strange quark content of the nucleon [274, 275, 210]. For spin-dependent scattering, we use the following inputs: $\Delta u_p = 0.842$, $\Delta d_p = -0.427$, and $\Delta s_p = -0.085$ [210].

Appendix C Mapping the Singlet-doublet Model to MSSM

The analysis presented in Sec. 5.1 can be translated to the neutralino sector in the minimal supersymmetric standard model (MSSM), with the wino state decoupled. In such a scenario, the neutralino mass matrix in the basis $(\widetilde{B}, \widetilde{H}_d^0, \widetilde{H}_u^0)$ is given by

$$M_N = \begin{pmatrix} M_1 & -M_Z s_W \cos\beta & M_Z s_W \sin\beta \\ -M_Z s_W \cos\beta & 0 & -\mu \\ M_Z s_W \sin\beta & -\mu & 0 \end{pmatrix}. \tag{C.1}$$

The phenomenology of tree-level spin-independent DM-quark interactions is then similar to what we obtained for the singlet-doublet model, with the following mapping between the couplings,

$$y \to -\sqrt{2}\frac{M_Z s_W}{v}. \tag{C.2}$$

The singlet and doublet fermion mass parameters M_S and M_D are replaced by the bino and Higgsino mass parameters, M_1 and μ, respectively. The coupling of the lighter Higgs boson state to the lightest neutralino is then given by

$$g^0_{h\chi_1\chi_1} \simeq \frac{eM_Z \tan\theta_W}{\mu^2 - M_1^2}\left(M_1 + \mu\sin(2\beta)\right). \tag{C.3}$$

In the MSSM, we also have the following DM coupling to the heavier CP-even Higgs boson

$$g^0_{H\chi_1\chi_1} \simeq -\frac{eM_Z \tan\theta_W}{\mu^2 - M_1^2}\mu\cos(2\beta). \tag{C.4}$$

Combining with the Higgs-quark Yukawa couplings and taking the alignment limit, at the leading order the DM-quark scalar effective couplings are then obtained to be

$$f_u = -\frac{g^0_{h\chi_1\chi_1}}{vm_h^2} + \frac{g^0_{H\chi_1\chi_1}}{vm_H^2}\cot\beta, \quad f_d = -\frac{g^0_{h\chi_1\chi_1}}{vm_h^2} - \frac{g^0_{H\chi_1\chi_1}}{vm_H^2}\tan\beta. \tag{C.5}$$

In the scenario with the heavy Higgs decoupled, we can now obtain the SI blind-spot condition for MSSM:

$$M_1 + \mu\sin(2\beta) = 0, \tag{C.6}$$

with $\mathrm{sgn}\,(M_1/\mu) = -1$.

Appendix D Field-dependent Mass

The field-dependent masses for the scalar degrees of freedom with $n_S = 1$ are

$$
\begin{aligned}
m_h^2 &= m_H^2 + \frac{3\lambda_H}{2}h_0^2 + \frac{\lambda_{H11}}{2}\omega_3^2 + \frac{\lambda_{H22}}{2}\varphi_2^2, && \text{(D.1)}\\
m_{G_0}^2 &= m_{G_1}^2 = m_{G_2}^2 = m_H^2 + \frac{\lambda_H}{2}h_0^2 + \frac{\lambda_{H11}}{2}\omega_3^2 + \frac{\lambda_{H22}}{2}\varphi_2^2, && \text{(D.2)}\\
m_{\varphi_1}^2 &= m_{22}^2 + \frac{\lambda_{H22}}{2}h_0^2 + \frac{\lambda_2}{2}\varphi_2^2 + \frac{\lambda_3}{2}\omega_3^2, && \text{(D.3)}\\
m_{\varphi_2}^2 &= m_{22}^2 + \frac{\lambda_{H22}}{2}h_0^2 + \frac{3\lambda_2}{2}\varphi_2^2 + \frac{\lambda_3}{2}\omega_3^2, && \text{(D.4)}\\
m_{\varphi_3}^2 &= m_{22}^2 + \frac{\lambda_{H22}}{2}h_0^2 + \frac{\lambda_2}{2}\varphi_2^2 + \frac{\lambda_3+\lambda_4}{2}\omega_3^2, && \text{(D.5)}\\
m_{\omega_1}^2 &= m_{11}^2 + \frac{\lambda_{H11}}{2}h_0^2 + \frac{\lambda_3}{2}\varphi_2^2 + \frac{\lambda_1}{2}\omega_3^2, && \text{(D.6)}\\
m_{\omega_2}^2 &= m_{11}^2 + \frac{\lambda_{H11}}{2}h_0^2 + \frac{\lambda_3+\lambda_4}{2}\varphi_2^2 + \frac{\lambda_1}{2}\omega_3^2, && \text{(D.7)}\\
m_{\omega_3}^2 &= m_{11}^2 + \frac{\lambda_{H11}}{2}h_0^2 + \frac{\lambda_3}{2}\varphi_2^2 + \frac{3\lambda_1}{2}\omega_3^2. && \text{(D.8)}
\end{aligned}
$$

Similarly the field-dependent masses for the vector degrees of freedom with $n_{\tilde{W}} = n_Z = 3$ and $n_W = 6$ are

$$
\begin{aligned}
&m_{\tilde{W}_1}^2 = \tilde{g}^2(\varphi_1^2 + \varphi_2^2),\ m_{\tilde{W}_2}^2 = \tilde{g}^2\varphi_1^2,\ m_{\tilde{W}_3}^2 = \tilde{g}^2\varphi_2^2,\\
&m_W^2 = \frac{g_2^2}{4}h^2,\ m_Z^2 = \frac{g_2^2+g_1^2}{4}h^2.
\end{aligned}
\tag{D.9}
$$

Finally, the field-dependent masses for the fermion degrees of freedom with $n_t = 12$ is

$$
m_t^2 = \frac{y_t^2}{2}h^2. \tag{D.10}
$$

Appendix E Stable Conditions for All the Minima

The stable conditions for the extrema in Table 10 are

Type-1 scenario:
$$m_H^2,\ m_{11}^2,\ m_{22}^2 > 0, \tag{E.1}$$

Type-2 scenario:
$$m_H^2 < 0,\ \lambda_{H11} m_H^2 - \lambda_H m_{11}^2 < 0,\ \lambda_{H22} m_H^2 - \lambda_H m_{22}^2 < 0 \tag{E.2}$$

Type-3 scenario:
$$m_{11}^2 < 0,\ \lambda_{H11} m_{11}^2 - \lambda_1 m_H^2 < 0,\ \lambda_3 m_{11}^2 - \lambda_1 m_{22}^2 < 0 \tag{E.3}$$

Type-4 scenario:
$$m_{22}^2 < 0,\ \lambda_{H22} m_{22}^2 - \lambda_2 m_H^2 < 0,\ \lambda_3 m_{22}^2 - \lambda_2 m_{11}^2 < 0 \tag{E.4}$$

Type-5 scenario:
$$\begin{aligned} &\lambda_H \lambda_1 - \lambda_{H11}^2 > 0, \lambda_{H11} m_H^2 - \lambda_H m_{11}^2 > 0,\ \lambda_{H11} m_{11}^2 - \lambda_1 m_H^2 > 0, \\ &m_{22}^2 + \frac{\lambda_3(\lambda_{H11} m_H^2 - \lambda_H m_{11}^2)}{\lambda_H \lambda_1 - \lambda_{H11}^2} + \frac{\lambda_{H22}(\lambda_{H11} m_{11}^2 - \lambda_1 m_H^2)}{\lambda_H \lambda_1 - \lambda_{H11}^2} > 0 \end{aligned} \tag{E.5}$$

Type-6 scenario:
$$\begin{aligned} &\lambda_1 \lambda_2 - \lambda_3^2 > 0, \lambda_3 m_2^2 - \lambda_2 m_{11}^2 > 0,\ \lambda_3 m_{22}^2 - \lambda_2 m_{11}^2 > 0, \\ &m_H^2 + \frac{\lambda_{H11}(\lambda_3 m_{22}^2 - \lambda_2 m_{11}^2)}{\lambda_1 \lambda_2 - \lambda_3^2} + \frac{\lambda_{H22}(\lambda_3 m_{11}^2 - \lambda_1 m_{22}^2)}{\lambda_1 \lambda_2 - \lambda_3^2} > 0, \end{aligned} \tag{E.6}$$

Type-7 scenario:
$$\begin{aligned} &\lambda_H \lambda_2 - \lambda_{H22}^2 > 0, \lambda_{H22} m_H^2 - \lambda_H m_{22}^2 > 0,\ \lambda_{H22} m_{22}^2 - \lambda_2 m_H^2 > 0, \\ &m_{11}^2 + \frac{\lambda_3(\lambda_{H22} m_H^2 - \lambda_H m_{22}^2)}{\lambda_H \lambda_2 - \lambda_{H22}^2} + \frac{\lambda_{H11}(\lambda_{H22} m_{22}^2 - \lambda_2 m_H^2)}{\lambda_H \lambda_2 - \lambda_{H22}^2} > 0. \end{aligned} \tag{E.7}$$

Those cases are summarized in Table 10. For Type-8 scenario, we refer to Ref. [232] due to the complicity and irrelevance.

Appendix F Further Description for the Phase Transition Process

The effective potential is a polynomial of the fields $(h_0, \omega_3, \varphi_2)$ up to quartic terms by renormalizibility. The coefficients of the quartic terms are required to be positive as the potential is bounded from below. For the quadratic terms, they can be generically put into the form

$$V \sim D_i(T^2 - T_i^2)\phi_i^2 \tag{F.1}$$

with ϕ_i denoting one of the three fields. For $D_i > 0$ and $T > T_i$, this term remains positive and enforces a minimum at $\phi_i = 0$, which is in a symmetric phase. As T decreases below T_i, the minimum at $\phi_i = 0$ will roll away from the origin and takes a non-zero value, corresponding to a continuous phase transition. This is indeed what happens for the continuous transitions in Eq. (6.85) and Eq. (6.86), where the potential minimum corresponds to a non-zero field value at some temperature. The same story can happen to any of the three fields. If the parameters are such that two minima coexist across a time duration, then a first order phase transition can happen when the universe tunnels from one minimum to another, characteristic for a first-order phase transition (FOPT), as shown in these two benchmarks in the text. This analytical understanding can provide a way of identifying the parameter space giving a first order phase transition, as demonstrated in [276, 186]. In practice, however, there is a challenge in this procedure. Whether or not a transition takes place between two coexisting minima depends on the tunneling probability and it is sensitive to the potential shape such as the height of the barrier separating them and the potential difference at the two minima, which however is difficult to understand analytically (see [277, 268] for relevant analyses and discussions). This presents an uncertainty for the presence of a FOPT even if we perceive the coexistence of two minima at the same time. As such, some numerical techniques, such as scanning over a large parameter space, may be unavoidable, as we did in our analyses.

There are also subtleties in classifying second-order/higher-order phase transitions and a smooth cross-over. A proper classification could be specified by a dimensionless susceptibility, see, *e.g.* Ref. [227].

Bibliography

[1] Ivan Esteban, M. C. Gonzalez-Garcia, Michele Maltoni, Ivan Martinez-Soler, and Jordi Salvado. Updated constraints on non-standard interactions from global analysis of oscillation data. JHEP, 08:180, 2018. [Addendum: JHEP 12, 152 (2020)].

[2] D. S. Akerib et al. Projected WIMP Sensitivity of the LUX-ZEPLIN (LZ) Dark Matter Experiment. 2018.

[3] J. Aalbers et al. DARWIN: towards the ultimate dark matter detector. JCAP, 1611:017, 2016.

[4] Georges Aad et al. Constraints on new phenomena via Higgs boson couplings and invisible decays with the ATLAS detector. JHEP, 11:206, 2015.

[5] Adam Falkowski, Christian Gross, and Oleg Lebedev. A second Higgs from the Higgs portal. JHEP, 05:057, 2015.

[6] Morad Aaboud et al. Combination of searches for heavy resonances decaying into bosonic and leptonic final states using 36 fb^{-1} of proton-proton collision data at $\sqrt{s} = 13$ TeV with the ATLAS detector. Phys. Rev., D98:052008, 2018.

[7] D. Lpez-Val and T. Robens. Δr and the W-boson mass in the singlet extension of the standard model. Phys. Rev., D90:114018, 2014.

[8] M. Tanabashi et al. Review of Particle Physics. Phys. Rev. D, 98(3):030001, 2018.

[9] L. Wolfenstein. Neutrino Oscillations in Matter. Phys. Rev. D, 17:2369–2374, 1978.

[10] Tommy Ohlsson. Status of non-standard neutrino interactions. Rept. Prog. Phys., 76:044201, 2013.

[11] O. G. Miranda and H. Nunokawa. Non standard neutrino interactions: current status and future prospects. New J. Phys., 17(9):095002, 2015.

[12] Y. Farzan and M. Tortola. Neutrino oscillations and Non-Standard Interactions. Front.in Phys., 6:10, 2018.

[13] W. Buchmuller and D. Wyler. Effective Lagrangian Analysis of New Interactions and Flavor Conservation. Nucl. Phys. B, 268:621–653, 1986.

[14] B. Grzadkowski, M. Iskrzynski, M. Misiak, and J. Rosiek. Dimension-Six Terms in the Standard Model Lagrangian. JHEP, 10:085, 2010.

[15] Brian Henning, Xiaochuan Lu, and Hitoshi Murayama. How to use the Standard Model effective field theory. JHEP, 01:023, 2016.

[16] Ilaria Brivio and Michael Trott. The Standard Model as an Effective Field Theory. Phys. Rept., 793:1–98, 2019.

[17] S. P. Mikheyev and A. Yu. Smirnov. Resonance Amplification of Oscillations in Matter and Spectroscopy of Solar Neutrinos. Sov. J. Nucl. Phys., 42:913–917, 1985.

[18] Jogesh C. Pati and Abdus Salam. Lepton Number as the Fourth Color. Phys. Rev. D, 10:275–289, 1974. [Erratum: Phys.Rev.D 11, 703–703 (1975)].

[19] R.N. Mohapatra and Jogesh C. Pati. A Natural Left-Right Symmetry. Phys. Rev. D, 11:2558, 1975.

[20] G. Senjanovic and Rabindra N. Mohapatra. Exact Left-Right Symmetry and Spontaneous Violation of Parity. Phys. Rev. D, 12:1502, 1975.

[21] Jogesh C. Pati and Abdus Salam. Unified Lepton-Hadron Symmetry and a Gauge Theory of the Basic Interactions. Phys. Rev. D, 8:1240–1251, 1973.

[22] Ingolf Bischer and Werner Rodejohann. General neutrino interactions from an effective field theory perspective. Nucl. Phys. B, 947:114746, 2019.

[23] Francisco del Aguila, Shaouly Bar-Shalom, Amarjit Soni, and Jose Wudka. Heavy Majorana Neutrinos in the Effective Lagrangian Description: Application to Hadron Colliders. Phys. Lett. B, 670:399–402, 2009.

[24] Alberto Aparici, Kyungwook Kim, Arcadi Santamaria, and Jose Wudka. Right-handed neutrino magnetic moments. Phys. Rev. D, 80:013010, 2009.

[25] Subhaditya Bhattacharya and José Wudka. Dimension-seven operators in the standard model with right handed neutrinos. Phys. Rev. D, 94(5):055022, 2016. [Erratum: Phys.Rev.D 95, 039904 (2017)].

[26] Yi Liao and Xiao-Dong Ma. Operators up to Dimension Seven in Standard Model Effective Field Theory Extended with Sterile Neutrinos. Phys. Rev. D, 96(1):015012, 2017.

[27] Manfred Lindner, Werner Rodejohann, and Xun-Jie Xu. Coherent Neutrino-Nucleus Scattering and new Neutrino Interactions. JHEP, 03:097, 2017.

[28] Gerard Jungman, Marc Kamionkowski, and Kim Griest. Supersymmetric dark matter. Phys. Rept., 267:195–373, 1996.

[29] Gianfranco Bertone, Dan Hooper, and Joseph Silk. Particle dark matter: Evidence, candidates and constraints. Phys. Rept., 405:279–390, 2005.

[30] E. Aprile et al. Dark Matter Search Results from a One Tonne×Year Exposure of XENON1T. Phys. Rev. Lett., 121(11):111302, 2018.

[31] D. S. Akerib et al. Results from a search for dark matter in the complete LUX exposure. Phys. Rev. Lett., 118(2):021303, 2017.

[32] Xiangyi Cui et al. Dark Matter Results From 54-Ton-Day Exposure of PandaX-II Experiment. Phys. Rev. Lett., 119(18):181302, 2017.

[33] Jim Alexander et al. Dark Sectors 2016 Workshop: Community Report. 8 2016.

[34] Wendy L. Freedman. Cosmology at a Crossroads. Nature Astron., 1:0121, 2017.

[35] David N. Spergel and Paul J. Steinhardt. Observational evidence for self-interacting cold dark matter. Phys. Rev. Lett., 84:3760–3763, 2000.

[36] Celine Boehm, Alain Riazuelo, Steen H. Hansen, and Richard Schaeffer. Interacting dark matter disguised as warm dark matter. Phys. Rev. D, 66:083505, 2002.

[37] Mark Vogelsberger, Jesus Zavala, Francis-Yan Cyr-Racine, Christoph Pfrommer, Torsten Bringmann, and Kris Sigurdson. ETHOS –an effective theory of structure formation: dark matter physics as a possible explanation of the small-scale CDM problems. Mon. Not. Roy. Astron. Soc., 460(2):1399–1416, 2016.

[38] Brian Patt and Frank Wilczek. Higgs-field portal into hidden sectors. 5 2006.

[39] D. de Florian et al. Handbook of LHC Higgs Cross Sections: 4. Deciphering the Nature of the Higgs Sector. 2016.

[40] J. de Blas et al. Higgs Boson Studies at Future Particle Colliders. JHEP, 01:139, 2020.

[41] Michael J. Ramsey-Musolf. The electroweak phase transition: a collider target. JHEP, 09:179, 2020.

[42] Anupam Mazumdar and Graham White. Cosmic phase transitions: their applications and experimental signatures. 2018.

[43] Peisi Huang, Andrew J. Long, and Lian-Tao Wang. Probing the Electroweak Phase Transition with Higgs Factories and Gravitational Waves. Phys. Rev., D94(7):075008, 2016.

[44] V.A. Kuzmin, V.A. Rubakov, and M.E. Shaposhnikov. On the Anomalous Electroweak Baryon Number Nonconservation in the Early Universe. Phys. Lett. B, 155:36, 1985.

[45] M.E. Shaposhnikov. Possible Appearance of the Baryon Asymmetry of the Universe in an Electroweak Theory. JETP Lett., 44:465–468, 1986.

[46] M.E. Shaposhnikov. Baryon Asymmetry of the Universe in Standard Electroweak Theory. Nucl. Phys. B, 287:757–775, 1987.

[47] David E. Morrissey and Michael J. Ramsey-Musolf. Electroweak baryogenesis. New J. Phys., 14:125003, 2012.

[48] James M. Cline. Baryogenesis. In Les Houches Summer School - Session 86: Particle Physics and Cosmology: The Fabric of Spacetime Les Houches, France, July 31-August 25, 2006, 2006.

[49] Graham Albert White. A Pedagogical Introduction to Electroweak Baryogenesis. 2016.

[50] A. D. Sakharov. Violation of CP Invariance, C asymmetry, and baryon asymmetry of the universe. Pisma Zh. Eksp. Teor. Fiz., 5:32–35, 1967. [Usp. Fiz. Nauk161,no.5,61(1991)].

[51] Tao Han, Jiajun Liao, Hongkai Liu, and Danny Marfatia. Nonstandard neutrino interactions at COHERENT, DUNE, T2HK and LHC. JHEP, 11:028, 2019.

[52] M. M. Guzzo, A. Masiero, and S. T. Petcov. On the MSW effect with massless neutrinos and no mixing in the vacuum. Phys. Lett. B, 260:154–160, 1991.

[53] Corey Kownacki, Ernest Ma, Nicholas Pollard, and Mohammadreza Zakeri. Generalized Gauge U(1) Family Symmetry for Quarks and Leptons. Phys. Lett. B, 766:149–152, 2017.

[54] A. Konaka et al. Search for Neutral Particles in Electron Beam Dump Experiment. Phys. Rev. Lett., 57:659, 1986.

[55] E. M. Riordan et al. A Search for Short Lived Axions in an Electron Beam Dump Experiment. Phys. Rev. Lett., 59:755, 1987.

[56] J. D. Bjorken, S. Ecklund, W. R. Nelson, A. Abashian, C. Church, B. Lu, L. W. Mo, T. A. Nunamaker, and P. Rassmann. Search for Neutral Metastable Penetrating Particles Produced in the SLAC Beam Dump. Phys. Rev., D38:3375, 1988.

[57] A. Bross, M. Crisler, Stephen H. Pordes, J. Volk, S. Errede, and J. Wrbanek. A Search for Shortlived Particles Produced in an Electron Beam Dump. Phys. Rev. Lett., 67:2942–2945, 1991.

[58] M. Davier and H. Nguyen Ngoc. An Unambiguous Search for a Light Higgs Boson. Phys. Lett., B229:150–155, 1989.

[59] D. Banerjee et al. Search for a Hypothetical 16.7 MeV Gauge Boson and Dark Photons in the NA64 Experiment at CERN. Phys. Rev. Lett., 120(23):231802, 2018.

[60] Julian Heeck, Manfred Lindner, Werner Rodejohann, and Stefan Vogl. Non-Standard Neutrino Interactions and Neutral Gauge Bosons. SciPost Phys., 6(3):038, 2019.

[61] S. Davidson, C. Pena-Garay, N. Rius, and A. Santamaria. Present and future bounds on nonstandard neutrino interactions. JHEP, 03:011, 2003.

[62] Alejandro Ibarra, Eduard Masso, and Javier Redondo. Systematic approach to gauge-invariant relations between lepton flavor violating processes. Nucl. Phys. B, 715:523–535, 2005.

[63] Jiajun Liao, Danny Marfatia, and Kerry Whisnant. Degeneracies in long-baseline neutrino experiments from nonstandard interactions. Phys. Rev. D, 93(9):093016, 2016.

[64] R. Acciarri et al. Long-Baseline Neutrino Facility (LBNF) and Deep Underground Neutrino Experiment (DUNE). 2015.

[65] K. Abe et al. Hyper-Kamiokande Design Report. 2018.

[66] Jiajun Liao, Danny Marfatia, and Kerry Whisnant. Nonstandard neutrino interactions at DUNE, T2HK and T2HKK. JHEP, 01:071, 2017.

[67] D. Akimov et al. The COHERENT Experiment at the Spallation Neutron Source. 2015.

[68] D. Akimov et al. COHERENT Collaboration data release from the first observation of coherent elastic neutrino-nucleus scattering. 2018.

[69] Spencer R. Klein and Joakim Nystrand. Interference in exclusive vector meson production in heavy ion collisions. Phys. Rev. Lett., 84:2330–2333, 2000.

[70] D. Akimov et al. Observation of Coherent Elastic Neutrino-Nucleus Scattering. Science, 357(6356):1123–1126, 2017.

[71] J. I. Collar, A. R. L. Kavner, and C. M. Lewis. Response of CsI[Na] to Nuclear Recoils: Impact on Coherent Elastic Neutrino-Nucleus Scattering (CEνNS). 2019.

[72] Alexey Konovalov. private communication.

[73] D. Akimov et al. COHERENT 2018 at the Spallation Neutron Source. 2018.

[74] Bhaskar Dutta, Shu Liao, Samiran Sinha, and Louis E. Strigari. Searching for Beyond the Standard Model Physics with COHERENT Energy and Timing Data. 2019.

[75] D. Aristizabal Sierra, Jiajun Liao, and D. Marfatia. Impact of form factor uncertainties on interpretations of coherent elastic neutrino-nucleus scattering data. JHEP, 06:141, 2019.

[76] J. Alwall, R. Frederix, S. Frixione, V. Hirschi, F. Maltoni, O. Mattelaer, H. S. Shao, T. Stelzer, P. Torrielli, and M. Zaro. The automated computation of tree-level and

next-to-leading order differential cross sections, and their matching to parton shower simulations. JHEP, 07:079, 2014.

[77] Richard D. Ball, Valerio Bertone, Stefano Carrazza, Luigi Del Debbio, Stefano Forte, Alberto Guffanti, Nathan P. Hartland, and Juan Rojo. Parton distributions with QED corrections. Nucl. Phys., B877:290–320, 2013.

[78] Adam Alloul, Neil D. Christensen, Cline Degrande, Claude Duhr, and Benjamin Fuks. FeynRules 2.0 - A complete toolbox for tree-level phenomenology. Comput. Phys. Commun., 185:2250–2300, 2014.

[79] Torbjorn Sjostrand, Stephen Mrenna, and Peter Z. Skands. PYTHIA 6.4 Physics and Manual. JHEP, 05:026, 2006.

[80] Torbjorn Sjostrand, Stephen Mrenna, and Peter Z. Skands. A Brief Introduction to PYTHIA 8.1. Comput. Phys. Commun., 178:852–867, 2008.

[81] Johan Alwall et al. Comparative study of various algorithms for the merging of parton showers and matrix elements in hadronic collisions. Eur. Phys. J., C53:473–500, 2008.

[82] J. de Favereau, C. Delaere, P. Demin, A. Giammanco, V. Lematre, A. Mertens, and M. Selvaggi. DELPHES 3, A modular framework for fast simulation of a generic collider experiment. JHEP, 02:057, 2014.

[83] Georges Aad et al. Search for high-mass dilepton resonances using 139 fb^{-1} of pp collision data collected at $\sqrt{s}$ =13 TeV with the ATLAS detector. 2019.

[84] Vardan Khachatryan et al. Search for narrow resonances in dilepton mass spectra in proton-proton collisions at $\sqrt{s} = 13$ TeV and combination with 8 TeV data. Phys. Lett., B768:57–80, 2017.

[85] Roel Aaij et al. Search for $A' \to \mu^+\mu^-$ decays. 2019.

[86] Philip Ilten, Yotam Soreq, Mike Williams, and Wei Xue. Serendipity in dark photon searches. JHEP, 06:004, 2018.

[87] J. P. Lees et al. Search for a muonic dark force at BABAR. Phys. Rev., D94(1):011102, 2016.

[88] Albert M Sirunyan et al. Search for an $L_\mu - L_\tau$ gauge boson using Z$\to 4\mu$ events in proton-proton collisions at $\sqrt{s} = 13$ TeV. Phys. Lett., B792:345–368, 2019.

[89] Luca Barze, Guido Montagna, Paolo Nason, Oreste Nicrosini, Fulvio Piccinini, and Alessandro Vicini. Neutral current Drell-Yan with combined QCD and electroweak corrections in the POWHEG BOX. Eur. Phys. J., C73(6):2474, 2013.

[90] https://twiki.cern.ch/twiki/bin/view/LHCPhysics/TtbarNNLO.

[91] Nikolaos Kidonakis. Two-loop soft anomalous dimensions for single top quark associated production with a W- or H-. Phys. Rev., D82:054018, 2010.

[92] T. Gehrmann, M. Grazzini, S. Kallweit, P. MaierhÃfer, A. von Manteuffel, S. Pozzorini, D. Rathlev, and L. Tancredi. W^+W^- Production at Hadron Colliders in Next to Next to Leading Order QCD. Phys. Rev. Lett., 113(21):212001, 2014.

[93] Massimiliano Grazzini, Stefan Kallweit, Dirk Rathlev, and Marius Wiesemann. $W^\pm Z$ production at hadron colliders in NNLO QCD. Phys. Lett., B761:179–183, 2016.

[94] F. Cascioli, T. Gehrmann, M. Grazzini, S. Kallweit, P. MaierhÃfer, A. von Manteuffel, S. Pozzorini, D. Rathlev, L. Tancredi, and E. Weihs. ZZ production at hadron colliders in NNLO QCD. Phys. Lett., B735:311–313, 2014.

[95] Morad Aaboud et al. Search for additional heavy neutral Higgs and gauge bosons in the ditau final state produced in 36 fb^{-1} of pp collisions at $\sqrt{s} = 13$ TeV with the ATLAS detector. JHEP, 01:055, 2018.

[96] Vardan Khachatryan et al. Search for heavy resonances decaying to tau lepton pairs in proton-proton collisions at $\sqrt{s} = 13$ TeV. JHEP, 02:048, 2017.

[97] Kaoru Hagiwara, Tong Li, Kentarou Mawatari, and Junya Nakamura. TauDecay: a library to simulate polarized tau decays via FeynRules and MadGraph5. Eur. Phys. J., C73:2489, 2013.

[98] Radja Boughezal, Xiaohui Liu, and Frank Petriello. W-boson plus jet differential distributions at NNLO in QCD. Phys. Rev., D94(11):113009, 2016.

[99] Elizabeth E. Jenkins, Aneesh V. Manohar, and Michael Trott. Renormalization Group Evolution of the Standard Model Dimension Six Operators I: Formalism and lambda Dependence. JHEP, 10:087, 2013.

[100] Elizabeth E. Jenkins, Aneesh V. Manohar, and Michael Trott. Renormalization Group Evolution of the Standard Model Dimension Six Operators II: Yukawa Dependence. JHEP, 01:035, 2014.

[101] Rodrigo Alonso, Elizabeth E. Jenkins, Aneesh V. Manohar, and Michael Trott. Renormalization Group Evolution of the Standard Model Dimension Six Operators III: Gauge Coupling Dependence and Phenomenology. JHEP, 04:159, 2014.

[102] K. N. Abazajian et al. Light Sterile Neutrinos: A White Paper. 4 2012.

[103] Nicole F. Bell, Vincenzo Cirigliano, Michael J. Ramsey-Musolf, Petr Vogel, and Mark B. Wise. How magnetic is the Dirac neutrino? Phys. Rev. Lett., 95:151802, 2005.

[104] Mikael Chala and Arsenii Titov. One-loop running of dimension-six Higgs-neutrino operators and implications of a large neutrino dipole moment. JHEP, 09:188, 2020.

[105] Tao Han, Jiajun Liao, Hongkai Liu, and Danny Marfatia. Scalar and tensor neutrino interactions. JHEP, 07:207, 2020.

[106] Alakabha Datta, Jacky Kumar, Hongkai Liu, and Danny Marfatia. Anomalous dimensions from gauge couplings in SMEFT with right-handed neutrinos. JHEP, 02:015, 2021.

[107] Alakabha Datta, Jacky Kumar, Hongkai Liu, and Danny Marfatia. Anomalous dimensions from Yukawa couplings in SMNEFT: four-fermion operators. 3 2021.

[108] Gary Prezeau and Andriy Kurylov. Neutrino mass constraints on mu-decay and $\pi_0 \to \nu\bar{\nu}$. Phys. Rev. Lett., 95:101802, 2005.

[109] Takeyasu M. Ito and Gary Prezeau. Neutrino mass constraints on beta decay. Phys. Rev. Lett., 94:161802, 2005.

[110] Arthur Loureiro et al. On The Upper Bound of Neutrino Masses from Combined Cosmological Observations and Particle Physics Experiments. Phys. Rev. Lett., 123(8):081301, 2019.

[111] M. Aker et al. Improved Upper Limit on the Neutrino Mass from a Direct Kinematic Method by KATRIN. Phys. Rev. Lett., 123(22):221802, 2019.

[112] Xun-Jie Xu. Tensor and scalar interactions of neutrinos may lead to observable neutrino magnetic moments. Phys. Rev., D99(7):075003, 2019.

[113] Vincenzo Cirigliano and Ignasi Rosell. Two-loop effective theory analysis of $\pi(K) \to e\bar{\nu}_e[\gamma]$ branching ratios. Phys. Rev. Lett., 99:231801, 2007.

[114] Vincenzo Cirigliano, Susan Gardner, and Barry Holstein. Beta Decays and Non-Standard Interactions in the LHC Era. Prog. Part. Nucl. Phys., 71:93–118, 2013.

[115] D. I. Britton et al. Measurement of the $\pi^+ \to e^+$ neutrino branching ratio. Phys. Rev. Lett., 68:3000–3003, 1992.

[116] D. I. Britton et al. Measurement of the $\pi^+ \to e^+$ neutrino branching ratio. Phys. Rev., D49:28–39, 1994.

[117] G. Czapek et al. Branching ratio for the rare pion decay into positron and neutrino. Phys. Rev. Lett., 70:17–20, 1993.

[118] Vincenzo Cirigliano and Ignasi Rosell. $\pi/K \to e\bar{\nu}_e$ branching ratios to $\mathrm{O}(e^2p^4)$ in Chiral Perturbation Theory. JHEP, 10:005, 2007.

[119] B. Ananthanarayan and B. Moussallam. Four-point correlator constraints on electromagnetic chiral parameters and resonance effective Lagrangians. JHEP, 06:047, 2004.

[120] Sebastien Descotes-Genon and Bachir Moussallam. Radiative corrections in weak semi-leptonic processes at low energy: A Two-step matching determination. Eur. Phys. J., C42:403–417, 2005.

[121] S. Aoki et al. FLAG Review 2019: Flavour Lattice Averaging Group (FLAG). Eur. Phys. J., C80(2):113, 2020.

[122] Martin Gonzalez-Alonso, Oscar Naviliat-Cuncic, and Nathal Severijns. New physics searches in nuclear and neutron β decay. Prog. Part. Nucl. Phys., 104:165–223, 2019.

[123] Jens Erler and Shufang Su. The Weak Neutral Current. Prog. Part. Nucl. Phys., 71:119–149, 2013.

[124] J. Dorenbosch et al. Experimental Verification of the Universality of ν_e and ν_μ Coupling to the Neutral Weak Current. Phys. Lett., B180:303–307, 1986.

[125] G. P. Zeller et al. A Precise Determination of Electroweak Parameters in Neutrino Nucleon Scattering. Phys. Rev. Lett., 88:091802, 2002. [Erratum: Phys. Rev. Lett.90,239902(2003)].

[126] Hung-Liang Lai, Marco Guzzi, Joey Huston, Zhao Li, Pavel M. Nadolsky, Jon Pumplin, and C. P. Yuan. New parton distributions for collider physics. Phys. Rev., D82:074024, 2010.

[127] D. B. Clark, E. Godat, and F. I. Olness. ManeParse : A Mathematica reader for Parton Distribution Functions. Comput. Phys. Commun., 216:126–137, 2017.

[128] W. Bentz, I. C. Cloet, J. T. Londergan, and A. W. Thomas. Reassessment of the NuTeV determination of the weak mixing angle. Phys. Lett., B693:462–466, 2010.

[129] Martin Hoferichter, J. Ruiz de Elvira, Bastian Kubis, and Ulf-G. Meiner. High-Precision Determination of the Pion-Nucleon σ Term from Roy-Steiner Equations. Phys. Rev. Lett., 115:092301, 2015.

[130] Tanmoy Bhattacharya, Vincenzo Cirigliano, Saul Cohen, Rajan Gupta, Huey-Wen Lin, and Boram Yoon. Axial, Scalar and Tensor Charges of the Nucleon from 2+1+1-flavor Lattice QCD. Phys. Rev. D, 94(5):054508, 2016.

[131] Julien Alcaide, Shankha Banerjee, Mikael Chala, and Arsenii Titov. Probes of the Standard Model effective field theory extended with a right-handed neutrino. JHEP, 08:031, 2019.

[132] Torbjrn Sjstrand, Stefan Ask, Jesper R. Christiansen, Richard Corke, Nishita Desai, Philip Ilten, Stephen Mrenna, Stefan Prestel, Christine O. Rasmussen, and Peter Z. Skands. An Introduction to PYTHIA 8.2. Comput. Phys. Commun., 191:159–177, 2015.

[133] Georges Aad et al. Search for a heavy charged boson in events with a charged lepton and missing transverse momentum from pp collisions at $\sqrt{s} = 13$ TeV with the ATLAS detector. Phys. Rev., D100(5):052013, 2019.

[134] Prospects for searches for heavy Z' and W' bosons in fermionic final states with the ATLAS experiment at the HL-LHC. Technical Report ATL-PHYS-PUB-2018-044, CERN, Geneva, Dec 2018.

[135] Fernando Cornet and Javier Rico. Contact terms in charged current processes at HERA. Phys. Lett., B412:343–349, 1997.

[136] Marco Cirelli, Nicolao Fornengo, and Alessandro Strumia. Minimal dark matter. Nucl. Phys., B753:178–194, 2006.

[137] Marco Cirelli, Alessandro Strumia, and Matteo Tamburini. Cosmology and Astrophysics of Minimal Dark Matter. Nucl. Phys., B787:152–175, 2007.

[138] Junji Hisano, Koji Ishiwata, and Natsumi Nagata. A complete calculation for direct detection of Wino dark matter. Phys. Lett., B690:311–315, 2010.

[139] Junji Hisano, Koji Ishiwata, and Natsumi Nagata. QCD Effects on Direct Detection of Wino Dark Matter. JHEP, 06:097, 2015.

[140] Louis E. Strigari. Neutrino Coherent Scattering Rates at Direct Dark Matter Detectors. New J. Phys., 11:105011, 2009.

[141] J. Billard, L. Strigari, and E. Figueroa-Feliciano. Implication of neutrino backgrounds on the reach of next generation dark matter direct detection experiments. Phys. Rev., D89(2):023524, 2014.

[142] Philipp Grothaus, Malcolm Fairbairn, and Jocelyn Monroe. Directional Dark Matter Detection Beyond the Neutrino Bound. Phys. Rev., D90(5):055018, 2014.

[143] Ciaran A. J. O'Hare, Anne M. Green, Julien Billard, Enectali Figueroa-Feliciano, and Louis E. Strigari. Readout strategies for directional dark matter detection beyond the neutrino background. Phys. Rev., D92(6):063518, 2015.

[144] Clifford Cheung, Lawrence J. Hall, David Pinner, and Joshua T. Ruderman. Prospects and Blind Spots for Neutralino Dark Matter. JHEP, 05:100, 2013.

[145] Athanasios Dedes and Dimitrios Karamitros. Doublet-Triplet Fermionic Dark Matter. Phys. Rev., D89(11):115002, 2014.

[146] Peisi Huang and Carlos E. M. Wagner. Blind Spots for neutralino Dark Matter in the MSSM with an intermediate m_A. Phys. Rev., D90(1):015018, 2014.

[147] Andreas Crivellin, Martin Hoferichter, Massimiliano Procura, and Lewis C. Tunstall. Light stops, blind spots, and isospin violation in the MSSM. JHEP, 07:129, 2015.

[148] Ayres Freitas, Susanne Westhoff, and Jure Zupan. Integrating in the Higgs Portal to Fermion Dark Matter. JHEP, 09:015, 2015.

[149] Shankha Banerjee, Shigeki Matsumoto, Kyohei Mukaida, and Yue-Lin Sming Tsai. WIMP Dark Matter in a Well-Tempered Regime: A case study on Singlet-Doublets Fermionic WIMP. JHEP, 11:070, 2016.

[150] Tao Han, Felix Kling, Shufang Su, and Yongcheng Wu. Unblinding the dark matter blind spots. JHEP, 02:057, 2017.

[151] Sebastian Baum, Marcela Carena, Nausheen R. Shah, and Carlos E. M. Wagner. Higgs portals for thermal Dark Matter. EFT perspectives and the NMSSM. JHEP, 04:069, 2018.

[152] Rakhi Mahbubani and Leonardo Senatore. The Minimal model for dark matter and unification. Phys. Rev., D73:043510, 2006.

[153] Francesco D'Eramo. Dark matter and Higgs boson physics. Phys. Rev., D76:083522, 2007.

[154] Tao Han, Hongkai Liu, Satyanarayan Mukhopadhyay, and Xing Wang. Dark Matter Blind Spots at One-Loop. JHEP, 03:080, 2019.

[155] Clifford Cheung and David Sanford. Simplified Models of Mixed Dark Matter. JCAP, 1402:011, 2014.

[156] Thomas Hahn. Generating Feynman diagrams and amplitudes with FeynArts 3. Comput. Phys. Commun., 140:418–431, 2001.

[157] Vladyslav Shtabovenko, Rolf Mertig, and Frederik Orellana. New Developments in FeynCalc 9.0. Comput. Phys. Commun., 207:432–444, 2016.

[158] R. Mertig, M. Bohm, and Ansgar Denner. FEYN CALC: Computer algebraic calculation of Feynman amplitudes. Comput. Phys. Commun., 64:345–359, 1991.

[159] Ansgar Denner, Stefan Dittmaier, and Lars Hofer. Collier: a fortran-based Complex One-Loop LIbrary in Extended Regularizations. Comput. Phys. Commun., 212:220–238, 2017.

[160] Ansgar Denner and S. Dittmaier. Reduction of one loop tensor five point integrals. Nucl. Phys., B658:175–202, 2003.

[161] Ansgar Denner and S. Dittmaier. Reduction schemes for one-loop tensor integrals. Nucl. Phys., B734:62–115, 2006.

[162] A. Denner and S. Dittmaier. Scalar one-loop 4-point integrals. Nucl. Phys., B844:199–242, 2011.

[163] Nikhil Anand, A. Liam Fitzpatrick, and W. C. Haxton. Weakly interacting massive particle-nucleus elastic scattering response. Phys. Rev., C89(6):065501, 2014.

[164] C. Amole et al. Dark Matter Search Results from the PICO-2L C_3F_8 Bubble Chamber. Phys. Rev. Lett., 114(23):231302, 2015.

[165] C. Amole et al. Dark matter search results from the PICO-60 CF_3I bubble chamber. Phys. Rev., D93(5):052014, 2016.

[166] C. Amole et al. Dark Matter Search Results from the PICO-60 C_3F_8 Bubble Chamber. Phys. Rev. Lett., 118(25):251301, 2017.

[167] Morad Aaboud et al. Search for electroweak production of supersymmetric particles in final states with two or three leptons at $\sqrt{s} = 13\,\mathrm{TeV}$ with the ATLAS detector. 2018.

[168] A. M. Sirunyan et al. Search for electroweak production of charginos and neutralinos in multilepton final states in proton-proton collisions at $\sqrt{s} = 13$ TeV. JHEP, 03:166, 2018.

[169] Search for Supersymmetry at the high luminosity LHC with the ATLAS experiment. Technical Report ATL-PHYS-PUB-2014-010, CERN, Geneva, Jul 2014.

[170] Supersymmetry discovery potential in future LHC and HL-LHC running with the CMS detector. Technical Report CMS-PAS-SUS-14-012, CERN, Geneva, 2015.

[171] Amin Aboubrahim and Pran Nath. Supersymmetry at a 28 TeV hadron collider: HE-LHC. Phys. Rev., D98(1):015009, 2018.

[172] Tao Han, Satyanarayan Mukhopadhyay, and Xing Wang. Electroweak Dark Matter at Future Hadron Colliders. Phys. Rev., D98(3):035026, 2018.

[173] Morad Aaboud et al. Search for squarks and gluinos in final states with jets and missing transverse momentum at $\sqrt{s} = 13$ TeV with the ATLAS detector. Eur. Phys. J., C76(7):392, 2016.

[174] Tathagata Ghosh, Huai-Ke Guo, Tao Han, and Hongkai Liu. Electroweak Phase Transition with an SU(2) Dark Sector. 12 2020.

[175] Thomas Hambye. Hidden vector dark matter. JHEP, 01:028, 2009.

[176] S. Baek, P. Ko, and Wan-Il Park. Hidden sector monopole, vector dark matter and dark radiation with Higgs portal. JCAP, 10:067, 2014.

[177] Cheng-Wei Chiang, Takaaki Nomura, and Jusak Tandean. Nonabelian Dark Matter with Resonant Annihilation. JHEP, 01:183, 2014.

[178] Valentin V. Khoze and Gunnar Ro. Dark matter monopoles, vectors and photons. JHEP, 10:061, 2014.

[179] Celine Boehm, Matthew J. Dolan, and Christopher McCabe. A weighty interpretation of the Galactic Centre excess. Phys. Rev. D, 90(2):023531, 2014.

[180] Chuan-Hung Chen and Takaaki Nomura. $SU(2)_X$ vector DM and Galactic Center gamma-ray excess. Phys. Lett. B, 746:351–358, 2015.

[181] Chuan-Hung Chen and Takaaki Nomura. Searching for vector dark matter via Higgs portal at the LHC. Phys. Rev. D, 93(7):074019, 2016.

[182] Christian Gross, Oleg Lebedev, and Yann Mambrini. Non-Abelian gauge fields as dark matter. JHEP, 08:158, 2015.

[183] Ryuji Daido, Shu-Yu Ho, and Fuminobu Takahashi. Hidden monopole dark matter via axion portal and its implications for direct detection searches, beam-dump experiments, and the H_0 tension. JHEP, 01:185, 2020.

[184] P. Ko, Takaaki Nomura, and Hiroshi Okada. Dark matter physics in dark $SU(2)$ gauge symmetry with non-Abelian kinetic mixing. 7 2020.

[185] Eleanor Hall, Thomas Konstandin, Robert McGehee, Hitoshi Murayama, and Géraldine Servant. Baryogenesis From a Dark First-Order Phase Transition. JHEP, 04:042, 2020.

[186] Jose R. Espinosa, Thomas Konstandin, and Francesco Riva. Strong Electroweak Phase Transitions in the Standard Model with a Singlet. Nucl. Phys., B854:592–630, 2012.

[187] Ken'ichi Saikawa. A review of gravitational waves from cosmic domain walls. Universe, 3(2):40, 2017.

[188] A. Arhrib, R. Benbrik, M. Chabab, G. Moultaka, M.C. Peyranere, L. Rahili, and J. Ramadan. The Higgs Potential in the Type II Seesaw Model. Phys. Rev. D, 84:095005, 2011.

[189] Alexandre Poulin and Stephen Godfrey. Multicomponent dark matter from a hidden gauged SU(3). Phys. Rev. D, 99(7):076008, 2019.

[190] Ligong Bian, Tianjun Li, Jing Shu, and Xiao-Chuan Wang. Two component dark matter with multi-Higgs portals. JHEP, 03:126, 2015.

[191] Tania Robens and Tim Stefaniak. Status of the Higgs Singlet Extension of the Standard Model after LHC Run 1. Eur. Phys. J., C75:104, 2015.

[192] Ashutosh V. Kotwal, Michael J. Ramsey-Musolf, Jose Miguel No, and Peter Winslow. Singlet-catalyzed electroweak phase transitions in the 100 TeV frontier. Phys. Rev., D94(3):035022, 2016.

[193] T. Huang, J. M. No, L. Perni, M. Ramsey-Musolf, A. Safonov, M. Spannowsky, and P. Winslow. Resonant di-Higgs boson production in the $b\bar{b}WW$ channel: Probing the electroweak phase transition at the LHC. Phys. Rev., D96(3):035007, 2017.

[194] Alexandre Alves, Dorival Gonalves, Tathagata Ghosh, Huai-Ke Guo, and Kuver Sinha. Di-Higgs Production in the $4b$ Channel and Gravitational Wave Complementarity. JHEP, 03:053, 2020.

[195] Shekhar Adhikari, Ian M. Lewis, and Matthew Sullivan. Beyond the Standard Model Effective Field Theory: The Singlet Extended Standard Model. 3 2020.

[196] Seungwon Baek, P. Ko, and Wan-Il Park. Search for the Higgs portal to a singlet fermionic dark matter at the LHC. JHEP, 02:047, 2012.

[197] Study of the double Higgs production channel $H(\to b\bar{b})H(\to \gamma\gamma)$ with the ATLAS experiment at the HL-LHC. 1 2017.

[198] Projected performance of Higgs analyses at the HL-LHC for ECFA 2016. 2017.

[199] Junping Tian and Keisuke Fujii. Measurement of Higgs couplings and self-coupling at the ILC. PoS, EPS-HEP2013:316, 2013.

[200] Philipp Roloff, Ulrike Schnoor, Rosa Simoniello, and Boruo Xu. Double Higgs boson production and Higgs self-coupling extraction at CLIC. Eur. Phys. J. C, 80(11):1010, 2020.

[201] A. Abada et al. FCC-hh: The Hadron Collider: Future Circular Collider Conceptual Design Report Volume 3. Eur. Phys. J. ST, 228(4):755–1107, 2019.

[202] Tao Han, Da Liu, Ian Low, and Xing Wang. Electroweak couplings of the Higgs boson at a multi-TeV muon collider. Phys. Rev. D, 103(1):013002, 2021.

[203] Jonathan L. Feng, Huitzu Tu, and Hai-Bo Yu. Thermal Relics in Hidden Sectors. JCAP, 10:043, 2008.

[204] Y. Akrami et al. Planck 2018 results. I. Overview and the cosmological legacy of Planck. 7 2018.

[205] N. Aghanim et al. Planck 2018 results. VI. Cosmological parameters. 7 2018.

[206] Kevork Abazajian et al. CMB-S4 Science Case, Reference Design, and Project Plan. 7 2019.

[207] P.A.R. Ade et al. Planck 2015 results. XIII. Cosmological parameters. Astron. Astrophys., 594:A13, 2016.

[208] Lotty Ackerman, Matthew R. Buckley, Sean M. Carroll, and Marc Kamionkowski. Dark Matter and Dark Radiation. pages 277–286, 10 2008.

[209] Mark Srednicki, Richard Watkins, and Keith A. Olive. Calculations of Relic Densities in the Early Universe. Nucl. Phys. B, 310:693, 1988.

[210] G. Belanger, F. Boudjema, A. Pukhov, and A. Semenov. micrOMEGAs_3: A program for calculating dark matter observables. Comput. Phys. Commun., 185:960–985, 2014.

[211] Junji Hisano, Koji Ishiwata, Natsumi Nagata, and Masato Yamanaka. Direct Detection of Vector Dark Matter. Prog. Theor. Phys., 126:435–456, 2011.

[212] Volker Springel et al. Simulating the joint evolution of quasars, galaxies and their large-scale distribution. Nature, 435:629–636, 2005.

[213] James S. Bullock and Michael Boylan-Kolchin. Small-Scale Challenges to the ΛCDM Paradigm. Ann. Rev. Astron. Astrophys., 55:343–387, 2017.

[214] Jonathan L. Feng, Manoj Kaplinghat, Huitzu Tu, and Hai-Bo Yu. Hidden Charged Dark Matter. JCAP, 07:004, 2009.

[215] Prateek Agrawal, Francis-Yan Cyr-Racine, Lisa Randall, and Jakub Scholtz. Make Dark Matter Charged Again. JCAP, 05:022, 2017.

[216] Jesus Zavala, Mark Vogelsberger, and Matthew G. Walker. Constraining Self-Interacting Dark Matter with the Milky Way's dwarf spheroidals. Mon. Not. Roy. Astron. Soc., 431:L20–L24, 2013.

[217] Mark B. Hindmarsh, Marvin Lüben, Johannes Lumma, and Martin Pauly. Phase transitions in the early universe. 8 2020.

[218] K. Farakos, K. Kajantie, K. Rummukainen, and Mikhail E. Shaposhnikov. 3-d physics and the electroweak phase transition: A Framework for lattice Monte Carlo analysis. Nucl. Phys. B, 442:317–363, 1995.

[219] K. Kajantie, M. Laine, K. Rummukainen, and Mikhail E. Shaposhnikov. The Electroweak phase transition: A Nonperturbative analysis. Nucl. Phys. B, 466:189–258, 1996.

[220] Guy D. Moore and Kari Rummukainen. Electroweak bubble nucleation, nonperturbatively. Phys. Rev. D, 63:045002, 2001.

[221] Andrei D. Linde. Infrared Problem in Thermodynamics of the Yang-Mills Gas. Phys. Lett. B, 96:289–292, 1980.

[222] Tomáš Brauner, Tuomas V. I. Tenkanen, Anders Tranberg, Aleksi Vuorinen, and David J. Weir. Dimensional reduction of the Standard Model coupled to a new singlet scalar field. JHEP, 03:007, 2017.

[223] Jens O. Andersen, Tyler Gorda, Andreas Helset, Lauri Niemi, Tuomas V. I. Tenkanen, Anders Tranberg, Aleksi Vuorinen, and David J. Weir. Nonperturbative Analysis of

the Electroweak Phase Transition in the Two Higgs Doublet Model. Phys. Rev. Lett., 121(19):191802, 2018.

[224] Lauri Niemi, Hiren H. Patel, Michael J. Ramsey-Musolf, Tuomas V.I. Tenkanen, and David J. Weir. Electroweak phase transition in the real triplet extension of the SM: Dimensional reduction. Phys. Rev. D, 100(3):035002, 2019.

[225] Tyler Gorda, Andreas Helset, Lauri Niemi, Tuomas V.I. Tenkanen, and David J. Weir. Three-dimensional effective theories for the two Higgs doublet model at high temperature. JHEP, 02:081, 2019.

[226] Oliver Gould, Jonathan Kozaczuk, Lauri Niemi, Michael J. Ramsey-Musolf, Tuomas V.I. Tenkanen, and David J. Weir. Nonperturbative analysis of the gravitational waves from a first-order electroweak phase transition. Phys. Rev. D, 100(11):115024, 2019.

[227] Lauri Niemi, Michael Ramsey-Musolf, Tuomas V.I. Tenkanen, and David J. Weir. Thermodynamics of a two-step electroweak phase transition. 5 2020.

[228] Djuna Croon, Oliver Gould, Philipp Schicho, Tuomas V.I. Tenkanen, and Graham White. Theoretical uncertainties for cosmological first-order phase transitions. 9 2020.

[229] Andreas Papaefstathiou and Graham White. The Electro-Weak Phase Transition at Colliders: Confronting Theoretical Uncertainties and Complementary Channels. 10 2020.

[230] Hiren H. Patel and Michael J. Ramsey-Musolf. Baryon Washout, Electroweak Phase Transition, and Perturbation Theory. JHEP, 07:029, 2011.

[231] Mariano Quiros. Finite temperature field theory and phase transitions. In Proceedings, Summer School in High-energy physics and cosmology: Trieste, Italy, June 29-July 17, 1998, pages 187–259, 1999.

[232] Thibault Vieu, Antnio P. Morais, and Roman Pasechnik. Electroweak phase transitions in multi-Higgs models: the case of Trinification-inspired THDSM. JCAP, 1807(07):014, 2018.

[233] Hiren H. Patel and Michael J. Ramsey-Musolf. Stepping Into Electroweak Symmetry Breaking: Phase Transitions and Higgs Phenomenology. Phys. Rev., D88:035013, 2013.

[234] Chiara Caprini et al. Science with the space-based interferometer eLISA. II: Gravitational waves from cosmological phase transitions. JCAP, 1604(04):001, 2016.

[235] Michael S. Turner, Erick J. Weinberg, and Lawrence M. Widrow. Bubble nucleation in first order inflation and other cosmological phase transitions. Phys. Rev., D46:2384–2403, 1992.

[236] Carroll L. Wainwright. CosmoTransitions: Computing Cosmological Phase Transition Temperatures and Bubble Profiles with Multiple Fields. Comput. Phys. Commun., 183:2006–2013, 2012.

[237] Huai-Ke Guo, Kuver Sinha, Daniel Vagie, and Graham White. Phase Transitions in an Expanding Universe: Stochastic Gravitational Waves in Standard and Non-Standard Histories. 7 2020.

[238] Riccardo Apreda, Michele Maggiore, Alberto Nicolis, and Antonio Riotto. Gravitational waves from electroweak phase transitions. Nucl. Phys., B631:342–368, 2002.

[239] Mark Hindmarsh and Mulham Hijazi. Gravitational waves from first order cosmological phase transitions in the Sound Shell Model. JCAP, 1912(12):062, 2019.

[240] Dietrich Bodeker and Guy D. Moore. Electroweak Bubble Wall Speed Limit. JCAP, 1705(05):025, 2017.

[241] Rong-Gen Cai, Zhoujian Cao, Zong-Kuan Guo, Shao-Jiang Wang, and Tao Yang. The Gravitational-Wave Physics. Natl. Sci. Rev., 4:687–706, 2017.

[242] Chiara Caprini and Daniel G. Figueroa. Cosmological Backgrounds of Gravitational Waves. Class. Quant. Grav., 35(16):163001, 2018.

[243] Joseph D. Romano and Neil J. Cornish. Detection methods for stochastic gravitational-wave backgrounds: a unified treatment. Living Rev. Rel., 20:2, 2017.

[244] Nelson Christensen. Stochastic Gravitational Wave Backgrounds. Rept. Prog. Phys., 82(1):016903, 2019.

[245] Ryusuke Jinno and Masahiro Takimoto. Gravitational waves from bubble collisions: An analytic derivation. Phys. Rev., D95(2):024009, 2017.

[246] Stephan J. Huber and Thomas Konstandin. Gravitational Wave Production by Collisions: More Bubbles. JCAP, 0809:022, 2008.

[247] Arthur Kosowsky, Michael S. Turner, and Richard Watkins. Gravitational waves from first order cosmological phase transitions. Phys. Rev. Lett., 69:2026–2029, 1992.

[248] Arthur Kosowsky, Michael S. Turner, and Richard Watkins. Gravitational radiation from colliding vacuum bubbles. Phys. Rev., D45:4514–4535, 1992.

[249] Arthur Kosowsky and Michael S. Turner. Gravitational radiation from colliding vacuum bubbles: envelope approximation to many bubble collisions. Phys. Rev., D47:4372–4391, 1993.

[250] Ryusuke Jinno and Masahiro Takimoto. Gravitational waves from bubble dynamics: Beyond the Envelope. 2017.

[251] Hillary L. Child and Jr. Giblin, John T. Gravitational Radiation from First-Order Phase Transitions. JCAP, 10:001, 2012.

[252] Daniel Cutting, Mark Hindmarsh, and David J. Weir. Gravitational waves from vacuum first-order phase transitions: from the envelope to the lattice. Phys. Rev. D, 97(12):123513, 2018.

[253] Mark Hindmarsh, Stephan J. Huber, Kari Rummukainen, and David J. Weir. Gravitational waves from the sound of a first order phase transition. Phys. Rev. Lett., 112:041301, 2014.

[254] Mark Hindmarsh, Stephan J. Huber, Kari Rummukainen, and David J. Weir. Numerical simulations of acoustically generated gravitational waves at a first order phase transition. Phys. Rev., D92(12):123009, 2015.

[255] Mark Hindmarsh, Stephan J. Huber, Kari Rummukainen, and David J. Weir. Shape of the acoustic gravitational wave power spectrum from a first order phase transition. Phys. Rev., D96(10):103520, 2017.

[256] Daniel Cutting, Mark Hindmarsh, and David J. Weir. Vorticity, kinetic energy, and suppressed gravitational wave production in strong first order phase transitions. 2019.

[257] Mark Hindmarsh. Sound shell model for acoustic gravitational wave production at a first-order phase transition in the early Universe. Phys. Rev. Lett., 120(7):071301, 2018.

[258] David J. Weir. Gravitational waves from a first order electroweak phase transition: a brief review. Phil. Trans. Roy. Soc. Lond., A376(2114):20170126, 2018.

[259] Jose R. Espinosa, Thomas Konstandin, Jose M. No, and Geraldine Servant. Energy Budget of Cosmological First-order Phase Transitions. JCAP, 1006:028, 2010.

[260] John Ellis, Marek Lewicki, Jos Miguel No, and Ville Vaskonen. Gravitational wave energy budget in strongly supercooled phase transitions. JCAP, 06:024, 2019.

[261] John Ellis, Marek Lewicki, and Jos Miguel No. Gravitational waves from first-order cosmological phase transitions: lifetime of the sound wave source. 3 2020.

[262] Chiara Caprini et al. Detecting gravitational waves from cosmological phase transitions with LISA: an update. JCAP, 03:024, 2020.

[263] Ue-Li Pen and Neil Turok. Shocks in the Early Universe. Phys. Rev. Lett., 117(13):131301, 2016.

[264] Alberto Roper Pol, Sayan Mandal, Axel Brandenburg, Tina Kahniashvili, and Arthur Kosowsky. Numerical Simulations of Gravitational Waves from Early-Universe Turbulence. Phys. Rev. D, 102:083512, 2020.

[265] Jose M. No. Large Gravitational Wave Background Signals in Electroweak Baryogenesis Scenarios. Phys. Rev., D84:124025, 2011.

[266] Alexandre Alves, Tathagata Ghosh, Huai-Ke Guo, and Kuver Sinha. Resonant Di-Higgs Production at Gravitational Wave Benchmarks: A Collider Study using Machine Learning. 2018.

[267] Alexandre Alves, Tathagata Ghosh, Huai-Ke Guo, Kuver Sinha, and Daniel Vagie. Collider and Gravitational Wave Complementarity in Exploring the Singlet Extension of the Standard Model. JHEP, 04:052, 2019.

[268] Alexandre Alves, Dorival Gonçalves, Tathagata Ghosh, Huai-Ke Guo, and Kuver Sinha. Di-Higgs Blind Spots in Gravitational Wave Signals. 7 2020.

[269] Heather Audley et al. Laser Interferometer Space Antenna. 2017.

[270] Xuefei Gong et al. Descope of the ALIA mission. J. Phys. Conf. Ser., 610(1):012011, 2015.

[271] Jun Luo et al. TianQin: a space-borne gravitational wave detector. Class. Quant. Grav., 33(3):035010, 2016.

[272] Hideaki Kudoh, Atsushi Taruya, Takashi Hiramatsu, and Yoshiaki Himemoto. Detecting a gravitational-wave background with next-generation space interferometers. Phys. Rev., D73:064006, 2006.

[273] Ansgar Denner. Techniques for calculation of electroweak radiative corrections at the one loop level and results for W physics at LEP-200. Fortsch. Phys., 41:307–420, 1993.

[274] L. Alvarez-Ruso, T. Ledwig, J. Martin Camalich, and M. J. Vicente-Vacas. Nucleon mass and pion-nucleon sigma term from a chiral analysis of lattice QCD data. Phys. Rev., D88(5):054507, 2013.

[275] Parikshit Junnarkar and Andre Walker-Loud. Scalar strange content of the nucleon from lattice QCD. Phys. Rev., D87:114510, 2013.

[276] Wei Chao, Huai-Ke Guo, and Jing Shu. Gravitational Wave Signals of Electroweak Phase Transition Triggered by Dark Matter. JCAP, 1709(09):009, 2017.

[277] Mikael Chala, Valentin V. Khoze, Michael Spannowsky, and Philip Waite. Mapping the shape of the scalar potential with gravitational waves. Int. J. Mod. Phys. A, 34(33):1950223, 2019.